FLUCTUATIONS IN AND OUT OF EQUILIBRIUM:
Thermalization, quantum measurements and Coulomb disorder

I n a u g u r a l – D i s s e r t a t i o n

zur

Erlangung des Doktorgrades

der Mathematisch-Naturwissenschaftlichen Fakultät

der Universität zu Köln

vorgelegt von

Jonathan Lux

aus Essen

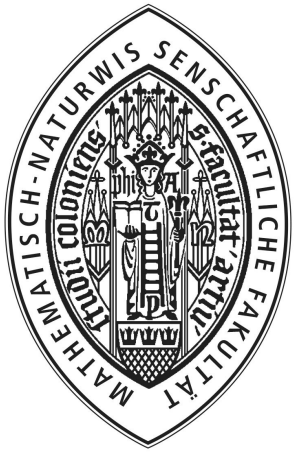

Köln
2016

Berichterstatter: Prof. Dr. Achim Rosch
Prof. Dr. Sebastian Diehl

Tag der letzten mündlichen Prüfung: 24.5.2016

Summary

This purely theoretical thesis covers aspects of two contemporary research fields: the non-equilibrium dynamics in quantum systems and the electronic properties of three-dimensional topological insulators.

In the first part we investigate the non-equilibrium dynamics in closed quantum systems. Thanks to recent technologies, especially from the field of ultracold quantum gases, it is possible to realize such systems in the laboratory. The focus is on the influence of hydrodynamic slow modes on the thermalization process. Generic systems in equilibrium, either classical or quantum, in equilibrium are described by thermodynamics. This is characterized by an ensemble of maximal entropy, but constrained by macroscopically conserved quantities. We will show that these conservation laws slow down thermalization and the final equilibrium state can be approached only algebraically in time. When the conservation laws are violated thermalization takes place exponential in time. In a different study we calculate probability distributions of projective quantum measurements. Newly developed quantum microscopes provide the opportunity to realize new measurement protocols which go far beyond the conventional measurements of correlation functions.

The second part of this thesis is dedicated to a new class of materials known as three-dimensional topological insulators. Also here new experimental techniques have made it possible to fabricate these materials to a high enough quality that their topological nature is revealed. However, their transport properties are not fully understood yet. Motivated by unusual experimental results in the optical conductivity we have investigated the formation and thermal destruction of spatially localized electron- and hole-doped regions. These are caused by charged impurities which are introduced into the material in order to make the bulk insulating. Our theoretical results are in agreement with the experiment and can explain the results semi-quantitatively. Furthermore, we study emergent lengthscales in the bulk as well as close to the conducting surface.

Deutsche Zusammenfassung

Die vorliegende rein theoretische Arbeit behandelt Aspekte zweier aktueller Forschungsbereiche: die Nicht-Gleichgewichtsdynamik von Quantensystemen und die elektronischen Eigenschaften von topologischen Isolatoren.

Im ersten Teil untersuchen wir die die Nicht-Gleichgewichtsdynamik in abgeschlossenen Quantensystemen. Dank neuartiger Technologien, vor allem im Bereich ultrakalter Quantengase, ist es möglich solche Systeme im Labor zu realisieren. Der Schwerpunkt liegt auf der Untersuchung des Einflusses langsamer hydrodynamischer Moden auf den Prozess der Thermalisierung. Generische Systeme im Gleichgewicht könne mittels Thermodynamik beschrieben werden. Diese ist charakterisiert durch ein Ensemble maximaler Entropie, unter Bedingungen die durch makroskopische Erhaltungssätze auferlegt werden. Wir werden zeigen, dass diese Erhaltungsgrößen die Thermalisierung verlangsamen, und der finale thermische Zustand nur algebraisch in der Zeit erreicht werden kann. Werden die Erhaltungssätze verletzt, erfolgt die Thermalisierung exponentiell in der Zeit. In einer anderen Studie berechnen wir Wahrscheinlichkeitsverteilungen von projektiven Quantenmessungen. Neu entwickelte Quantenmikroskope bieten die Möglichkeit neuartige Messprotokolle zu realisieren, die weit über die konventionellen Messungen von Korrelationsfunktionen hinausgehen.

Im zweiten Teil der Arbeit widmen wir uns neuartigen Materialien, welche in die Klasse der dreidimensionalen topologischen Isolatoren fallen. Auch hier haben neuartige experimentelle Methoden dazu geführt, dass diese Materialien in sehr guter Qualität hergestellt werden können und die topologischen Eigenschaften zum Vorschein treten. Ihr Transportverhalten ist jedoch noch nicht vollständig verstanden. Motiviert durch ungewöhnliche Messergebnisse in der optischen Leitfähigkeit, haben wir die Entstehung und thermische Vernichtung von räumlich begrenzten Elektron und Loch-Bereichen in diesen Materialien untersucht. Diese werden verursacht durch geladene Fremdatome welche ins Material eingebracht wurden um es isolierend zu machen. Unsere Ergebnisse sind im Einklang mit dem Experiment, welches durch diese Mechanismen semi-quantitativ erklärt werden kann. Des weiteren untersuchen wir emergente Längenskalen in diesen Systemen, sowohl im Inneren, als auch nahe der leitenden Oberfläche.

Contents

PART I:
Semiclassical dynamics after quantum quenches:
Hydrodynamic long-time tails and projective measurements **1**

1 Introduction I **2**

2 Ultracold atoms in optical lattices **15**
2.1 Producing a lattice for neutral atoms 15
2.2 Interactions 17
2.3 Quantum microscopes 19
2.4 Observing the unitary time evolution 21

3 Methods **23**
3.1 Derivation of effective Hamiltonians 23
3.2 Lattice scattering theory in $1d$ 25
3.3 Quasiparticle momentum distribution 34
3.4 Semiclassical dynamics after weak quantum quenches 39

4 Diffusion and fluctuating hydrodynamics **43**
4.1 Random Walks 44
4.2 Fluctuations 45
4.3 Scaling analysis of the diffusion equation 50
4.4 Long-time tails 51
4.5 Violation of the conservation laws 56
4.6 Mode couplings 58

5 Hydrodynamic long-time tails after a quantum quench **60**
5.1 Diffusive thermalization after weak quenches 63
5.2 Equilibrium results 69
5.3 Comparison to the Boltzmann equation 74
5.4 Exact diagonalization for strong quenches 76

6 Violation of the conservation laws: Numerical Results **79**
6.1 Thermalization in the absence of conservation laws 80
6.2 Relaxation in the driven system 82
6.3 Adiabatic limit 85

7 Quench dynamics and statistics of measurements **90**
7.1 Creation of quasiparticles 92
7.2 Scattering and emission 94
7.3 Time dependent results 97
7.4 Characterization of the final ensemble 100

8 Outlook I **104**

PART II:
Coulomb disorder in three-dimensional topological insulators **107**

9 Introduction II **108**

10 The experiment **112**
10.1 Optical properties of solids 114
10.2 Experimental results for the optical conductivity 115
10.3 Experimental results for the optical weight 117
10.4 Contribution of the surface states 119

11 Theoretical description of compensated semiconductors **121**
11.1 Doped semiconductors 121
11.2 The model 125
11.3 Numerical implementation 128

12 Low temperatures: Puddles and lengthscales **132**
12.1 Coulomb gap 132
12.2 Correlation functions and lengthscales 135
12.3 Puddles 151

13 Puddle destruction at finite temperatures **155**
13.1 Thermal screening 155
13.2 Numerical results 157
13.3 Comparison to the experiment 160

14 Including the surface states **162**
14.1 Dirac systems 162
14.2 Screening theory 163
14.3 Numerical implementation 168

14.4 Numerical results 169
14.5 Connection to the bulk lengthscales 177

15 Outlook II **179**

References **181**

PART I

Semiclassical dynamics after quantum quenches:

Hydrodynamic long-time tails and projective measurements

1 Introduction I

Non-equilibrium is the absence of equilibrium. A system in equilibrium is described by thermodynamics, a coarse-grained theory which only has the macroscopically conserved quantities of the system as degrees of freedom. The density matrix is of a universal form. Its structure is determined by having the highest entropy consistent with the values of the conserved quantities. Equilibrium is accompanied by a temporal invariance and expectation values are said to be time-independent. However, expectation values of non-conserved quantities fluctuate on microscopic scales. A macroscopic description is implicit in the notion of equilibrium. On the coarse-grained scales, correlations between different times depend only on the time difference.

Out of equilibrium this is in general not the case. Exceptions include non-equilibrium steady states. For example, externally driven systems can show a steady current flow. By contrast, in equilibrium the (average) current is zero. Due to the more complex temporal structure of non-equilibrium systems it is generically harder to describe these theoretically as compared to equilibrium systems. We start by introducing some terminology inherent to modern non-equilibrium quantum mechanics.

Closed quantum systems. In theoretical approaches to condensed matter systems it is (almost) always assumed that the system of interest is in thermal equilibrium. A coupling to an environment is implicitly assumed. The many degrees of freedom of the environment enter the description only via their statistical properties, for example via the temperature. If the environment is in equilibrium, and is much larger than the system of interest, it is called a *bath*. The Hilbert space of the total system is $\mathcal{H} = \mathcal{H}_{\text{system}} \otimes \mathcal{H}_{\text{environment}}$ where $\otimes$ denotes the tensor product. If the degrees of freedom of $\mathcal{H}_{\text{environment}}$ are traced out the dynamics in $\mathcal{H}_{\text{system}}$ is not unitary any more. Furthermore the state of the system has to be described as a mixed state, in contrast to the state of the full system which might be a pure state. In this approach also the energy stored in the degrees of freedom of $\mathcal{H}_{\text{system}}$ is not necessarily conserved any more. We will refer to this subsystem as an *open (quantum) system*.

We will consider the dynamics in *closed quantum systems*. They are defined by the property that they are isolated from their environment and are described by a time-independent Hamiltonian. This implies that the time evolution is unitary and that the energy is conserved. It is obvious that the closedness of a system, if it is not the full universe, can only be an approximation. However, in many experiments closed-

ness is a decent approximation. In particular in recent years new techniques have allowed experimentalists to realize quantum systems which are effectively closed on the timescales of the experiments. These systems are, among others, ultracold atoms in optical lattices. We will introduce them in the next section in more detail. Often these systems are well described by Hamiltonians known from condensed matter systems, like Hubbard models or Heisenberg models. The reason is that in both systems the relevant (low-energy) degrees of freedom are interacting particles in a periodic potential. While typical condensed matter are performed at temperatures between $10^{-3}K$ (^{3}He/ ^{4}He dilution refrigerator) and room temperature, ultracold atom experiments are performed at temperatures $10^{-9} - 10^{-4}\,K$.

In condensed matter systems the periodic potential is provided by the atomic nuclei. There collective low-energy excitations, phonons, are often assumed to be in equilibrium. They provide the aforementioned bath for the electronic and/or magnetic degrees of freedom. In optical lattices neutral atoms are trapped in periodic laser potentials. Regimes can be reached where there is no energy exchange between the atom and laser degrees of freedom. Therefore the atomic system can often be considered as closed on the experimental timescales. However, other processes restrict these timescales, for example atom losses.

In contrast to condensed matter systems, in optical lattice experiments the microscopic parameters can be tuned, among them are dimensionality, lattice structure and the interaction strength, exploring new regimes which are not realized in condensed matter systems. Furthermore quantities which are inaccessible in condensed matter systems can be measured. Quantum microscopes, for example, can resolve positions of individual atoms with single site precision. Due to the high control over the microscopic parameters also new experimental protocols can be realized.

Quantum quenches. In a quantum quench a parameter in the Hamiltonian is changed on very short timescale. If this is done fast enough, on a timescale smaller than all intrinsic timescales of the system, the quantum state does not change. This is in contrast to an *adiabatic* change of parameters. If the change of the parameter is performed very slowly, on a timescale much larger than all intrinsic timescales, the system remains in its time-evolving eigenstate if there are no energy crossings. This is the statement of the *adiabatic theorem*. Since in a quantum quench the time evolution operator is changed, but the quantum state is not, dynamical processes are induced. This is the case even if the system was in an equilibrium state, for example in the groundstate, before. The most-studied protocol, at least theoretically,

of a quantum quench is the following[1]:

(QQ1) Prepare the system in the groundstate of a Hamiltonian $\hat{H}(J_{\mathrm{ini}})$.

(QQ2) Instantaneously change $J_{\mathrm{ini}} \to J_{\mathrm{final}}$ to obtain the Hamiltonian $\hat{H}(J_{\mathrm{final}}) = \hat{H}_{\mathrm{f}}$.

(QQ3) Study the time evolution of an observable $\langle \hat{O} \rangle(t)$ with the new Hamiltonian $\hat{H}_{\mathrm{f}}$.

As the system was in the groundstate before the quench, but it is not afterwards, this can be viewed as a well-defined way to pump energy into the system. The problem of a quantum quench can formally be solved easily:

(SQ1) Diagonalize the final Hamiltonian $\hat{H}_{\mathrm{f}} |n\rangle = E_n |n\rangle$.

(SQ2) Decompose the initial state into the eigenstates $\{|n\rangle\}$ of $\hat{H}_{\mathrm{f}}$: $|\mathrm{ini}\rangle = \sum_n c_n |n\rangle$.

(SQ3) Calculate the unitary the time evolution for $t > t_{\mathrm{ini}}$ as

$$|t\rangle = \mathrm{e}^{-i\hat{H}_{\mathrm{f}}(t-t_{\mathrm{ini}})} |\mathrm{ini}\rangle = \sum_n c_n \mathrm{e}^{-i\hat{H}_{\mathrm{f}}(t-t_{\mathrm{ini}})} |n\rangle = \sum_n c_n \mathrm{e}^{-iE_n(t-t_{\mathrm{ini}})} |n\rangle \,. \tag{1.1}$$

(SQ4) Evaluate the observable of interest as (we use $t_{\mathrm{ini}} = 0$)

$$\begin{aligned} \langle \hat{O} \rangle(t) = \langle t|\hat{O}|t\rangle &= \sum_{n,m} c_m^* \, c_n \, \mathrm{e}^{i(E_m - E_n)t} \, \hat{O}_{mn} \\ &= \sum_n |c_n|^2 \, \hat{O}_{nn} + \sum_{n \neq m} c_m^* \, c_n \, \mathrm{e}^{i(E_m - E_n)t} \, \hat{O}_{mn}. \end{aligned} \tag{1.2}$$

In practice one already fails at step (SQ1). Here an exponentially large (in the number of particles) matrix has to be diagonalized. One can make use of symmetries, if present, to block-diagonalize $\hat{H}$ and in this way split the problem into smaller pieces. But nevertheless in general it is a hopeless task. It is possible to use brute-force numerical exact diagonalization methods (ED) to perform the scheme described above. But for interacting systems this is restricted to a small number of particles, typically $10 - 20$ on present day computers. Nevertheless it can be very useful. For short times one can use time-dependent perturbation theory. But also here the complexity grows exponentially with the order of perturbation theory.

[1]Throughout this thesis we use $\hbar = 1$. Then the unit of energy E is equal to the unit of frequency ω and the unit of momenta p is equal to the unit of $1/\mathrm{length} = 1/l$. The dimensions can be restored by $E = \hbar\omega$ and $p = \hbar/l$. We will reintroduce $\hbar$ only for dimensional considerations. Furthermore we use the common notation that operators acting on the Hilbert space $\mathcal{H}$ are denoted with a hat on top, for example $\hat{H}$ denotes the Hamilton operator. In addition we use the braket notation for quantum states as introduced in standard textbooks of quantum mechanics. Matrix elements of an operator $\hat{O}$ in a basis $\{|n\rangle\}$ are denoted by $\langle m|\hat{O}|n\rangle = \hat{O}_{mn}$. In continuous systems the sums have to be replaced by integrals. We further use the term "observable" for hermitian linear operators ($\hat{O} = \hat{O}^\dagger$) having real eigenvalues.

The formal solution, Eq. (1.2), does not really give any physical insight. In equilibrium, mean field theories and renormalization group schemes are very successful in identifying the relevant (low-energy) degrees of freedom. Nothing like this seems to be within reach here. Non-equilibrium field theory methods are often needed to make any progress [1–3].

In recent years time-dependent extensions of sophisticated numerical methods have been developed: most prominently, the non-equilibrium dynamical mean field theory (NEQ-DMFT) [4], and the time-dependent density matrix renormalization group (t-DMRG) [5]. Both are tailored to a certain class of models. DMFT is a self-consistent method for lattice models. The decisive approximation is the locality of the self energy. This approximation is better the higher the dimension or, more precisely, the larger the coordination number of the lattice. DMRG methods are only applicable for $1d$ systems or $2d$ systems in a rod geometry. In the modern formulation DMRG works with matrix product states, which can only partially capture the entanglement growth in generic non-equilibrium systems. Therefore the time range in which reasonable results are obtained is restricted.

From Eq. (1.2) one can see that the expectation values of conserved quantities are time-independent. A conserved quantity is defined by the property that the corresponding operator $\hat{C}$ commutes with the Hamiltonian: $[\hat{C}, \hat{H}] = 0$. Then the eigenstates of $\hat{C}$ are also eigenstates of $\hat{H}$ and the second term in Eq. (1.2) vanishes. The result is $\langle \hat{C} \rangle(t) = \sum_n |c_n|^2 \hat{C}_{nn}$ and independent of t. For example, the expectation value of the energy is $\langle \hat{H} \rangle(t) = \sum_n |c_n|^2 \hat{H}_{nn} = \sum_n |c_n|^2 E_n$.

Integrability. An exceptions to the failure of step (SQ1) are *integrable* models. Here the *Bethe ansatz* [6–9], a unitary transformation to a non-interacting model [10] or bosonization [11] allows one to diagonalize the Hamiltonian. In some cases it is even possible to analytically calculate the time dependence of observables after a quantum quench [12–19]. The hallmark of integrability is the existence of a macroscopic number of *local* conservation laws, called charges or constants of motion. Often this is the case in one dimensional models with short-ranged interactions. For example, the Heisenberg XXX [6] and XXZ chain [20], the transverse field Ising model [10], the Fermi Hubbard model [21, 22], the Luttinger liquid [11, 23], the Kondo model [24] and the Lieb-Liniger model [25, 26] are integrable in one dimension. They have been solved (diagonalized) in the respective references given above. In this models the dynamics is highly constrained as the initial expectation values of all the conserved charges cannot change during the time evolution. By contrast, generic

models only have a small number of conserved quantities related to the fundamental symmetries. Therefore integrable models cannot be described by conventional thermodynamics. Rather their stationary properties are described by generalized Gibbs ensembles (GGEs) [27, 28]. Here all the conserved charges have to be included into the density matrix.

From Eq. (1.2) it can be directly seen, with the projection onto the eigenstates $\hat{O} = |n\rangle \langle n|$, that there are always as many conserved quantities as the dimension of the Hilbert space. The addition local is essential. Here locality means that the conserved quantity can be written as a sum over a density which has its support on a finite number of lattice sites. Well-known examples include the energy, as a sum over the energy density, and the particle number, as a sum over the particle density. In general it can be very hard to find all conserved charges. It has also turned out that in some models quasi-local charges exist and are important to understand the dynamics [29]. For lattice models quasi-locality means that the corresponding density cannot be defined on a finite number of lattice sites but has exponential tails. Non-interacting models also have a macroscopic number of conserved quantities: the individual one-particle quantum numbers.

For real systems integrability can only be an approximation. Almost any additional term in the models mentioned above breaks the integrability, for example adding longer-ranged interactions. However, many recent experiments can be described by integrable models [30–35]. On the timescales of the experiments the dynamics is effectively integrable.

Another approach to distinguish integrable from non-integrable models is based on random matrix theory. It is known that the level spacing distribution of generic random matrices is described by Wigner-Dyson statistics [36]. The probability to find two subsequent eigenstates with a (normalized) distance s is $P_{\text{generic}}(s) \sim s^{\beta} \, \mathrm{e}^{-\gamma s^2}$. $\beta > 1$ and $\gamma > 0$ depend on the symmetry class. In either case the probability to find eigenvalues very close in energy, $s \to 0$, vanishes. In contrast to that, in integrable models a state does not "feel" the presence of the other states and the eigenvalues are uncorrelated. This leads to a Poisson distribution of the level spacings $P_{\text{integrable}}(s) \sim \mathrm{e}^{-\gamma s}$ [37].

Equilibration. A further observation can be made from Eq. (1.2): if $\langle \hat{O} \rangle (t)$ ever reaches a time-independent value, it can only be $\sum_n |c_n|^2 \, \hat{O}_{nn}$. Only if there are degeneracies in the spectrum, the second term in Eq. (1.2) can yield a time-independent contribution. But for generic systems we do not expect any degeneracies (in a sec-

tor with fixed particle number and, possibly, total momentum or magnetization). The reason is level repulsion: as described above the probability distribution of the level spacings in non-integrable models is $\sim s^{\beta>1}\,\mathrm{e}^{-\gamma s^2}$. The probability to have degeneracies $s \to 0$ is zero. Therefore, we expect for non-integrable models that $\langle \hat{O} \rangle(t) = \sum_n |c_n|^2 \, \hat{O}_{nn} + F^{\mathrm{ini}}_{\hat{O}}(t)$ where $F_{\hat{O}}$ has no time-independent term, and the superscript "ini" indicates that F depends on the initial state, see Eq. (1.2). A possible definition of equilibration is that for all initial states and all reasonable observables $\hat{O}$, to be specified below,

$$F^{\mathrm{ini}}_{\hat{O}}(t) = \sum_{n \neq m} c^*_m \, c_n \, \mathrm{e}^{i(E_m - E_n)t} \, \hat{O}_{mn} \underset{t\to\infty}{\longrightarrow} 0. \tag{1.3}$$

For finite systems, as for example simulated in ED, this definition can never be fulfilled. There are finite size corrections which lead to fluctuations on the right hand side. A pragmatic way is to take the definition in the thermodynamic limit. Furthermore there are *quantum revivals* [38, 39]. If there is only a finite number of eigenstates the right hand side of Eq. (1.2), it is a sum of finitely many periodic terms. Then, for mathematical reasons, $F^{\mathrm{ini}}_{\hat{O}}(t)$ returns arbitrarily close to its initial value during the time evolution. However, for generic systems this happens only on very long time scales. Following [40], the time evolution in a Hilbertspace of dimension N can be visualized by N clocks representing the phases ϕ of the individual eigenstates. The probability to find a specific configuration, for example the initial one, within a precision $\Delta\phi$ is $\sim (\frac{\Delta\phi}{2\pi})^N$. The recurrence time of the full wavefunction is then $R \sim (\frac{\Delta\phi}{2\pi})^{-N}/\omega$ where ω is the typical angular velocity – the energy. For $\frac{\Delta\phi}{2\pi} = 0.01$ and $\omega = 1eV \sim 1.52 \times 10^{15} sec^{-1}$ R exceeds the age of the universe already for $N = 17$. Nevertheless observables can show recurrences at smaller times but for macroscopic systems they are usually not of any relevance. Exceptions in a many particle system can occur in Bose Einstein condensates where the phases are locked [41].

Eq. (1.3) depends on the observable $\hat{O}$, which means that some observables can equilibrate while others do not. This is generically the case; for example, the energy does always equilibrate in this sense. But let us consider the operator $\hat{O}_{ab} = |a\rangle \langle b| + |b\rangle \langle a|$ where $|a\rangle$ and $|b\rangle$ are eigenstates with $E_a - E_b = \omega_{ab} \neq 0$ and $c_a, c_b \neq 0$. Then $\hat{O}_{ab}$ does never equilibrate.

The definition, Eq. (1.3), is only useful for *measurable* quantities. A broad class of measurable observables are local. Again, locality means that it can be written as a sum of local terms: $\hat{O}_{\mathrm{local}} = \sum_j \hat{O}_j$ where $\hat{O}_j$ has support (is non-zero) only in a small region of space. In lattice models it must have support only on a small

number of connected lattices sites. A prime example is the total magnetization in lattice spin models: $\hat{M} = \sum_j \sigma_j^z$. Thanks to linearity of the time-evolution, it is $F^{\mathrm{ini}}_{\hat{O}_{\mathrm{local}}}(t) = \sum_j F^{\mathrm{ini}}_{\hat{O}_j}(t)$. Then all parts $\hat{O}_j$ equilibrate independently and the rest of the system can serve as an environment. One can decompose the Hilbertspace as a tensor product $\mathcal{H} = \otimes_j \mathcal{H}_j$. The measurement is then performed only in one sector $\mathcal{H}_j$ and the result is averaged over j. Higher order correlation functions include more sectors. As long as the number of involved sectors is much smaller than the particle number, the rest of the system can still serve as an environment.

An important quantity which does not fall into this class is the occupation of the momentum modes $\hat{n}_k$. It can be accessed in time of flight measurements [42–44]. The equilibration of $\hat{n}_k$ implies *detailed balance*. The transition rate into the single-particle state $|k\rangle$ has to be equal to the transition rate out of $|k\rangle$. We will show further examples for the measurement of distribution functions in the next section.

Prethermalization. Some systems show an emergent integrability on short time-scales – *prethermalization* [45]. In this regime expectation values of observables show prethermalization plateaus which means that they are time independent for some time [46, 47]. But these values are not consistent with the thermal values. Only at later times the non-integrability eventually leads to true thermalization. Many numerical studies, for example [46, 48], and recent experimental studies, for example [32, 49], have investigated this regime. The quasi-stationary properties can be described by generalized Gibbs ensembles as in integrable systems. To be precise, all real world manifestations of integrable models are in the prethermalized regime. As aforementioned integrability can only be an approximation for real systems, which are then rather described as prethermalized.

Irreversibility. The microscopic equations underlying the dynamics, either quantum or classical, are time-reversal invariant. This is seemingly in contradiction to the second law of thermodynamics: it states that the entropy (almost) always increases, thereby distinguishing the two time directions. The system spontaneously "finds" its highest entropy state – the equilibrium. If the system of interest is coupled to a bath, it is plausible that the equilibrium, and thereby the time direction, in the subsystem is externally imposed. But what about closed systems?

Irreversibility requires a coarse-grained point of view. Formally, this is achieved by distinguishing microstates and macrostates. In a microstate all degrees of freedoms of the system are specified. In classical physics this corresponds to one point in

phase space, and in quantum mechanics this implies a knowledge of the full wavefunction or density matrix. This cannot be measured let alone experienced by the sensory organs. A macrostate is obtained by fixing the (average) values of some observables. This defines a probability distribution – an *ensemble* – as a macrostate is compatible with many microstates. In quantum mechanics, an ensemble is described by a mixed state and represented in terms of a density matrix. In this description the observables which are taken into account and all other degrees of freedom play a very different role. The fact that the microstate is not specified leads to fluctuations on microscopic scales.

In thermodynamics only the (average) values of macroscopically conserved quantities are specified. Usually these are the energy and the particle number. The corresponding thermodynamical ensemble is defined by having the largest entropy among all ensembles consistent with the given values. This is the fundamental assumption of statistical mechanics. Experience shows that this is often sufficient to describe experimental results. The entropy of a probability distribution $P = \{p_1, p_2, ...| \sum_j p_j = 1\}$ (a density matrix $\hat{\rho}$) is defined as

$$S(P) = -\sum_j p_j \log(p_j) \quad (S(\hat{\rho}) = -Tr\left(\hat{\rho}\log(\hat{\rho})\right)). \tag{1.4}$$

Under reasonable assumptions (most importantly additivity) the structure of the formula given above can be uniquely determined, see for example [40]. The prefactor has to be fixed by convention or normalization. The entropy is a measure for the lack of information. The maximum entropy assumption and the second law of thermodynamics then state that the time direction is fixed by the loss of information. This is, of course, not the full story. Most importantly broken symmetries are ubiquitous on all scales from particle physics to cosmology. By contrast, thermodynamic ensembles respect the symmetries of the system, see for example the famous article "More Is Different" by P. W. Anderson [50].

If a system can be locally described by a thermodynamic ensemble, a hydrodynamic description is appropriate. Here "locally" refers to a scale which is much smaller than the system size but much larger than any correlation length or mean free path. Then one can specify the time and space dependent temperature $T(\boldsymbol{r}, t)$ or, equivalently, the energy density $e(\boldsymbol{r}, t)$. The same holds for the densities of other conserved quantities. If one chooses a coarse-grained, thermodynamic or hydrodynamic, description of the system the fluctuations can be described only statistically.

It is common to refer to the equilibrium ensemble as the equilibrium state. We

will also use this terminology, however, one has to keep in mind that this refers to a probability distribution rather than to a (micro-)state.

A simple picture for irreversibility arises if one assumes that the dynamics is ergodic. Ergodicity means that during the time evolution with the microscopic equations the full available phase space is covered equally. Then, if the system is initialized in an atypical (=non-equilibrium) state, thermalization is just a matter of probabilities. For concreteness let us consider a classical closed system in which energy and particle number are conserved. Thermodynamically, this is described by a microcanonical ensemble where all microstates consistent with the given energy and particle number are equally probable. This probability distribution has the largest entropy among all possible distributions. Seemingly there are no atypical states.

However, from a coarse-grained perspective this is not true. We consider an oversimplified, yet very instructive, standard example: $N = 10^{23}$ molecules in a box. We assume that the probability for a distinguished particle to be in the left half of the box is $1/2$. We further assume that, independent of the energy, the number of available microstates in the macrostate $\{N_1, N_2 = N - N_1\}$ is $\binom{N}{N_1}$. Here N_1 denotes the number of molecules in the left half and N_2 denotes the number of molecules in the right half. We focus on a description with these macrostates giving a coarse-grained picture. We totally omit the energy conservation for conceptual clarity. And, obviously, quantum statistics is different.

The probability to find all the particles in one half of the box is $\sim 2^{-10^{23}}$. This number is so ridiculously small that one would need billions of terabytes to store its digits[2]. From the macroscopic point of view it is reasonable to call this an atypical state. The notion of equilibrium itself requires a coarse-grained, macroscopic, point of view. Otherwise it is not possible to distinguish typical from atypical, equilibrium from non-equilibrium, configurations. In practice an atypical state can be realized by connecting a ultrahigh vacuum chamber to a normal gas. If we release such a system it is intuitively clear that after some time the number of molecules in both boxes will be approximately the same (if they are of equal size). But we will never find that a macroscopic ultrahigh vacuum region emerges spontaneously. From the macroscopic point of view the process is irreversible. To produce an ultrahigh vacuum chamber requires a high effort and sophisticated technology. A non-equilibrium state is a highly fine-tuned state.

In equilibrium there will be fluctuations in the number of molecules per box. Assuming equal sized boxes and ergodicity, the expectation value per box is $\mu = N/2$.

[2]It is: 10^{23} bits $\sim 10^{22}$ bytes $\sim 10^{19}$ KB$\sim 10^{16}$ MB$\sim 10^{13}$ GB$\sim 10^{10}$ TB

The typical fluctuations are given by the square root of the variance of the corresponding probability distribution. The probability to find M excess molecules in the left or the right box, a macrostate $\{N/2+M, N/2-M\}$ or $\{N/2-M, N/2+M\}$, is

$$\begin{aligned} P_{\pm M} &= \frac{1}{2^N}\binom{N}{\frac{N}{2}\pm M} = \frac{1}{2^N}\frac{N!}{(\frac{N}{2}+M)!\ (\frac{N}{2}-M)!} \\ &\approx \frac{1}{2^N}\frac{\sqrt{2\pi N}\left(\frac{N}{\mathsf{e}}\right)^N}{\sqrt{4\pi^2((N/2)^2-M^2)}\left(\frac{\frac{N}{2}+M}{\mathsf{e}}\right)^{\frac{N}{2}+M}\left(\frac{\frac{N}{2}-M}{\mathsf{e}}\right)^{\frac{N}{2}-M}} \\ &= \frac{1}{\sqrt{2\pi(N/4-M^2/N)}}\mathsf{e}^{N\log\frac{N}{\sqrt{N^2-4M^2}}}\,\mathsf{e}^{M\log\frac{N-2M}{N+2M}} \approx \frac{1}{\sqrt{\frac{\pi}{2}N}}\,\mathsf{e}^{-\frac{2M^2}{N}}, \end{aligned} \tag{1.5}$$

where we have used Stirling's formula in the second line. The final result, valid in the limit $N \gg M$, is just a Gaussian distribution with variance $\sigma^2 = N/4$. Thus the typical number of excess molecules in one of the boxes is $\sigma = \sqrt{N}/2$: this describes the thermal fluctuations.

Note that we have not used the notion of time yet. By means of the ergodicity assumption, the temporal average is replaced by an ensemble average. The fluctuation formula, Eq. (1.5), is valid on large timescales. We can fix a macrostate at some instant of time by reintroducing the barrier and thereby cutting the box in half. We will find a macrostate $\{N/2+M_1, N/2-M_1\}$ with probability P_{M_1}. If we again release the barrier, say at time t_1, we can ask "What is the typical number of excess molecules M_2 at time $t_2 > t_1$?". This is an example of an unequal time correlation function and the answer depends only on $\Delta t = t_2 - t_1$. It is clear that $M_2(\Delta t \to 0) = M_1$ and $M_2(\Delta t \to \infty) = 0$. In formulating the question we have implicitly defined a non-equilibrium ensemble. At t_1 only microstates compatible with the macrostate $\{N/2+M_1, N/2-M_1\}$ are allowed and this is not the ensemble with the highest entropy consistent with N molecules.

Averaged over all possible $\{N/2+M_1, N/2-M_1\}$ macrostates at t_1, with the corresponding probability, one obtains the equilibrium unequal-time autocorrelation function $\langle M(t_1)M(t_2\rangle_{\rm eq}$. Its equal time value is $\sum_M M^2 P_M \approx \sigma^2 = N/4$. In diffusive systems functions of this type show algebraic long-time tails. If not averaged over all M_1, a non-equilibrium initial condition, they also dominate the thermalization process at late times.

Also in finite classical systems, due to mathematical reasons, the system will come back arbitrarily close to its initial configuration as described by the Poincaré recurrence theorem [51]. However, the recurrence time for a system of 10 or 20 particles

is again much larger than the age of the universe [52]. Thus it does not have any physical consequences for macroscopic systems.

The initial states in quantum quench setups are very often low entanglement states. Groundstates of gapped Hamiltonians, often chosen as initial states, show area laws for the entanglement entropy [53]. Often product states are chosen. Only the high effort of the experimentalists to prepare such an atypical state, by lowering the entropy using sophisticated cooling schemes, make it possible to investigate the non-equilibrium. Theorists don't care since product states are easily written down and can be nicely depicted. We will make use of this later.

All processes taking place in nature are accompanied by an entropy growth (referred to as friction or heating), an unavoidable consequence of the tendency to thermalize – or statistics. Even if it would be possible to microscopically change the time direction (for example by letting $\hat{H}$ to $-\hat{H}$ in a quantum system), the tiniest perturbation, which is unavoidable in practice, will hinder system to go back to its initial non-equilibrium state. Only if the non-equilibrium is artificially maintained, for example by driving, the (sub-)system can be prevented from going to equilibrium. Exceptions can arise in highly inhomogeneous systems as further discussed below.

Thermalization. Eq. (1.2) can also be written in terms of a density matrix $\rho_{\mathrm{QQ}}(t)$ as $\langle \hat{O} \rangle (t) = \mathrm{Tr}\left(\hat{O}\, \rho_{\mathrm{QQ}}(t) \right)$. The time-independent part is called the *diagonal ensemble*, its density matrix $\hat{\rho}_{\mathrm{DE}}$ is defined by

$$\hat{\rho}_{\mathrm{DE}} = \sum_n |c_n|^2 \, |n\rangle \, \langle n| \quad , \text{ then } \sum_n |c_n|^2 \, \hat{O}_{nn} = \mathrm{Tr}\left(\hat{O}\, \hat{\rho}_{\mathrm{DE}} \right). \tag{1.6}$$

$\hat{\rho}_{\mathrm{DE}}$ depends on all the details of the initial state via the macroscopically many numbers c_n. This is in vast contrast to the equilibrium density matrix $\hat{\rho}_{\mathrm{eq}}$, which only depends on a very small number of parameters. The full density matrix after a quantum quench can never become a thermal density matrix. The density matrix of the canonical ensemble $\hat{\rho}_{\mathrm{can}} = \exp\left(-\beta \hat{H}\right) / Z_{\mathrm{can}}$ depends only on one parameter, the temperature T, or, equivalently, its inverse $\beta = 1/T$ (we use $k_{\mathrm{B}} = 1$ throughout). $Z_{\mathrm{can}} = \mathrm{Tr}\left(\exp\left(-\beta \hat{H}\right) \right)$ denotes the canonical partition function. A possible definition of thermalization might be the following: a quantum system thermalizes if for all measurable observables $\hat{O}$ and all initial states:

$$\mathrm{Tr}\left(\hat{O}\, \hat{\rho}_{\mathrm{DE}} \right) = \mathrm{Tr}\left(\hat{O}\, \hat{\rho}_{\mathrm{eq}}(T, \dots) \right). \tag{1.7}$$

This implicitly defines the temperature T and possibly other, but only very few, pa-

rameters (fixed by the few macroscopically conserved quantities) as indicated by the dots. Again, the definition has to be understood modulo finite size effects and quantum revivals. According to the definition integrable models do not thermalize as they have many conserved quantities. But they can, and often do, equilibrate.

Another class of interacting systems which fail to thermalize are many-body localized systems [54, 55]. While in non-interacting disordered systems the single-particle states are, completely or partially (depending on the dimensionality) localized [56, 57], many-body localization is a complex interplay of disorder and interactions. First experiments have been reported recently [58, 59].

A widely accepted mechanism which leads to thermalization in closed quantum systems is the *eigenstate thermalization hypothesis* (ETH) [60, 61]. The essential assumptions are that 1) the diagonal matrix elements $\hat{O}_{nn} = O(E_n)$ depend smoothly on the energy and that 2) the off-diagonal matrix elements $\hat{O}_{m\neq n}$ are typically much smaller than the diagonal elements: $|\hat{O}_{m\neq n}| \ll |\hat{O}_{nn}|$. If we assume that the distribution of the energies is confined to the interval $I_{\langle\hat{H}\rangle,\Delta E} = [\langle\hat{H}\rangle - \Delta E/2, \langle\hat{H}\rangle + \Delta E/2]$ containing $\mathcal{N}_{\langle\hat{H}\rangle,\Delta E}$ states, we obtain from Eq. (1.2)

$$\begin{aligned}\langle\hat{O}\rangle(t) &\underset{t\to\infty}{\longrightarrow} \sum_n |c_n|^2\, \hat{O}_{nn} + \sum_{n\neq m} c_m^*\, c_n\, \mathrm{e}^{i(E_m-E_n)t}\, \hat{O}_{mn} \\ &\approx \sum_n |c_n|^2\, O(E_n) \approx \frac{1}{\mathcal{N}_{\hat{H},\Delta E}} \sum_{E\in I_{\langle\hat{H}\rangle,\Delta E}} O(E). \end{aligned} \tag{1.8}$$

The last formula is exactly the definition of the microcanonical ensemble. For $\Delta E \to 0$ the result is just $\langle\hat{O}\rangle(t) \underset{t\to\infty}{\longrightarrow} O(\langle\hat{H}\rangle)$, and only depends on one number: the expectation value of the energy $\langle\hat{H}\rangle$. In this way the universal regime of thermodynamics can be recovered. Since the result does not depend on the eigenstate that is picked out of $I_{\langle\hat{H}\rangle,\Delta E}$, provided that ΔE is small enough, this implies that each eigenstate is intrinsically thermal. A numerical study and further details on the ETH can be found in [62]. The ETH suggests a mechanism how thermalization arises in quantum systems. Following [62], in the initial state the thermal properties are hidden by fine-tuned phases of the contributing eigenstates. During the time evolution the different eigenstates dephase and, eventually, reveal their thermal nature. However, a full theory of quantum thermalization is not available at present.

In either case, quantum or classical, the non-equilibrium to equilibrium transition is unavoidable and is irreversible on all reasonable timescales. There are exceptions in inhomogeneous systems: either if the Hamiltonian itself is highly inhomogeneous, for example in systems showing many-body localization, or if the initial state is inho-

mogeneous. In the latter case the system can fail to thermalize in the thermodynamic limit. Consider, for example, the two boxes as above one filled with a gas of molecules the other initially empty. If we, hypothetically, increase the size of both boxes to an infinite volume, it is obvious that in the box which was initially empty there are always regions that are still empty. If the maximal velocity of the molecules is c, then regions which have a distance larger than ct from the former barrier cannot contain any molecule. Therefore, the density can never become homogeneous and the system fails to thermalize. This can be easily extended to quantum systems, where a maximal velocity is provided by Lieb-Robinson bounds [63].

Our work. We will consider two different quantum quenches which, in principle, can be realized with ultracold atoms in optical lattices.

In the first study we will investigate the bottleneck for thermalization in diffusive homogeneous system: the build-up of thermal fluctuations. While many theoretical approaches predict an exponential decay towards equilibrium, we find only an algebraic decay. We will describe the thermalization on a coarse-grained scale by fluctuating hydrodynamics. This generically leads to long-time tails. If we accept that quantum systems thermalize, we also have to accept that – close to equilibrium – they are described by hydrodynamics. As an example to demonstrate this, we will investigate the $1d$ bosonic Hubbard model. We will find that numerical results are in perfect agreement with predictions from hydrodynamics and linear response theory. Some of the results can be found in the publication [P1].

In a second study we will calculate the full distribution function of an observable. In conventional experiments only, usually first or second, moments are measured. The new experimental techniques make it possible to go beyond this. We will consider the fragmentation of a spin line into bound states. We will calculate the bound state distribution which arises as a result of projective quantum measurements. The model we use is the XXZ Heisenberg model. The results can be found in the publication [P2].

As a preparation, we will introduce the experimental systems we have in mind and the methods we have used in the next two sections. This is followed by a section on fluctuating hydrodynamics and diffusion.

2 Ultracold atoms in optical lattices

The field of ultracold quantum gases has offered a lot of trend-setting experiments during the last years and no doubt there are still more to come. Many review articles are available by now, we have mainly used [43, 44, 64–67] for the foundations presented below.

At the present day, temperatures as low as $\sim 10^{-9}\,K$ for bosons [68] and $\sim 10^{-5}\,K$ for fermions [69] can be realized in experiments. To reach these ultralow temperatures, sophisticated cooling schemes have been developed [64, 70, 71]. In experimental systems usually alkali atoms are used, having only a single valence electron. Depending on the number of neutrons they can be either bosonic (B) or fermionic (F). The most commonly used atoms are ^{87}Rb (B), ^{23}Na (B), ^{7}Li (B), ^{6}Li (F) and ^{40}K (F) [66]. Also the trapping of monoatomic [72] and diatomic [73] molecules has been reported.

We will focus on trapping neutral atoms with optical dipole traps. Alternatives include the trapping by inhomogeneous magnetic fields [74, 75]. Another related field is the realm of trapped atomic ions [76, 77].

2.1 Producing a lattice for neutral atoms

The reason that neutral alkali atoms can be trapped with laser light is that they have a simple dipole transition from $nS\,(l=0)$ to $nP\,(l=1)$ where l denotes the angular momentum quantum number and n the principal quantum number. For Alkali atoms, the energy difference is $\omega_0 = 1.5-2eV$, corresponding to a photon wavelengths of $1600-1200\,nm$. For simplicity, let us consider a toy atom that only has these two states, denoted by $|0\rangle$ and $|1\rangle$. Furthermore we assume only two constituents: a positive nucleus+core electrons, kept fix at a position $\boldsymbol{R}$ with total charge $+|e|$, and a negative valence electron with charge $-|e|$. Although this is of course oversimplified, it captures all the relevant physics and is a decent approximation for alkali atoms at low energies.

In second order perturbation theory, the energy shift of the groundstate in a static electric field $\boldsymbol{E}$ is given by $\alpha = |\langle 0|\hat{\mathrm{d}}\cdot\boldsymbol{E}|1\rangle|^2/\omega_0$. Here $\hat{\mathrm{d}} = e(\hat{\boldsymbol{r}}_e - \boldsymbol{R})$ denotes the dipole operator and α is the static polarizability. Laser fields are oscillating with a frequency ω. We denote the corresponding electric field by $\boldsymbol{E}(\boldsymbol{r},t) = \boldsymbol{E}_0(\boldsymbol{r})\,2\cos(\omega t) = \hat{\boldsymbol{e}}\,E_0(\boldsymbol{r})\,2\cos(\omega t)$. The oscillating field induces an oscillating dipole moment $\boldsymbol{p} = \hat{\boldsymbol{e}}\,p(\boldsymbol{r})2\cos(\omega t)$ in the atom. Its amplitude is given by $p(\boldsymbol{r}) = \alpha(\omega)E_0(\boldsymbol{r})$ where α is the dynamic polarizability, which depends on the laser frequency ω. The

induced dipole moment gives rise to an effective interaction potential for the atom [65]

$$V_{\text{dipole}}(\boldsymbol{r}) = -\tfrac{1}{2}\,\langle \boldsymbol{p}\cdot\boldsymbol{E}\rangle_t = -\tfrac{1}{2}\,\mathrm{Re}\,(\alpha(\omega))\;|E_0(\boldsymbol{r})|^2\,. \tag{2.1}$$

Here $\langle\cdot\rangle_t$ denotes an average over the rapidly oscillating terms, it arises as the timescale of the atom motion is much larger than $1/\omega$. $|E_0(\boldsymbol{r})|^2 = I(\boldsymbol{r})$ is the intensity of the laser field. The potential leads to a force $\boldsymbol{F} = -\nabla V_{\text{dipole}}(\boldsymbol{r}) = \frac{1}{2}\mathrm{Re}(\alpha(\omega))\nabla I(\boldsymbol{r})$.

The polarizability can be calculated to be [65]

$$\alpha(\omega) = \frac{2\omega_0}{\omega_0^2 - \omega^2 - i(\omega^3/\omega_0^2)\Gamma}\left|\langle 0|\hat{\mathbf{d}}\cdot\hat{\boldsymbol{e}}\,|1\rangle\right|^2 \quad \text{where } \Gamma = \frac{\omega_0^3}{3\pi\varepsilon_0 c^2}\left|\langle 0|\hat{\mathbf{d}}\cdot\hat{\boldsymbol{e}}\,|1\rangle\right|^2 \tag{2.2}$$

is the decay rate of the excited state. In the experimentally relevant regime [44] $\Gamma \ll |\Delta| \ll \omega_0$ where $\Delta = \omega - \omega_0$ is the *detuning*, it follows that $\mathrm{Re}\,(\alpha(\omega)) \approx -\left|\langle 0|\hat{\mathbf{d}}\cdot\hat{\boldsymbol{e}}\,|1\rangle\right|^2/\Delta = -\frac{3\pi\varepsilon_0 c^2}{\omega_0^3}\frac{\Gamma}{\Delta}$ and thus

$$V_{\text{dipole}}(\boldsymbol{r}) = \frac{\left|\langle 0|\hat{\mathbf{d}}\cdot\hat{\boldsymbol{e}}\,|1\rangle\right|^2}{2\Delta}\,I(\boldsymbol{r}) = \frac{3\pi\varepsilon_0 c^2}{2\omega_0^3}\frac{\Gamma}{\Delta}\,I(\boldsymbol{r}). \tag{2.3}$$

A spatially varying intensity provides a trapping potential for the atoms. Depending on whether the laser is red detuned ($\Delta < 0$) or blue detuned ($\Delta > 0$), the atoms can be attracted or repelled from the intensity maxima. The decay rate Γ limits the lifetime of the experimental system. Absorption of a single photon, with an energy $\sim eV$, heats the system up considerably. In the same limit considered above, the atom-photon scattering rate is given by $\Gamma_{\text{sc}} = \frac{3\pi\varepsilon_0 c^2}{2\omega_0^3}(\frac{\Gamma}{\Delta})^2\,I(\boldsymbol{r})$ such that $\Gamma_{\text{sc}} = \frac{\Gamma}{\Delta}V_{\text{dipole}}$. Typical experimental values are $\frac{\Gamma}{\Delta} \sim 10^{-6}$ [66], which guarantees that there is no energy exchange between the atoms and the laser system on a reasonable timescale. If $I(\boldsymbol{r})$ is periodic in space, the laser forms a periodic potential for the atoms. This can be reached by interference of counter propagating laser beams: the potential is then given as $V_{\text{dipole}}(\boldsymbol{r}) = V_0(\sin^2(k_x x) + \sin^2(k_y y) + \sin^2(k_z z))$. In addition, an harmonic trapping potential is used to prevent the atoms from leaving the lattice. By using different trappings in different directions, the motion of the atoms can effectively be confined to two or one spatial dimension.

The typical energy of an optical lattice is the *recoil energy*

$$E_r = \frac{\hbar^2}{2m^2\lambda^2} \tag{2.4}$$

where λ is the wavelength of the laser and m is the mass of the alkali atom. For

typical experimental values ($\lambda = 1000\,nm$ and $m = 85u$ for an Rb atom), the recoil energy is $\approx 10^{-11}\,eV \sim 10^{-7}\,K \sim 2\,kHz$. If the intensity of the laser is high enough, the atoms are confined to the potential minima (or maxima). The natural description of such a system at low energies is a lattice model using Wannier functions. The tunneling amplitude, or hopping strength, between the minima depends on the depth of the optical lattice V_0. It can be tuned in experiments. Tunneling to non-nearest neighbor sites is highly suppressed and lattice models with only nearest neighbor (nn) hopping provide a very good approximation [44]. In the limit $V_0 \gg E_r$, the nn-hopping amplitude J is approximately given by [44]

$$J \approx \frac{4}{\sqrt{\pi}} \left(\frac{V_0}{E_r}\right)^{3/4} \mathrm{e}^{-2\sqrt{V_0/E_r}}\, E_r. \tag{2.5}$$

In the Wannier basis, this leads to the hopping Hamiltonian

$$\hat{H}_0 = -J \sum_{\langle i,j \rangle} \hat{b}_i^\dagger \hat{b}_j \tag{2.6}$$

where i and j label the lattice sites and $\langle i, j \rangle$ indicates only nn-hopping.

2.2 Interactions

Optically trapped neutral atoms interact via van der Waals interactions due to the induced dipole moments. We will focus on two-particle scattering here. At large distances $r > r_c$, where r_c is an atomic lengthscale ($\sim nm$), this decays as $-C_6/r^6$ with $C_6 > 0$. The van der Waals interaction defines a lengthscale $a_c = (2m_r C_6/\hbar^2)^{1/4} \gg r_c$ where m_r is the reduced mass.

Two-particle scattering only depends on the relative coordinates and can therefore effectively be described by one-particle potential scattering. In $3d$ scattering theory, the outgoing wavefunction can be decomposed into parts having different rotational symmetry. They are distinguished by the angular momentum quantum number l. The isotropic part ($l = 0$) is called s-wave scattering, the $l = 1$ part is called p-wave scattering, etc. , as in the labeling of atomic orbitals. The energy of the $l > 0$ channels is separated from the s-wave channel by an energy $R_c \sim \hbar^2/(m_r a_c^2)$. Typical experimental values are $R_c \sim mK$ and if $T \ll R_c$ the $l > 0$ channels are effectively closed and only s-wave scattering is relevant, or open. This can be taken as the definition of the regime of ultracold atoms [44]. The s-wave scattering at low energies can be parametrized by a single parameter, the scattering length $a_s \sim a_c$. The corresponding scattering amplitude for radial momentum k is given by $f(k) = \frac{-a_s}{1+ika_s}$. This is the

exact result for a pseudopotential $V_{\text{pseudo}}(\boldsymbol{r}) = \frac{4\pi\hbar^2 a_s}{2m_r}\delta(\boldsymbol{r}) = g\delta(\boldsymbol{r})$. However, the regularization of the δ-function can cause problems [44, 66]. The important result is that the effective interaction is short-ranged and parametrized by a single parameter a_s. For indistinguishable fermions there is no s-wave scattering due to anti-symmetry. At low energies, $ka_s \ll 1$, they are effectively non-interacting.

In the pseudopotential approximation, the interaction between bosons is

$$\hat{H}_{\text{int}} = \tfrac{g}{2}\int d^3\boldsymbol{r}\, \hat{b}^\dagger_{\boldsymbol{r}}\, \hat{b}^\dagger_{\boldsymbol{r}}\, \hat{b}_{\boldsymbol{r}}\, \hat{b}_{\boldsymbol{r}}. \tag{2.7}$$

In the Wannier basis used for the lattice description this corresponds to an on-site interaction U. In the limit $V_0 \gg E_r$, this is given by [44]

$$U \approx \sqrt{\frac{8}{\pi}}\,\frac{a_s}{l}\,\left(\frac{V_0}{E_r}\right)^{3/4} E_r, \tag{2.8}$$

where l is the lattice constant. In combination with the hopping term, Eq. (2.6), this leads to the bosonic Hubbard model

$$\hat{H}_{\text{BH}} = -J\sum_{<i,j>}\hat{b}^\dagger_i\,\hat{b}_j + U\sum_i \hat{b}^\dagger_i\,\hat{b}^\dagger_i\,\hat{b}_i\,\hat{b}_i\,. \tag{2.9}$$

This one band approximation is valid as long as the energy to the first excited band is much larger than the temperature and U. Furthermore the Wannier functions have to decay on a smaller length than the lattice constant l. The ratio $J/U \approx \sqrt{2}\,(l/a_s)\,\mathrm{e}^{-2\sqrt{V_0/E_r}}$ can be tuned by the lattice depth V_0.

The bosonic Hubbard model has two quantum phases: the Mott insulator and the Bose-Einstein condensate (BEC). The corresponding quantum phase transition has been first observed in $3d$ [78]. The critical value of U/J depends on the dimensionality. In [78] it was estimated to $(U/J)_{\text{exp},3d} \approx 36$. The theoretical value (obtained from quantum Monte Carlo) is $(U/J)_{\text{theory},3d} \approx 29.34$ [79].

Bound states do usually not change the scattering picture given above. In the pseudopotential approximation, there is only a single bound state, the pole of $f(k)$, with binding energy $E_b = \hbar^2/(2m_r a_s^2)$ (for $a_s > 0$) below the scattering continuum. In real systems there are many bound states: approximately 100 for ^{87}Rb [44]. However, at low energies they are not in resonance with the scattering states. The energy of the bound states can, under the conditions described below, be tuned by Feshbach resonances [44, 66]. In this way, the scattering length can be directly tuned. The common situation is the presence of different atomic species, usually hyperfine

states, which have different magnetic moments in the open and closed channels. For different fermion species there can be s-wave scattering if the spin, here the nuclear spin, wavefunction is in a triplet state. If there is a bound state in the closed (singlet) channel at the appropriate energy, the wavefunctions hybridize and a resonance is encountered. The scattering length can then be effectively described by $a_s(B) = a_s\,(1 - \frac{\Delta B}{B-B_0})$ [44] where B denotes the magnetic field, and B_0 and ΔB are the position and the width of the resonance, respectively. The scattering length, and thereby the interaction strength $\sim a_s$, can be tuned from $-\infty$ to ∞. The is widely used, especially to explore the BCS-BEC crossover $k_F|a_s| \sim 1$ [80, 81] and the unitary limit $k_F a_s \to \infty$ [82, 83].

A new regime is offered by the trapping of polar molecules with a permanent dipole moment [84–86], leading to long-ranged interactions. This can be used to design effective spin-spin interactions which, for example, can support to topological phases [87].

2.3 Quantum microscopes

In the first course on quantum mechanics one usually learns that measurements on a quantum mechanical systems lead to a collapse of the wavefunction. Let us assume that the quantum system is in a state $|\Psi\rangle$ and that the measurement operator is given by $\hat{O} = \sum_n O_n \,|n\rangle\,\langle n|$. Then it is said that the probability to measure O_n is $P_n(\hat{O}) = |\,\langle\Psi|n\rangle\,|^2$ and that the system is in the state $|n\rangle$ after the measurement. If only one measurement is performed, with an outcome O_{n_1}, the only information that can be extracted is that $P_{n_1}(\hat{O}) \neq 0$. But if many measurements are performed on the same quantum state, one can, in principle, obtain the distribution function $P_n(\hat{O})$.

Probability distributions can be fully characterized by their moments. For a Gaussian distribution, all higher moments can be obtained from the first (expectation value) and second (variance) moments. In almost all condensed matter experiments expectation values or second order correlation functions are measured. Exceptions include the measurement of full counting statistics of charge transfer in quantum dots [89–91]. Quantum microscopes go beyond this as they can detect the position of individual atoms in an optical lattice with single site precision. The first quantum microscopes were build for bosonic atoms [88, 92]. Recently, in 2015, several groups also reported on the realization of quantum microscopes for fermions [69, 93–95]. In Fig. 2.1 quantum microscope images taken from [88] are shown. To obtain the images, the lattice depth V_0 is increased by a factor of ~ 100 to fix the position of the atoms. This is the actual measurement process in the sense described above. To detect the

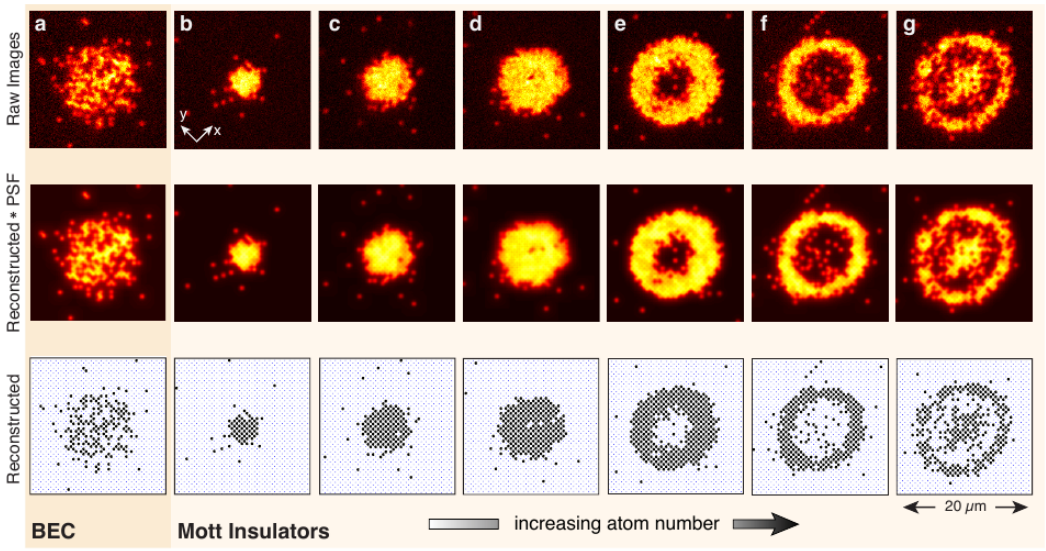

Figure 2.1: **Quantum microscope images showing the BEC to Mott insulator transition.** (taken from [88]) The light dots in the upper two rows indicate the presence of an atom. In the lowest row reconstructed pictures are shown, depicting the full lattice configuration of the atom cloud. The position of single atoms can be determined with single-site precision. Ring shaped structures arise due to the harmonic trapping potential. In the Mott insulating phase, number fluctuations are highly suppressed, as can be directly seen from the images.

atoms fluorescence imaging is used. Near resonant light is shone onto the sample and the scattered photons are detected. Due to pairwise losses, the atom number can be measured only modulo 2 in this way. The corresponding measurement operator is the projection operator onto product states ($\hat{N} = \hat{n}_1 \otimes \hat{n}_2 \otimes \dots$). It can already be seen from the single-shots in Fig. 2.1 that the typical configurations (those occurring with a high probability) are quite different in the respective quantum phases, see also [96]. While in the BEC phase the occupation numbers highly fluctuate from site to site, the occupation in the Mott phase is almost uniform. From the images, in principle, full distribution functions of $\hat{N}$ can be obtained. This was, for example, used to detect string order [97] and to measure the entanglement entropy for the first time [98].

For ultracold gases, also other techniques exist to measure higher order correlation functions or even full distribution functions [49, 99–101]. For example, in [100] correlation functions up to 8th order were measured by matter wave-interferometry of one-dimensional superfluids. The authors performed a direct test of the Wick decomposition of higher order correlation functions into lower order ones, a pillar of quantum field theory.

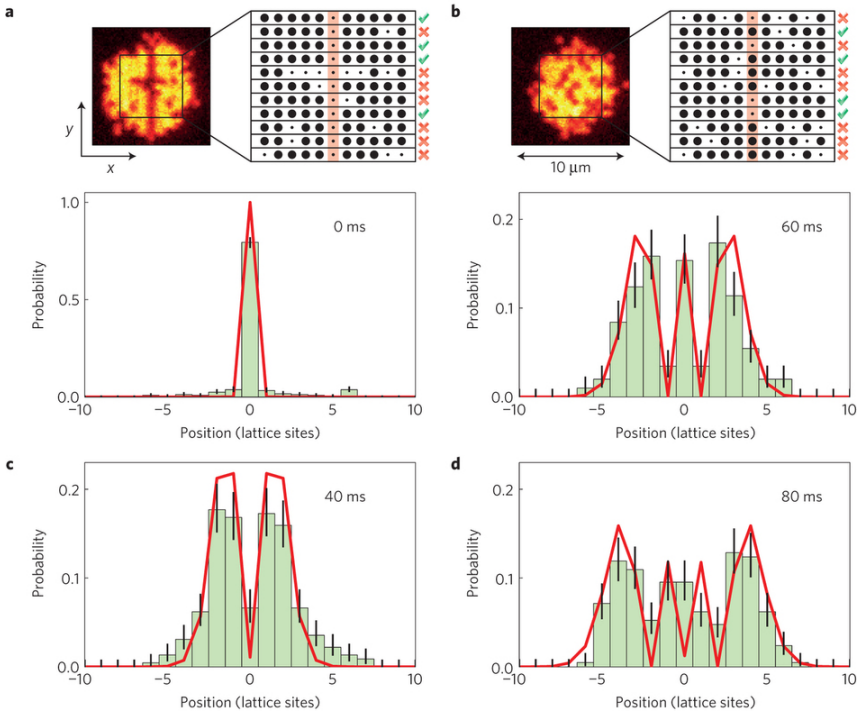

Figure 2.2: **Time evolution of the probability distribution of a single particle in a $1d$ lattice.** (taken from [102]) Panels a) and b) show the quantum microscope images from which the distribution functions were obtained. Post-selection was used to restrict the initial state. The hopping in y-direction was suppressed leading to an array of decoupled $1d$ systems. The Hamiltonian governing the unitary time-evolution is of nearest neighbor hopping type. This single-particle problem can be exactly solved, see the main text, and the result is indicated by the red lines.

2.4 Observing the unitary time evolution

To investigate the non-equilibrium, the quantum microscopes were used to measure time and spatially resolved probability distributions [102–107]. To do so the system has to be prepared in the same non-equilibrium state many times and the measurements are performed at different times. The simplest example of a free particle hopping on a $1d$ lattice was demonstrated in [102]. The main result from this publication is shown in Fig. 2.2. Here many decoupled $1d$ lattices were measured at the same time. The experiment made use of the fact that it is not only possible to read out configurations with the quantum microscope, but that also the hyperfine states of the atoms can be addressed with single-site precision [108]. In the Mott insulating phase, the two different hyperfine species can effectively realize an isotropic Heisenberg model [109, 110]. In the experiment, a single "spin-flip" was performed in a "ferromagnetic" background. This one magnon problem can be solved exactly. As the

magnetization is conserved, it is equivalent to a free particle hopping on a lattice. If the flipped spin was at the initial time t_{ini} at lattice site 0, the probability to find it at time t on site n is $J_n^2\left(J_{\mathrm{ex}}(t-t_{\mathrm{ini}})\right)$ [102]. Here J_n denotes the n-th Bessel function of the first kind and J_{ex} is the effective exchange coupling, estimated by the experimentalists to $\approx 65\,Hz$. This exact result is shown by the red lines in Fig. 2.2. One can see the very good agreement with the experimental data. This demonstrates that the time evolution is unitary, implying that the system is closed on the timescales of the experiment. Deviations are due to the imperfect initial state, see the picture at $0\,ms$, and residual temperature effects.

3 Methods

In this section we will provide the methods that we have used to study the dynamics after quantum quenches. In the limit we will consider, the dynamics can be described in terms of a dilute (low-density) gas of long-lived quasiparticles. The quasiparticles are protected by a large gap and we will not consider excitations above this gap. These, however, will emerge on large time scales. The creation and the scattering of quasiparticles will be calculated fully quantum mechanically. We will use the exact two-particle creation and scattering rates in the effective Hilbertspace without gap excitations. The negligence of higher order scattering is justified by the low density of quasiparticles. Their propagation will be treated semi-classically which, again, is a valid approximation in the dilute limit. The dynamics of the quasiparticles is governed by effective Hamiltonians in the respective subspace.

3.1 Derivation of effective Hamiltonians

The typical situation we will encounter is the following: the Hamiltonian

$$\hat{H} = \begin{pmatrix} \hat{H}_0 & \hat{H}_J & 0 & \\ \hat{H}_J^\dagger & \hat{H}_U & \hat{H}_J & \vdots \\ 0 & \hat{H}_J^\dagger & \hat{H}_{2U} & \\ & \cdots & & \ddots \end{pmatrix} \tag{3.1}$$

naturally divides the Hilbertspace in different sectors. They are separated by an energy U and coupled by an energy $J \ll U$. We are interested in the dynamics in a sector with fixed U energy. In this subsection, we use the notation that the subscript s on the Hamiltonian $\hat{H}_s$ indicates the maximal energy of its matrixelements. We include the couplings to the other sectors only perturbatively. One possibility to achieve this, is to employ a unitary transformation $\hat{U}$ such that the new Hamiltonian has the structure

$$\hat{\tilde{H}} = \hat{U}\hat{H}\hat{U}^\dagger = \begin{pmatrix} \hat{H}_0 & \hat{H}_{\frac{J^2}{U}} & 0 & \\ \hat{H}^\dagger_{\frac{J^2}{U}} & \hat{H}_U & \hat{H}_{\frac{J^2}{U}} & \vdots \\ 0 & \hat{H}^\dagger_{\frac{J^2}{U}} & \hat{H}_{2U} & \\ & \cdots & & \ddots \end{pmatrix}. \tag{3.2}$$

A well-known example is the Schrieffer-Wolff transformation, originally used to derive the Kondo Hamiltonian from the Anderson Hamiltonian [111]. Further applica-

tions include the derivation of the Heisenberg model from the Hubbard model [112] and the strong disorder renormalization group [113]. In [111], the authors used the following formulation: the Hamiltonian is split into $\hat{H} = \hat{H}_0 + \hat{H}_1$ where H_0 acts within the Hilbertspace of interest and $\hat{H}_1$ collects all other terms. The unitary transformation is written as $\hat{U} = \mathrm{e}^{\hat{S}}$ where $\hat{S}$ is anti-unitary $\hat{S}^\dagger = -\hat{S}$, then:

$$\begin{aligned}\hat{\tilde{H}} =& \hat{U}\hat{H}\hat{U}^\dagger = \mathrm{e}^{\hat{S}}\left(\hat{H}_0 + \hat{H}_1\right)\mathrm{e}^{-\hat{S}} = (1 + \hat{S} + \tfrac{1}{2}\hat{S}^2 + \dots)\left(\hat{H}_0 + \hat{H}_1\right)(1 - \hat{S} + \tfrac{1}{2}\hat{S}^2 + \dots) \\ =& \hat{H}_0 + \hat{H}_1 + [\hat{S}, \hat{H}_0 + \hat{H}_1] \\ & - \hat{S}\left(\hat{H}_0 + \hat{H}_1\right)\hat{S} + \tfrac{1}{2}\hat{S}^2\left(\hat{H}_0 + \hat{H}_1\right) + \tfrac{1}{2}\left(\hat{H}_0 + \hat{H}_1\right)\hat{S}^2 + \mathcal{O}\left(\hat{S}^3\right). \end{aligned} \tag{3.3}$$

If the condition $[\hat{S}, \hat{H}_0] \stackrel{!}{=} -\hat{H}_1$ is fulfilled, it is $\hat{\tilde{H}} = \hat{H}_0 + \frac{1}{2}[\hat{S}, \hat{H}_1] + \mathcal{O}\left(\hat{S}^3\right)$. If H_0 has matrixelements $\sim U$ and H_1 has matrixelements $\sim J$, the matrixelements of $\hat{S}$ are $\sim J/U$. If $|J/U| \ll 1$ a perturbative expansion in $\hat{S}$ is justified. Then the effective Hamiltonian to leading order reads

$$\hat{H}_{\text{eff}} = \underbrace{\hat{H}_0}_{\sim U} + \underbrace{\tfrac{1}{2}[\hat{S}, \hat{H}_1]}_{\sim J^2/U} + \mathcal{O}\left(J^3/U^2\right). \tag{3.4}$$

An equivalent approach is the following: the Schrödinger equation is written as

$$\begin{pmatrix} \hat{H}_U & \hat{H}_J \\ \hat{H}_J^\dagger & \hat{H}_0 \end{pmatrix} \begin{pmatrix} \Psi_U \\ \Psi_0 \end{pmatrix} = E \begin{pmatrix} \Psi_U \\ \Psi_0 \end{pmatrix}, \tag{3.5}$$

where Ψ_U and Ψ_0 denote the wavefunction in the high-energy and low-energy subspace, respectively. The first equation can be solved for Ψ_U to obtain $\Psi_U = (E - \hat{H}_U)^{-1}\hat{H}_J\Psi_0$. Inserting this into the second equation yields

$$\left(\hat{H}_0 + \hat{H}_J^\dagger (E - \hat{H}_U)^{-1}\hat{H}_J\right)\Psi_0 = E\,\Psi_0. \tag{3.6}$$

If we now replace the energy E on the left hand side by the energy scale of interest and $\hat{H}_U$ by the typical size of its matrixelements, we obtain $E - \hat{H}_U \to -U$. Then the effective Hamiltonian can be read off from the effective Schrödinger equation in the low-energy subspace

$$\hat{H}_{\text{eff}}\,\Psi_0 = \left(\hat{H}_0 - \frac{1}{U}\hat{H}_J^\dagger\hat{H}_J\right)\Psi_0 = E\,\Psi_0. \tag{3.7}$$

Again, the leading order correction is $\sim J^2/U$.

The physical process associated with this are excitations into the gapped states,

called *virtual processes*. For example in the Heisenberg model, when derived from the Hubbard model, these describe spin flips. They can occur only via charge excitations (double occupancies), which leads to a spin-flip rate of $\sim J^2/U$.

3.2 Lattice scattering theory in $1d$

On a lattice, the dispersion of a free particle is of $\cos$ form. If the hopping amplitude on the lattice is $-J$ and the lattice constant is a, the dispersion in one dimension reads $\epsilon(k) = -2J\cos(ak)$. The corresponding group velocity is $v_k = \partial_k \epsilon(k) = 2Ja\sin(ak)$. The momenta are defined only modulo $2\pi/a$. We will refer to this as the lattice momentum. We restrict ourselves to the first Brillouin zone (1. BZ), such that all momenta are defined in the interval $(-\pi/a, \pi/a]$. Equations involving different momenta have to be understood in that context. Furthermore we will use $a = 1$ for convenience. The momenta are then dimensionless, to be understood as measured in units $\hbar/a$. On a finite lattice the momenta are discrete in steps of $2\pi/L$ where L denotes the number of lattice sites. We assume periodic boundary conditions and an even number of lattice sites for the moment. The possible momenta in the first Brillouin zone, as defined above, are then $k_n = \frac{2\pi n}{L}$, where $n = -L/2+1, \ldots, L/2-1, L/2$ is an integer. In the limit $L \to \infty$ the lattice momenta become continuous, and the momentum sums can be replaced by integrals:

$$\frac{1}{L}\sum_k f(k) = \frac{1}{2\pi}\sum_k \Delta k\, f(k) \underset{L\to\infty}{\longrightarrow} \int_{-\pi}^{\pi} \frac{dk}{2\pi} f(k). \tag{3.8}$$

In elastic two-particle scattering the total momentum and the total energy are conserved. This gives $d+1$ equations for $2d$ unknown variables: the momenta of the outgoing particles. In $d = 1$ we have two equations for two unknowns. This fixes the lattice momenta, and thereby the energy, of the outgoing particles completely. However, there can be *Umklapp scattering*, which does not conserve the total momentum but only the total lattice momentum. We will use the convention that incoming momenta are denoted by k_1, k_2 and outgoing momenta are denoted by p_1, p_2. The total momentum is denoted by K. If both particles have the same hopping amplitude, say $-J$, the individual lattice momenta are conserved:

$$\begin{aligned} k_1 + k_2 &= p_1 + p_2 \\ 2J\cos(k_1) + 2J\cos(k_2) &= 2J\cos(p_1) + 2J\cos(p_2) \\ \underset{k_1+k_2\neq\pm\pi}{\Longrightarrow} \quad & (p_1 = k_1 \text{ and } p_2 = k_2) \;\text{ or }\; (p_1 = k_2 \text{ and } p_2 = k_1)\,. \end{aligned} \tag{3.9}$$

An exception arises when $k_1+k_2=\pm\pi$. Then the total energy is zero and all outgoing momenta $p_1=\pi/2+q, p_2=\pi/2-q$ with $q\in(-\pi/2,\pi/2)$ fulfill energy and momentum conservation. As there are L different momentum states, the probability to have $k_1+k_2=\pm\pi$ is (assuming an approximate uniform distribution) $\sim 1/L$. Therefore the effect can be neglected in the limit $L\to\infty$.

The conservation of the individual lattice momenta, Eq. (3.9), is not present in higher dimensions. It is the reason that many one dimensional can be solved exactly, which are precisely the integrable models which we introduced in the introduction. The task in solving such models is then to find the degrees of freedom which maintain their momenta. As an example, we consider the transverse field Ising model [10]

$$\hat{H}=-J\sum_i(g\hat{\sigma}_i^x+\hat{\sigma}_i^z\hat{\sigma}_{i+1}^z). \tag{3.10}$$

In the ferromagnetic (assuming $J>0$) phase, $g<1$, these are domain walls which separate spin-up and spin-down domains (in the $\hat{\sigma}^z$ basis). In the paramagnetic phase, $g>1$, these are flipped spins (in the $\hat{\sigma}^x$ basis) [10]. In the ferromagnetic phase, up-down domain walls have the same hopping amplitude as down-up domain walls, namely $-Jg$. In the paramagnetic phase there is only one excitation having a hopping amplitude of $-J$. In either case the individual momenta in a scattering event are conserved and the wavefunction can acquire only a phase. As aforementioned these models fail to thermalize.

However, if two (quasi-)particles with different hopping amplitudes scatter they can exchange momentum and energy. For example in the bosonic Hubbard model with large U/J, holons (empty sites) and doublons (doubly occupied sites) serve as stable quasiparticles and they show different hopping rates.

In the general case of the scattering of two different species with hopping amplitudes $-J_1$ and $-J_2$, it is

$$\begin{aligned} k_1+k_2&=p_1+p_2\\ 2J_1\cos(k_1)+2J_2\cos(k_2)&=2J_1\cos(p_1)+2J_2\cos(p_2)\\ \implies&(p_1=k_1 \text{ and } p_2=k_2) \end{aligned} \tag{3.11}$$

$$\text{or}\quad\begin{cases} p_1 &= 2\,\mathrm{ArcTan}\left(\dfrac{J_2\sin\left(\frac{k_1}{2}+k_2\right)-J_1\sin\left(\frac{k_1}{2}\right)}{J_2\cos\left(\frac{k_1}{2}+k_2\right)+J_1\cos\left(\frac{k_1}{2}\right)}\right)\\ p_2 &= 2\,\mathrm{ArcTan}\left(\dfrac{J_1\sin\left(\frac{k_2}{2}+k_1\right)-J_2\sin\left(\frac{k_2}{2}\right)}{J_1\cos\left(\frac{k_2}{2}+k_1\right)+J_2\cos\left(\frac{k_2}{2}\right)}\right) \end{cases}. \tag{3.12}$$

The first solution, Eq. (3.11) describes a transmission event, if microscopically possible, where the individual momenta are conserved. By contrast the second solution, Eq. (3.12), does change the individual momenta (if $J_1 \neq J_2$) and describes a reflection event.

As a concrete example we consider the situation when the transmission only occurs via a state which is separated by an energy gap. This is precisely the situation we will encounter in the bosonic Hubbard model. Here the transmission channel in doublon-holon scattering can be accessed only via a state without double occupancy. We denote the different hopping amplitudes by J_1 and J_2 and choose a basis $\{\{|x_1, x_2\rangle, x_1 \in \mathbb{Z}, x_2 \in \mathbb{Z}, x_1 \neq x_2\}, \{|x, x\rangle \equiv |x\rangle, x \in \mathbb{Z}\}\}$. Here x_1 and x_2 denote the position of the particle of species 1 and species 2, respectively. The state with $x_1 = x_2$ is denoted by $|x\rangle$ and separated by an energy gap U from the states with $x_1 \neq x_2$. The hopping onto this state can have a possibly different amplitude J_3. The Hamiltonian can be written as

$$\hat{H}|x\rangle = U|x\rangle + J_3\left(|x+1, x\rangle + |x-1, x\rangle + |x, x+1\rangle + |x, x-1\rangle\right) \tag{3.13}$$

$$\hat{H}|x, x-1\rangle = J_1|x+1, x-1\rangle + J_3|x-1\rangle + J_3|x\rangle + J_2|x, x-2\rangle \tag{3.14}$$

$$\hat{H}|x, x+1\rangle = J_1|x-1, x+1\rangle + J_3|x+1\rangle + J_3|x\rangle + J_2|x, x+2\rangle \tag{3.15}$$

$$\begin{aligned}\hat{H}|x, x+r\rangle =& J_1\left(|x-1, x+r\rangle + |x-1, x+r\rangle\right) \\ &+ J_2\left(|x, x+r-1\rangle + |x, x+r+1\rangle\right)\end{aligned} \tag{3.16}$$

where the last line holds for $r \geq 2$ and $r \leq -2$. The eigenstates of this Hamiltonian can be classified as bound states and scattering states. For the calculation of the scattering rates it is convenient to use relative coordinates: we define $r = x_1 - x_2$ and $R = \frac{x_1+x_2}{2}$. Note that R can take half-integer values but to have $x_1, x_2 \in \mathbb{Z}$ it is $R \in \mathbb{Z} + \frac{1}{2}$ if r odd and $R \in \mathbb{Z}$ if r even. We could have also chosen $\tilde{R} = x_1 + x_2$ but, of course, at the end the result does not depend on the choice of the basis.

The new basis is $\{\{|r, R\rangle, r \neq 0, (r \in 2\mathbb{Z}, R \in \mathbb{Z}) \text{ or } (r \in 2\mathbb{Z}+1, R \in \mathbb{Z}+\frac{1}{2})\}, \{|0, R\rangle \equiv |R\rangle, R \in \mathbb{Z}\}\}$. We then perform a Fourier transformation in the center of position coordinate R. We define

$$|r, K\rangle = \frac{1}{\sqrt{L}} \sum_{R \in \mathbb{Z} + \frac{1}{2}(r \bmod 2)} \mathrm{e}^{iKR}|r, R\rangle \text{ and } |r, R\rangle = \frac{1}{\sqrt{L}} \sum_{K \in 1.\mathrm{BZ}} \mathrm{e}^{-iKR}|r, K\rangle \tag{3.17}$$

$$|K\rangle = \frac{1}{\sqrt{L}} \sum_{R \in \mathbb{Z}} \mathrm{e}^{iKR}|R\rangle \text{ and } |R\rangle = \frac{1}{\sqrt{L}} \sum_{K \in 1.\mathrm{BZ}} \mathrm{e}^{-iKR}|K\rangle\,. \tag{3.18}$$

In this new basis the Hamiltonian reads

$$\hat{H}\,|K\rangle = U\,|K\rangle + 2J_3\,\cos\left(\tfrac{K}{2}\right)\,|1,K\rangle + 2J_3\,\cos\left(\tfrac{K}{2}\right)\,|-1,K\rangle \tag{3.19}$$

$$\hat{H}\,|1,K\rangle = 2J_3\,\cos\left(\tfrac{K}{2}\right)\,|K\rangle + J_K^*\,|2,K\rangle \tag{3.20}$$

$$\hat{H}\,|-1,K\rangle = 2J_3\,\cos\left(\tfrac{K}{2}\right)\,|K\rangle + J_K\,|-2,K\rangle \tag{3.21}$$

$$\hat{H}\,|r,K\rangle = J_K\,|r-1,K\rangle + J_K^*\,|r+1,K\rangle \tag{3.22}$$

where again the last line is valid $r \geq 2$ or $r \leq -2$. We have defined

$$J_K = \mathsf{e}^{iK/2}J_1 + \mathsf{e}^{-iK/2}J_2 = \mathsf{e}^{i\phi_K}I_K \tag{3.23}$$

where $\phi_K \in [0, 2\pi)$ and $I_K > 0$. The Hamiltonian does not couple sectors with different K. It is now an effective one-particle Hamiltonian, which only parametrically depends on K.

Before we consider the scattering states we first calculate the bound states. To this end, we make the ansatz

$$|K\rangle_B = \frac{1}{N}\left(b\,|K\rangle + \sum_{r>0}\mathsf{e}^{-\kappa r}\,\mathsf{e}^{-i\phi_K(r-1)}\,|r,K\rangle + \sum_{r<0}\mathsf{e}^{\kappa r}\,\mathsf{e}^{-i\phi_K(r+1)}\,|r,K\rangle\right). \tag{3.24}$$

To have a bound state we need $\mathrm{Re}\,(\kappa) > 0$, and N denotes a normalization constant. Projection of this state onto Eqns. (3.19) - (3.22) yields

$$E_B = I_K(\mathsf{e}^{\kappa} + \mathsf{e}^{-\kappa}) \tag{3.25}$$

$$E_B = I_K\mathsf{e}^{-\kappa} + 2J_3\,\cos(K/2)\mathsf{e}^{\kappa}\,b \tag{3.26}$$

$$(E_B - U)\,b = 2J_3\,\cos(K/2)\,(\mathsf{e}^{\kappa} + \mathsf{e}^{-\kappa}) \tag{3.27}$$

where E_B denotes the energy of the bound state: $\hat{H}\,|K\rangle_B = E_B\,|K\rangle_B$. We define $y = \mathsf{e}^{\kappa}$ and find the equation $y = \frac{8J_3^2\,\cos^2\left(\frac{K}{2}\right)}{I_K^2\,(y+1/y) - U/I_K}$ with the solutions

$$\begin{aligned} y_{\pm} &= \frac{U \pm \sqrt{U^2 + 32J_3^2\cos^2(K/2) - 4I_K^2}}{2I_K} \\ &= \frac{U}{2I_K} \pm \sqrt{\left(\frac{U}{2I_K}\right)^2 + 8\left(\frac{J_3}{I_K}\right)^2\cos^2(K/2) - 1}. \end{aligned} \tag{3.28}$$

To have a well-defined bound state the condition $|\mathrm{Re}\,(y)\,| > 1$ has to be fulfilled, see Eq. (3.24). If, for example, $U = 0$ and $J_1 = J_2 = J$, it is $I_K = 2J\cos^2(K/2) \rightarrow y_{\pm} =$

$\pm\sqrt{2(J_3/J)^2-1}$: bound states exist if $|J_3| > |J|/\sqrt{2}$.

From Eq. (3.25) the energy of the boundstates can be calculated as

$$\begin{aligned} E_B(K) &= I_K(y_+ + 1/y_+) \\ &= \frac{U I_K^2 - 2\,J_3^2\,(1+\cos(K))\left(U + \sqrt{U^2 + 16\,J_3^2\,(1+\cos(K)) - 4I_K^2}\right)}{I_K^2 - 4\,J_3^2\,(1+\cos(K))} \qquad (3.29) \\ &\underset{|J_1|,|J_2|,|J_3|\ll|U|}{\longrightarrow} U + \frac{8J_3^2\,\cos^2\left(\frac{K}{2}\right)}{U} + \ldots \qquad (3.30) \end{aligned}$$

The limit $|J_1|, |J_2|, |J_3| \ll |U|$ we could have obtained much faster: by perturbation theory on Eq. (3.19). The width of the boundstate can be obtained by $l = 1/\mathrm{Re}\,(\kappa) = 1/\ln(|y_+|)$. From Eq. (3.27) we can also obtain b and, finally, the normalization N in Eq. (3.24).

We now consider the scattering states. The ansatz $|q,K\rangle = \frac{1}{\sqrt{L}}\sum_r \mathrm{e}^{iqr}\,|r,K\rangle$ solves Eq. (3.22), as here $\hat{H}\,|q,K\rangle = (2J_1\cos(K/2+q) + 2J_2\cos(K/2-q))\,|q,K\rangle$. We have to identify $k_1 = K/2+q$ and $k_2 = K/2-q$, or $K = k_1+k_2$ and $q = (k_1-k_2)/2$. The total momentum K has an extended 1.BZ, $K \in (-2\pi, 2\pi]$ as underlying spatial coordinate R can take half-integer values. The energy of the scattering states is given by $E_S(q,K) = 2J_1\cos(K/2+q) + 2J_2\cos(K/2-q)$. We now make an ansatz for the scattering including the incoming plane wave, having amplitude 1; the reflected part, with amplitude $R(q,K)$; and the transmitted part, with amplitude $T(q,K)$:

$$\begin{aligned} |q,K\rangle_S = c\,|K\rangle + \sum_{r>0}\left(\mathrm{e}^{iq(r-1)} + R(q,K)\,\mathrm{e}^{ip(q,K)(r-1)}\right)|r,K\rangle \\ + \sum_{r<0} T(q,K)\,\mathrm{e}^{iq(r+1)}\,|r,K\rangle\,. \qquad (3.31) \end{aligned}$$

Here we have assumed that the incoming wave is at $r > 0$, the case $r < 0$ is completely analogous. The relative momentum in the reflection channel $p(q,K)$ is given by Eq. (3.12) as

$$\begin{aligned} p(q,K) = \frac{p_1-p_2}{2} =& \mathrm{ArcTan}\left(\frac{J_2\sin(\frac{1}{4}(K-2q)) - J_1\sin(\frac{1}{4}(3K+2q))}{J_2\cos(\frac{1}{4}(K-2q)) + J_1\cos(\frac{1}{4}(3K+2q))}\right) \\ &+ \mathrm{ArcTan}\left(\frac{J_2\sin(\frac{1}{4}(3K-2q)) - J_1\sin(\frac{1}{4}(K+2q))}{J_2\cos(\frac{1}{4}(3K-2q)) + J_1\cos(\frac{1}{4}(K+2q))}\right). \qquad (3.32) \end{aligned}$$

One has to be careful with the direct evaluation of Eq. (3.32): for Umklapp scattering events one has to shift K to the first Brillouin zone. We define $B_K = 2J_3\cos\left(\frac{K}{2}\right)$ and the relative velocity $v_S(q,K) = 2\,J_2\,\sin\left(\frac{K}{2}-q\right) - 2\,J_1\,\sin\left(\frac{K}{2}+q\right)$. In a reflection event

this is reversed, such that $v_S(q,K) = -v_S(p(q,K),K)$. Projection of the scattering ansatz, Eq. (3.31), onto the Hamiltonian Eqns. (3.19)–(3.22), yields

$$(E_s - iv_S)\, T = 2B_K c \tag{3.33}$$

$$(E_S - U)\, c = B_K\,(1 + T + R) \tag{3.34}$$

$$(E_s + iv_S) = 2B_K c - (E_S - iv_S)\, R. \tag{3.35}$$

The solutions for the scattering amplitudes R and T are

$$R = \frac{4B_K^2 E_S - (E_S^2 + v_S^2)(E_S - U)}{(E_S - iv_S)((E_S - iv_S)(E_S - U) - 4B_K^2)} \tag{3.36}$$

$$T = \frac{-4iv_S\, B_K^2}{(E_S - iv_S)((E_S - iv_S)(E_S - U) - 4B_K^2)}. \tag{3.37}$$

From this we obtain the reflection and transmission probabilities as

$$|R|^2 = \frac{\left(4B_K^2 E_S - (E_S^2 + v_S^2)(E_S - U)\right)^2}{\left(E_S^2 + v_S^2\right)\left((E_S(E_S - U) - 4B_K^2)^2 + v_S^2(E_S - U)^2\right)} \tag{3.38}$$

$$|T|^2 = \frac{16 v_S^2\, B_K^4}{\left(E_S^2 + v_S^2\right)\left((E_S(E_S - U) - 4B_K^2)^2 + v_S^2(E_S - U)^2\right)}. \tag{3.39}$$

Since the velocities in both channels are equal (up to the sign) it is $|R|^2 + |T|^2 = 1$. In the limit $|J_1|, |J_2|, |J_3| \ll |U|$ we find

$$|R|^2 \underset{|U|\to\infty}{\longrightarrow} 1 - \frac{16\, B_K^4\, v_S^2}{(E_S^2 + v_S^2)^2\, U^2}, \tag{3.40}$$

$$|T|^2 \underset{|U|\to\infty}{\longrightarrow} \frac{16\, B_K^4\, v_S^2}{(E_S^2 + v_S^2)^2\, U^2}. \tag{3.41}$$

Now we have completely solved the problem and have found all eigenstates. Extensions to more scattering channels and more intermediate states are possible.

Later, we will encounter situations where one dimensional channels are locally coupled to a two dimensional continuum but we are only interested in the one dimensional dynamics. We will include this into the formalism by an effective emission channel. Again, we present a simple example. The toy Hamiltonian consists of a one dimensional wire coupled to a two dimensional region as illustrated in Fig. 3.1. It reads

$$\hat{H}\,|x < 0\rangle = J_1\,(|x + 1\rangle + |x - 1\rangle) \tag{3.42}$$

$$\hat{H}\,|x > 0\rangle = J_2\,(|x + 1\rangle + |x - 1\rangle) \tag{3.43}$$

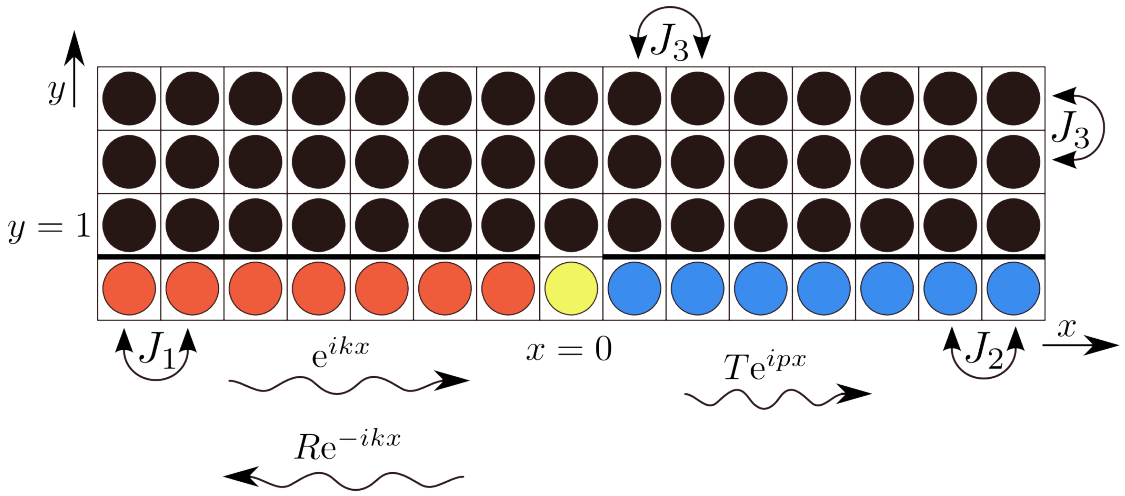

Figure 3.1: **Illustration of the toy model Eqns. (3.42) - (3.47) and the scattering problem.** A one dimensional wire at $y = 0$ is coupled to a $2d$ region at one lattice site $x = 0, y = 0$. The hopping amplitudes in the wire for $x < 0$ and $x > 0$ can be different and are denoted by J_1 and J_2, respectively. The coupling in the $2d$ region is J_3. An incoming plane wave e^{ikx} is scattered at $x = 0$. It can either be reflected as Re^{-ikx}, transmitted as Te^{ipx} (with a possibly different wavelength) or it can be scattered into the two dimensional region $y \geq 1$. We refer to this as emission.

$$\hat{H}\,|0\rangle = J_2\,|1\rangle + J_1\,|-1\rangle + J_3\,|0,1\rangle \tag{3.44}$$

$$\hat{H}\,|0,1\rangle = J_3\,|0\rangle + J_3\,(|0,2\rangle + |1,1\rangle + |-1,1\rangle) \tag{3.45}$$

$$\hat{H}\,|x \neq 0,1\rangle = J_3\,(|x,2\rangle + |x+1,1\rangle + |x-1,1\rangle) \tag{3.46}$$

$$\hat{H}\,|x,y>1\rangle = J_3\,(|x+1,y\rangle + |x-1,y\rangle + |x,y+1\rangle + |x,y-1\rangle)\,. \tag{3.47}$$

Eq. (3.47) can be solved by the ansatz

$$|\boldsymbol{q}\rangle = \frac{\sqrt{2}}{L}\sum_{x,y>0} e^{iq_x x}\,\sin(q_y y)\;\;|x,y\rangle \tag{3.48}$$

and the corresponding energy is $\epsilon_{\boldsymbol{q}} = 2J_3(\cos(q_x) + \cos(q_y))$. Using this new basis the Hamiltonian becomes

$$\hat{H}\,|x<0\rangle = J_1\,(|x+1\rangle + |x-1\rangle) \tag{3.49}$$

$$\hat{H}\,|x>0\rangle = J_2\,(|x+1\rangle + |x-1\rangle) \tag{3.50}$$

$$\hat{H}\,|0\rangle = J_2\,|1\rangle + J_1\,|-1\rangle + \frac{\sqrt{2}J_3}{L}\sum_{\boldsymbol{q}}\sin(q_y)\,|\boldsymbol{q}\rangle \tag{3.51}$$

$$\hat{H}\,|\boldsymbol{q}\rangle = \epsilon_{\boldsymbol{q}}\,|\boldsymbol{q}\rangle + \frac{\sqrt{2}J_3\,\sin(q_y)}{L}\,|0\rangle\,. \tag{3.52}$$

We now consider the scattering of a plane wave incoming from $x \to -\infty$. The ansatz for the scattering states is

$$|\psi\rangle_S = \sum_{\boldsymbol{q}} \phi^*_{\boldsymbol{q}} \, |\boldsymbol{q}\rangle + c^* \, |0\rangle + \sum_{x<0} \left(\mathsf{e}^{ik(x+1)} + R^* \, \mathsf{e}^{-ik(x+1)} \right) \, |x\rangle + \sum_{x>0} T^* \, \mathsf{e}^{ip(x-1)} \, |x\rangle \,, \tag{3.53}$$

where the energy is given by the energy of the incoming wave to $E_S = 2\,J_1 \cos(q)$. At $x = 0$ the wave can be reflected to $x < 0$, transmitted into $x > 0$ or it can be scattered into the $2d$ region $y > 0$, we refer to this as emission. The momentum p in the transmission channel has to be found from energy conservation $2\,J_1 \cos(q) \stackrel{!}{=} 2\,J_2 \cos(p)$:

$$p(q) = \begin{cases} \mathbf{Arccos}\left(\frac{J_1}{J_2}\,\cos(q)\right) & , |\frac{J_1}{J_2}\cos(q)| \leq 1 \\ i\,\left|\mathbf{Arccosh}\left(\frac{J_1}{J_2}\,\cos(q)\right)\right| & , |\frac{J_1}{J_2}\cos(q)| > 1. \end{cases} \tag{3.54}$$

When transmission is not allowed due to energy conservation ($|\frac{J_1}{J_2}\cos(q)| > 1$) this channel is closed and p is imaginary. Then the wavefunction decays exponentially for $x > 1$.

Projection of ${}_S\langle\psi|$ on Eqns.(3.49)–(3.52) and eliminating the $\phi_{\boldsymbol{q}}$ yields

$$(1+R)\,E_S = J_1\,c + J_1\,\left(\mathsf{e}^{ik} + R\,\mathsf{e}^{-ik}\right) \tag{3.55}$$

$$T\,E_S = J_2\,c + J_2\,T\mathsf{e}^{-ip} \tag{3.56}$$

$$E_S c = J_1\,(1+R) + J_2\,T + c\,\Delta^+(E_S) \tag{3.57}$$

In Eq. (3.57) we have defined

$$\begin{aligned} \Delta^{\pm}(\omega) &= \frac{2\,J_3^2}{L} \sum_{\boldsymbol{q}} \frac{\sin^2(q_y)}{\omega - \epsilon_{\boldsymbol{q}} \pm i\varepsilon} \underset{L\to\infty}{\longrightarrow} \frac{J_3^2}{\pi^2} \int_0^\pi dq_y \int_{-\pi}^{\pi} dq_x \, \frac{\sin^2(q_y)}{\omega - 2J_3(\cos(q_x)+\cos(q_y)) \pm i\varepsilon} \\ &= \frac{\omega}{2} - \frac{J_3}{2\pi} \int_{-\pi}^{\pi} dq_x \, \sqrt{\left(\tfrac{\omega}{2J_3} - \cos(q_x)\right)^2 - 1}\; \mathbf{Sign}\left(\tfrac{\omega}{2J_3} - \cos(q_x)\right) \Theta\left(\left|\tfrac{\omega}{2J_3} - \cos(q_x)\right| - 1\right) \\ &\mp i \frac{J_3}{2\pi} \int_{-\pi}^{\pi} dq_x \, \sqrt{1 - \left(\tfrac{\omega}{2J_3} - \cos(q_x)\right)^2}\; \Theta\left(1 - \left(\tfrac{\omega}{2J_3} - \cos(q_x)\right)^2\right). \end{aligned} \tag{3.58}$$

If $|\frac{E_S}{2J_3} \pm 1| < 1$, implying that the energy of incoming scatterer is in the $2d$ spectrum, $\Delta^{\pm}(E_S)$ has a finite imaginary part. Eqns.(3.55) - (3.57) can be solved for R, T and c:

$$R = \frac{1/2(E_S - \Delta^+(E_S))(E_S - iv'_S)(E_S + iv_S) - J_1^2(E_S - iv'_S) - 2J_1\,J_2^2}{J_2^2(E_S - iv_S) + (E_S - iv'_S)(J_1^2 - 1/2(E_S - iv_S)(E_S - \Delta^+(E_S)))} \tag{3.59}$$

$$T = \frac{-2i\,J_1\,J_2\,v_S}{J_2^2(E_S - iv_S) + (E_S - iv'_S)(J_1^2 - 1/2(E_S - iv_S)(E_S - \Delta^+(E_S)))} \tag{3.60}$$

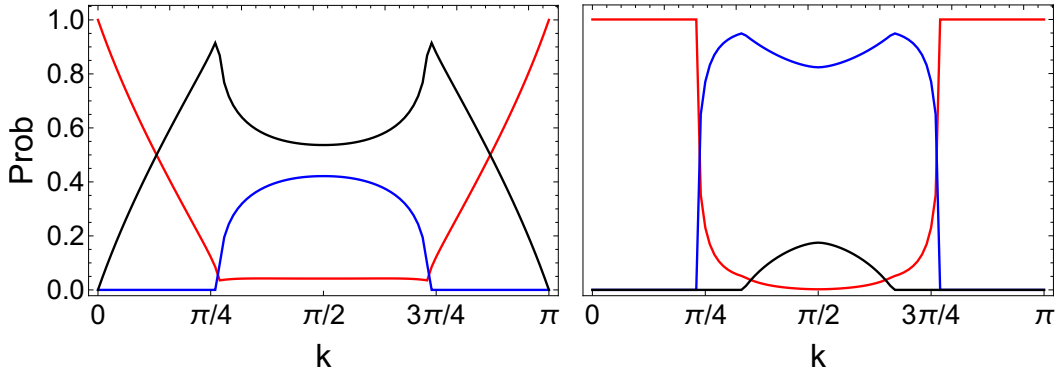

Figure 3.2: **Examples for the scattering and emission probabilities.** k denotes the momentum of the incoming wave. The red lines show the reflection probabilities, the blue lines show the transmission probabilities and the black lines are the emission probabilities. In the left panel it is $J_1 = 3$, $J_2 = 2$ and $J_3 = 4$. Emission is always possible, while the transmission channel is closed for $k > \text{Arccos}(-2/3) \approx 2.3$ and $k < \text{Arccos}(2/3) \approx 0.84$ due to energy conservation. In the right panel it is $J_1 = 4$, $J_2 = 3$ and $J_3 = 1$. The transmission channel is closed for $k > \text{Arccos}(-3/4) \approx 2.4$ and $k < \text{Arccos}(3/4) \approx 0.72$. Due to the smallness of J_3 also the emission channel is closed for slow scatters. Seen here for $k > \text{Arccos}(-1/2) = 2\pi/3$ and $k < \text{Arccos}(1/2) = \pi/3$.

$$c = \frac{-i\, J_1\, v_S\, (E_S - i v_S')}{J_2^2(E_S - i v_S) + (E_S - i v_S')(J_1^2 - 1/2(E_S - i v_S)(E_S - \Delta^+(E_S)))}. \tag{3.61}$$

We have defined the scattering velocity $v_S = -2J_1\, \sin(k)$ and the velocity in the transmission channel $v_S' = -2J_2\, \sin(p)$, where p was defined in Eq. (3.54). If we denote the emission probability by $|E|^2$, conservation of the probability current dictates that

$$|R|^2 + \left|\frac{v_S'}{v_S}\right| |T|^2 = 1 - |E|^2. \tag{3.62}$$

If p is imaginary, v_S' has to be chosen to 0 here. From Eq. (3.62) we obtain the emission probability as

$$|E|^2 = \frac{2\, J_1^2\, v_S\, (E_S^2 + v_S'^2)\; (-\text{Im}\,(\Delta^+(E_S)))}{\left|J_2^2(E_S - i v_S) + (E_S - i v_S')(J_1^2 - 1/2(E_S - i v_S)(E_S - \Delta^+(E_S)))\right|^2}. \tag{3.63}$$

The sign of $\Delta^\pm$ is chosen such that $\text{Im}\,(\Delta^\pm(E_S)) < 0$ for $v_S > 0$. It is generically $|E|^2 \sim |\text{Im}\,(\Delta(E_S))\,|$. Two examples for the scattering- and emission-rates are shown in Fig. 3.2.

We have found the exact scattering amplitudes in the $1d$ wire. The strategy formulated above can be extended to more complex situations including more reflection

channels, transmission channels and intermediate states that can emit. Also the generalization to two-particle scattering is possible, since in relative and center of position coordinates this is an effective one-particle problem. For all setups, the problem can be cast as a system of linear equations for the amplitudes $R, T_1, T_2, \ldots$ and the occupation of the intermediate states $c_1, c_2, \ldots$

$$S \cdot \Big(R, \quad T_1 \quad T_2, \quad \cdots, \quad c_1, \quad c_2, \quad \cdots \Big)^T = I, \tag{3.64}$$

where S denotes the scattering matrix. The vector I on the right hand side has to be chosen according to the incoming channel. The scattering amplitudes are found through inversion of S as

$$\Big(R, \quad T_1, \quad T_2, \quad \cdots, \quad c_1, \quad c_2, \quad \cdots \Big)^T = S^{-1} \cdot I. \tag{3.65}$$

The emission probability is then given by $|E|^2 = 1 - |R|^2 - \sum_i |v_i'/v_S| \ |T_i|^2$. Later in section 7 we will encounter two-particle scattering problems with 3 transmission channels, 3 reflection channels, emission and more than 30 intermediate states.

3.3 Quasiparticle momentum distribution

In the quantum quenches we will study a low-density of quasiparticles is induced by the quench. These are created in pairs and only quasiparticles originating from the same pair are entangled initially. Therefore, we can calculate the momentum distribution of a pair with an effective Hamiltonian acting only on a the zero- and two-particle Hilbertspace.

We study a concrete example: a quench in the bosonic Hubbard model. The initial state is given by the product state with one boson per site, denoted by $|\mathrm{ini}\rangle = |\ldots 111 \ldots\rangle$. We use the usual conventions and write the Hamiltonian as

$$\hat{H} = -J \sum_{<i,j>} \hat{b}_i^\dagger \, \hat{b}_j + \frac{U}{2} \sum_i \hat{b}_i^\dagger \, \hat{b}_i \left(\hat{b}_i^\dagger \, \hat{b}_i - 1 \right) - U \tag{3.66}$$

where $U, J > 0$. We have subtracted a constant for convenience such that $\langle \mathrm{ini}|\hat{H}|\mathrm{ini}\rangle = -U$. We are interested in the limit $U \gg J$ and consider the effective Hamiltonian in the subspace including $|\mathrm{ini}\rangle$ and all states which have one doublon and one holon. To leading order, the doublon and holon dispersion and the corresponding group veloci-

ties are, respectively,

$$\epsilon_D(k) = -4\,J\,\cos(k)\ \ , v_D(k) = \frac{d\,\epsilon_D(k)}{dk} = 4\,J\,\sin(k), \tag{3.67}$$

$$\epsilon_H(k) = -2\,J\,\cos(k)\ \ , v_H(k) = \frac{d\,\epsilon_H(k)}{dk} = 2\,J\,\sin(k). \tag{3.68}$$

When x_H is the position of the holon and x_D the position of the doublon, this state will be denoted by $|x_H, x_D\rangle$. Since $|\mathrm{ini}\rangle$ is translationally invariant, it couples only to states with zero total momentum $K = 0$. We define the Fourier transformation in relative and center of position coordinates

$$|K, q > 0\rangle = \frac{1}{\sqrt{2}L} \sum_{x_D, x_H} \mathrm{e}^{iK\frac{x_D + x_H}{2}}\ \sin(q|x_D - x_H|)\ \left(|x_H, x_D\rangle + |x_D, x_H\rangle\right), \tag{3.69}$$

which is properly normalized. Due to the spatial symmetrization used here we have to restrict $q > 0$.

To lowest order in J/U we obtain the effective Hamiltonian in the $K = 0$ sector

$$\hat{H} = -U\,\hat{a}^\dagger\hat{a} + \sum_q \epsilon_q \hat{c}_q^\dagger \hat{c}_q + \sum_q V_q\ \left(\hat{c}_q^\dagger \hat{a} + \hat{a}^\dagger \hat{c}_q\right), \tag{3.70}$$

where $\hat{a}^\dagger, \hat{a}$ are the creation and annihilation operators of $|\mathrm{ini}\rangle$ and $\hat{c}_q^\dagger, \hat{c}_q$ are the creation and annihilation operators of $|K = 0, q\rangle$. Furthermore we have defined $\epsilon_q = -6J\cos(q)$ and $V_q = -2\sqrt{2}J\sin(q)$.

Starting from $|\mathrm{ini}\rangle$ as the initial state, the time evolution creates doublon-holon pairs with relative momentum q. We want to calculate the occupation probability $\tilde{W}_q$ after long times:

$$\tilde{W}_q \equiv \tilde{W}_q(t \to \infty) = \lim_{t\to\infty}\ \langle \mathrm{ini}|\ \mathrm{e}^{i\hat{H}t}\,\hat{c}_q^\dagger \hat{c}_q\,\mathrm{e}^{-i\hat{H}t}\,|\mathrm{ini}\rangle = \lim_{t\to\infty}\ \left|\langle \mathrm{vac}|\hat{\mathrm{c}}_\mathrm{q}\ \mathrm{e}^{-\mathrm{i}\hat{\mathrm{H}}\mathrm{t}}\ \hat{\mathrm{a}}^\dagger|\mathrm{vac}\rangle\right|^2 \tag{3.71}$$

where we have used the vacuum state $|\mathrm{vac}\rangle$ and we assumed the quench is performed at $t_0 = 0$. The second equality holds since we consider a single particle problem and start from the vacuum.

We define the retarded propagator from the initial state to a quasiparticle pair with momenta q and its Fourier transformed

$$G_q^R(t) = -i\,\Theta(t)\,\langle \mathrm{vac}|\hat{\mathrm{c}}_\mathrm{q}\ \mathrm{e}^{-\mathrm{i}\hat{\mathrm{H}}\mathrm{t}}\ \hat{\mathrm{a}}^\dagger|\mathrm{vac}\rangle\,, \tag{3.72}$$

$$G_q^R(\omega) = \int_{-\infty}^{\infty} dt\,\mathrm{e}^{i\omega t} G_q^R(t), \tag{3.73}$$

such that $\tilde{W}_q = \lim_{t\to\infty} |G_q^R(t)|^2$. If we define the free retarded Green functions of the initial state and the quasiparticle pairs as

$$g_{\rm ini}^R(\omega) = \frac{1}{\omega + U + i\varepsilon}, \tag{3.74}$$

$$g_q^R(\omega) = \frac{1}{\omega - \epsilon_q + i\varepsilon}, \tag{3.75}$$

we obtain

$$\begin{aligned} G_q^R(\omega) &= g_{\rm ini}^R(\omega)\, V_q\, g_q^R(\omega) + g_{\rm ini}^R(\omega) \overbrace{\int_0^\pi \frac{dq'}{\pi} V_{q'}\, g_{q'}^R(\omega)\, V_{q'}}^{=\Delta(\omega)}\; g_{\rm ini}^R(\omega)\, V_q\, g_q^R(\omega) + \ldots \\ &= g_{\rm ini}^R(\omega)\, V_q\, g_q^R(\omega)\left(1 + g_{\rm ini}^R(\omega)\,\Delta(\omega) + (g_{\rm ini}^R(\omega)\,\Delta(\omega))^2 + \ldots\right) \\ &= g_{\rm ini}^R(\omega)\, V_q\, g_q^R(\omega)\sum_{n=0}^{\infty}(g_{\rm ini}^R(\omega)\,\Delta(\omega))^n \\ &= \frac{g_{\rm ini}^R(\omega)\, V_q\, g_q^R(\omega)}{1 - g_{\rm ini}^R(\omega)\,\Delta(\omega)} = \frac{V_q\, g_q^R(\omega)}{g_{\rm ini}^R(\omega)^{-1} - \Delta(\omega)}, \end{aligned} \tag{3.76}$$

which has a nice interpretation in terms of diagrams, see Fig. 3.3. $\Delta(\omega)$ can be calculated as

$$\begin{aligned} \Delta(\omega) = \int_0^\pi \frac{dq}{\pi} V_q^2\, g_q^R(\omega) &= \frac{8J^2}{\pi}\int_0^\pi dq \frac{\sin^2(q)}{\omega + 6J\cos(q) + i\varepsilon} \\ =& \frac{8J^2}{\pi}\int_0^\pi dq \frac{\sin^2(q)\;(\omega + 6J\cos(q))}{(\omega + 6J\cos(q))^2 + \varepsilon^2} - i8J^2\int_0^\pi dq\,\sin^2(q)\delta\left(\omega + 6J\cos(q)\right) \\ =& \frac{2\,\omega}{9} - \frac{2}{9}\mathrm{sign}(\omega/J)\sqrt{\omega^2 - 36J^2}\;\Theta\left(\omega^2 - 36J^2\right) \\ & - i\frac{2}{9}\sqrt{36J^2 - \omega^2}\;\Theta\left(36J^2 - \omega^2\right). \end{aligned} \tag{3.77}$$

We then obtain for the occupation probability

$$\tilde{W}_q(t) = V_q^2\left|\int_{-\infty}^{\infty}\frac{d\omega}{2\pi}\,\frac{\mathrm{e}^{i\omega t}}{\omega + 6J\cos(q) + i\varepsilon}\;\times\;\frac{1}{\omega + U - \Delta(\omega)}\right|^2 \tag{3.78}$$

$$\begin{aligned} &\xrightarrow[\text{time average for } t\to\infty]{} V_q^2\left|\frac{i\,\mathrm{e}^{-i\epsilon_q t}}{\epsilon_q + U - \Delta(\epsilon_q)}\right|^2 \\ &\qquad = \frac{8\,J^2\,\sin^2 q}{|\epsilon_q + U + 4/3\,J\,(\cos(q) + i\sin(q))\,|^2} \end{aligned} \tag{3.79}$$

The limit $t \to \infty$ in Eq. (3.78) is a bit subtle. It turns out that in the time-averaged result only the pole of $g_q^R(\omega)$ contributes, and one can simply use the Residue theorem to find Eq. (3.79). We have checked this by exact diagonalization.

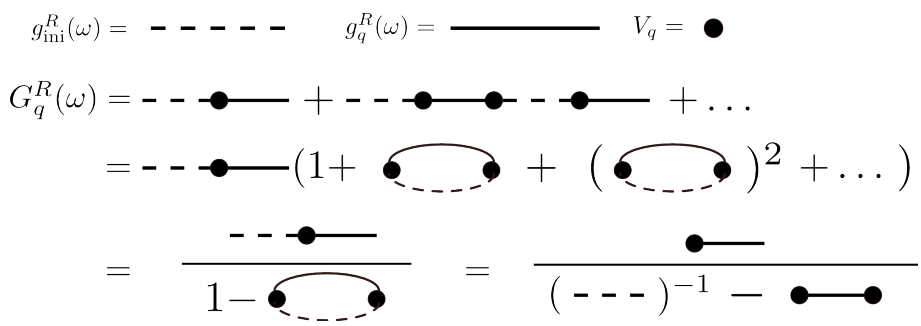

Figure 3.3: **Diagrammatic derivation of the formula Eq. (3.76).** The propagation of the initial state into a state with momentum q can occur via different paths. The resulting diagrams can be summed in a geometric series which leads to the final result.

However, $\frac{1}{\omega+U-\Delta(\omega)}$ has branch cuts, which have to be found by analytic continuation of Eq. (3.77) to the upper complex plane. They do matter a short times: $P_q(t) \to 0$ for $t \to 0$ as the initial state had no doublon-holon pairs. They also lead to late time oscillations such that a time average is necessary. Unfortunately, it was not possible to obtain any reasonable results by direct numerical integration of Eq. (3.78). Therefore we present a second calculation to check the result in Eq. (3.79).

To this end we rewrite the problem in terms of a scattering problem. We consider the Hamiltonian given above in the form

$$\hat{H}\,|\text{ini}\rangle = -U\,|\text{ini}\rangle - 2J\,|1\rangle\,, \tag{3.80}$$

$$\hat{H}\,|1\rangle = -2J\,|\text{ini}\rangle - 3J\,|3\rangle\,, \tag{3.81}$$

$$\hat{H}\,|r>1\rangle = -3J\,|r+1\rangle - 3J\,|r-1\rangle\,. \tag{3.82}$$

Here $|r\rangle$ denotes the spatially symmetrized doublon-holon wavefunction

$$|r\rangle = 1/\sqrt{2}(|x_H, x_D\rangle + |x_D, x_H\rangle) \text{ with } |x_D - x_H| = r \tag{3.83}$$

and fixed center of position coordinate $R = \frac{x_H+x_D}{2}$. We do not consider the bound state but calculate only the scattering states. We make the ansatz

$$|q\rangle_S = c_q^*\,|ini\rangle + \sum_r (\mathsf{e}^{iq(r-1)} + R^*\mathsf{e}^{-iq(r-1)})\,|r\rangle \tag{3.84}$$

and find

$$(\epsilon_q + U)\,c_q = -2J\,(1+R) \text{ and } (1+R)\,\epsilon_q = -2J\,c_q - 3J(\mathsf{e}^{-iq} + R\mathsf{e}^{iq}). \tag{3.85}$$

This has the solution

$$R = -\mathrm{e}^{2iq}\,\frac{\epsilon_q + U + \frac{4}{3}\,J\,\mathrm{e}^{-iq}}{\epsilon_q + U + \frac{4}{3}\,J\,\mathrm{e}^{iq}}, \tag{3.86}$$

$$c_q = i\mathrm{e}^{iq}\,\frac{4J\sin(q)}{\epsilon_q + U + \frac{4}{3}\,J\,\mathrm{e}^{iq}}. \tag{3.87}$$

Of course it is $|R|^2 = 1$. c_q gives the overlap of the initial state with the q-scattering state (which is not normalized) as $c_q = \langle \mathrm{ini}|q\rangle_S^*$. However, the relative weight is

$$\overline{W}_q = |c_q|^2 = \frac{16J^2\,\sin^2(q)}{|\epsilon_q + U + 4/3\,J\mathrm{e}^{iq}|^2} \tag{3.88}$$

and agrees up to a factor of 2 with the result found above in Eq. (3.79). This indicates that we have not calculated the same quantity. Indeed, in the first calculation we considered the decay of the initial state into free momentum states, which are not eigenstates. Here the result is time dependent and one has to use time averaging. In the second calculation we have decomposed the initial state into exact eigenstates, which gives a time independent result. Therefore the first method presented above, albeit intuitive, is not really suitable to calculate the momentum distribution. Nevertheless it gives results very similar, a disagreement by a factor of two, to that obtained from the exact two-particle eigenstates. In [114], also a factor of two was found in the occupation of bare and dressed excitations after a quantum quench in the fermionic Hubbard model. In the following we will use the exact two-particle weights in Eq. (3.88). In the limit $U \gg J$ we find

$$W_q = \frac{16J^2\,\sin^2(q)}{|\epsilon_q + U + 4/3\,J\mathrm{e}^{iq}|^2}, \quad (-\pi < q \leq \pi) \tag{3.89}$$

$$\underset{U\gg J}{\longrightarrow}\;\; 16\,\left(\frac{J}{U}\right)^2 \sin^2(q). \tag{3.90}$$

Eq. (3.89) is the final result for the momentum distribution, it is not a probability distribution as it is not normalized. The result in the limit $U \gg J$ can be obtained by perturbation theory, for example by a Schrieffer-Wolff transformation as presented in section 3.1 [115]. In this limit the total number of pair excitations can be calculated to be

$$N = \sum_q 16\,\left(\frac{J}{U}\right)^2 \sin^2(q) = 16\,L\,\left(\frac{J}{U}\right)^2 \int_{-\pi}^{\pi} \frac{dq}{2\pi}\sin^2(q) = 8\,L\,\left(\frac{J}{U}\right)^2 \tag{3.91}$$

and is proportional to the system size L. The density of quasiparticle pairs is given

by $\rho = N/L = 8\,(\frac{J}{U})^2$. Accordingly, their mean distance is $\rho^{-1} = 1/8(\frac{U}{J})^2$.

The generalization of the formulas given above to more creation channels is possible. For example, for a Hamiltonian with two channels

$$\begin{aligned}\hat{H} = -U\,\hat{a}^\dagger\hat{a} + \sum_q \epsilon_{1,q}\hat{c}^\dagger_{1,q}\hat{c}_{1,q} + \sum_q V_{1,q}\left(\hat{c}^\dagger_{1,q}\hat{a} + \hat{a}^\dagger\hat{c}_{1,q}\right) \\ + \sum_q \epsilon_{2,q}\hat{c}^\dagger_{2,}q\hat{c}_{2,q} + \sum_q V_{2,q}\left(\hat{c}^\dagger_{2,q}\hat{a} + \hat{a}^\dagger\hat{c}_{2,q}\right),\end{aligned} \tag{3.92}$$

we find

$$P_{j,q}(t\to\infty) = \left|\frac{V_{j,q}}{\epsilon_{j,q} + U - \Delta_1(\epsilon_{j,q}) - \Delta_2(\epsilon_{j,q})}\right|^2. \tag{3.93}$$

We will need this formula later in section 7.

3.4 Semiclassical dynamics after weak quantum quenches

In the next sections we will study weak quenches where the density of quasiparticles is low. Before the quench the system is in a product state. After the quench quasiparticle pairs are created and their momentum distribution can be calculated as shown above. In this limit, only quasiparticles originating from the same pair are entangled, while quasiparticles created at different space points are incoherent [116, 117]. As the mean distance of quasiparticles is large and they are protected by a large gap, their propagation can be treated semiclassically with their respective group velocity [118, 119]. A schematic picture is shown in Fig. 3.4.

The semiclassical method was first introduced by Sachdev,Young and Damle to calculate equilibrium correlation functions [118, 119]. It was extended to out of equilibrium situations by Calabrese and Cardy [116, 117]. In [116], it was used to calculate the entanglement entropy after a quantum quench. The method was further used for analytic calculations of the dynamics after a quantum quench in the transverse field Ising model within the ferromagnetic phase [120]. The authors reproduced the leading order of the exact result [13]. However, in this integrable model the scattering is trivial and the system does not thermalize.

We have adapted the method to the quantum dynamics of non-integrable models. We have performed semiclassical simulations along the following lines: at the initial time, quasiparticle pairs are created with opposite momenta. These were chosen randomly according to the exact two-particle creation rates, calculated as shown in section 3.3. The quasiparticles propagate with different velocities as they have different dispersions, see for example Eqns. (3.67) and (3.68) for the quench in the Hub-

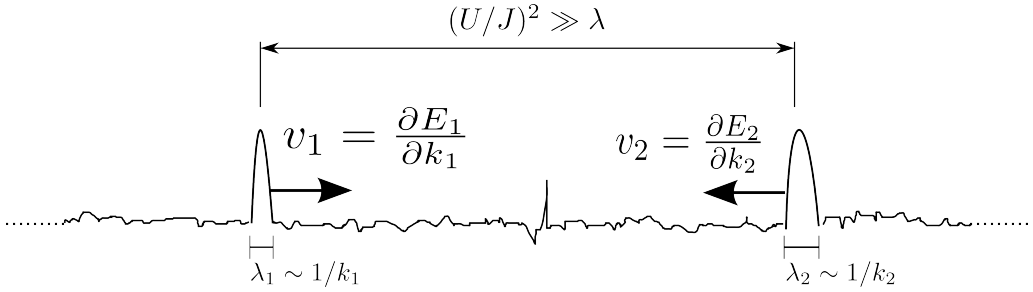

Figure 3.4: **Schematic illustration of the semiclassical quasiparticles.** In the limit $U \gg J$ the mean distance of quasiparticles is much larger larger than their wavelength. Then their propagation can be treated semiclassically, the velocity is given by the corresponding group velocity.

bard model. The scattering was evaluated locally in space and time with the exact two-particle scattering rates. This leads to a worldline picture for the quasiparticle trajectories, see Fig. 3.5 for a schematic example with two different quasiparticles (doublons and holons). There can be three qualitatively different scattering events as indicated by the circled numbers in Fig. 3.5: when two quasiparticles of the same kind scatter, ①, the individual momenta are conserved and the corresponding worldlines are straight. When two quasiparticles of different kind scatter, ② and ③, the momenta are changed and energy is exchanged: the corresponding worldlines show kinks. There can be scattering events where the total momentum is conserved, as in ②. Due to the underlying lattice structure there can also be Umklapp scattering events where the total momentum is not conserved, as in ③.

The algorithm we have used works as follows:

(SCD1) `Randomly choose the positions and momenta of the quasiparticle pairs according to the quantum mechanical distribution functions;`

(SCD2) `Make a sorted list TLIST of the future scattering events;`

(SCD3) `Take the first element of TLIST and erase it;`
`Evaluate the scattering according to`
`the quantum mechanical scattering rates;`
`Update the involved quasiparticles and the time;`
`Calculate the future scatterings of the involved quasiparticles;`
`Sort them into TLIST;`
`IF(required)(Calculate observables;)`

(SCD4) `Repeat` (SCD3) `as long as you want;`

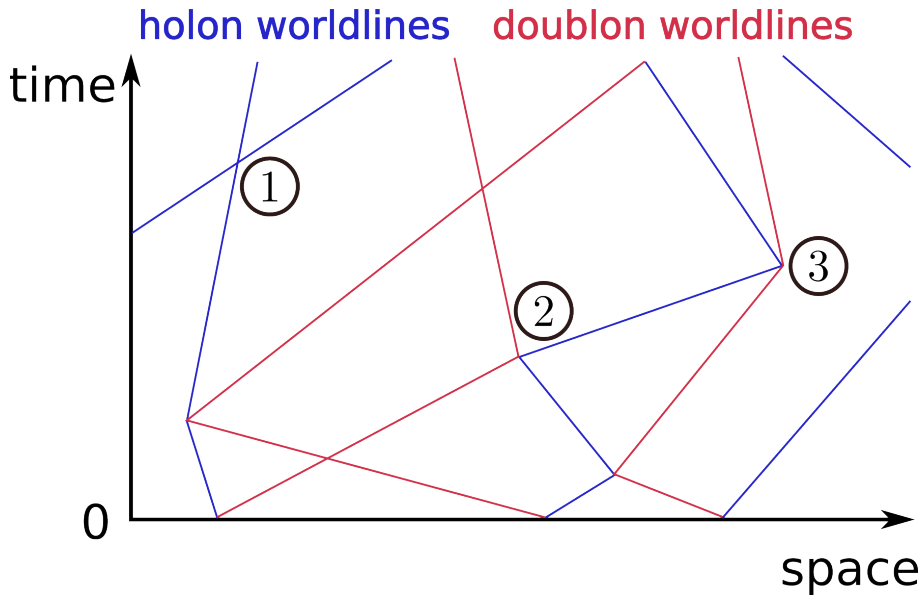

Figure 3.5: **Schematic illustration of the semiclassical dynamics.** The lines have to be understood as worldlines of quasiparticles. Shown is an example with two different quasiparticles , holons and doublons, as present in the bosonic Hubbard model. At time $t = 0$ quasiparticles are created in pairs with opposite momentum q and $-q$. As doublons and holons have a different dispersion, they propagate with different group velocities. ① The scattering of like quasiparticles is trivial and no momentum is exchanged. ② In the scattering of unlike quasiparticles momentum is exchanged. ③ Umklapp scattering can lead to unusual worldlines.

(SCD5) `Average over many realizations;`

If an appropriate data structure is used for `TLIST` this works very efficiently: sorting into a sorted list can be done in log time and is, for example, implemented in the `multimap` class of C++. The length of `TLIST` is $\sim N$ where N denotes the number of quasiparticles, this implies that each scattering event in (SCD3) has a runtime of $\mathcal{O}(\log(N))$. The number of scattering events can be used as an exit condition in (SCD4). By demanding that each quasiparticle scatters $\sim s$ times, the runtime is $\mathcal{O}(s\,N\,\log(N))$. In this way simulations with millions of quasiparticles can be performed, where each of them scatters thousands of times.

To make further contact to quantum mechanics, a possible interpretation could be the following: a single run of the algorithm, a path, represents an (approximate) eigenstate contributing to the dynamics. It was argued in the introduction that different eigenstates dephase and interference effects can be omitted in the long-time limit. Then it is reasonable to assume that the long-time behavior is correctly described by the ensemble of paths. In this way the diagonal ensemble of the initial

state is sampled. As interference of paths is omitted, and the initial state has fine-tuned phases, the short time behavior is not correctly described. The validity requires stable long-lived quasiparticles and can be valid only on timescales below the lifetime of these. We will consider only cases where the lifetime of the quasiparticles is exponentially large in the gap. Then it is expected the correct (to leading order) quantum mechanical correlation functions can be extracted [118, 119].

Similar algorithms were used to simulate classical models of particles with alternating masses interacting via hard-core collisions [121–123].

4 Diffusion and fluctuating hydrodynamics

According to a general principle due to Onsager, the final stages of the relaxation can be described by macroscopic hydrodynamic equations [124, 125]. Or, put in the words of Kubo [126], p.1204:

> *The average behavior of fluctuation of a physical quantity in an aged system is governed by the macroscopic physical law which governs the macroscopic change of the corresponding macroscopic variable.*

He called this *Onsager's assumption* (ibid.). This principle manifests itself in fluctuation-dissipation relations [126–128]. The response to an externally applied perturbation, provided that it is small enough, is the same as the response to spontaneous fluctuations. This leads to the regime of linear response, where transport coefficients can be calculated by means of equilibrium correlation functions as described by Kubo formulas [126–128].

In this section we consider the diffusive behavior of macroscopically conserved quantities. We focus on the generic conservation laws of energy and particle number. In the lattice models we will investigate later, momentum is not conserved due to Umklapp scattering. An introduction to the general principles of hydrodynamics can be found in volume 6 of Landau's and Lifshitz' *Course of Theoretical Physics* [129].

We take a coarse-grained point of view and explicitly exclude long-ranged, power-law, interactions. The time differences have to be much larger than all scattering times and the lengthscales have to be much larger than any mean free path and correlation length. This is the limit of long wavelength and low frequencies. We will keep only terms which are most relevant in this limit. Therefore, we cannot expect that the short time and small distance behavior is correctly described. Correlations on microscopic scales will be assumed to be δ-correlated.

Due to the many scattering events in this limit, a *tagged* single-particle effectively performs a random walk. We first consider a simple example. However, we will see below that a gradient in the density causes a directed flow. Furthermore, long-ranged correlations in time will show that the motion of different particles is highly correlated. And of course in quantum-mechanical systems, *tagged* must not be taken literally. Here diffusion characterizes by a different scaling behavior when compared to ballistic scaling. In clean non-interacting or integrable systems there is no diffractive scattering and everything presented below is not applicable. Disordered non-interacting systems can also show diffusive behavior [1, 130].

We restrict ourselves to homogenous, inversion-symmetric systems. Furthermore, we explicitly exclude situations where the system is close to a (quantum-)critical point [131] or in an ordered phase [132]. In both cases there are additional long wavelength modes which have to be included into the theory. Most importantly, the order parameter describing the broken symmetry has long-ranged correlations. Close to critical points, a variety of systems is described in the Hohenberg-Halperlin classification of dynamic universality classes [131]. Hydrodynamics in broken symmetry phases is discussed in the book by Forster [132]. Our considerations are restricted to energy scales well above any ordering temperature. In a quantum quench setup the temperature, determined by the excess energy, has to be larger than the temperature of any phase transition, if present.

4.1 Random Walks

The prime example of diffusive scaling is a random walk. Let us assume that a $1d$ particle is located at $x = x_0$ at time $t_0 = 0$. It shall evolve in time by performing random, uncorrelated steps of $\pm a$ at discrete times Δt. After a time $t_n = t_0 + n\Delta t$ its position is $x_n = x_0 + a\sum_{j=1}^{n} p_j$, where $\{p_1, p_2, \ldots, p_n\}$ is a random sequence of ± 1. The probability to have $m \in \{0, 1, \ldots, n\}$ times $+1$ (implying $n - m$ times -1) is $\binom{n}{m}/2^n$. The probability to have covered a distance $\Delta x = al$, $l \in \{-n, \ldots, n\}$, is then $P_n(l) = \binom{2n}{n+l}/2^{2n}$. By means of Stirling's approximation one then finds in the limit $n \to \infty$ and $|l| \ll n$

$$P_n(l) \to \frac{1}{\sqrt{2\pi n}} \exp\left(-\frac{l^2}{2n}\right). \tag{4.1}$$

The probability to come back to the initial position ($l = 0$) after many steps ($n \gg 1$) decreases as $n^{-1/2}$. The typical distance at a large time $t = n\,\Delta t$ from the starting position is then $(\Delta x)_{\mathrm{typ}} = a\sqrt{n}$ or, equivalently,

$$\langle x^2 \rangle = a^2 n = \frac{a^2}{\Delta t}\, t \equiv 2D\, t. \tag{4.2}$$

The constant $D = a^2/(2\Delta t)$ is the *diffusion constant*. Its dimension is $\frac{\mathsf{LENGTH}^2}{\mathsf{TIME}}$: diffusive behavior is characterized by a scaling $\mathsf{LENGTH}^2 \sim \mathsf{TIME}$. This is in contrast to ballistic behavior as found in free particle or integrable systems: here the propagation scaling is $\mathsf{LENGTH} \sim \mathsf{TIME}$ and the corresponding proportionality constant is the velocity with dimension $\frac{\mathsf{LENGTH}}{\mathsf{TIME}}$. After inserting $n = \frac{t}{\Delta t}$ and $l = \frac{\Delta x}{a}$ in Eq. (4.1), and dividing by a to obtain a proper probability density, one finds in the limit $a \to 0, \Delta t \to 0$

with $D =$ constant:

$$P_n(l) \to P_t(\Delta x) = \frac{1}{\sqrt{4\pi D t}} \exp\left(-\frac{\Delta x^2}{4Dt}\right). \tag{4.3}$$

In d dimensions, this generalizes to

$$P_t(\Delta x_1, \Delta x_2, \ldots, \Delta x_d) = \frac{1}{(4\pi D t)^{\frac{d}{2}}} \exp\left(-\frac{\sum_{i=1}^{d} \Delta x_i^2}{4Dt}\right). \tag{4.4}$$

Below we will see that diffusion is characterized by a propagator which has exactly the same structure as the distribution in Eq. (4.4).

4.2 Fluctuations

Arguably the simplest example to see that fluctuations are necessary to correctly describe the equilibrium is the following [128, 132, 133]. Consider a fast, heavy particle which is damped by a bath of light particles at temperature T. Its equation of motion is

$$m\frac{d}{dt}\boldsymbol{v} + \gamma \boldsymbol{v} = 0. \tag{4.5}$$

where $\boldsymbol{v}$ is the velocity, m the mass and γ denotes the damping constant. The solution to Eq. (4.5) for an initial velocity $\boldsymbol{v}^0$ at $t = 0$ is $\boldsymbol{v}(t) = \boldsymbol{v}^0 \mathrm{e}^{-\gamma t/m} \underset{t\to\infty}{\to} 0$. This is the correct result, since in equilibrium $\langle \boldsymbol{v} \rangle_{\mathrm{eq}} = 0$.

However, by the equipartition theorem, the average kinetic energy of the particle in equilibrium is $\langle E_{\mathrm{kin}} \rangle_{\mathrm{eq}} = \frac{m}{2}\langle \boldsymbol{v}^2 \rangle_{\mathrm{eq}} = \frac{d}{2}T$ or, in components, $\langle v_i v_j \rangle_{\mathrm{eq}} = T/m$. This is not correctly described by Eq. (4.5). The energy of the damped particle is not conserved: it is an open system coupled to a huge number of degrees of freedom– the bath. Having chosen this approach, the feedback of the bath can be described only statistically. A fluctuating term $\boldsymbol{\xi}(t)$ has to be included on the right hand side:

$$m\frac{d}{dt}\boldsymbol{v} + \gamma \boldsymbol{v} = \boldsymbol{\xi}(t). \tag{4.6}$$

This equation has the solution

$$\boldsymbol{v}(t) = \boldsymbol{v}^0 \mathrm{e}^{-\gamma t/m} + \frac{1}{m}\int_0^t dt'\, \mathrm{e}^{-\gamma(t-t')/m}\, \boldsymbol{\xi}(t'). \tag{4.7}$$

Eq. (4.6) is the simplest example of a *Langevin equation* [133]. The velocity $\boldsymbol{v}$ has to be interpreted as a stochastic variable. Eq. (4.6) can be rewritten into a deterministic equation for the probability distribution, a Fokker-Planck equation [128]. To obtain

$\langle \boldsymbol{v} \rangle_{\rm eq} = 0$, the first moment of $\boldsymbol{\xi}$ has to be zero $\langle \boldsymbol{\xi}(t) \rangle = 0$. But to obtain $\langle E_{\rm kin} \rangle_{\rm eq} = \frac{d}{2} T$, its second moment must be nonzero. We write $\langle \xi_i(t) \xi_j(t') \rangle = \delta_{ij} \eta \delta(t - t')$ and obtain from Eq. (4.7)

$$\begin{aligned} \langle v_i(t) v_j(t) \rangle &= v_i^0 v_j^0 \mathrm{e}^{-2\gamma t/m} + \frac{1}{m} \int_0^t dt' \int_0^t dt'' \, \mathrm{e}^{-\gamma/m(2t - t' - t'')} \, \langle \xi_i(t') \xi_j(t'') \rangle_{\rm eq} \\ &= v_i^0 v_j^0 \mathrm{e}^{-2\gamma t/m} + \delta_{ij} \, \frac{\eta \, m}{2\gamma} \left(1 - \mathrm{e}^{-2t\gamma/m} \right) . \end{aligned} \tag{4.8}$$

To match the thermal fluctuations in the limit $t \gg m/\gamma$ we have to choose $\eta = 2\gamma \, T$ and thus

$$\langle \xi_i(t) \xi_j(t') \rangle = 2\gamma \, T \, \delta_{ij} \delta(t - t'). \tag{4.9}$$

The relation $\eta \sim \gamma T$ is the manifestation of a fluctuation-dissipation theorem [128] and was first derived, in a slightly different form, by Einstein [134].

The stochastic approach is sufficient, or even necessary, for many practical purposes. However, it needs some phenomenological input: here the equipartition theorem, which is a consequence of the maximum entropy principle. Supposed that we could solve the system of coupled differential equations for all $M \sim 10^{23}$ particles with fixed energy $E_{\rm tot} = M \frac{d}{2} T$ (assuming hard-core collisions without any interaction energy). This would lead to the same conclusion, namely that the *time-averaged* energy of each particle is $\langle E_{\rm kin} \rangle_{\rm time} = \frac{d}{2} T$.

The situation we are aiming to describe is a system in local equilibrium. The condition of local equilibrium gives the notion of a local temperature and a local chemical potential. Equivalently, one can use the space-dependent energy density and particle density. If those very slowly in space and time, the limit $\boldsymbol{q} \to$ and $\omega \to 0$, the time evolution of the conserved densities is described by hydrodynamic equations [124, 125, 127–129, 135].

For simplicity we first consider systems with a single conserved quantity – it might be either the energy or the particle number. Its density will be denoted by $n(x, t)$ and the corresponding current by $\boldsymbol{j} = \boldsymbol{v} \, n$ where $\boldsymbol{v}$ is the velocity. The density n and the current $\boldsymbol{j}$ have to be interpreted as stochastic fields. Its expectation values and correlations can be obtained from a statistical average of a, in general non-equilibrium, ensemble of the microscopic variables or, for quantum theories, operators. This ensemble is provided by all the microscopic degrees of freedom which are not part of the description. $n(x, t)$ describes a macrostate which may have different microscopic realizations. In equilibrium this ensemble coincides with the equilibrium ensemble. The fluctuation theory treated here phenomenologically can be made

rigorous by means of the memory function formalism due to Zwanzig [136] and Mori [137], reviewed in [132].

The macroscopic conservation law can be cast in a *continuity equation*

$$\partial_t n + \partial_{\boldsymbol{x}} \boldsymbol{j} = 0. \tag{4.10}$$

For convenience we use the notation that $\partial_{\boldsymbol{x}} = \nabla = (\partial_{x_1}, \dots, \partial_{x_d})$ and $\partial_{\boldsymbol{x}}^2 = \nabla \cdot \nabla = \sum_{i=1}^d \partial_{x_i}^2$. From Eq. (4.10) we obtain

$$\partial_t \int_V d^d\boldsymbol{x}\, n(\boldsymbol{x},t) = \int_V d^d\boldsymbol{x}\, \partial_{\boldsymbol{x}} \boldsymbol{j} \underset{\text{Stokes}}{=} \int_{\partial V} d^{d-1}\boldsymbol{x}\, \boldsymbol{j}|_{\partial V} = 0. \tag{4.11}$$

In the last equality we have made use of the fact that we are dealing with a closed system and there is no current flow across the boundary ∂V. Then the local continuity equation, Eq. (4.10), is equivalent to the macroscopic conservation law in Eq. (4.11).

If the density is inhomogeneous this causes a current flow

$$\boldsymbol{j} = -\boldsymbol{F}(\partial_{\boldsymbol{x}} n, \partial_{\boldsymbol{x}}^2 n, \partial_{\boldsymbol{x}} n^2, \dots). \tag{4.12}$$

This can be motivated by the highest entropy principle: in equilibrium all densities are spatially uniform (on average). A homogenous state is more probable than an inhomogeneous state and therefore an inhomogeneous density will have the tendency to flatten.

Inserting Eq. (4.12) into Eq. (4.10) yields a partial differential equation for the density

$$\partial_t n - \partial_{\boldsymbol{x}} \boldsymbol{F}(\partial_{\boldsymbol{x}} n, \partial_{\boldsymbol{x}}^2 n, \partial_{\boldsymbol{x}} n^2, \dots) = 0. \tag{4.13}$$

For systems with more conserved quantities there will generically be couplings. For example, a gradient in the particle density can cause an energy current flow and vice versa. Close to equilibrium, this coupling is described by the *Onsager relations* [124, 125]. We will first ignore these couplings and come back to that below in subsection 4.6.

If the inhomogeneity is not too strong, to be specified below in section 4.3, we can expand $\boldsymbol{F}(\partial_{\boldsymbol{x}} n, \partial_{\boldsymbol{x}}^2 n, \dots) = D_n\, \partial_{\boldsymbol{x}} n + \dots$, where we have included only the leading order linear term. $D_n > 0$ denotes the diffusion constant related to the transport of the density n. It can be calculated from the Kubo formula of the corresponding current. The relation

$$\boldsymbol{j} = -D_n\, \partial_{\boldsymbol{x}} n \tag{4.14}$$

is known as *Fick's law* [138]. Inserting this into Eq. (4.13) yields the *diffusion equation*

$$\partial_t n - D_n \, \partial_{\boldsymbol{x}}^2 n = 0. \tag{4.15}$$

While the conservation law in Eq. (4.10) is exact, the current is subject to fluctuations. To include those, we alter Fick's law to $\boldsymbol{j} = -D_n \, \partial_{\boldsymbol{x}} n - \boldsymbol{\xi}$. A constant contribution can clearly be excluded as it implies a persistent current. Therefore it must be $\langle \boldsymbol{\xi} \rangle = 0$. The average $\langle \cdot \rangle$ has to be interpreted as an ensemble average over the aforementioned ensemble provided by all the microscopic degrees of freedom that are omitted in the coarse-grained description. We will refer to $\boldsymbol{\xi}$ as a *noise* or *fluctuating* term. The noisy, or fluctuating, diffusion equation then reads

$$\partial_t n - D_n \, \partial_{\boldsymbol{x}}^2 n = \partial_{\boldsymbol{x}} \boldsymbol{\xi}. \tag{4.16}$$

We assume that the fluctuations in the different directions are uncorrelated and write

$$\langle \xi_i(\boldsymbol{x}, t) \, \xi_j(\boldsymbol{x}', t') \rangle = \frac{\delta_{ij}}{d} \eta_n \, \delta(\boldsymbol{x} - \boldsymbol{x}') \, \delta(t - t') \tag{4.17}$$

$$\langle \boldsymbol{\xi}(\boldsymbol{x}, t) \, \boldsymbol{\xi}(\boldsymbol{x}', t') \rangle = \eta_n \, \delta(\boldsymbol{x} - \boldsymbol{x}') \, \delta(t - t'). \tag{4.18}$$

where η_n determines the strength of the fluctuations for the current of n.

By means of Fourier transformation,

$$\begin{pmatrix} n(\boldsymbol{x}, t) \\ \boldsymbol{\xi}(\boldsymbol{x}, t) \end{pmatrix} = \int \frac{d^d \boldsymbol{q}}{(2\pi)^d} \int \frac{d\omega}{2\pi} \mathrm{e}^{-i\boldsymbol{q}\cdot\boldsymbol{x} + i\omega t} \begin{pmatrix} n(\boldsymbol{q}, \omega) \\ \boldsymbol{\xi}(\boldsymbol{q}, \omega) \end{pmatrix}, \tag{4.19}$$

the fluctuating diffusion equation, Eq. (4.16), can be rewritten as

$$\left(i\omega + D_n q^2 \right) n(\boldsymbol{q}, \omega) = -i \boldsymbol{q} \cdot \boldsymbol{\xi}(\boldsymbol{q}, \omega), \tag{4.20}$$

which can be solved easily to

$$n(\boldsymbol{q}, \omega) = \frac{-i \boldsymbol{q} \cdot \boldsymbol{\xi}(\boldsymbol{q}, \omega)}{i\omega + D_n \boldsymbol{q}^2}. \tag{4.21}$$

The fluctuations, Eq. (4.18), transform to

$$\langle \boldsymbol{\xi}(\boldsymbol{q}, \omega) \, \boldsymbol{\xi}(\boldsymbol{q}', \omega') \rangle = \eta_n \, (2\pi)^{d+1} \, \delta(\boldsymbol{q} + \boldsymbol{q}') \, \delta(\omega + \omega'). \tag{4.22}$$

The right hand side of Eq. (4.20) has correlations $\sim q^2$, which is the hallmark of a conserving noise [131, 132]. In the following we assume $\langle n \rangle_{\mathrm{eq}} = 0$, which can always

be reached by a redefinition $n \to n - \langle n \rangle_{\rm eq}$. Here and in the following $\langle \cdot \rangle_{\rm eq}$ denotes an average over the equilibrium ensemble. The equilibrium fluctuations of the density can then be obtained as

$$\begin{aligned}
\langle n(\boldsymbol{x},t)\, n(\boldsymbol{x}',t')\rangle_{\rm eq} &= \int \tfrac{d^d\boldsymbol{q}}{(2\pi)^d} \int \tfrac{d\omega}{2\pi} \int \tfrac{d^d\boldsymbol{q}'}{(2\pi)^d} \int \tfrac{d\omega'}{2\pi} \mathsf{e}^{-i\boldsymbol{q}\cdot\boldsymbol{x}+i\omega t - i\boldsymbol{q}'\cdot\boldsymbol{x}'+i\omega' t'} \, \langle n(\boldsymbol{q},\omega)\, n(\boldsymbol{q}',\omega')\rangle_{\rm eq} \\
&= \eta_n \int \tfrac{d^d\boldsymbol{q}}{(2\pi)^d} \int \tfrac{d\omega}{2\pi} \mathsf{e}^{-i\boldsymbol{q}\cdot(\boldsymbol{x}-\boldsymbol{x}')+i\omega(t-t')} \frac{\boldsymbol{q}^2}{\omega^2 + D_n^2\,\boldsymbol{q}^4} \\
&= \frac{\eta_n}{2D_n} \, \frac{\exp\left(-\frac{|\boldsymbol{x}-\boldsymbol{x}'|^2}{8D_n|t-t'|}\right)}{(4\pi D_n|t-t'|)^{d/2}} \qquad (4.23) \\
&\underset{t\to t'}{\longrightarrow} \frac{\eta_n}{2D_n}\, \delta(\boldsymbol{x}-\boldsymbol{x}'). \qquad (4.24)
\end{aligned}$$

In the last line we have taken the limit $|t-t'| \to 0$. On the coarse-grained scale beyond any mean free path and correlation length, the equal-time equilibrium correlations of a conserved quantity can generally be expressed as $\langle n(\boldsymbol{x})\, n(\boldsymbol{x}')\rangle_{\rm eq} = C_n\, \delta(\boldsymbol{x}-\boldsymbol{x}')$. Most importantly, C_n is independent of the diffusion constant D_n as it can be calculated from the thermodynamical ensemble. This leads to the relation $\eta_n = 2D_nC_n$. Again, this is a manifestation of the fluctuation-dissipation relation [128, 129, 132]. If $n \equiv e$ is the energy density, it is $C_e = T^2 c_V$ where c_V is the specific heat per volume [129]. If n is the particle density, it is $C_n = n_0^2\, T\, \kappa_T$ where κ_T is the isothermal compressibility per volume and n_0 is the equilibrium density [139]. This implies

$$\langle \boldsymbol{\xi}_e(\boldsymbol{x},t)\, \boldsymbol{\xi}_e(\boldsymbol{x}',t')\rangle = 2\, D_e\, T^2\, c_V\, \delta(\boldsymbol{x}-\boldsymbol{x}')\, \delta(t-t') \qquad (4.25)$$

$$\langle \boldsymbol{\xi}_n(\boldsymbol{x},t)\, \boldsymbol{\xi}_n(\boldsymbol{x}',t')\rangle = 2\, D_n\, n_0^2\, T\, \kappa_T\, \delta(\boldsymbol{x}-\boldsymbol{x}')\, \delta(t-t'). \qquad (4.26)$$

These current fluctuations reproduce the correct equilibrium correlations of the densities. Due to the fluctuation-dissipation relations, we can then expect that also the time evolution of non-equilibrium correlations in systems close to equilibrium is governed by Eqns. (4.25) and (4.26). Here "close to equilibrium" refers to regimes where linear response theory is valid. For convenience we will use C_n as the prefactor of the current fluctuations in the following, keeping in mind that this refers to Eqns. (4.25) and (4.26).

From Eq. (4.23) we make the following observation: if we fix one time, for example $t' = 0$, and consider the limit $t \gg \frac{|\boldsymbol{x}-\boldsymbol{x}'|^2}{D_n}$, we find

$$\langle n(\boldsymbol{x},t)\, n(\boldsymbol{x}',0)\rangle_{\rm eq} \underset{t\gg\frac{|\boldsymbol{x}-\boldsymbol{x}'|^2}{D_n}}{\longrightarrow} \frac{C_n}{(4\pi D_n t)^{d/2}} \sim \frac{1}{t^{d/2}}. \qquad (4.27)$$

Here we have encountered a hydrodynamic long-time tail for an equilibrium correlation function. Before we discuss long-time tails in section 4.4 in more detail, we first consider the scaling properties of the fluctuating diffusion equation.

4.3 Scaling analysis of the diffusion equation

The fluctuating diffusion equation in combination with the correlations

$$\partial_t n - D_n \, \partial_{\boldsymbol{x}}^2 n = \partial_{\boldsymbol{x}} \boldsymbol{\xi} \tag{4.28}$$

$$\langle \boldsymbol{\xi}(\boldsymbol{x},t) \, \boldsymbol{\xi}(\boldsymbol{x}',t') \rangle = 2 \, D_n \, C_n \, \delta(\boldsymbol{x}-\boldsymbol{x}') \, \delta(t-t') \tag{4.29}$$

defines a fixpoint relative to which we can investigate the effect of further possible terms.

Let us consider a scaling transformation $\lambda \tilde{\boldsymbol{x}} = \boldsymbol{x}$ with $\lambda > 1$. If we assume that the diffusion constant is scale invariant, the left hand side of Eq. (4.28) implies $\tilde{t} = \lambda^{-2} \, t$. From Eq. (4.29) we find $\tilde{\boldsymbol{\xi}} = \lambda^{(1+d/2)} \, \boldsymbol{\xi}$. Finally, inserting this into Eq. (4.28) yields $\tilde{n} = \lambda^{d/2} \, n$

We adapt the notation of the book by Altland and Simons [140] and denote the rescaling of a quantity by square brackets, for example $[n] = \lambda^{d/2}$ corresponds to a rescaling $n \to \lambda^{d/2} n = \tilde{n}$. The exponent, here $d/2$, is called the *scaling dimension* or *engineering dimension*. Terms which have a negative scaling dimension are called *irrelevant*, as they become unimportant on larger length- and timescales. By contrast, terms showing a positive scaling dimension are called *relevant*. If such terms exist one may have chosen the wrong fixpoint and one has to include these terms into the theory. Terms with scaling dimension zero are called *marginal*.

Let us first consider terms with higher order derivatives: $\alpha_j \, \partial_{\boldsymbol{x}}^j n$. The scaling dimension of α_j is $2-j$ as $[\alpha_j] = \lambda^{2-j}$ and all terms with $j > 2$ are irrelevant. Next, we consider terms which are of higher order in the densities but have second order derivatives: $\beta_j \, \partial_{\boldsymbol{x}}^2 n^j$. We find $[\beta_j] = \lambda^{d/2(1-j)}$, corresponding to a scaling dimension $d/2 \, (1-j)$, and terms with $j > 1$ are irrelevant.

Let us now discuss terms with lower order derivatives. Including all possible terms, we add

$$\gamma_j \; (n(\boldsymbol{x},t) - n_f)^j + \boldsymbol{\zeta}_j \cdot \partial_{\boldsymbol{x}} n^j(\boldsymbol{x},t) \tag{4.30}$$

with $j \geq 1$. The various terms transform according to $[\gamma_j] = \lambda^{2+(1-j)d/2}$ and $[\boldsymbol{\zeta}_j] = \lambda^{1+(1-j)d/2}$, implying scaling dimensions $2 + (1-j) \, d/2$ and $1 + (1-j) \, d/2$ respectively.

As the densities in the terms $\sim \gamma_j$ do not carry a spatial derivative, these terms

cannot be derived from the current. This implies that the continuity equation, Eq. (4.10), is violated. The most relevant term, given for $j = 1$, is relevant in any dimension. For consistency the (physical) dimension of γ_1 is $\frac{1}{TIME}$ and we write $\gamma_1 = 1/\tau_f$ to obtain $\partial_t n - D_n \partial_{\boldsymbol{x}}^2 n + (n - n_f)/\tau_f = \partial_{\boldsymbol{x}} \cdot \boldsymbol{\xi}$, where n_f is constant. We will discuss this equation in more detail below in section 4.5.

The terms $\sim \boldsymbol{\zeta}_j$ yields the equation $\partial_t n - D_n \partial_{\boldsymbol{x}}^2 n + \boldsymbol{\zeta}_j \cdot \partial_{\boldsymbol{x}} n^j = \partial_{\boldsymbol{x}} \cdot \boldsymbol{\xi}$. The most relevant term is again given for $j = 1$. However, for inversion symmetric systems it is not allowed: if we consider a inversion symmetry transformation $x \xrightarrow{\mathrm{I}} -x$, this term does not transform as the other terms independent of whether $n \xrightarrow{\mathrm{I}} n$ or $n \xrightarrow{\mathrm{I}} -n$. Note that $\boldsymbol{\xi}$ transforms as a current and thus in the opposite way as the corresponding density.

The next term $\sim \boldsymbol{\zeta}_2$ yields the equation of motion

$$\partial_t n - D_n \partial_{\boldsymbol{x}}^2 n + 2\, n\, \boldsymbol{\zeta}_2 \cdot \partial_{\boldsymbol{x}} n = \partial_{\boldsymbol{x}} \cdot \boldsymbol{\xi}. \tag{4.31}$$

If $n \xrightarrow{\mathrm{I}} n$, it is again not allowed by inversion symmetry. However if $n \xrightarrow{\mathrm{I}} -n$, it is allowed and it is relevant in $d < 2$ and marginal in $d = 2$. The transformation $n \xrightarrow{\mathrm{I}} -n$ is fulfilled for the momentum density but not for the energy density or the particle density. In one dimensional systems with momentum conservation this leads to a breakdown of linear hydrodynamics and an anomalous transport behavior [141–143]. This has also been confirmed numerically [121, 144–147]. The corresponding fixpoint is described by the Kardar-Parisi-Zhang (KPZ) universality class [148, 149].

4.4 Long-time tails

Long-time tails were first observed in numerical molecular dynamic studies of hard disks ($2d$) and hard spheres ($3d$) around 1970 by Alder and Wainwright [150–152]. The authors found a decay of the equilibrium velocity-velocity correlation function as t^{-1} in $2d$ and $t^{-3/2}$ in $3d$. Reviews discussing the kinetic origin and the history of long-time tails can be found in [153–156]. The interest in the unequal time equilibrium autocorrelation functions can be rationalized by the fact that they naturally appear as integrands in the calculation of transport coefficients in the Kubo formalism [126–128].

Soon after the long-time tails have been detected, theoretical work reproduced the asymptotic behavior $\sim t^{-d/2}$ [157–160]. Ultimately, the long-time tails rely only on hydrodynamical slow modes. Thus they arise in very different areas of physics, including non-equilibrium steady states [161, 162], critical phenomena [163] and cos-

mology [164, 165]. In the following we will see, both analytically and numerically, that they also dominate the thermalization process.

There exist different formalisms which are able to capture the physics relevant for the long-time tails, taken together under the name *mode-coupling theories* [135, 153]. The approach we use is fluctuating hydrodynamics as already used in the first theory paper by Ernst, Hauge and van Leeuwen [157]. Connection to microscopic equations is provided by the memory function formalism [136, 137]. In [158, 159] Dorfman and Cohen derived the long-time tails from microscopic kinetic theory, see also [153]. Here the term "kinetic theory" is used much more general as it is usually done. Often it is used as a synonym for conventional Boltzmann equation approaches. However, in the long-time tail literature it is used for equations also including n-particle distribution functions. The physics of the long-time tails is captured by the two-particle (pair) distribution function [158, 159].

To derive the long-time tails in this framework, the correlation function is written in a power series of the density. The coefficients can be represented graphically in terms of collision diagrams [166]. It has been noticed before that in the density expansion of the pair distribution function divergences appear [167]. The origin are multiple binary collisions of the same two particles where one of the particles has scattered with other particles in between. Including only a few other particles, the contributions of such events do not converge for long times and small wavenumbers. However when including all other particles, it is very unlikely that a particle has not scattered after a few scattering times. This leads to an exponential suppression in space and time and a natural cutoff for the divergent integrals. Resummation of the most divergent terms leads to terms logarithmic in the density [166]. In [158, 159], Dorfman and Cohen showed that this resummation in a density expansion of the correlation functions also leads to the observed long-time tails, see also [168]. They are undoubtedly a correlation effect and thus cannot be reproduced by Boltzmann type equations, which assume uncorrelated collisions. Furthermore, the long-time tails cannot be captured by low order perturbation theory due to the divergences.

In Eq. (4.27) we have already seen that the unequal time density-density equilibrium correlation function decays as $t^{-d/2}$. To calculate further equilibrium correlation functions and, eventually, non-equilibrium correlation functions it is useful to introduce the general solution of the diffusion equation. As Eq. (4.20) is linear, it can be solved by the Greens function method. We define the diffusion propagator $G_{D_n}(\boldsymbol{x}, t)$ by

$$\partial_t G_{D_n}(\boldsymbol{x}, t) - D_n \partial_{\boldsymbol{x}}^2 G_{D_n}(\boldsymbol{x}, t) = \delta(\boldsymbol{x})\delta(t) \rightarrow G_{D_n}(\boldsymbol{q}, \omega) = \frac{1}{i\omega + D_n \boldsymbol{q}^2} \tag{4.32}$$

and thus

$$G_{D_n}(\boldsymbol{x},t) = \Theta(t)\frac{\exp\left(-\frac{\boldsymbol{x}^2}{4D_n t}\right)}{(4\pi D_n t)^{d/2}}. \tag{4.33}$$

Up to normalization, this is exactly the result obtained above for the probability distribution of a random walk, see Eq. (4.4). This remarkable agreement, obtained from totally different starting points, shows the connection between diffusion (arising from a very complicated many-body problem) and random walks (arising from a very simple stochastic problem).

Solutions of an arbitrary right hand side in Eq. (4.32) are then found from Eq. (4.33) by convolution. From Eq. (4.20) we obtain

$$\begin{aligned} n(\boldsymbol{x},t) =& \Theta(t) \int d^d\boldsymbol{y}\, \frac{\exp\left(-\frac{|\boldsymbol{x}-\boldsymbol{y}|^2}{4D_n t}\right)}{(4\pi D_n t)^{d/2}}\, n_i(\boldsymbol{y}) \\ &+ \int d^d\boldsymbol{y} \int_0^t dt' \frac{\exp\left(-\frac{|\boldsymbol{x}-\boldsymbol{y}|^2}{4D_n (t-t')}\right)}{(4\pi D_n (t-t'))^{d/2}}\, \partial_{\boldsymbol{y}} \boldsymbol{\xi}(\boldsymbol{y},t'), \end{aligned} \tag{4.34}$$

where we have imposed an initial condition $n(\boldsymbol{x},0) = n_i(\boldsymbol{x})$ at $t = 0$.

As a further equilibrium quantity we calculate the unequal time, local current -current correlation function. From Eq. (4.34) we find with the equilibrium initial condition $\langle n_i(\boldsymbol{y}) n_i(\boldsymbol{y}')\rangle = C_n\, \delta(\boldsymbol{y}-\boldsymbol{y}')$

$$\begin{aligned} \langle \partial_{\boldsymbol{x}} n(\boldsymbol{x},t)\, \partial_{\boldsymbol{x}'} n(\boldsymbol{x}',t+\Delta t)\rangle_{\rm eq} &= C_n \int d^d\boldsymbol{y}\, \partial_{\boldsymbol{x}}\partial_{\boldsymbol{x}'} \frac{\mathrm{e}^{-\frac{|\boldsymbol{x}-\boldsymbol{y}|^2}{4D_n t}}\, \mathrm{e}^{-\frac{|\boldsymbol{x}'-\boldsymbol{y}|^2}{4D_n (t+\Delta t)}}}{\left(4\pi D_n \sqrt{t(t+\Delta t)}\right)^d} \\ + \int d^d(\boldsymbol{y},\boldsymbol{y}') \int_0^t dt' \int_0^{t+\Delta t} dt''\, & \frac{\partial_{\boldsymbol{x}}\partial_{\boldsymbol{x}'}\, \mathrm{e}^{-\frac{|\boldsymbol{x}-\boldsymbol{y}|^2}{4D_n (t-t')} - \frac{|\boldsymbol{x}'-\boldsymbol{y}'|^2}{4D_n (t+\Delta t-t'')}}}{(4\pi D_n \sqrt{(t-t')(t+\Delta t-t'')})^d} \partial_{\boldsymbol{y}}\partial_{\boldsymbol{y}'} \langle \boldsymbol{\xi}(\boldsymbol{y},t')\, \boldsymbol{\xi}(\boldsymbol{y}',t'')\rangle \\ \xrightarrow[|\boldsymbol{x}-\boldsymbol{x}'|\to 0]{} & \frac{d\,\pi}{2}\, \frac{C_n}{(4\pi\, D_n\, \Delta t)^{d/2+1}}. \end{aligned} \tag{4.35}$$

The result, of course, depends only on Δt. The equilibrium current autocorrelation function decays faster as its density counterpart, namely as $t^{-(1+d/2)}$. The spatial derivatives suppress two scaling dimensions, which corresponds to a factor t^{-1}. In systems with momentum conservation the energy current autocorrelation function decays as $t^{-3/5}$ (in $1d$), t^{-1} (in $2d$) and $t^{-3/2}$ (in $3d$) [169].

Let us now consider non-equilibrium correlation functions. We assume that the system is in the regime of linear response – implying that it is close to equilibrium.

From Eqns. (4.18), (4.21), (4.23), (4.34) we then find for $t > 0$

$$\begin{aligned}
\langle n(\boldsymbol{x},t)n(\boldsymbol{x}',t)\rangle &= \int d^d\boldsymbol{y}\int d^d\boldsymbol{y}'\,\frac{\mathsf{e}^{-\frac{|\boldsymbol{x}-\boldsymbol{y}|^2+|\boldsymbol{x}'-\boldsymbol{y}'|^2}{4D_nt}}}{(4\pi D_nt)^d}\langle n_i(\boldsymbol{y})n_i(\boldsymbol{y}')\rangle \\
&+\int d^d(\boldsymbol{y},\boldsymbol{y}')\int_0^t dt'\int_0^t dt''\frac{\mathsf{e}^{-\frac{|\boldsymbol{x}-\boldsymbol{y}|^2}{4D_n(t-t')}-\frac{|\boldsymbol{x}'-\boldsymbol{y}'|^2}{4D_n(t-t'')}}}{(4\pi D_n\sqrt{(t-t')(t-t'')})^d}\partial_{\boldsymbol{y}}\partial_{\boldsymbol{y}'}\langle\boldsymbol{\xi}(\boldsymbol{y},t')\,\boldsymbol{\xi}(\boldsymbol{y}',t'')\rangle \\
&=\int d^d(\boldsymbol{y},\boldsymbol{y}')\frac{\mathsf{e}^{-\frac{|\boldsymbol{x}-\boldsymbol{y}|^2+|\boldsymbol{x}'-\boldsymbol{y}'|^2}{4D_nt}}}{(4\pi D_nt)^d}\langle n_i(\boldsymbol{y})n_i(\boldsymbol{y}')\rangle + C_n\int\frac{d^d\boldsymbol{q}}{(2\pi)^d}\,e^{-i\boldsymbol{q}\cdot(\boldsymbol{x}-\boldsymbol{x}')}(1-e^{-2D_ntq^2}) \\
&=\int d^d(\boldsymbol{y},\boldsymbol{y}')\frac{\mathsf{e}^{-\frac{|\boldsymbol{x}-\boldsymbol{y}|^2+|\boldsymbol{x}'-\boldsymbol{y}'|^2}{4D_nt}}}{(4\pi D_nt)^d}\langle n_i(\boldsymbol{y})n_i(\boldsymbol{y}')\rangle + C_n\delta(\boldsymbol{x}-\boldsymbol{x}') - C_n\frac{\mathsf{e}^{-\frac{|\boldsymbol{x}-\boldsymbol{x}'|^2}{8D_nt}}}{(8\pi D_nt)^{d/2}}. \qquad (4.36)
\end{aligned}$$

If the initial correlations are short-ranged $\langle n_i(\boldsymbol{y})n_i(\boldsymbol{y}')\rangle = A_n\,\delta(\boldsymbol{y}-\boldsymbol{y}')$, this yields

$$\begin{aligned}
&\langle n(\boldsymbol{x},t)n(\boldsymbol{x}',t)\rangle - \langle n(\boldsymbol{x},t)n(\boldsymbol{x}',t)\rangle_{\rm eq} = \langle n(\boldsymbol{x},t)n(\boldsymbol{x}',t)\rangle - C_n\delta(\boldsymbol{x}-\boldsymbol{x}') \\
=&(A_n-C_n)\,\frac{\exp\left(-\frac{|\boldsymbol{x}-\boldsymbol{x}'|^2}{8D_nt}\right)}{(8\pi D_nt)^{d/2}}\underset{t\gg|\boldsymbol{x}-\boldsymbol{x}'|^2/(8D_n)}{\longrightarrow}\frac{A_n-C_n}{(8\pi D_nt)^{d/2}}. \qquad (4.37)
\end{aligned}$$

If the initial state was an equilibrium state, $A_n = C_n$, we recover the equilibrium fluctuations. However, if the initial state was not an equilibrium state, $A_n \neq C_n$, we find that the thermal fluctuations are built-up only algebraically $\sim 1/t^{d/2}$. Therefore we expect that generically the thermalization is dominated by hydrodynamic long-time tails. This can be viewed as the bottleneck for thermalization. This also includes the case when the initial state was an equilibrium state at a different temperature or density. The short-rangeness of the initial correlations is often fulfilled in quantum quench setups, for example if the initial state was a product state. The prefactor of the non-equilibrium long-time tails depends on the initial state via the coefficient A_n. By contrast, the prefactors of the equilibrium long-time tails are determined by equilibrium correlation functions, see for example Eqns. (4.27) and (4.35).

Finally, we consider long-ranged initial correlations $\langle n_i(\boldsymbol{y})n_i(\boldsymbol{y}')\rangle = \frac{A_n}{|\boldsymbol{y}-\boldsymbol{y}'|^\nu}$ realized, for example, if the initial state was critical [10] or a free fermion system. If $0 < \nu < d$, we find

$$\begin{aligned}
&\langle n(\boldsymbol{x},t)n(\boldsymbol{x}',t)\rangle - \langle n(\boldsymbol{x},t)n(\boldsymbol{x}',t)\rangle_{\rm eq} \\
&=\int d^d\boldsymbol{y}\int d^d\boldsymbol{y}'\frac{\mathsf{e}^{-\frac{|\boldsymbol{x}-\boldsymbol{y}|^2+|\boldsymbol{x}'-\boldsymbol{y}'|^2}{4D_nt}}}{(4\pi D_nt)^d}\frac{A_n}{|\boldsymbol{y}-\boldsymbol{y}'|^\nu} - \frac{C_n}{(8\pi D_nt)^{d/2}} \\
&=\frac{A_n}{(4\pi D_nt)^d}\int d^d\boldsymbol{y}\frac{\mathsf{e}^{-\frac{|\boldsymbol{y}-\boldsymbol{x}+\boldsymbol{x}'|^2}{4D_nt}}}{|\boldsymbol{y}|^\nu}\int d^d\boldsymbol{y}'\mathsf{e}^{-\frac{|\boldsymbol{y}'|^2+\boldsymbol{y}'\cdot(\boldsymbol{y}-\boldsymbol{x}+\boldsymbol{x}')}{2D_nt}} - \frac{C_n}{(8\pi D_nt)^{d/2}}
\end{aligned}$$

$$= \frac{A_n}{(8D_n t)^{\nu/2}} \frac{\Gamma\left(\frac{d-\nu}{2}\right)}{\Gamma\left(\frac{d}{2}\right)} {}_1F_1\left(\tfrac{\nu}{2}, \tfrac{d}{2}, -\tfrac{|\boldsymbol{x}-\boldsymbol{x}'|^2}{8D_n t}\right) - \frac{C_n}{(8\pi D_n t)^{d/2}} \tag{4.38}$$

where Γ denotes the Euler gamma function and ${}_1F_1(a,b,z)$ is the Kummer confluent hypergeometric function. The local correlations are found by ${}_1F_1(a,b,0) = 1$. For $|\boldsymbol{x}-\boldsymbol{x}'| \gg \sqrt{8D_n t}$ we can expand ${}_1F_1(\frac{\nu}{2}, \frac{d}{2}, z \to -\infty) \to (-z)^{-\nu/2}\ \Gamma(\frac{d-\nu}{2})/\Gamma(\frac{d}{2})$. With $z = -\frac{|\boldsymbol{x}-\boldsymbol{x}'|^2}{8D_n t}$ we recover the initial correlations. The decay of the first term is slower than the decay of the second term, since $\nu < d$, and the thermalization is as slow as $\sim 1/t^{\nu/2}$.

For $\nu \geq d$ the integral leading to Eq. (4.38) does not converge and one has to introduce a short distance cutoff a. For free fermions, for example, this is naturally given by the inverse Fermi momentum. As a concrete example, we consider a free fermion quench in $3d$. We calculate only the relaxation of the density correlations. This is not intended to give a full picture, as we do not consider couplings to the other conserved quantities, but just as an example for a calculation with long-ranged initial correlations where $\nu > d$.

We denote the groundstate of the non-interacting fermions, the *Fermi sea*, by

$$|\mathrm{FS}\rangle = \prod_{s=\uparrow,\downarrow;|\boldsymbol{k}|<k_F} \hat{\Psi}^\dagger_{\boldsymbol{k},s} |\mathrm{vac}\rangle \tag{4.39}$$

where k_F denotes the Fermi momentum. We consider a hypothetical quench where suddenly a local interaction U is switched on. In the continuum, the expectation value of the density

$$\hat{n}(\boldsymbol{x}) = \hat{\Psi}^\dagger_\uparrow(\boldsymbol{x})\hat{\Psi}_\uparrow(\boldsymbol{x}) + \hat{\Psi}^\dagger_\downarrow(\boldsymbol{x})\hat{\Psi}_\downarrow(\boldsymbol{x}) \tag{4.40}$$

and its correlations are given by

$$\langle \mathrm{FS}|\, \hat{n}(\boldsymbol{x})\, |\mathrm{FS}\rangle = \frac{k_F^3}{3\pi^2} \equiv \rho_F \tag{4.41}$$

$$\langle \mathrm{FS}|\, \hat{n}(\boldsymbol{x})\hat{n}(\boldsymbol{x}')\, |\mathrm{FS}\rangle = \rho_F\ \delta\left(\boldsymbol{x}-\boldsymbol{x}'\right) - \frac{\left(\sin(k_F r) - k_F r\cos(k_F r)\right)^2}{2\pi^4 r^6} \tag{4.42}$$

where $r = |\boldsymbol{x}-\boldsymbol{x}'|$ and ρ_F denotes the total density. The initial correlations decay as $\cos^2(k_F r)/r^4$ at large distances and a short distance cutoff is provided by $1/k_F$, as

$$\langle \mathrm{FS}|\, \hat{n}(\boldsymbol{x})\hat{n}(\boldsymbol{x}')\, |\mathrm{FS}\rangle - \rho_F\ \delta\left(\boldsymbol{x}\right) \underset{k_F r \to 0}{\longrightarrow} -k_F^6/(18\pi^4) = -\rho_F^2/2. \tag{4.43}$$

Calculating the relaxation of the density as in Eq. (4.38), we find

$$\begin{aligned}&\langle n(\boldsymbol{x},t)n(\boldsymbol{x}',t)\rangle - \langle n(\boldsymbol{x},t)n(\boldsymbol{x}',t)\rangle_{\rm eq}\\ &\underset{|\boldsymbol{x}-\boldsymbol{x}'|\to 0}{\longrightarrow} \quad \frac{\rho_F - C_U}{(8\pi D_U t)^{3/2}} - \frac{3\,\rho_F}{16\pi\,(4\pi D_U t)^{3/2}} + \mathcal{O}(t^{-2}).\end{aligned} \tag{4.44}$$

Here D_U denotes the diffusion constant and we have assumed that the final equilibrium correlations are given by

$$\langle n(\boldsymbol{x},t)n(\boldsymbol{x}',t)\rangle_{\rm eq} = C_U\,\delta(\boldsymbol{x}-\boldsymbol{x}') \tag{4.45}$$

which is valid only on large scales beyond any correlation length. The first term in Eq. (4.44) arises from the change in the local part of the correlations and decays as $t^{-3/2}$. The second term arises from the destruction of the long-range correlations in Eq. (4.42) and also decays as $t^{-3/2}$.

4.5 Violation of the conservation laws

In section 4.3 we have seen that a term $\frac{n(\boldsymbol{x},t)-n_f}{\tau_f}$ in the diffusion equation is relevant but violates the underlying conservation law. The continuity equation has to be rewritten to $\partial_t n + \partial_{\boldsymbol{x}}\boldsymbol{j} = -(n-n_f)/\tau_f$ and the (former) diffusion equation has a new relevant term and now reads

$$\partial_t n(\boldsymbol{x},t) - D\,\partial_{\boldsymbol{x}}^2 n(\boldsymbol{x},t) + \frac{n(\boldsymbol{x},t)-n_f}{\tau_f} = 0. \tag{4.46}$$

From now on we omit the constant term n_f, which can always be absorbed in the definition of $n(\boldsymbol{x},t)$. We find the propagator of Eq. (4.46) as

$$\begin{aligned}&\partial_t G_{D_n,\tau_f}(\boldsymbol{x},t) - D_n\partial_{\boldsymbol{x}}^2 G_{D_n,\tau_f}(\boldsymbol{x},t) + \frac{G_{D_n,\tau_f}(\boldsymbol{x},t)}{\tau_f} = \delta(\boldsymbol{x})\delta(t)\\ \rightarrow\ &G_{D_n,\tau_f}(\boldsymbol{x},t) = \Theta(t)\frac{\mathrm{e}^{-t/\tau_f}\ \mathrm{e}^{-\frac{|\boldsymbol{x}-\boldsymbol{x}'|^2}{4D_n t}}}{(4\pi D_n t)^{d/2}}.\end{aligned} \tag{4.47}$$

As the macroscopic conservation law is not valid any more, we expect that there is a new fluctuating term in the continuity equation. It will be denoted by μ which yields

$$\partial_t n + \partial_{\boldsymbol{x}}\boldsymbol{j} = -n/\tau_f + \mu(\boldsymbol{x},t), \tag{4.48}$$

$$\langle\mu(\boldsymbol{x},t)\rangle = 0 \qquad \langle\mu(\boldsymbol{x},t)\mu(\boldsymbol{x}',t')\rangle = \frac{2B_n}{\tau_f}\,\delta(\boldsymbol{x}-\boldsymbol{x}')\,\delta(t-t'). \tag{4.49}$$

The final equation then reads

$$\partial_t n - D\,\partial_{\boldsymbol{x}}^2 n + n/\tau_f = \partial_{\boldsymbol{x}}\boldsymbol{\xi} + \mu. \tag{4.50}$$

This description can only be valid if τ_f is a large timescale, much larger than the scattering time. Then the continuity equation approximately holds for some scattering events and we expect that the corresponding mode is still slow. The correlations of the new noise term have a finite value at $q = 0$: they are not $\sim q^2$ for $q \to 0$, indicating the non-conserving origin. One can argue, or show by a scaling analysis, that the fluctuations of the current can be omitted in the limit $q \to 0$. However, we will keep the $\boldsymbol{\xi}$ term but omit correlations of μ and $\boldsymbol{\xi}$: we use $\langle \mu(\boldsymbol{x},t)\,\boldsymbol{\xi}(\boldsymbol{x}',t')\rangle = 0$. Then the equilibration can be calculated as in Eq. (4.36) to be

$$\begin{aligned}
\langle n(\boldsymbol{x},t)n(\boldsymbol{x}',t)\rangle &= \int d^d(\boldsymbol{y},\boldsymbol{y}')\frac{\mathsf{e}^{-2t/\tau_f}\,\mathsf{e}^{-\frac{|\boldsymbol{x}-\boldsymbol{y}|^2+|\boldsymbol{x}'-\boldsymbol{y}'|^2}{4D_n t}}}{(4\pi D_n t)^d}\langle n_i(\boldsymbol{y})n_i(\boldsymbol{y}')\rangle \\
&+ \int d^d(\boldsymbol{y},\boldsymbol{y}')\int_0^t dt'\int_0^t dt''\frac{\mathsf{e}^{-(t-t')/\tau_f-(t-t'')/\tau_f}\,\mathsf{e}^{-\frac{|\boldsymbol{x}-\boldsymbol{y}|^2}{4D_n(t-t')}-\frac{|\boldsymbol{x}'-\boldsymbol{y}'|^2}{4D_n(t-t'')}}}{(4\pi D_n\sqrt{(t-t')(t-t'')})^d} \\
&\times \left(\partial_{\boldsymbol{y}}\partial_{\boldsymbol{y}'}\langle\boldsymbol{\xi}(\boldsymbol{y},t')\,\boldsymbol{\xi}(\boldsymbol{y}',t'')\rangle + \langle\mu(\boldsymbol{y},t)\mu(\boldsymbol{y}',t')\rangle\right) \\
&= \mathsf{e}^{-2t/\tau_f}\int d^d(\boldsymbol{y},\boldsymbol{y}')\frac{\mathsf{e}^{-\frac{|\boldsymbol{x}-\boldsymbol{y}|^2+|\boldsymbol{x}'-\boldsymbol{y}'|^2}{4D_n t}}}{(4\pi D_n t)^d}\langle n_i(\boldsymbol{y})n_i(\boldsymbol{y}')\rangle + C_n\delta(\boldsymbol{x}-\boldsymbol{x}') \\
&- (B_n+C_n)\,S_d(|\boldsymbol{x}-\boldsymbol{x}'|) + (B_n-C_n)\,\frac{\mathsf{e}^{-2t/\tau_f}\,\mathsf{e}^{-\frac{|\boldsymbol{x}-\boldsymbol{x}'|^2}{8D_n t}}}{(8\pi D_n t)^{d/2}} + \mathcal{O}\left(\frac{\mathsf{e}^{-2t/\tau_f}}{t^{d/2+1}}\right)
\end{aligned} \tag{4.51}$$

where the final result is valid if $t > \sqrt{\frac{|\boldsymbol{x}-\boldsymbol{x}'|^2\tau_f}{16D_n}}$. We find two modifications: most importantly, the decay towards the stationary state is not algebraic any more, but it is exponential. Furthermore, this stationary state has additional non-local, not δ-correlated, static correlations $\sim S_d$ given in the respective dimensions by

$$S_1(r) = \frac{\mathsf{e}^{-\frac{r}{\sqrt{D_n\tau_f}}}}{2\sqrt{D_n\tau_f}}, \tag{4.52}$$

$$S_2(r) = \frac{K_0\left(\frac{r}{\sqrt{D_n\tau_f}}\right)}{2\pi D_n\tau_f} \longrightarrow \begin{cases} \frac{-\log(\frac{r}{\sqrt{D_n\tau_f}})}{2\pi D_n\tau_f} & , r \ll \sqrt{D_n\tau_f}, \\ \frac{\mathsf{e}^{-\frac{r}{\sqrt{D_n\tau_f}}}}{\sqrt{8\pi r}(D_n\tau_f)^{3/4}} & , r \gg \sqrt{D_n\tau_f}, \end{cases} \tag{4.53}$$

$$S_3(r) = \frac{\mathsf{e}^{-\frac{r}{\sqrt{D_n\tau_f}}}}{4\pi D_n\tau_f\, r}. \tag{4.54}$$

For $\tau_f \to \infty$ we recover the results of section 4.4. In this limit, the correlation length $\sqrt{\tau_f D_n}$ of the static correlations S_d diverges while the amplitude is suppressed in a way such that

$$\int d^d\boldsymbol{r} S_d(|\boldsymbol{r}|) = 1. \tag{4.55}$$

If the initial correlations were short-ranged, $\langle n_i(\boldsymbol{y}) n_i(\boldsymbol{y}')\rangle = A_n\,\delta(\boldsymbol{y}-\boldsymbol{y}')$, the final result for $t >= \sqrt{\frac{|\boldsymbol{x}-\boldsymbol{x}'|^2\tau_f}{16 D_n}} = r\sqrt{\frac{\tau_f}{16 D_n}}$ can be written as

$$\begin{aligned}
&\langle n(\boldsymbol{x},t) n(\boldsymbol{x}',t)\rangle - C_n \delta(\boldsymbol{x}-\boldsymbol{x}') \\
&= -(B_n + C_n)\, S_d(r) + (A_n + B_n - C_n)\,\frac{\mathrm{e}^{-2t/\tau_f}\,\mathrm{e}^{-\frac{r^2}{8 D_n t}}}{(8\pi D_n t)^{d/2}} + \mathcal{O}\left(\frac{\mathrm{e}^{-2t/\tau_f}}{t^{d/2+1}}\right).
\end{aligned} \tag{4.56}$$

We will find numerical evidence for the static correlations, including the divergent correlation length, predicted by Eq. (4.52) later in section 6.

4.6 Mode couplings

In generic systems the diffusive modes of different conserved quantities are coupled. Here we consider the case when particle density n and the energy density e fulfill a continuity equation. The respective currents are now given by $\boldsymbol{j}_n = -D_n \partial_{\boldsymbol{x}} n - \kappa^{(1)} \partial_{\boldsymbol{x}} e + \boldsymbol{\xi}_n$ and $\boldsymbol{j}_e = -D_e \partial_{\boldsymbol{x}} e - \kappa^{(2)} \partial_{\boldsymbol{x}} n + \boldsymbol{\xi}_e$, where we have included only the relevant terms, see section 4.3. Close to equilibrium, the coupling is symmetric due to microscopic reversibility as described by the *Onsager relations* [124, 125]. $\kappa^{(1)}$ and $\kappa^{(2)}$ can be calculated via the Kubo formula from the equilibrium correlation functions. For charged particles, the coupling leads to a variety of thermoelectric effects, including the Peltier effect, the Thomson effect and the Seebeck effect [170]. The coupled fluctuating diffusion equations read

$$\partial_t n - D_n\,\partial_{\boldsymbol{x}}^2 n - \kappa^{(1)}\,\partial_{\boldsymbol{x}}^2 e = \partial_{\boldsymbol{x}} \boldsymbol{\xi}_n, \tag{4.57}$$

$$\partial_t e - D_e\,\partial_{\boldsymbol{x}}^2 e - \kappa^{(2)}\,\partial_{\boldsymbol{x}}^2 n = \partial_{\boldsymbol{x}} \boldsymbol{\xi}_e. \tag{4.58}$$

In general the fluctuations of the energy current and the particle current are correlated: $\langle \boldsymbol{\xi}_n \cdot \boldsymbol{\xi}_e \rangle \neq 0$. Eqns. (4.57) and (4.58) can be cast in a matrix structure, which after Fourier transformation is given by

$$\boldsymbol{D} \cdot \begin{pmatrix} n \\ e \end{pmatrix} = \begin{pmatrix} i\omega + D_n q^2 & \kappa^{(1)} q^2 \\ \kappa^{(2)} q^2 & i\omega + D_e q^2 \end{pmatrix} \cdot \begin{pmatrix} n \\ e \end{pmatrix} = \begin{pmatrix} i\,\boldsymbol{q}\cdot\boldsymbol{\xi}_n \\ i\,\boldsymbol{q}\cdot\boldsymbol{\xi}_e \end{pmatrix}. \tag{4.59}$$

Assuming that $D_e, D_n, \kappa^{(1)}$ and $\kappa^{(2)}$ are scale-invariant, a scaling analysis as in section 4.3 shows that both n and e have the same scaling dimension. The results obtained there are applicable, one rather has to use a two-component field. Therefore we do not expect that the form of the long-time tails is changed by the coupling.

Finally, let us consider a situation where one of the conservation laws is violated, but the other remains intact. One could just argue that one can exclude the non-conserved quantity from the theory. Again, one finds the same scaling behavior and the same form of the long-time tails. Nevertheless, we want to see how this arises from the coupled equations

$$\partial_t n - D_n \, \partial_{\boldsymbol{x}}^2 n - \kappa^{(1)} \, \partial_{\boldsymbol{x}}^2 e = \partial_{\boldsymbol{x}} \boldsymbol{\xi}_n \tag{4.60}$$

$$\partial_t e - D_e \, \partial_{\boldsymbol{x}}^2 e - \kappa^{(2)} \, \partial_{\boldsymbol{x}}^2 n = -\frac{e}{\tau_f} + \partial_{\boldsymbol{x}} \boldsymbol{\xi}_e + \mu \tag{4.61}$$

where the energy conservation is explicitly violated. Fourier transformation yields

$$\left(i\omega + D_n q^2\right) n + \kappa^{(1)} q^2 e = i\boldsymbol{q} \cdot \boldsymbol{\xi}_n. \tag{4.62}$$

$$\left(i\omega + D_e q^2 + 1/\tau_f\right) e + \kappa^{(2)} q^2 n = i\boldsymbol{q} \cdot \boldsymbol{\xi}_e + \mu, \tag{4.63}$$

Solving Eq. (4.63) for e and inserting the result into Eq. (4.62) gives

$$\begin{aligned} &\left(i\omega + D_n q^2\right) n - \frac{\kappa^{(1)} \, \kappa^{(2)} q^4}{i\omega + D_e q^2 + 1/\tau_f} \, n = i\boldsymbol{q} \cdot \boldsymbol{\xi}_n - \frac{\kappa^{(1)} q^2}{i\omega + D_e q^2 + 1/\tau_f} \left(i\boldsymbol{q} \cdot \boldsymbol{\xi}_e + \mu\right) \\ &\overset{\omega, q \to 0}{\longrightarrow} \left(i\omega + D_n q^2 - \tau_f \, \kappa^{(1)} \, \kappa^{(2)} \, q^4\right) n = i\boldsymbol{q} \cdot \boldsymbol{\xi}_n - \tau_f \, \kappa^{(1)} q^2 \left(i\boldsymbol{q} \cdot \boldsymbol{\xi}_e + \mu\right). \end{aligned} \tag{4.64}$$

In the second line we have kept only the term in the denominator which is finite in the limit $q \to 0$ and $\omega \to 0$. The new term on the left hand side, $\sim q^4$, corresponds to a term $\partial_{\boldsymbol{x}}^4 n$ and it is irrelevant as shown in section 4.3. The new noise terms on the right side are suppressed by a factor q^2, two scaling dimensions, relative to the noise term of the n-current. Therefore they can also be omitted in the scaling limit.

5 Hydrodynamic long-time tails after a quantum quench

In this section we will give numerical evidence for the hydrodynamic long-time tails as discussed in section 4.4. We consider a quantum quench following the scheme given in the introduction. As a model we have chosen the bosonic Hubbard model, the "standard model" of ultracold bosons, which was already presented in section 2 and whose Hamiltonian reads

$$\hat{H} = -J \sum_i \left(\hat{b}_i^\dagger \, \hat{b}_{i+1} + \hat{b}_{i+1}^\dagger \, \hat{b}_i \right) + \frac{U}{2} \sum_i \hat{b}_i^\dagger \, \hat{b}_i \left(\hat{b}_i^\dagger \, \hat{b}_i - 1 \right). \tag{5.1}$$

We restrict ourselves to one dimension since here the problem is numerically tractable. In contrast to many other $1d$ models, the bosonic Hubbard model is not integrable (except for the trivial cases $U/J = 0$ and $U/J = \infty$) and we expect that it thermalizes after a quantum quench. We will study the time evolution towards the thermal state and will find that, indeed, this is approached only algebraically as predicted by hydrodynamics. As the initial state we have chosen the product state with one boson per site. This is the groundstate of the model for $U/J \to \infty$. We then consider a sudden quench to finite U/J, which can be realized experimentally by changing the lattice depth, see section 2. A graphical illustration is shown in Fig. 5.1.

In the limit $U \gg J$ we can use the semiclassical dynamics as introduced in section 3. This is not applicable any more when $U \sim J$. We have investigated this regime by exact diagonalization. In the semiclassical regime, the doublon lifetime is exponentially large in U/J, as confirmed experimentally in a fermionic Hubbard setup [171]. For recombination, or creation of new pairs at late times, the doublon energy U has to be converted into kinetic energy or vice versa. For a single particle the kinetic energy is of order J. Therefore a scattering process involving $\sim U/J$ particles is required to fulfill the local energy conservation. These processes are not covered by our semiclassical simulations. This implies that the total kinetic energy is constant in this approximation.

In the following we will use leading order results in U/J for all expressions. Then the doublon and holon dispersions become $\epsilon_D(k) = -4\,J\,\cos(k)$ and $\epsilon_H(k) = -2\,J\,\cos(k)$, respectively. The transmission amplitude for doublon-holon scattering can be obtained from the calculations in section 3.2: inserting $J_1 = J, J_2 = 2J$ and $J_3 = \sqrt{2}J$ in Eq. (3.41), we find that the transmission probability for a scattering of a

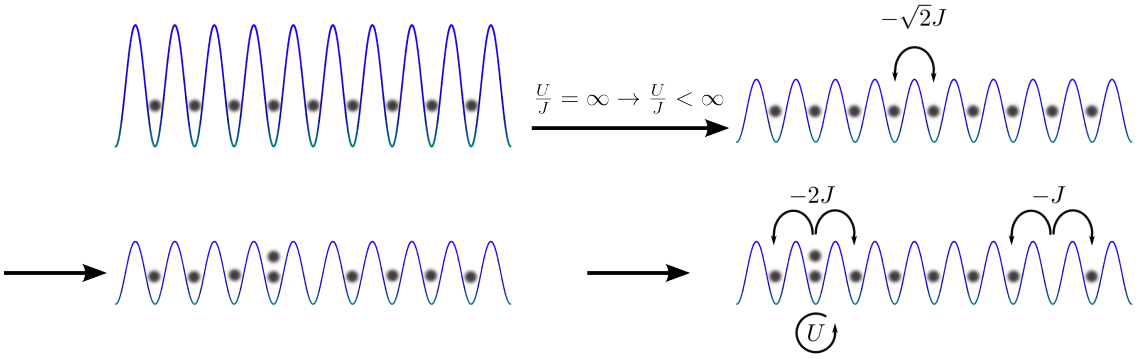

Figure 5.1: **Graphical illustration the quantum quench in the $1d$ bosonic Hubbard model.** The initial state is the groundstate with $U/J = \infty$, a product state with one boson per site. The lattice depth is lowered such that $U/J < \infty$ and hopping is possible. Doublon-holon pairs are created on neighboring lattice sites and can propagate through the lattice. Due to the bosonic statistics they have different hopping amplitudes $-2J$ and $-J$, respectively. A doublon has an additional interaction energy cost of U. In the limit $U \gg J$ this protects doublon-holon pairs from recombination for exponentially large times $\sim \mathrm{e}^{U/J}$, as explained in the main text. Scattering of doublons and holons leads to thermalization. Very similar quenches have already been realized experimentally [103, 172].

doublon with momentum k_D and a holon with momentum k_H is

$$|T|^2 = \frac{128\,\cos^4\left(\frac{k_D+k_H}{2}\right)\,\left(2\sin(k_D)-\sin(k_H)\right)^2}{\left(5+4\cos(k_D+k_H)\right)^2}\,\left(\frac{J}{U}\right)^2. \tag{5.2}$$

Therefore the transmission probability is $\sim (J/U)^2$ and thus highly suppressed in the semiclassical regime. All results below are shown for a transmission probability of zero. We have checked that including a tiny transmission rate, for example with $U = 100\,J$, does not change the results qualitatively. It only has a very small quantitative effect. However, omitting the transmission channel introduces a new macroscopically conserved quantity: the sequence of quasiparticles. We will come back to that below.

In the following all lengths are measured in units of the mean distance of quasiparticle pairs $\rho^{-1} = 1/8(\frac{U}{J})^2$, where ρ is the pair density see Eq. (3.91), and time is measured in units of the doublon-holon scattering time τ_{dh}. Then all semiclassical results are independent of U/J. Furthermore, if not stated otherwise, we measure energies in units of J which was set to 1 in the simulations. Since the quasiparticle velocity is $v \sim J$, it is $\tau_{dh} \sim \rho^{-1}/v \sim U^2/J^3$. The prefactor was found numerically to be 0.031, which yields $\tau_{dh} \approx 0.031\,U^2/J^3$. For small times $t \ll \tau_{dh}$ no scattering has taken place yet. This can be interpreted as the prethermalized regime, where

the individual momenta are conserved. All observables have stationary values and equilibration only starts when $t \sim \tau_{dh}$. However, at short times interference effects are important and this regime is not correctly described by our simulations.

The density of quasiparticle pairs can also be obtained by other means. It is easy to show that for a system with L lattice sites it is $\langle \hat{H} \rangle = \langle 0 | \hat{H} | 0 \rangle = 0$ and $\langle \hat{H}^2 \rangle = 4\,J^2\,L$. Here $|0\rangle$ denotes the initial state and the Hamiltonian was given in Eq. (5.1). Furthermore the energy of the groundstate, the Mott insulator, is in second order perturbation theory given by $E_{\mathrm{GS}}^{(2)} = -8L\,J^2/U$. Let us denote the operator which counts quasiparticle pairs by $\hat{N}$. To leading order, omitting the kinetic energy $\sim J$, each pair has an energy of U. To match the condition $\langle \hat{H} \rangle = 0$ we find $E_{\mathrm{GS}}^{(2)} + \langle \hat{N} \rangle U = 0$, or $\langle \hat{N} \rangle = 8L\,J^2/U^2$. This also gives a density $\rho = \langle \hat{N} \rangle / L = 8\,(J/U)^2$, in full agreement with the calculation in section 3.3.

Exactly the same results can be obtained from a leading order Schrieffer-Wolff transformation, see section 3.1, with

$$\hat{S} \approx \frac{2\sqrt{2}\,J}{U} \sum_{j=1}^{L} \left(\hat{b}_{j+1}^{\dagger}\, \hat{b}_j - \text{h. c.} \right). \tag{5.3}$$

When acting with $\mathrm{e}^{\hat{S}}$ on the initial state one obtains a wavefunction in the quasiparticle basis containing any number of pairs. The quasiparticle pairs follow an approximate Poisson distribution due to the exponential. This is in accordance with the intuition that the creation of different quasiparticle pairs is uncorrelated in the low density limit. We use this explicitly in the semiclassical simulations. It is further supported by the work of Calabrese and Cardy [116] who showed that quasiparticles originating from different pairs are not entangled initially. The subleading corrections to the Poisson distribution come from the rare processes where pairs are created very close to each other. The probability to find n pairs is $P_n \approx \lambda^n\, \mathrm{e}^{-\lambda}/(n!)$ where $\lambda = 8\,L\,(J/U)^2$. Again, the expectation value of the density is

$$\rho = \frac{\langle \hat{N} \rangle}{L} = \frac{1}{L} \sum_{n=0}^{\infty} n\,P_n = \frac{\lambda}{L} = 8 \left(\frac{J}{U} \right)^2. \tag{5.4}$$

In the quasiparticle basis the overlap with the initial state is exponentially small in the system size L: $\left| \langle 0 |\, \mathrm{e}^{\hat{S}}\, | 0 \rangle \right|^2 \approx \mathrm{e}^{-\lambda} = \mathrm{e}^{-8\,L\,(J/U)^2}$.

Related quenches in high dimensional Fermi Hubbard models have been studied in [114] and [173]. The same quench as studied by us has been investigated in [174]. The authors compared numerical results (ED and t-DMRG) to the assumptions un-

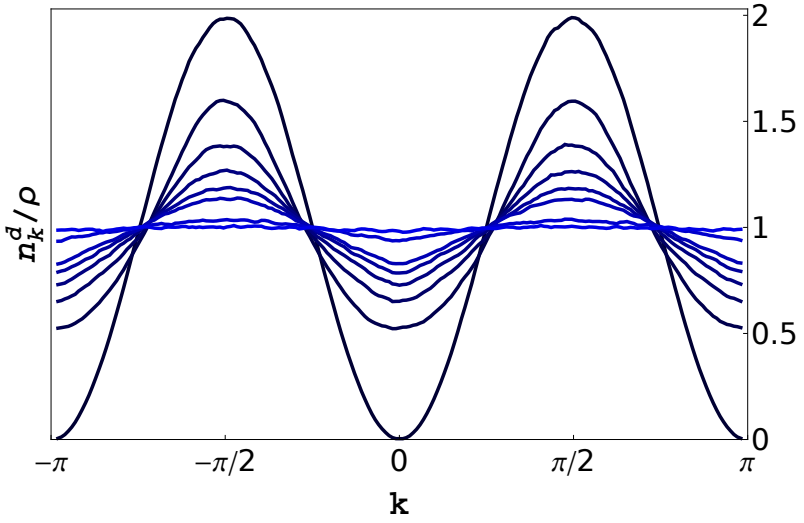

Figure 5.2: **Thermalization of the doublon momentum distribution.** It is shown in units of the density ρ. The initial distribution is $2\rho \sin^2(k)$. If thermalizes to a flat, infinite temperature, distribution. Shown is data for $t = 0, 1, 2, 3, 4, 5, 10, 20\, \tau_{dh}$ after the quench.

derlying the ETH and different thermodynamic ensembles.

Quantum quenches very similar to the one studied here have already been realized experimentally [103, 172]. In [103] a ballistic short time expansion of correlations was observed, a light-cone-like effect. In [172] the expansion dynamics of a localized bosonic cloud was investigated in one and two dimensions.

5.1 Diffusive thermalization after weak quenches

We now consider the time evolution after the quench in the semiclassical limit $U \gg J$. On short timescales $\sim 1/J$ after the quench doublon-holon pairs are created with a density $\rho = 8(\frac{J}{U})^2$. Their initial momentum distribution was calculated in section 3.3 to sin^2. This implies that the total kinetic energy of the system in the initial state is zero:

$$\langle E_{\text{kin}} \rangle = \frac{M}{2} \int_{-\pi}^{\pi} dk \frac{sin^2(k)}{\pi} \left((-4\, J\, \cos(k)) + (-2\, J\, \cos(k)) \right) = 0. \tag{5.5}$$

As we do not consider recombination or creation of pairs at late times, the kinetic energy is conserved. The thermal state is then given by an infinite temperature state ($\beta = 0$), where all momenta are equally probable, shown in section 5.2 below. The numerical result for the time evolution of the doublon momentum distribution is shown Fig. 5.2.

As observables, we define the moments of the momentum distributions as

$$Q_m^{D/H}(t) = \langle \cos(m\, k_i(t)) \rangle_{D/H}. \tag{5.6}$$

The subindex i labels the quasiparticles in an ordered way and k_i denotes the kinetic energy of the i-th quasiparticle. The expectation value $\langle\cdot\rangle$ in Eq. (5.6) includes a spatial average, a sum over i, and additionally an average over different initial configurations. The subscript D or H indicates that the average is taken only with regard to the momenta of the doublons or holons, respectively.

In the dimensionless units the initial distribution is $P_k(t) = \sin^2(k)/\pi = \frac{1}{2\pi}(1 - \cos(2k))$ and the initial values of $Q_m^{D/H}$ are given by

$$Q_0^{D/H} = \frac{1}{2}, \quad Q_2^{D/H} = -\frac{1}{2}, \quad Q_{m\neq 0,2}^{D/H} = 0. \tag{5.7}$$

Since Q_2 is nonzero initially and zero in the long-time thermal state, it is instructive to study its relaxation in detail. As $\cos(2k) = 2\cos^2(k) - 1$, Q_2 is also directly related to the kinetic energy squared.

As further observables we define energy-energy correlation functions as

$$T_n(t) = \langle \epsilon_i(t)\, \epsilon_{i+n}(t) \rangle \tag{5.8}$$

where ϵ_i denotes the kinetic energy of the i-th quasiparticle. In the initial state it is

$$T_0(t=0) = \int_{-\pi}^{\pi} \frac{dk}{\pi} \sin^2(k)\, \frac{1}{2} \left((-4\cos(k))^2 + (-2\cos(k))^2 \right) = \frac{5}{2} \tag{5.9}$$

$$T_1(t=0) = \int_{-\pi}^{\pi} \frac{dk}{\pi} \sin^2(k)\, \frac{1}{2} \Big(-4\cos(k) \Big) \Big(-2\cos(k) \Big) = 1 \tag{5.10}$$

$$T_{n>1}(t=0) = 0. \tag{5.11}$$

In Fig. 5.3 we show the time evolution of T_1 after the quench. It can be clearly seen that this quantity shows very pronounced algebraic long-time tails. The prediction from hydrodynamics, a decay as $t^{-1/2}$, is met only for more than approximately 300 scattering times. This means that each particle has, on average, scattered 300 times. The data are obtained from simulations with $\sim 10^6$ quasiparticles and are averaged over ~ 1600 initial configurations. This implies that more than $10^6 \times 10^3 \times 10^3 = 10^{12}$ collisions have been evaluated to obtain the plot.

Fitting with a single exponent for times $30\tau_{dh} < t < 200\tau_{dh}$ yields $0.19\,(t/\tau_{dh})^{-0.664}$, shown by the gray dotted line in the inset. The exponent is very close to the value

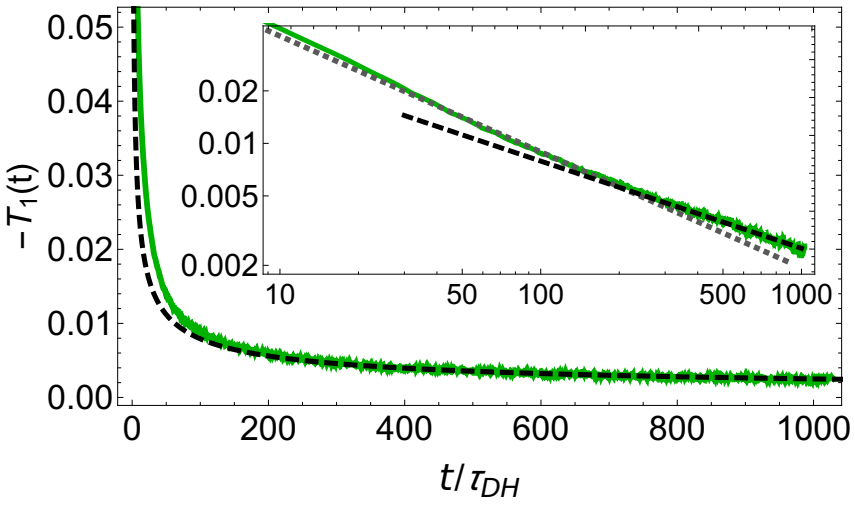

Figure 5.3: **Non-equilibrium long-time tails in the energy-energy correlation function.** The dashed black line is a fit according to the hydrodynamic prediction $0.079\,(t/\tau_{dh})^{-1/2}$. This asymptotic behavior is seen only for more than ~ 300 scattering times. The inset shows the data in a log-log plot. In the time range $t = 10 \ldots 200\,\tau_{dh}$ a fit to the data with a single exponent yields $0.19\,(t/\tau_{dh})^{-0.66}$, shown by the gray dotted line.

expected in the KPZ universality class which is $-2/3$ [121, 146]. However, an effectively momentum conserving regime over such long times can be excluded from the fact that approximately $1/4$ of the doublon-holon scatterings are Umklapp scattering events. The long timescale needed to see the asymptotic behavior is probably due to the fact that slowest subleading term decays only as $\sim t^{-3/4}$. The leading order irrelevant term in $1d$ is of the form $\sim (\partial_x e)^2$ with a scaling dimension $-d/2$, see section 4.3. Rescaling of the diffusion equation as in section 4.3 with $\lambda > 1$ shows that this term is suppressed only as $\lambda^{-d/2}$. The engineering dimension of the time is -2, meaning that $t \to \lambda^2 t$ upon rescaling. This implies that that the long-time tails are described by $\sim\, t^{-1/2}\, S(\frac{t}{\lambda^2}, \frac{\alpha}{\lambda^{1/2}}, \ldots)$, where we have extracted the asymptotically known $t^{-1/2}$ factor. To reach $S \to$constant for $t \to \infty$ we have to set $\lambda = \sqrt{t}$, which yields

$$t^{-1/2}\, S \overset{\lambda=\sqrt{t}}{\longrightarrow} t^{-1/2}\, S(1, \alpha/t^{1/4}, \ldots) \overset{t\to\infty}{\longrightarrow} t^{-1/2} + \mathcal{O}(t^{-3/4}). \tag{5.12}$$

A fit of the data of the form $a\,t^{-1/2} + b\,t^{-3/4}$ in the range $30\,\tau_{dh} < t < 200\,\tau_{dh}$ yields $0.032\,t^{-1/2} + 0.180\,t^{-3/4}$. The subleading term(s) seem to have large prefactors, which explains why the $t^{-1/2}$ behavior can be seen only after that many scattering times.

As the long-time tails originate from diffusive transport of energy we expect that all observables which are sensitive to energy fluctuations will eventually show long-

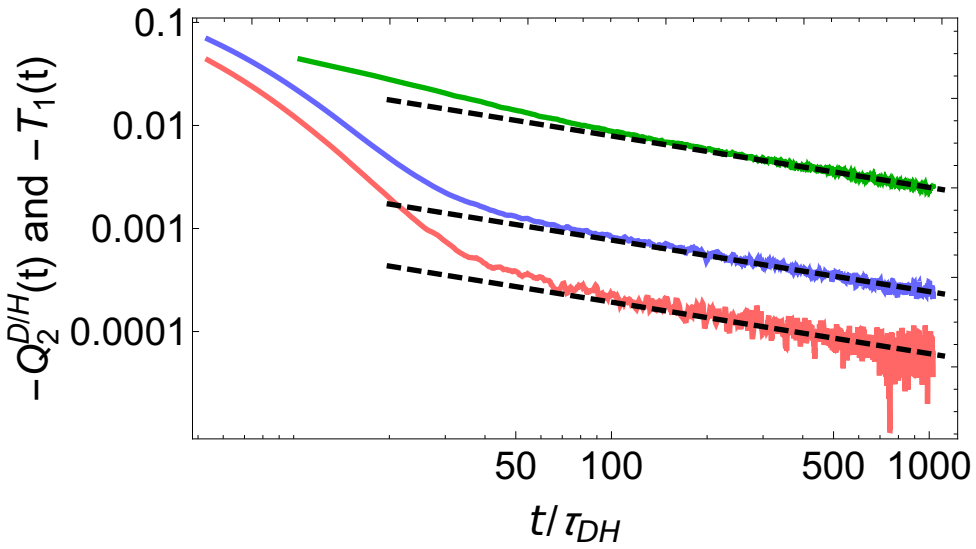

Figure 5.4: **Hydrodynamic long-time tails in the momentum distribution.** The second moment of doublon and holon momentum distribution are shown in blue and red, respectively. The green curve is the data for T_1 already shown in Fig. 5.3. The dashed black lines are of the form according to the hydrodynamic prediction $\sim t^{-1/2}$. The lines for $Q_2^{D/H}$ are not fitted, but predicted from the prefactor of the tail in T_1, by an equilibrium calculation, see the main text. Up to ~ 30 scattering times the decay of Q_2 is exponential on a timescale $\tau_{\text{local}} \approx 4$. Data are averaged over two scattering times (4 data points) to reduce the noise level.

time tails. In section 5.2 we will show that in equilibrium close to infinite temperature, $\beta J \approx 0$, it is

$$Q^D_{2,\text{eq.}} = 2\,(\beta J)^2, Q^H_{2,\text{eq.}} = 1/2\,(\beta J)^2 \text{ and } T_{1,\text{eq.}} = 41/2\,J^2\,(\beta J)^2. \tag{5.13}$$

Therefore for $J = 1$ as used in the simulations

$$Q^D_{2,\text{eq.}} = \tfrac{4}{41}\,T_{2,\text{eq.}} \text{ and } Q^H_{2,\text{eq.}} = \tfrac{1}{41}\,T_{2,\text{eq.}}. \tag{5.14}$$

From Eq. (5.19) below, we see that $\beta(\langle e\rangle_{\text{eq.}}) = -1/5\langle e\rangle_{\text{eq.}}/J^2$. If we assume that the system is in local equilibrium, we can promote this equation to a local equation, $\beta(x) = -1/5\,e(x)/J^2$. Inserting this in Eq. (5.13) we find that Q_2^D, Q_2^H and T_1 depend on $\langle e^2(x)\rangle$ with the same relative prefactors as given above.

Furthermore, we can even use this equilibrium prefactors to predict the relative prefactors of the non-equilibrium long-time tails. This is shown in Fig. 5.4 for $Q_2^D(t)$ and $Q_2^H(t)$. The black dashed lines there are not fits, but are calculated from the fit of $T_1(t) \overset{t\gtrsim 300\,\tau_{dh}}{\longrightarrow} 0.079\,t^{-1/2}$ by means of Eq. (5.14). We see a very good agreement for

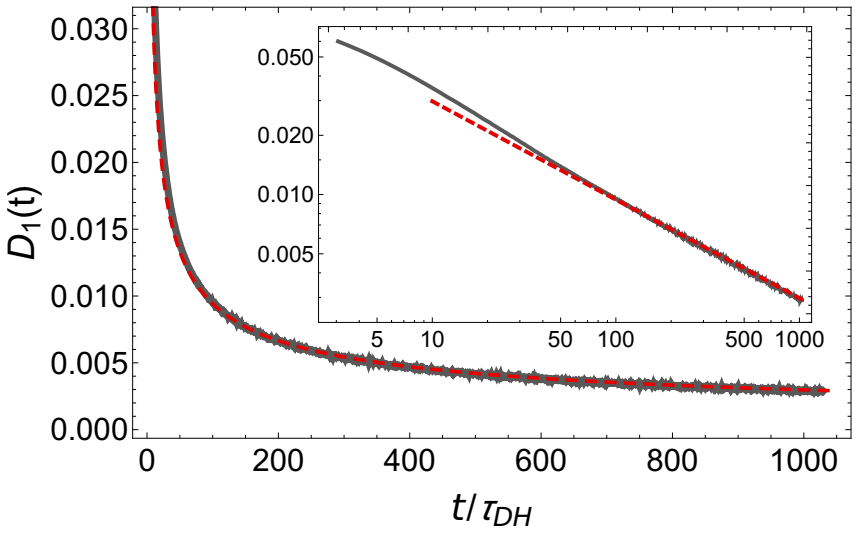

Figure 5.5: **Hydrodynamic long-time tails in the distance-distance correlation function.** The red dashed line shows a fit $0.094\,(t/\tau_{dh})^{-1/2}$. As can be seen in the log-log plot in the inset, this matches the numerical result for times larger than ~ 200 scattering times. This long-time tail is caused by particle number conservation.

$t \gtrsim 200\,\tau_{dh}$. This agreement shows that the relaxation is determined by the linear response of the equilibrium ensemble. This justifies our assumptions in the hydrodynamic calculations presented in section 4. However, there is an absolute prefactor which depends on the initial state and cannot be calculated from the coarse-grained description.

For times $t \lesssim 30\,\tau_{dh}$ both, $Q_2^D(t)$ and $Q_2^H(t)$, decay exponentially. This is a consequence of local equilibration. The observables equilibrate locally to a value slightly smaller or larger than the real temperature would dictate. Typically this already happens after a few collisions. An exponential fit to times $5\,\tau_{dh} < t < 20\,\tau_{dh}$ yields the local equilibration times $\tau_{\mathrm{local},D} \approx 4.67\,\tau_{dh}$ and $\tau_{\mathrm{local},H} \approx 3.97\,\tau_{dh}$ for doublons and holons, respectively. This regime can approximately be described by the Boltzmann equation, as shown below in section 5.3.

In addition to the energy also the particle number is conserved in the dynamics. Therefore we expect to see long-time tails also in the density-density correlation function and in all observables which are sensitive to density fluctuations. To measure the density we could subdivide the system into segments of equal length and calculate the correlation functions in this way. We have chosen a different observable, which is directly related to the density, namely the distance-distance correlation function. To

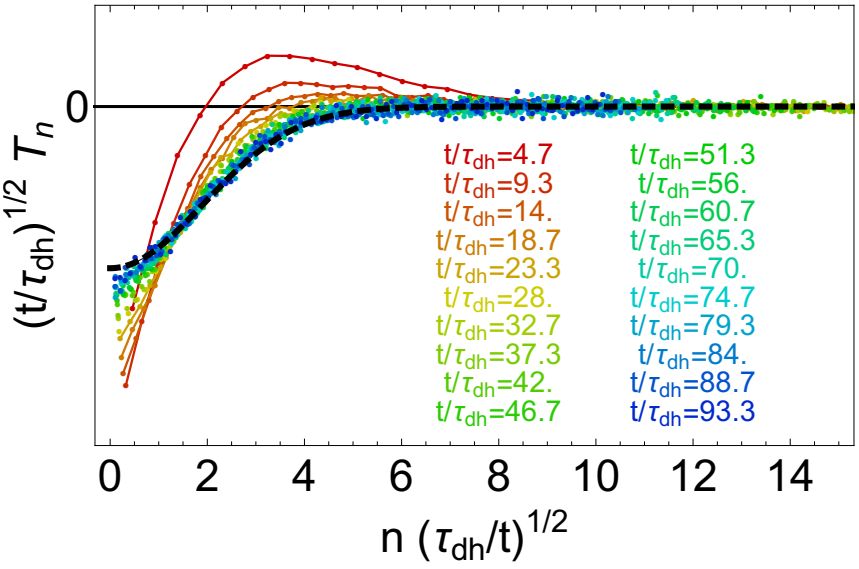

Figure 5.6: **Diffusive scaling of the energy-energy correlations.** T_n was defined in Eq. (5.8) as $T_n(t) = \langle \epsilon_i(t)\, \epsilon_{i+n}(t) \rangle$. Data for $n = 1, 2, \ldots, 99$ is included. The black dashed line is the scaled diffusion propagator, where the diffusion constant was calculated in equilibrium via the Kubo formula. For small times $t/\tau_{dh} \lesssim 20$ after the quench clear deviations from the scaling behavior can be seen. At later times the scaling is fulfilled for $n \gtrsim \sqrt{t/\tau_{dh}}$.

this end we define

$$D_n(t) = \frac{\langle d_i d_{i+n} \rangle - \langle d_i \rangle \langle d_{i+n} \rangle}{\langle d_i \rangle^2} \tag{5.15}$$

where d_i is the distance between particle i and particle $i+1$. The normalization is chosen such that the result does not depend on the mean distance used in the simulations. In Fig. 5.5 we show $D_1(t)$. It also shows very clear long-time tails with a prefactor ≈ 0.1. The $t^{-1/2}$ behavior can be observed for $t \gtrsim 200\, \tau_{dh}$, see the log-log plot in the inset. As the energy does not depend on the density there are no couplings between the the energy and the particle diffusion in the simulated model. Both, energy and particle density, thermalize independently. This is an artifact for models with hard-core collisions of point-like particles.

Up to now we have considered only nearest-neighbor correlation functions, but hydrodynamics also predicts a scaling TIME $\sim$ LENGTH^2: a decay of non-local correlations as $\sim t^{-1/2} \mathrm{e}^{-|x-x'|^2/(8D_e t)}$, see section 4.4. In Fig. 5.6 we show a scaling plot of $\sqrt{t} T_n$ as a function of $n/t^{1/2}$. For $t \gtrsim 20\, \tau_{dh}$ and $n \gtrsim \sqrt{t/\tau_{dh}}$ a scaling collapse of the data can be observed within the numerical precision. As the long time-tails of T_n rely on the energy conservation we expect that the energy diffusion constant D_e appears here. In the dimensionless units we obtain a dimensionless energy diffusion constant

as $\tilde{D}_e = D_e \rho^2 \tau_{dh}$. Then the correlation function becomes $\sim t^{-1/2} \mathrm{e}^{-n^2/(8\tilde{D}_e t/\tau_{dh})}$. We have determined $\tilde{D}_e$ numerically in equilibrium by means of the Kubo formula to $\tilde{D}_e \approx 0.91$, details are postponed to the next section. The thick black line in Fig. 5.6 is the scaled diffusion propagator prediction $\mathrm{e}^{-x^2/7.28}$. Only the absolute prefactor was adjusted. One can see that the width of the numerical data match the value predicted from the equilibrium correlation function. This finally shows that the thermalization is really diffusive.

Also the crossover to integrability can be studied with the same methods in the same model. Suppose that that initial state is not the product state with one boson per site but with $n \gg 1$ bosons per site. Then the dispersions of the $n+1$ and $n-1$ bosons per sites excitations, formerly known as doublon and holons, become $-2\,J\,(n+1)\cos(k)$ and $-2\,J\,n\cos(k)$ respectively. The relative difference in the hopping amplitudes becomes smaller with increasing n and finally, for $n \to \infty$, they are equal excluding thermalization. This limit has been studied by Marvin Pinkwart in his Bachelor thesis [175].

5.2 Equilibrium results

In this section we will provide some equilibrium results which, partially, have already been used above. Since the energy of the system depends only on the momenta but not on the position of the particles, the partition function Z_M for M doublon-holon pairs can be calculated as

$$\begin{aligned} Z_M &= \sum_{\{k_1^D, k_1^H, k_2^D, k_2^H \dots\}} \mathrm{e}^{-\beta\, E(k_1^D, k_1^H, \cdots)} = \sum_{\{k_1^{D/H}, k_2^{D/H}, \dots\}} \mathrm{e}^{-\beta \sum_j \epsilon(k_j^{D/H})} \\ &= \sum_{\{k_1^{D/H}, \dots\}} \prod_j \mathrm{e}^{-\beta\epsilon(k_j^D)}\, \mathrm{e}^{-\beta\epsilon(k_j^H)} = \prod_j \sum_{k^D, k^H} \mathrm{e}^{-\beta\epsilon(k^D)}\, \mathrm{e}^{-\beta\epsilon(k^H)} \\ &= \left(\left(\sum_{k^D} \mathrm{e}^{-\beta\epsilon(k^D)} \right) \left(\sum_{k^H} \mathrm{e}^{-\beta\epsilon(k^H)} \right) \right)^M \equiv \left(Z_D\, Z_H \right)^M . \end{aligned} \tag{5.16}$$

It factorizes into a product of pair partition functions. This is a consequence of the hard-core collisions and the aforementioned fact that the energy does not depend on the density.

In the last line we have defined the partition function of a single doublon and a single holon, respectively, as

$$Z_D = \sum_k \mathrm{e}^{4\beta J \cos(k)} \to \int_{-\pi}^{\pi} \frac{dk}{2\pi} \mathrm{e}^{4\beta J \cos(k)} = I_0(4\beta J) \tag{5.17}$$

$$Z_H = \sum_k \mathrm{e}^{2\beta J\cos(k)} \to \int_{-\pi}^{\pi} \frac{dk}{2\pi} \mathrm{e}^{2\beta J\cos(k)} = I_0(2\beta J) \tag{5.18}$$

where I_0 denotes the modified Bessel function of the first kind.

From the partition function we can directly calculate thermodynamic expectation values. As the partition function factorizes we can do this for each particle-pair independently. We are interested in the regime $\beta J \approx 0$ and thus we calculate the observables to leading order in βJ. The expectation value of the energy density is given by

$$\begin{aligned}\langle e\rangle_{\text{eq.}} =& \frac{1}{2}\left(\frac{1}{Z_D}\int_{-\pi}^{\pi}\frac{dk}{2\pi}(-4J\cos(k))\,\mathrm{e}^{4\beta J\cos(k)} + \frac{1}{Z_H}\int_{-\pi}^{\pi}\frac{dk}{2\pi}(-2J\cos(k))\,\mathrm{e}^{2\beta J\cos(k)}\right)\\ =& -\frac{4\,J\,I_1(4\beta J)}{I_0(4\beta J)} - \frac{2\,J\,I_1(2\beta J)}{I_0(2\beta J)} = -5\,J^2\beta + \mathcal{O}\left(J(J\beta)^3\right).\end{aligned} \tag{5.19}$$

From this we can see that, indeed, a kinetic energy of zero implies that the thermal state is at infinite temperature as stated in section 5.1. The local energy-energy correlation function is obtained as

$$\begin{aligned}&\langle e(x)e(x)\rangle_{\text{eq.}} =\\ &\frac{1}{2}\left(\frac{1}{Z_D}\int_{-\pi}^{\pi}\frac{dk}{2\pi}(-4J\cos(k))^2\,\mathrm{e}^{4\beta J\cos(k)} + \frac{1}{Z_H}\int_{-\pi}^{\pi}\frac{dk}{2\pi}(-2J\cos(k))^2\,\mathrm{e}^{2\beta J\cos(k)}\right)\\ &= 10\,J^2 - \frac{J\,I_1(2\beta J)}{\beta\,I_0(2\beta J)} - \frac{2\,J\,I_1(4\beta J)}{\beta\,I_0(4\beta J)} = 5\,J^2 + \frac{17}{2}J^2(J\beta)^2 + \mathcal{O}\left(J^2(J\beta)^4\right).\end{aligned} \tag{5.20}$$

The expectation value of the second moments of the momentum distributions for doublons and holons are given by

$$Q^D_{2,\text{eq.}} = \langle\cos(2k)\rangle_D = \frac{1}{Z_D}\int_{-\pi}^{\pi}\frac{dk}{2\pi}\cos(2k)\,\mathrm{e}^{4\beta J\cos(k)} = 2\,J^2\beta^2 + \mathcal{O}\left((J\beta)^4\right) \tag{5.21}$$

$$Q^H_{2,\text{eq.}} = \langle\cos(2k)\rangle_H = \frac{1}{Z_H}\int_{-\pi}^{\pi}\frac{dk}{2\pi}\cos(2k)\,\mathrm{e}^{2\beta J\cos(k)} = \frac{1}{2}\,J^2\beta^2 + \mathcal{O}\left((J\beta)^4\right). \tag{5.22}$$

Finally, the nearest neighbor energy-energy function can be calculated to be

$$\begin{aligned}T_{1,\text{eq.}} =& \frac{1}{8}\left(\frac{1}{Z_D}\int_{-\pi}^{\pi}\frac{dk}{2\pi}(-4J\cos(2k))\,\mathrm{e}^{4\beta J\cos(k)}\right)^2\\ &+ \frac{1}{8}\left(\frac{1}{Z_H}\int_{-\pi}^{\pi}\frac{dk}{2\pi}(-2J\cos(2k))\,\mathrm{e}^{2\beta J\cos(k)}\right)^2\\ &+ \frac{3}{4}\left(\frac{1}{Z_D}\int_{-\pi}^{\pi}\frac{dk}{2\pi}(-4J\cos(2k))\,\mathrm{e}^{4\beta J\cos(k)}\right)\left(\frac{1}{Z_H}\int_{-\pi}^{\pi}\frac{dk}{2\pi}(-2J\cos(2k))\,\mathrm{e}^{2\beta J\cos(k)}\right)\\ =& J^2\left(\frac{I_1^2(2\beta J)}{2I_0^2(2\beta J)} + \frac{2I_1^2(4\beta J)}{I_0^2(4\beta J)} + \frac{6I_1(4\beta J)I_1(2\beta J)}{I_0(4\beta J)\,I_0(2\beta J)}\right)\end{aligned}$$

$$= \frac{41}{2} J^4 \beta^2 + \mathcal{O}\left(J^2 (J\beta)^4\right). \tag{5.23}$$

Therefore in equilibrium for $J = 1$, it is $Q^D_{2,\text{eq.}} = \frac{4}{41} T_{2,\text{eq.}}$ and $Q^H_{2,\text{eq.}} = \frac{1}{41} T_{2,\text{eq.}}$. These relative prefactors were used above in section 5.1 to predict the relative prefactors of the non-equilibrium long-time tails.

The prefactors $1/8$, $1/8$ and $3/4$ as used in the calculation of $T_{2,\text{eq.}}$ are the probabilities that a randomly chosen pair of neighboring quasiparticles are two doublons, two holons or one doublon and one holon, respectively. This reflects that the quasiparticles maintain their initial order: a doublon (holon) cannot have two doublons (holons) as nearest neighbors. If transmission would be allowed, or the order is random for other reasons, this prefactors change to $1/4$, $1/4$ and $1/2$. The result would be $T_{1,\text{eq.}} = 25 J^4 \beta^2$, while $Q^D_{2,\text{eq.}}$ and $Q^H_{2,\text{eq.}}$ are not changed. The omission of the transmission channel has macroscopic consequences, although the microscopic effect is tiny. It introduces a new macroscopically conserved quantity: the sequence of quasiparticle species.

The energy diffusion constant D_e, as used in Fig. 5.6, can be calculated from the Kubo formula as follows [126, 127, 176]. In linear response, the heat conductivity κ can be calculated as the $\omega = 0$ component of the energy current autocorrelation function:

$$\kappa = \frac{2}{LT^2} \int_0^\infty dt \langle J_e(t) J_e(0) \rangle_{\text{eq.}}, \tag{5.24}$$

where J_e denotes the total energy current and L the system size. Then it is

$$D_e = \kappa \left(\frac{\partial \langle e \rangle_{\text{eq.}}}{\partial T} \right)^{-1} = \frac{1}{5L\, J^2} \int_0^\infty dt \langle J_e(t) J_e(0) \rangle_{\text{eq.}}, \tag{5.25}$$

where we have used Eq. (5.19). The current-current correlation function was determined numerically in equilibrium. From Eq. (5.25) we have obtained

$$D_e \approx 0.91\, \rho^{-2}\, \tau_{dh}^{-1} \approx 0.5\, \frac{U^2}{J}. \tag{5.26}$$

The energy-energy correlation function in equilibrium is also expected to show hydrodynamic long-time tails, see Eq. (4.27). In Fig. 5.7 we show the unequal time energy-energy correlation function

$$T_{0,\text{eq.}}(t_1, t_2) = \langle \epsilon_i(t_1)\, \epsilon_i(t_2) \rangle_{\text{eq.}} \equiv T_{0,\text{eq.}}\left(|t_2 - t_1|\right), \tag{5.27}$$

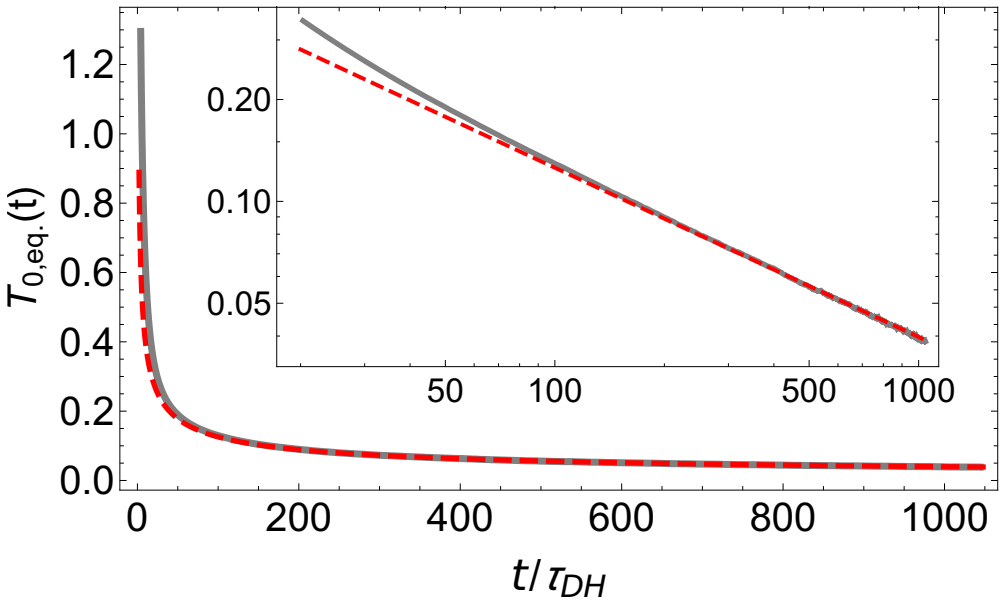

Figure 5.7: **Unequal times energy-energy correlations in equilibrium.** The red dashed line is a fit $1.26\,(t/\tau_{dh})^{-1/2}$. Again, the asymptotic behavior is reached only for large times $t \gtrsim 200\,\tau_{dh}$ as can be seen from the log-log plot in the inset.

which is a function of the time difference only. Its equal time value is given by

$$\int_{-\pi}^{\pi} \frac{dk}{2\pi}\,\frac{1}{2}\,\left((-2\cos(k))^2 + (-4\cos(k))^2\right) = 5, \tag{5.28}$$

the $\beta = 0$ and $J = 1$ result of Eq. (5.20). Again, the eventual $t^{-1/2}$ behavior is only seen after many scattering times $t \gtrsim 200\,\tau_{dh}$

Finally, we consider the local energy current–energy current correlation function

$$c_e(t_1, t_2) = \langle j_i^e(t_2) j_i^e(t_2)\rangle_{\text{eq.}} \equiv c_e\left(|t_2 - t_1|\right) \tag{5.29}$$

where $j_i^e(t) = v_i(t)\,\epsilon_i(t)$ denotes the energy current of the i-th particle at time t. Its equal time value can be calculated as

$$\begin{aligned} c_e(t,t) =& \frac{1}{2\,Z_D}\int_{-\pi}^{\pi}\frac{dk}{2\pi}\left((-4J\cos(k))(4J\sin(k))\right)^2\ \mathrm{e}^{4\beta J\cos(k)} \\ &+ \frac{1}{2\,Z_H}\int_{-\pi}^{\pi}\frac{dk}{2\pi}\left((-2J\cos(k))(2J\sin(k))\right)^2\ \mathrm{e}^{2\beta J\cos(k)} \\ =& -30\,\frac{J^2}{\beta^2} + \frac{4\,J(3J + 2J^2\beta^2)\,I_1(2\beta J)}{\beta^3\,I_0(2\beta J)} + \frac{4\,J(3 + 8J^2\beta^2)\,I_1(4\beta J)}{\beta^3\,I_0(4\beta J)} \\ =& 17\,J^4 - \frac{257}{24}J^4\ (J\beta)^4 + \mathcal{O}\left(J^4(J\beta)^8\right). \end{aligned} \tag{5.30}$$

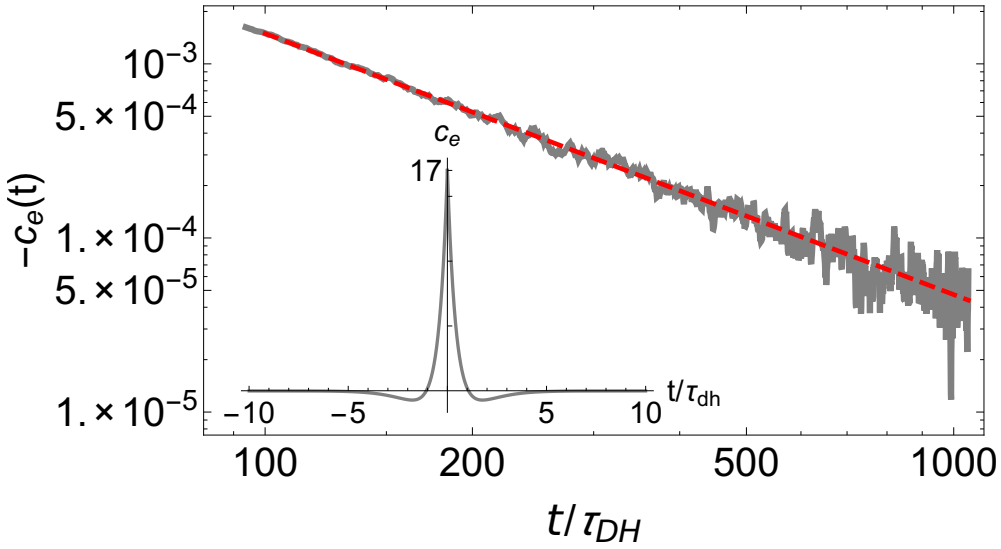

Figure 5.8: **Long time-tails in the equilibrium energy current autocorrelation function.** The red dashed line is a fit according to the hydrodynamic prediction $1.495\,(t/\tau_{dh})^{-3/2}$. The inset shows the short time behavior. It is dominated by a drastic reduction of the equal time correlation $17\,J^4$, see Eq. (5.30), to a small negative value.

In Fig. 5.8 we show numerical results for $c_e(t)$. As seen in the linear plot in the inset, the short time behavior is dominated by a sign change and a drastic reduction of the correlations. Within approximately two scattering times, c_e drops from its initial value $c_e(0) = 17$ to $c_e(t \sim 2\tau_{dh}) \approx -0.7$. Then it develops a small negative long-time tail. In section 4.4, see Eq. (4.35), we have shown that the local current autocorrelation function decays as $\sim t^{-3/2}$ in one dimension. A corresponding fit $1.495\,(t/\tau_{dh})^{-3/2}$ is shown by the red dashed line.

In the fluctuating hydrodynamics approach, as introduced in section 4, the short time behavior of c_e was approximated by a δ-peak. From the inset in Fig. 5.8 we see that this is a decent approximation on timescales larger than a scattering time. The negative part, including the long-time tail, of c_e arises from the coupling to the slow diffusion mode, and thus was not part of the fluctuating term ξ as used in section 4.

All numerical results presented above are in perfect agreement with the predictions from fluctuating hydrodynamics and linear response theory. We have shown that the exponents and *relative* prefactors of the, equilibrium and non-equilibrium, long-time tails can be calculated analytically within this framework.

5.3 Comparison to the Boltzmann equation

It is instructive to investigate the semiclassical relaxation as described above with the results from a Boltzmann equation approach. As this assumes uncorrelated collisions it can describe only local equilibration. It cannot reproduce the long-time tails as explained in section 4.

Denoting the semiclassical distribution functions of doublons and holons as n_k^D and n_k^H, respectively, the Boltzmann equation takes the form

$$\begin{aligned}\frac{\partial}{\partial t} n_k^D = &\int \frac{dq}{2\pi} \int \frac{dk'}{2\pi} \int \frac{dq'}{2\pi} W_{k,q;k',q'} \\ &\times \delta\big(\epsilon_k^D + \epsilon_q^H - (\epsilon_{k'}^D + \epsilon_{q'}^H)\big)\, \delta_U\big(k+q-(k'+q')\big)\, \left(n_{k'}^D\, n_{q'}^H - n_k^D\, n_q^H\right), \qquad (5.31) \\ \frac{\partial}{\partial t} n_q^H = &\int \frac{dk}{2\pi} \int \frac{dk'}{2\pi} \int \frac{dq'}{2\pi} W_{k,q;k',q'} \\ &\times \delta\big(\epsilon_k^D + \epsilon_q^H - (\epsilon_{k'}^D + \epsilon_{q'}^H)\big)\, \delta_U\big(k+q-(k'+q')\big)\, \left(n_{k'}^D\, n_{q'}^H - n_k^D\, n_q^H\right), \qquad (5.32)\end{aligned}$$

where $\delta_U(k) = \sum_n \delta(k + 2\pi\, n)$ guarantees conservation of the lattice momentum. The transition rate W for hard-core collisions in one dimension is exactly given by

$$W_{k,q;k',q'} = (2\pi)^2 |v_k^D - v_q^H||v_{k'}^D - v_{q'}^H| = (2\pi)^2 |\partial_k \epsilon_k^D - \partial_q \epsilon_q^H||\partial_{k'} \epsilon_{k'}^D - \partial_{q'} \epsilon_{q'}^H|. \qquad (5.33)$$

This can be obtained as follows: for small Δt the change in the distribution function n_k is

$$n_k(t+\Delta t) = n_k(t) + \Delta t \sum_p \left(W_{p\to k}^{\mathrm{IN}} n_p(t) - W_{k\to p}^{\mathrm{OUT}} n_k(t) \right), \qquad (5.34)$$

where the in and out scattering rates are given by

$$W_{p\to k}^{\mathrm{IN}} = \sum_{p',k'} n_{p'}\, \delta_E\, \delta_M\, |v_p - v_{p'}|\, f^{\mathrm{IN}}(k,k') \qquad (5.35)$$

$$W_{k\to p}^{\mathrm{OUT}} = \sum_{p',k'} n_{k'}\, \delta_E\, \delta_M\, |v_k - v_{k'}|\, f^{\mathrm{OUT}}(p,p'). \qquad (5.36)$$

δ_E and δ_M indicate, respectively, energy and momentum conservation. The probability that two particles with momenta p and p' collide within a very small time Δt is proportional to the relative velocity $|v_p - v_{p'}|$. To obtain detailed balance it is then necessary that $f^{\mathrm{IN}}(k,k') \propto |v_k - v_{k'}|$ and $f^{\mathrm{OUT}}(p,p') \propto |v_p - v_{p'}|$. The factors of 2π in Eq. (5.33) are a normalization and could be absorbed in the definition of $n^{D/H}$.

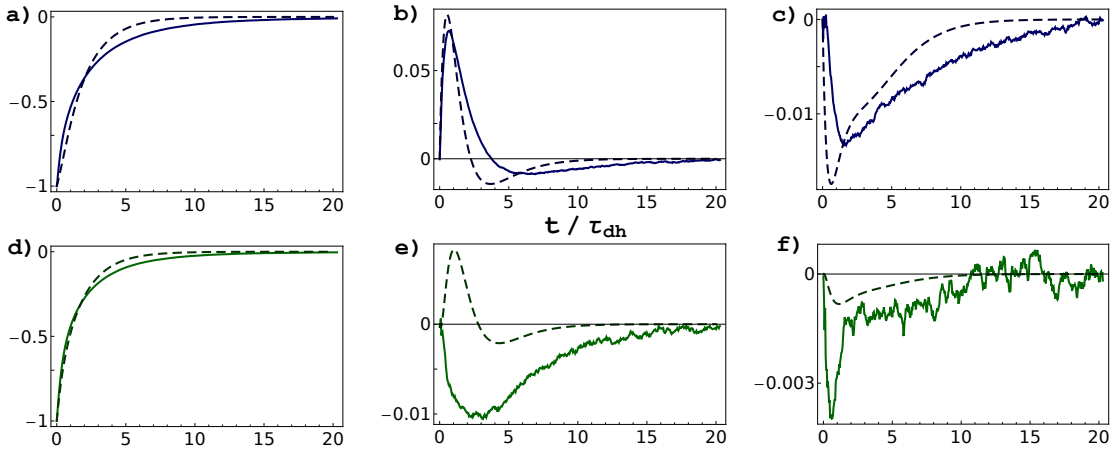

Figure 5.9: **Short time dynamics predicted by the Boltzmann equation and numerical results.** The solid lines show the numerical data, while the dashed lines show the results from the Boltzmann equation, Eqns. (5.38) and (5.39). The relaxation of the modes $\langle \cos(nk) \rangle$ is shown for $n = 2, 4, 6$ (from left to right) for doublons, panels a) - c), and holons, panels d) - f). The largest discrepancy is seen in panel e). But also here the tendency at very short times is the same, although this cannot be seen in the plot.

Performing the Fourier series expansion of the distribution functions as

$$n_k^{D,H} = \sum_m \cos(mk)\ d_m/h_m, \tag{5.37}$$

we find the following equations for the Fourier components:

$$\begin{aligned}
\frac{\partial}{\partial t} d_m =& 2 \sum_{m',m''} d_{m'} h_{m''} \int \frac{dk}{2\pi} \int \frac{dq}{2\pi} \cos(mk) \\
& \times |\partial_k \epsilon_k^d - \partial_q \epsilon_q^h| \left(\cos(m' k_d) \cos(m''(k+q-k_d)) - \cos(m'k)\cos(m''q) \right) \qquad (5.38) \\
\frac{\partial}{\partial t} h_m =& 2 \sum_{m',m''} d_{m'} h_{m''} \int \frac{dk}{2\pi} \int \frac{dq}{2\pi} \cos(mq) \\
& \times |\partial_k \epsilon_k^d - \partial_q \epsilon_q^h| \left(\cos(m' k_d) \cos(m''(k+q-k_d)) - \cos(m'k)\cos(m''q) \right). \qquad (5.39)
\end{aligned}$$

$k_d(k,q)$ is the doublon momentum after the scattering of a doublon with momentum k and a holon with momentum q, determined from energy and momentum conservation (modulo Umklapp scattering), see Eq. (3.12).

We have solved Eqns. (5.38) and (5.39) numerically, including all modes up to $m = 8$, with the initial conditions $h_0(0) = d_0(0) = -h_2(0) = -d_2(0) = \rho$ and $h_m(0) = d_m(0) = 0$ otherwise, to match the initial $\sin^2$ distribution. The results for the even

modes are compared to the results of the simulation in Fig. 5.9. The odd modes are all zero. The Boltzmann equation predicts correctly the times scale of relaxation, see Figs. 5.9a) and 5.9d). But even at short times there is no quantitative agreement. The reason is that in $1d$ there is high probability that the same particles scatter again and correlation effects set in quite quickly.

5.4 Exact diagonalization for strong quenches

The semiclassical approach used above is not applicable for quenches where $U \sim J$. Therefore we have used exact diagonalization (ED) to study the quench in this limit, we show results for $U = J$. The ED calculations have been performed in collaboration with Jan Müller using the ALPS code [177]. The same initial state as in the semiclassical regime was used: the product state with one boson per site. To reach larger system sizes, the maximal occupation of a single site was restricted to two. In principle, this corresponds to a different model where higher occupation is suppressed. Although this changes the results quantitatively, the qualitative behavior should be the same. Furthermore periodic boundary conditions were used. As the initial state is translationally invariant, we can restrict the analysis to the total momentum, $K = 0$, sector. In this way a system size of $L = 14$ could be reached, corresponding to a Hilbert space dimension of 44046. Unfortunately, it was not possible to simulate larger systems due to memory constraints.

As an observable, we define the doublon density operator as

$$\hat{d}_i = \frac{1}{2}\,\hat{b}_i^\dagger\,\hat{b}_i\left(\hat{b}_i^\dagger\,\hat{b}_i - 1\right) = \frac{1}{2}\,\hat{n}_i\,(\hat{n}_i - 1) \tag{5.40}$$

The number of doublons can be measured directly: either by the quantum microscopes introduced in section 2.3 or by other techniques [171, 178]. In the present setup $\langle\hat{d}_i\rangle$ does not depend on the site index i and is zero in the initial state. It is directly related to the energy as the total interaction energy is given by

$$\langle\hat{H}_{\text{int}}\rangle = U\sum_i\langle\hat{d}_i\rangle = UL\langle\hat{d}_{i_0}\rangle, \tag{5.41}$$

where i_0 is arbitrary. In the left panel of Fig. 5.10 we show the time evolution of $\langle\hat{d}_i\rangle$ for system sizes $L = 10, 12, 14$. The black solid line is the long time average obtained from the diagonal ensemble. For $L = 10$ and $L = 12$ the dynamics is distorted due to finite size fluctuations. The results for $L = 14$, however, clearly show that the long time value is approached only algebraically. But still, the finite size fluctuations are

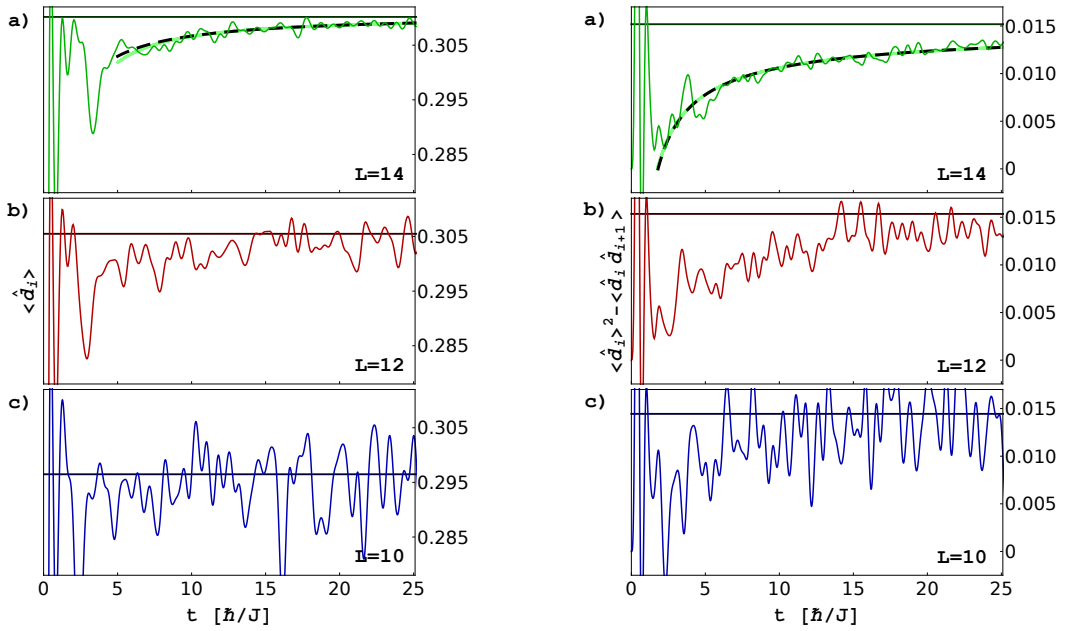

Figure 5.10: **Exact diagonalization results for different systems sizes $L = 10, 12, 14$ and $U = J$.** The solid black lines indicate the long time average obtained from the diagonal ensemble. In the left panel results for the doublon density $\langle \hat{d}_i \rangle$ are shown which is proportional to the interaction energy and can be measured experimentally[171]. The right panel shows nearest-neighbor doublon density correlations. For both observables the long time average is approached only algebraically, as can be clearly seen in the data for $L = 14$. Two fit functions are shown for each observable. For $\langle \hat{d}_i \rangle$, fitting a single exponent yields $-0.06(Jt)^{-1.23}$ (black, dashed line), but the data are described equally well with the hydrodynamic prediction $0.016(Jt)^{-1/2} - 0.048(Jt)^{-3/4}$ (solid green line). For the doublon correlations, a fit with a single exponent yields $-0.022(Jt)^{-0.69}$ (black, dashed line). Again, the data are described equally well with the hydrodynamic prediction $-0.0033(Jt)^{-1/2} - 0.02(Jt)^{-3/4}$ (solid green line).

too large for a reasonable quantitative analysis. We show, nevertheless, two different fit functions with two fitting parameters each. One is of the form $a\,(Jt)^b$ (black dashed line) and the other is of the form expected from hydrodynamics including a subleading term, see above, $a\,(Jt)^{-1/2} + b\,(Jt)^{-3/4}$ (green solid line). Both describe the data equally well.

In the right panel of Fig. 5.10 the nearest neighbor doublon density correlation function $\langle \hat{d}_i \rangle^2 - \langle \hat{d}_i\, \hat{d}_{i+1} \rangle$ is shown. Due to the translational invariance, this does also not depend on the site index i. Here the algebraic decay is more pronounced. Two fit functions of the form given above, $a\,(Jt)^b$ and $a\,(Jt)^{-1/2} + b\,(Jt)^{-3/4}$, are shown. Again, both describe the data equally well. As in the semiclassical simulations, the prefactor of the subleading term ($b \approx -0.02$) is larger than the prefactor of the eventual asymptotic term ($a \approx -0.0033$).

The ED results presented above are consistent with the prediction from hydrodynamics – if subleading corrections are included. If the transport is diffusive, as we believe, the time scales as L^2. This explains why the slow relaxation is visible already in the small 14 site system and is, potentially, also present in smaller systems. However, for $L = 10$ and $L = 12$ finite size fluctuations completely rule out any reasonable analysis, see panels b) and c) of Fig. 5.10.

Diffusive spreading of energy has also been observed in ED of a non-integrable variant of the transverse field Ising model with 16 sites (Hilbert space dimension 32896) [179]. Here the propagation of energy and entanglement after a local perturbation in a random product state was investigated. The authors found that entanglement spreads ballistically $\sim t$, while the energy spreads diffusively $\sim \sqrt{t}$. This is fully consistent with the quasiparticle worldline picture given in section 3.4. Initially only quasiparticles originating from the same pair are entangled. In each collision information is passed over to the outgoing quasiparticles: entanglement is not a conserved quantity, but it is generated in each collision. Thereby the entanglement spreads ballistically and shows a light cone effect. By contrast, the energy can be transported only diffusively as it is locally conserved.

Prethermalization can also lead to power law decay of correlation functions in the collisionless regime [14, 115]. However, the limit $U = J$ is not close to an integrable point. For the hopping rates of order J we expect that at times $Jt \sim 25$, the maximal time in Fig. 5.10, many scattering events must have taken place. In the ED results, Fig. 5.10, we further that it is the eventual value of the diagonal ensemble which is approached algebraically. Therefore, we conclude that the algebraic decay is probably not related to any quasi-stationary regime.

6 Violation of the conservation laws: Numerical Results

Since the hydrodynamic long-time tails rely on the macroscopic conservation laws, it is worthwhile to investigate what happens if these are violated. In this section we will study three different ways of doing so. In section 6.3 we will investigate the effect of a time-dependent dispersion. But first, we will consider a situation where the momenta of single quasiparticles are randomly changed. We will study two different setups: the first being that new momenta a chosen according to the eventual equilibrium distribution, as determined by the mean energy. In the second setup the new momenta are chosen according to a non-equilibrium distribution. This will lead to competition between thermalization and the exchange mechanism. In the long-time limit, this will lead to a stationary momentum distribution which is neither the full equilibrium distribution nor the exchange distribution. We will refer to this as a driven system.

We have implemented a setup, where the initial state was chosen as in section 5, including a momentum distribution $\sim \sin^2$. During the time evolution, the momenta, but not the positions, of randomly chosen quasiparticles are changed on some typical timescale $\tau_f = 1/\omega_f$ (for a single particle). The parameter which determines the influence of this exchange mechanism is the ratio of this new timescale and scattering time $\alpha = \tau_f/\tau_{dh}$.

In section 4.5 we have shown that an exponential decay of the correlation functions is expected if the conservation laws are violated. The long-time result was given in Eq. (4.56). Here we show the result again, in one dimension and for short-ranged initial correlations as realized in the numerical simulations:

$$\begin{aligned}
&\langle n(x,t)n(x',t)\rangle - C_n\delta(x-x') \\
&\underset{t\,\text{large}}{\longrightarrow} -(B_n+C_n)\,\frac{\mathsf{e}^{-\frac{|x-x'|}{\sqrt{D_n\tau_f}}}}{2\sqrt{D_n\tau_f}} + (A_n+B_n-C_n)\,\frac{\mathsf{e}^{-2t/\tau_f}\,\mathsf{e}^{-\frac{|x-x'|^2}{8D_nt}}}{(8\pi D_nt)^{1/2}} \\
&= \frac{F_n}{\alpha^{1/2}}\,\mathsf{exp}\left(-\frac{\tilde r}{(\tilde D_n\,\alpha)^{1/2}}\right) + \frac{G_n}{\tilde t^{1/2}}\,\mathsf{exp}\left(-\frac{\tilde t}{\alpha/2}\right)\;\times\;\mathsf{exp}\left(-\frac{\tilde r^2}{8\tilde D_n\,\tilde t}\right). \qquad (6.1)
\end{aligned}$$

"t large" and the prefactors A_n, B_n and C_n are explained in section 4.5. In the second line we have used dimensionless parameters and we have absorbed all constants in the definition of F_n and G_n. Explicitly, the dimensionless parameters are given by $\tilde D_n = \rho^2\tau_{dh}D_n$, $\tilde r = \rho\,|x-x'|$, $\alpha = \tau_f/\tau_{dh}$ and $\tilde t = t/\tau_{dh}$. The first term $\sim F_n$ describes possible stationary correlations, while the second term $\sim G_n$ describes how the stationary state is approached. While G_n depends on the initial state (via A_n), F_n does

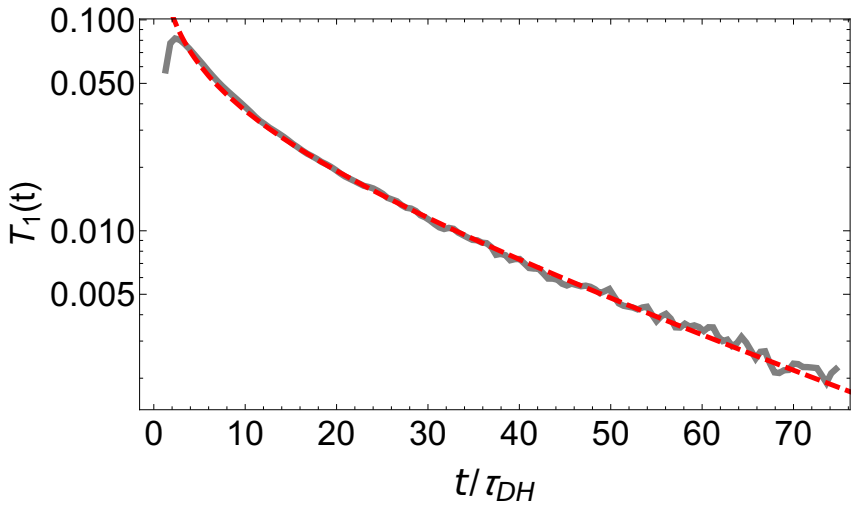

Figure 6.1: **Energy-energy correlation function in the absence of energy conservation.** The decay is exponential, the red dashed line is a fit according to the analytic formula Eq. (6.1), $0.16\,(t/\tau_{dh})^{-1/2}\,\mathrm{e}^{-0.031\,(t/\tau_{dh})}$. It describes the numerical data for $t \gtrsim 2\tau_{dh}$. Data is shown for $\alpha = \tau_f/\tau_{dh} \approx 77$.

not. We expect that when α is large the corresponding mode is still slow and the relaxation can be described by Eq. (6.1). In the derivation of Eq. (6.1), correlations between the noise of the current and the noise in the continuity equation were omitted. However, for $q \to 0$ the noise of the current becomes irrelevant (if $\tau_f < \infty$) and one can use $C_n \to 0$ in the formulas shown above. This leads to a redefinition of F_n and G_n but does not change the final result qualitatively.

6.1 Thermalization in the absence of conservation laws

We first consider the situation where the exchange distribution is chosen according to the eventual equilibrium distribution. In the present setup this corresponds to a infinite temperature distribution. We have changed only the momenta, but not the position, of randomly chosen particles with a single-particle rate $\omega_f = 1/\tau_f$. The behavior of the distance-distance correlation as defined in Eq. (5.15) function is totally unchanged. A fit to the data yields $0.0943\,t^{-1/2}$ (not shown, see Fig. 5.5). For the data obtained in the closed system the fit was $0.0941\,t^{-1/2}$. The agreement shows that a coupling between the energy and the particle number mode can be excluded within the precision of the data. Therefore we still find long-time tails related to the local conservation of the particle number.

By contrast, the behavior of the energy-energy correlations is drastically changed. The decay is now exponential rather than algebraic as predicted by Eq. (6.1). In

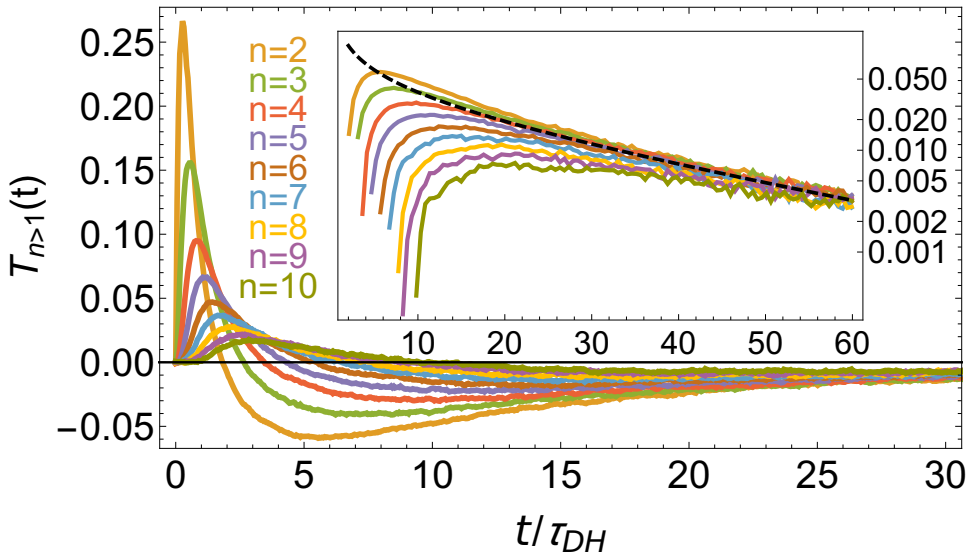

Figure 6.2: **Non-local energy-energy correlation functions.** The main panel shows the short time behavior. The inset shows the long-time behavior in a semi-log plot, here $-T_n$ is shown. The decay is exponential, the black dashed line is the fit obtained from T_1, see Fig. 6.1, $0.16\,(t/\tau_{dh})^{-1/2}\,\mathrm{e}^{-0.031\,(t/\tau_{dh})}$. For all n the correlations decay to zero, showing the absence of static correlations in the final state. Data is shown for $\alpha = \tau_f/\tau_{dh} \approx 77$.

Fig. 6.4 we show results for $\alpha \approx 77$. The red dashed line is a fit according to Eq. (6.1): $a\,(t/\tau_{dh})^{-1/2}\mathrm{e}^{-(t/\tau_{dh})/b}$, which yields $a \approx 0.16$ and $b \approx 33$. From Eq. (6.1) we expect $b = \alpha/2 \approx 38.5$. The final state is the $T = \infty$ equilibrium state and does not show any non-local correlations. This can be seen in Fig. 6.2, where we show the time evolution of T_n with $n > 1$. The main panel shows the evolution at times $t < 30\tau_{dh}$. At very short times, the behavior is dominated by the propagation of the positive initial correlations as seen by the positive peak. At $t = 0$ it is $T_0(t = 0) = 5/2$, $T_1(t = 0) = 1$ and $T_{n>1}(t = 0) = 0$, see Eqns. (5.9), (5.10) and (5.11). A sign change indicates the crossover to the relaxation regime. All T_n approach the stationary value, which is 0 here, from the negative side. The inset shows a semi-log plot of $-T_n$. At large times all curves collapse onto a single curve as shown by the black dashed line. This is the fit obtained for T_1 in Fig. 6.1. From Eq. (6.1) we expect that this happens for $t \gtrsim n^2$. This behavior can be seen in the scaling plot Fig. 6.3. Here we show $[-\sqrt{t}\,\mathrm{e}^{t/\tau_{\mathrm{fit}}}T_n(t)]_{t\to tn^2}$. From Eq. (6.1) we then expect that the result is independent of n and approaches a constant value at long times. This is confirmed by the numerical results. The constant value is approximately -0.16 as obtained from the fit of T_1 above. This shows that the diffusive scaling is still present in the relaxation. However, the relaxation towards the equilibrium is not dominated by the diffusion, but by the exchange mechanism.

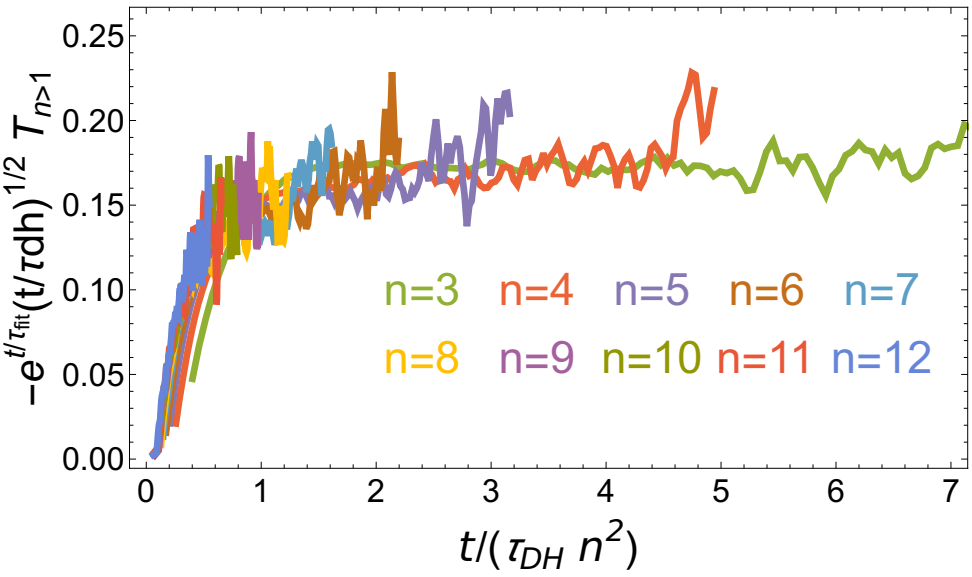

Figure 6.3: **Scaling of the non-local energy-energy correlation functions.** The $y-$axis is rescaled such that $T_n \to$ const. for $t \to \infty$, τ_{fit} is ≈ 33. The time is rescaled with n^2 such that the result is independent of n at long-times.

Gradients in the density can be compensated locally instead of globally: this leads to an exponential decay instead of an algebraic decay.

6.2 Relaxation in the driven system

This work was done in collaboration with Florian Lange and results very similar to those presented below can also be found in his Bachelor thesis [180]. The setup is the same as above but now the exchange distribution is not the equilibrium distribution but the initial $\sin^2$ distribution.

The momentum distribution is permanently filled around $\pm\pi/2$, the maxima of $\sin^2$. Therefore it will not be able to relax to the full equilibrium distribution. Rather we find that it becomes stationary with a finite value of $Q_2^{D/H} = \langle\cos(2k)\rangle_{D/H}$ which depends on α (not shown, see [180]). The equilibrium distribution has $Q_{2,\text{eq.}}^{D/H} = 0$ while the initial and the exchange distribution have $Q_{2,\text{ini.}}^{D/H} = -1/2$. Therefore it is

$$Q_{2,\text{driven}}^{D/H}(t) \underset{t\to\infty}{\longrightarrow} Q_{2,\text{stat.}}^{D/H}(\alpha) \in [-1/2, 0] \tag{6.2}$$

$$\text{with } Q_{2,\text{stat.}}^{D/H}(\alpha) \underset{\alpha\to\infty}{\longrightarrow} 0 \text{ and } Q_{2,\text{stat.}}^{D/H}(\alpha) \underset{\alpha\to 0}{\longrightarrow} -1/2. \tag{6.3}$$

In Fig. 6.4 we show the time evolution of the nearest neighbor energy correlations for different values of $\alpha = \tau_f/\tau_{dh}$. In the main panel the unscaled data is shown. Here

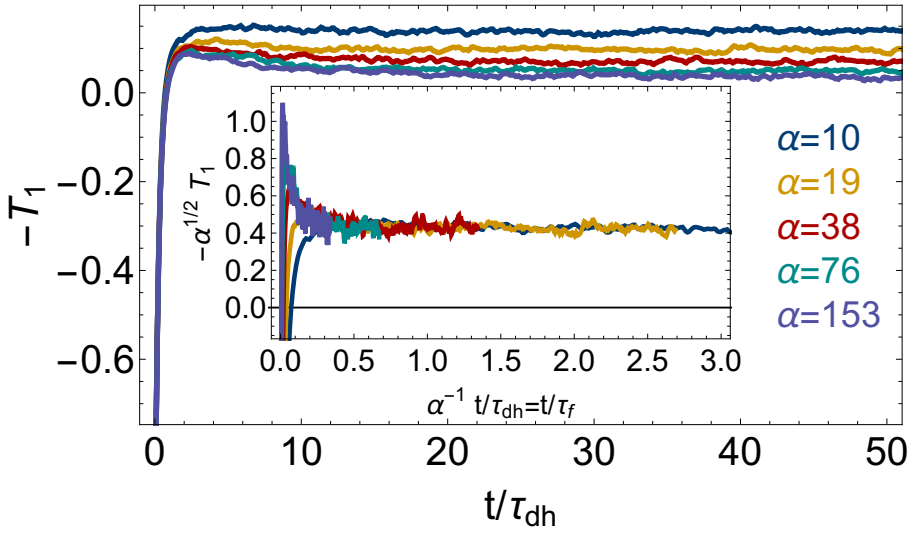

Figure 6.4: **Nearest neighbor energy-energy correlation function in the driven system.** The inset shows $-\alpha^{1/2}T_1$ as a function of t/τ_f. For $t \gtrsim 0.5\tau_f$ a stationary value $\sim \alpha^{1/2}$ is reached as predicted by Eq. (6.1). The main panel shows the unscaled data. At short times T_1 is independent of α. The smaller α, the earlier derivations can be seen.

one can see that at short times the results are independent of α. This is the regime where the effect of the exchange mechanism has not yet set in. The smaller α the earlier the curve deviates. At larger times the scaling behavior is reached if the data is plotted as a function of t/τ_f as shown in the inset. In the long time-limit T_1 shows a finite value $\sim \alpha^{-1/2}$ as predicted by Eq. (6.1).

Eq. (6.1) predicts an exponential decay of the non-local energy-energy correlations with a correlation length $\sim \sqrt{\alpha}$ and a prefactor $\sim 1/\sqrt{\alpha}$ in the stationary state. In Fig. 6.5 we demonstrate that this is indeed fulfilled here. We plot $\alpha^{1/2}\, T_n(t \to \infty) = \alpha^{1/2}\, T_n^{\text{stat.}}$ as a function of $x = n/\sqrt{\alpha}$. From Eq. (6.1) we then expect a scaling function $a\, \mathrm{e}^{-b\,x}$. An according fit with $a = -0.58$ and $b = 0.93$ is shown by the black dashed line.

The results show that there is a divergent correlation length in the limit $\tau_f \to \infty$. This implies that the weaker the deviation from the conserving regime, the larger the correlation length. This can be rationalized as follows. If the non-conserving events are very rare the system can adjust to this perturbation only diffusively. The rarer this non-conserving events, the larger is the length on which this has to be compensated. On length x a perturbation can be balanced within a time $\sim x^2/D$. Within a time t a perturbation can be balanced on a length $\sim \sqrt{Dt}$. When the perturbations occur in steps of τ_f this has influence on a length $x_c \sim \sqrt{D\tau_f}$, which is exactly the

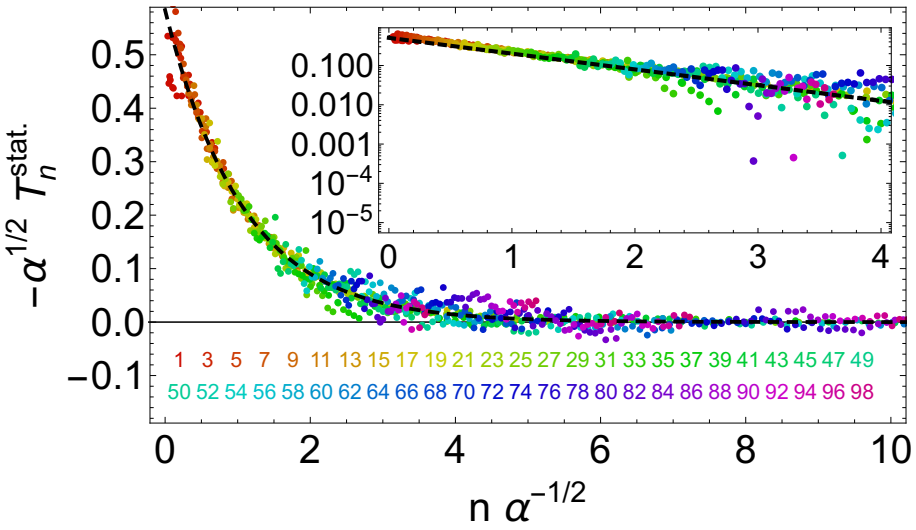

Figure 6.5: **Stationary values of the non-local energy-energy correlation function in the driven system.** There are non-local, albeit exponentially decaying, correlations in the steady state. Parameters included in the plot are $\alpha = 10, 19, 38, 77, 96, 191, 255, 383, 766$ and $n = 1 - 99$ (as shown by the colored numbers). The black dashed line is a fit according to the exponential in Eq. (6.1). The fit yields $-0.58\,\mathrm{e}^{-0.93x}$. This shows that the correlation length in the stationary state is $\sim \sqrt{\alpha}$.

correlation length found above. This is only valid if τ_f is larger than some scattering times and x_c is larger than some mean free path such that the diffusive scaling can develop.

6.3 Adiabatic limit

Above we have presented results for instantaneous quantum quenches. Now we want to consider a different limit namely the crossover to the adiabatic regime. In quantum mechanics the adiabatic theorem due to Born and Fock [181] states the following. Suppose that the system is in an eigenstate of a Hamiltonian $\hat{H}(\lambda)$ which is parametrized by λ. If λ is changed very slowly, on timescales much larger than all intrinsic timescales of the system (including the inverse level spacing), the system remains in the corresponding instantaneous eigenstate. An exception can occur when there are level crossings such that the occupied state is degenerate with another state at some time.

In classical equilibrium systems an adiabatic process is a process in which energy is transferred only as work but not as heat. To keep contact to quantum mechanics, we use a slightly different definition. We will use the word "adiabatic" for a time-dependent process which is so slow that the system is always in equilibrium. Then no entropy is produced and the process is reversible.

We will investigate a periodic modulation of the dispersion. This introduces a new time scale, the period $\tau_c \sim 1/\omega_c$ of one cycle. We study the system in the semiclassical limit and we consider the case where only one of the dispersions is time-dependent:

$$\varepsilon_0(k) = -2J_0 \cos(k) \tag{6.4}$$

$$\varepsilon_1(k,t) = -2J_1(t) \cos(k), \tag{6.5}$$

where $J_1(t) = J_1(0) + (J_2 - J_1(0))r(t/\tau_c)$ and r is periodic $r(0) = r(1) = 0$, $r(1/2) = 1$. For example we could use $r(t/\tau_c) = \sin(\pi t/\tau_c)$ or

$$r(t/\tau_c) = \begin{cases} \frac{2t}{\tau_c} & , t < \tau_c/2 \\ 2(1 - \frac{t}{\tau_c}) & , t > \tau_c/2 \end{cases} \tag{6.6}$$

which is just a triangular modulation of the dispersion. We haven chosen the modulation Eq. (6.6), because it is the easiest to implement numerically. In the semiclassical simulations, time is discretized by the scattering events. Therefore the sharp edges of r, as defined in Eq. (6.6), do not matter. In a true quantum mechanical framework, where time is continuous, one has to choose a smoother onset of the perturbation.

The positions of the quasiparticles can be calculated according to

$$x_0(t) = x_0(t_0) + \int_{t_0}^{t} dt' v_0(k) = x_0(t_0) + 2J_0 \sin(k)(t - t_0) \tag{6.7}$$

for species 1 and

$$x_1(t) = x_1(t_0) + \int_{t_0}^{t} dt' v_1(k,t) = x_1(t_0) + 2\sin(k)\int_{t_0}^{t} dt' J_1(t) \tag{6.8}$$

$$= x_1(t_0) + 2\sin(k)\int_{t_0}^{t} dt' (J_1(0) + (J_2 - J_1(0)2t/\tau_c)) \tag{6.9}$$

$$= x_1(t_0) + 2J_1(0)\sin(k)(t-t_0) + 2(J_2 - J_1(0))\sin(k)(t^2 - t_0^2)/\tau_c \tag{6.10}$$

for species 2 at $t, t_0 < \tau_c/2$. Then the calculation of next scattering position of neighboring particles $x_0(t_{hit}) = x_1(t_{hit}), x_{1a}(t_{hit}) = x_{1b}(t_{hit})$ are quadratic equations for the hitting time t_{hit}.

The Hamiltonian can be written as

$$\hat{H} = \hat{H}_0 + \hat{H}_1 + \hat{H}_{01} + \Delta\hat{H}(t), \text{ where } \Delta\hat{H}(t) = \lambda r(t/\tau_c)\hat{H}_1, \tag{6.11}$$

and we have defined $\lambda = \Delta J = J_2 - J_1(0)$.

We will consider the situation where the system is initially in equilibrium at some temperature T_{ini}. We then switch on the time dependence of the dispersion, which changes the energy of the system and therefore the equilibrium temperature. If the change is performed slowly enough, we expect that the response can be calculated from linear response theory.

We can calculate the change in the total energy E of the system according to

$$\Delta E(t) = E(t) - E(0) = \int_0^t dt' \frac{d}{dt'} E(t') = \int_0^t dt' \frac{d}{dt'} \langle \Delta\hat{H}(t') \rangle$$

$$= \int_0^t dt' \lambda \dot{r}(t') \langle \hat{H}_1 \rangle (t'). \tag{6.12}$$

The expectation value $\langle \hat{H}_1 \rangle (t')$ can be written in terms of a response function χ as

$$\langle \hat{H}_1 \rangle (t) = \int_0^t dt' \lambda r(t'/\tau_c) \chi_{\hat{H}_1,\hat{H}_1}(t-t'). \tag{6.13}$$

Within linear response theory the response function χ can be calculated in equilibrium and Eq. (6.13) becomes a Kubo formula [126–128]. In the classical limit we obtain [127, 128]

$$\chi_{\hat{H}_1,\hat{H}_1}(t) \to \chi_{H_1,H_1}(t) = \frac{1}{T}\frac{d}{dt}\left(\langle H_1(t) H_1(0) \rangle_{\text{eq.}} - \langle H_1 \rangle_{\text{eq.}}^2 \right), \tag{6.14}$$

In this high temperature limit χ has an additional prefactor ω/T when compared to

the quantum formulas.

As we know from the previous sections, see in particular section 4, the equilibrium energy-energy correlation function shows hydrodynamic long-time tails for $t \gg \tau_s$, where τ_s is the scattering time. This means that

$$\langle H_1(t)H_1(0)\rangle_{\text{eq.}} - \langle H_1\rangle^2_{\text{eq.}} = C_1\sqrt{\frac{\tau_s}{t}}, \text{ for } t \gg \tau_s. \tag{6.15}$$

With this result we can calculate the energy change in the system after a half cycle ($t = \tau_c/2$). From Eq. (6.12) and the linear response formula we obtain the deviation from the adiabatic case, where system is always in equilibrium, as

$$\begin{aligned}\Delta E\left(\frac{\tau_c}{2}; \tau_c \gg \tau_s\right) &= \int_0^{\tau_c/2} dt\lambda\dot{r}(t/\tau_c)\int_0^t dt' \frac{\lambda r(t'/\tau_c)}{T}\,\frac{(-1/2)\,\tau_s^{1/2}\,C_1}{t'^{3/2}} \\ &\approx -\frac{2\,\lambda^2\,C_1\,\tau_s^{1/2}}{T\tau_c^2}\int_{\tau_s}^{\tau_c/2} dt\int_{\tau_s}^t dt'\frac{1}{t'^{1/2}} = -\frac{2\sqrt{2}\,\lambda^2\,C_1}{3\,T}\,\left(\frac{\tau_s}{\tau_c}\right)^{1/2} + \mathcal{O}\left(\frac{\tau_s}{\tau_c}\right).\end{aligned} \tag{6.16}$$

We see that we can expect long-time tails as a function of the periodicity τ_c. In Fig. 6.6 we show numerical results for the ratio $\gamma(t = \tau_c/2) = E(t = \tau_c/2)/E(t = 0)$. The parameters used were $T_{\text{ini}} = 2, J_0 = 1, J_1(0) = 1.25, J_2 = 4$. In the limits $\tau_c \to 0$ and $\tau_c \to \infty$ we can calculate the result exactly.

For an instantaneous quench $\tau_c \to 0$ we just have to calculate the energy in the old equilibrium state with the new dispersion. The partition functions can be calculated as in section 5.2. As shown there we obtain a modified Bessel function I_0 and we define $Z_J(\beta) = I_0(2J\beta)$. The energy for the instantaneous change, E_{quench}, and energy in the initial equilibrium state can be calculated as

$$\begin{aligned}E_{\text{quench}} =& \frac{1}{2}\left(\int_{-\pi}^{\pi}\frac{dk}{2\pi}(-2J_0\cos(k))\,\frac{\mathrm{e}^{2J_0\cos(k)\,\beta_{\text{ini}}}}{Z_{J_0}(\beta_{\text{ini}})}\right. \\ &\left. + \int_{-\pi}^{\pi}\frac{dk}{2\pi}(-2J_2\cos(k))\,\frac{\mathrm{e}^{2J_1(0)\cos(k)\,\beta_{\text{ini}}}}{Z_{J_1(0)}(\beta_{\text{ini}})}\right),\end{aligned} \tag{6.17}$$

$$\begin{aligned}E_{\text{ini}} =& \frac{1}{2}\left(\int_{-\pi}^{\pi}\frac{dk}{2\pi}(-2J_0\cos(k))\,\frac{\mathrm{e}^{2J_0\cos(k)\,\beta_{\text{ini}}}}{Z_{J_0}(\beta_{\text{ini}})}\right. \\ &\left. + \int_{-\pi}^{\pi}\frac{dk}{2\pi}(-2J_1(0)\cos(k))\,\frac{\mathrm{e}^{2J_1(0)\cos(k)\,\beta_{\text{ini}}}}{Z_{J_1(0)}(\beta_{\text{ini}})}\right).\end{aligned} \tag{6.18}$$

With the parameters as used above ($\beta_{\text{ini}} = 1/2, J_0 = 1, J_1(0) = 1.25, J_2 = 4$) we obtain

$$\gamma_{\text{quench}}(\tau_c/2) = \frac{E_{\text{quench}}(t = \tau_c/2)}{E(t = 0)} = \frac{E_{\text{quench}}}{E_{\text{ini}}} \approx 2.3124. \tag{6.19}$$

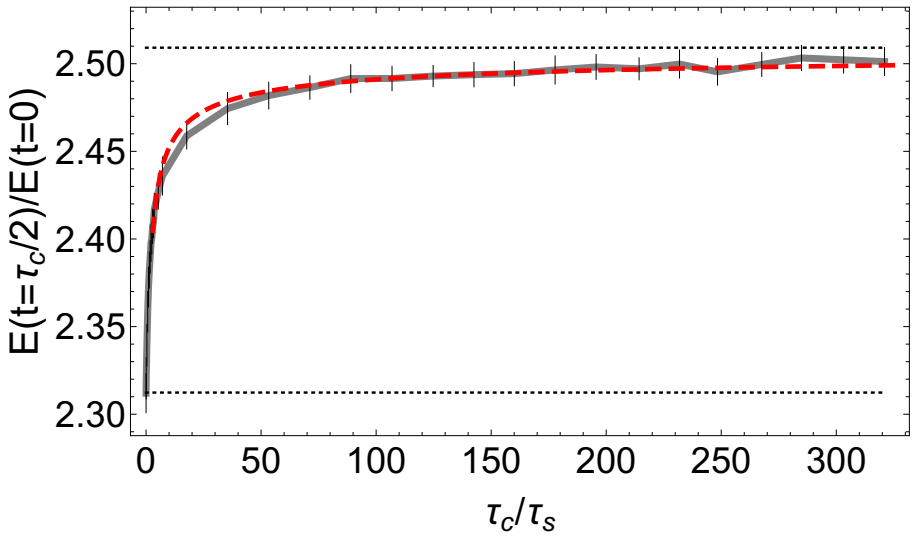

Figure 6.6: **Relative energy change in a half cycle $t = \tau_c/2$.** Parameters are $T = 2, J_0 = 1, J_1(0) = 1.25$, and $J_2 = 4$, error bars represent one standard deviation. The black dashed lines are the analytic results for an instantaneous and an infinitely slow change: $E_{\text{quench}}/E_0 = 2.3124$ and $E_{\text{adab}}/E_0 = 2.5091$. The red dashed line is a fit according to the prediction from linear response, see Eq. (6.16): $E_{\text{adab}}/E_0 - 0.18\,(\tau_c/\tau_s)^{-1/2}$.

This is shown by the lower black dashed line in Fig. 6.6.

In the adiabatic limit $\tau_c \to \infty$ the final temperature can calculated from the condition that the entropy S does not change. The entropy is given by

$$\begin{aligned} S(\beta, J) &= -\int_{-\pi}^{\pi} \frac{dk}{2\pi} \frac{\mathrm{e}^{2J_0 \cos(k)\,\beta}}{Z_J(\beta)} \log\left(\frac{\mathrm{e}^{2J_0 \cos(k)\,\beta}}{Z_J(\beta)}\right) \\ &= -\frac{2J\,\beta I_1(2J\beta)}{I_1(0, 2J\beta)} + \log\left(I_0(2J\beta)\right). \end{aligned} \tag{6.20}$$

Adiabaticity, as defined above, dictates

$$S_{\text{ini}} = S(\beta_{\text{ini}}, J_0) + S(\beta_{\text{ini}}, J_1(0)) \stackrel{!}{=} S_{\text{final}}(t = \tau_c/2) = S(\beta_{\text{final}}, J_0) + S(\beta_{\text{final}}, J_2) \tag{6.21}$$

and the temperature of the final state, $T_{\text{final}} = 1/\beta_{\text{final}}$, can be calculated by solving Eq. (6.21). The energy of the final equilibrium state is then given by

$$\begin{aligned} E_{\text{adab.}} =& \frac{1}{2}\left(\int_{-\pi}^{\pi} \frac{dk}{2\pi}(-2J_0\cos(k)) \frac{\mathrm{e}^{2J_0 \cos(k)\,\beta_{\text{final}}}}{Z_{J_0}(\beta_{\text{final}})} \right. \\ &\left. + \int_{-\pi}^{\pi} \frac{dk}{2\pi}(-2J_2\cos(k)) \frac{\mathrm{e}^{2J_1(0) \cos(k)\,\beta_{\text{final}}}}{Z_{J_1(0)}(\beta_{\text{final}})} \right). \end{aligned} \tag{6.22}$$

Solving Eq. (6.21) numerically with the parameters given above yields $T_{\text{final}} \approx 4.703$ or $\beta_{\text{final}} \approx 0.2126$. Inserting this into Eq. (6.22) yields the final energy $E_{\text{adab.}} \approx -2.7761$ and, finally,

$$\gamma_{\text{adab.}}(\tau_c/2) = \frac{E_{\text{adab.}}}{E_{\text{ini}}} \approx 2.50914. \tag{6.23}$$

This number is shown by the upper black dashed line Fig. 6.6.

The red dashed line is a fit according to the prediction from linear response theory $\gamma_{\text{adab.}}(\tau_c/2) - A(\tau_s/\tau_c)^{1/2}$. While it seems that the data are well described by the fit, a further analysis shows that the data can be described equally well by other fit functions. To clarify this point, results for longer timescales are needed. In section 5 we have seen that the eventual $1/\sqrt{t}$ behavior is only seen after more than 200 scattering times.

Results for a full cycle can be obtained analogously and do not give further insights. In both limits, (a) $\tau_c \to 0$ and (b) $\tau_c \to \infty$, it is $\Delta E = 0$ since in (a) nothing changes and in (b) the process is reversible.

7 Quench dynamics and statistics of measurements

In this section we study a quantum quench in two dimensions. We consider the dynamical fragmentation of a spin line into bound states. We will describe the system as an open, effectively one dimensional, system which is locally coupled to the two dimensional environment. This is justified for the initial state and the observables that we have studied. The feedback of the two dimensional environment onto the one dimensional dynamics is omitted. As the main result we obtain statistical information on quantum measurements which cannot be described by conventional correlation functions.

As an initial state we have chosen a line of flipped spins in y-direction in a ferromagnetic background (in $\hat{S}^z$ basis). This choice is motivated by an experimental setup realized in the group of Immanuel Bloch in Munich [102, 105, 108]. The Hamiltonian governing the time evolution is given by the 2-dimensional spin $1/2$ ferromagnetic, $J > 0$, XXZ Heisenberg model

$$\begin{aligned}\hat{H} = &- J \sum_{i_x,j_y} \left[\frac{1}{2} \left(\hat{S}^+_{i_x,j_y} \hat{S}^-_{i_x+1,j_y} + \hat{S}^+_{i_x+1,j_y} \hat{S}^-_{i_x,j_y} \right) + \Delta \hat{S}^z_{i_x,j_y} \hat{S}^z_{i_x+1,j_y} \right] \\ &- J\alpha \sum_{i_x,j_y} \left[\frac{1}{2} \left(\hat{S}^+_{i_x,j_y} \hat{S}^-_{i_x,j_y+1} + \hat{S}^+_{i_x,j_y+1} \hat{S}^-_{i_x,j_y} \right) + \Delta \hat{S}^z_{i_x,j_y} \hat{S}^z_{i_x,j_y+1} \right]\end{aligned} \tag{7.1}$$

We will consider the Ising limit $\Delta \gg 1$ only. In this limit we find stable quasiparticles which have a very long lifetime protected by the largeness of Δ. We can then use the semiclassical methods as presented in section 3. We expect that this gives accurate results to leading order in $1/\Delta$. The coupling in the y-direction, αJ, is assumed to be stronger than the coupling J in the x-direction: $\alpha - 1 > 1/\Delta$. In the following we present results for $\alpha = 2$, an arbitrary choice. We will call the interaction energy ($\sim \hat{S}^z \hat{S}^z$) the *Ising energy*.

It is possible to realize effective Heisenberg models with ultracold atoms in optical lattices [44, 182]. The parameters of the Hamiltonian, Eq. (7.1), can be adjusted by Feshbach resonances or by different atomic species showing different hopping amplitudes [182]. Slight modifications can already be obtained by varying the laser intensity [182]. Due to the high precision techniques, arbitrary product states in the $\hat{S}^z$ basis can be prepared [108].

The experimental protocol is shown in Fig. 7.1. Here and in all the following graphics the z-component of the spins is depicted. Spin-down is shown in orange, while up-spins are colored blue. At $t = 0$ a line of flipped spins is prepared in the

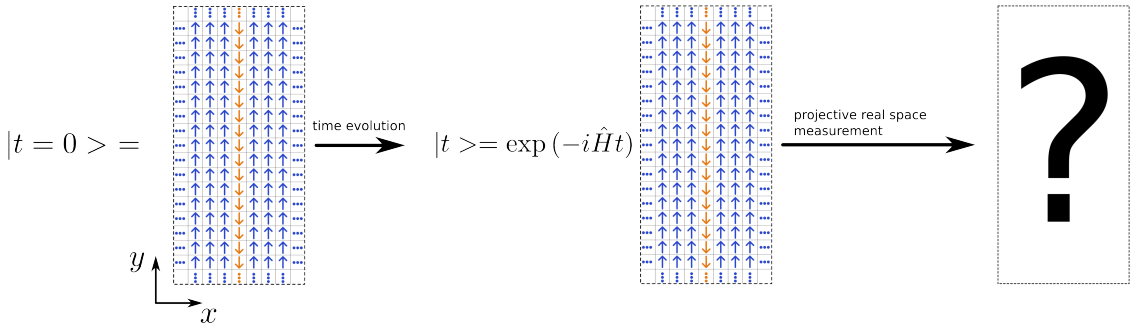

Figure 7.1: **The initial state and the experimental protocol.** The initial state is a line of flipped spins in a ferromagnetic background. Depicted are the z-components of the spins. The time evolution is according to the anisotropic XXZ Hamiltonian in the Ising limit. After long times, projective measurements are performed, as realized by the quantum microscope measurements, see section 2.3.

ferromagnetic background. The initial state, as depicted in the left panel of Fig. 7.1, was used in the experiment reported in [102]. However in [102], the Hamiltonian of the time evolution was in a limit where the individual rows were effectively decoupled, $\alpha \to 0$ in Eq. (7.1). After a time evolution with the Hamiltonian shown in Eq. (7.1) projective real space measurements in the $\hat{S}^z$ basis are performed. By means of the quantum microscopes, introduced in section 2.3, it is possible to perform such measurements. This, in principle, gives access to full distribution functions. In each run one obtains a different result, according to the quantum mechanical probabilities. The collection of possible final states weighted by their probabilities defines a time-dependent ensemble. We will investigate how these measurements can be described quantitatively. The goal is to obtain statistical properties of this ensemble after long times. This also contains information on typical single-shot results. Low order correlation functions are not sufficient to describe the ensemble of final states.

First, we will present the zoology of quasiparticles, their creation and their possible scatterings. The time evolution is characterized by the emission of single spins from the $1d$ line into the ferromagnetic background. We will consider only the $1d$ dynamics along the initial line. We will not keep track of the emitted spins. In the infinite system without boundaries there is a vanishing probability that they scatter, as they form a very dilute $2d$ gas. Therefore they will not influence the $1d$ dynamics. We will describe the $1d$ line as an effectively open system which can emit but not absorb. During the time evolution the quasiparticles can transform into each other and, as time evolves, more and more single spins are emitted from the $1d$ line. Eventually, this leads to freezing out of the $1d$ dynamics. The final ensemble consists of bound

states and defects which are immobile to leading order in $1/\Delta$. We will determine the probability distributions of these immobile objects, which describe the outcome of the projective measurements. The dynamics is calculated by means of semiclassical simulations as described in 3.4. As an analytical input, the exact quantum mechanical two-particle creation and scattering rates have been calculated. They were tabulated and the dynamics was simulated according to this rates.

7.1 Creation of quasiparticles

To describe the creation of quasiparticles, we use a Schrieffer-Wolff transformation as described in section 3.1 We demand the cancellation of $[\hat{S}, \hat{H}_0]$ and $\hat{H}_1$ only when acting on the initial state $|\Psi(0)\rangle$:

$$[\hat{S}, \hat{H}_0] \, |\Psi(0)\rangle = -\hat{H}_1 \, |\Psi(0)\rangle \tag{7.2}$$

where $\hat{H}_0$ describes the spin flip terms and $\hat{H}_1$ is the Ising Hamiltonian. As all spin flips raise the Ising energy by $2\alpha\Delta J$, see Fig. 7.2a)→b), we find:

$$\hat{S} \approx -\frac{1}{4\alpha\Delta} \sum_{j=1}^{L} \left(\hat{S}^{+}_{0,j} (\hat{S}^{-}_{1,j} + \hat{S}^{-}_{-1,j}) - \text{h. c.} \right) \tag{7.3}$$

where L is length of the $1d$ line. When $\mathrm{e}^{\hat{S}}$ acts on the initial state this creates a wavefunction containing any number of quasiparticles. Due to the exponential their distribution approximately follows a Poisson distribution. The overlap with the initial state is exponentially small in L and given by $\left| \langle \Psi(0)| \, \mathrm{e}^{\hat{S}} \, |\Psi(0)\rangle \right|^2 \approx \mathrm{e}^{-L/(8\,\alpha^2\Delta^2)}$.

To calculate the quasiparticle density, we denote the operator which counts the number of quasiparticles by $\hat{N}$. Its expectation value can be calculated to be

$$\langle \Psi(0)| \, \mathrm{e}^{-\hat{S}} \hat{N} \, \mathrm{e}^{\hat{S}} \, |\Psi(0)\rangle \approx \frac{2L}{(4\alpha\Delta)^2} = \frac{L}{8\,(\alpha\Delta)^2}. \tag{7.4}$$

We define the quasiparticle density ρ, their mean distance r_0 and a typical timescale τ_0 as

$$\rho = \frac{1}{8\,\alpha^2\,\Delta^2}, \;\; r_0 = 1/\rho = 8\,\alpha^2\,\Delta^2, \;\; \tau_0 = r_0/J = \frac{8\,\alpha^2\,\Delta^2}{J}. \tag{7.5}$$

If length and time are measured in these units, the results in the semiclassical limit ($\Delta \to \infty$) are independent of Δ.

The quasiparticles originating from the transformation Eq. (7.3) are depicted in Fig. 7.2. There are two creation channels. In one channel kink (k) - antikink ($\bar{k}$) pairs

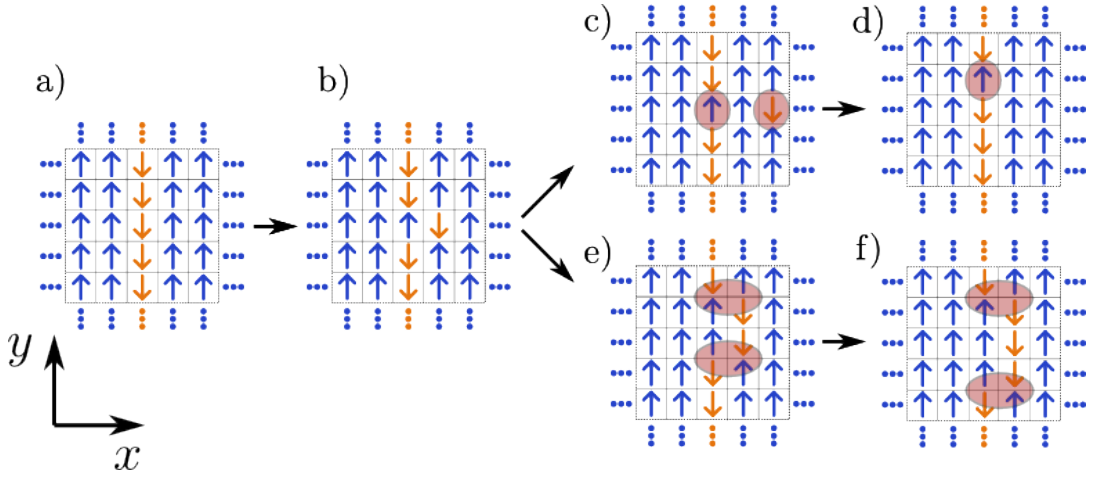

Figure 7.2: **Quasiparticle creation on short timescales.**
a) The initial state: A $1d$ line of flipped spins is prepared in a $2d$ ferromagnetic background.
b) The only state (up to translations and reflection) that can be reached from the initial state by a single spin flip. A second spin flip leads to state c) or e) without a change of the Ising energy.
c) A state with two quasiparticles, a hole (h, left marker) and a free spin (f, right marker).
d) While the free spin is emitted into the ferromagnetic background, the hole propagates along the line by spin flips in $y-$direction. In the absence of boundaries the emitted spin has a vanishing probability to influence the $1d$ dynamics along the line.
e) In a further channel, kink (k, lower marker) and antikink ($\bar{k}k$, upper marker) pairs are created.
f) Both, kink and antikink, propagate along the line by spin flips in $x-$direction.

are formed. They propagate along the $1d$ line with spin flips in $x-$direction and thus have a hopping rate of $-J/2$. In the other channel holes (h) are formed by the emission of single free spins (f) into the ferromagnetic background. The holes propagate along the $1d$ line with spin flips in $y-$direction, therefore having a hopping rate of $-\alpha\, J/2$. The low density of quasiparticles $\rho = (8\,\alpha^2\,\Delta^2)^{-1}$ permit a description where the quasiparticles propagate with their respective group velocities $\partial_q \varepsilon_q^{k/h}$. To lowest order in $1/\Delta$, the hole and kink/antikink dispersions are given by $\varepsilon_q^h \approx -\alpha J \cos(q)$ and $\varepsilon_q^{k/\bar{k}} \approx -J\cos(q)$, respectively. The propagation of a kink or antikink shifts the $1d$ line by one lattice spacing, see panels e) and f) in Fig. 7.2

The initial momentum distributions of kink-antikink pairs and holes are calculated as shown in section 3.3, see Eq. (3.93). We find

$$P_{k\bar{k}}(q) = \frac{2J^2\ \sin^2(q)}{|\varepsilon_q^{k\bar{k}} - J^2\,\Delta_0^{k\bar{k}}(\varepsilon_{q,0}^{k\bar{k}},0) - \frac{J^2}{4}\,\Delta_0^{hf}(\varepsilon_{q,0}^{k\bar{k}},0)|^2} \tag{7.6}$$

$$P_{hf}(k_y) = \int_0^{\pi} \frac{dk_x}{\pi} \frac{\frac{1}{2}J^2 \ \sin^2(k_x)}{|\varepsilon^{hf}_{\boldsymbol{k},0} - J^2\,\Delta_0^{k\bar{k}}(\varepsilon^{hf}_{\boldsymbol{k},0}, 0) - \frac{J^2}{4}\,\Delta_0^{hf}(\varepsilon^{hf}_{\boldsymbol{k},0}, 0)|^2} \tag{7.7}$$

where

$$\Delta_0^{k\bar{k}}(\omega, K_y) = \int_0^{\pi} \frac{dq}{\pi} \frac{2\sin^2(q)}{\omega - \varepsilon^{k\bar{k}}_{q,K_y} + i\epsilon} \tag{7.8}$$

$$\Delta_0^{hf}(\omega, K_y) = \int_{-\pi}^{\pi} \frac{dk_y}{2\pi} \int_0^{\pi} \frac{dk_x}{\pi} \frac{2\sin^2(k_x)}{\omega - \varepsilon^{hf}_{\boldsymbol{k},K_y} + i\epsilon} \tag{7.9}$$

and

$$\varepsilon^{k\bar{k}}_{q,K_y} = -2J\cos(\frac{K_y}{2})\cos(q) \tag{7.10}$$

$$\varepsilon^{hf}_{\boldsymbol{k},K_y} = -J\cos(k_x) - 2\alpha J\cos(\frac{K_y}{2})\cos(k_y). \tag{7.11}$$

We have checked numerically that $\int_0^{\pi} \frac{dq}{\pi} P_{k\bar{k}}(q) + \int_{-\pi}^{\pi} \frac{dk_y}{2\pi} P_{hf}(k_y) = 1$. As we are not interested in the k_x component of P_{hf} we integrate over this momentum in Eq. (7.7). For $\alpha = 2$ we find that $89.8\,\%$ of the created quasiparticle pairs are of kink-antikink type, while the remaining $10.2\,\%$ are holes and emitted spins. The initial quasiparticle creation can be cast in a reaction scheme, in analogy to a chemical reaction, as

$$|\Psi(0)\rangle \to \begin{cases} h + f & \text{(c1)} \\ k + \bar{k} & \text{(c2)} \end{cases}. \tag{7.12}$$

(c1) and (c2) denote the different possible channels. Once the quasiparticles are formed they are very stable and protected by the large gap $\sim J\Delta$. As for the doublons in section 5, a high order scattering process is needed to transform the Ising energy into kinetic energies of single quasiparticles.

7.2 Scattering and emission

As many kink-antikink pairs are created initially, the dominant reaction at the beginning of the time evolution is

$$k + \bar{k} \to \begin{cases} k + \bar{k} & \text{(o1)} \\ h + f & \text{(o2)} \end{cases} \tag{7.13}$$

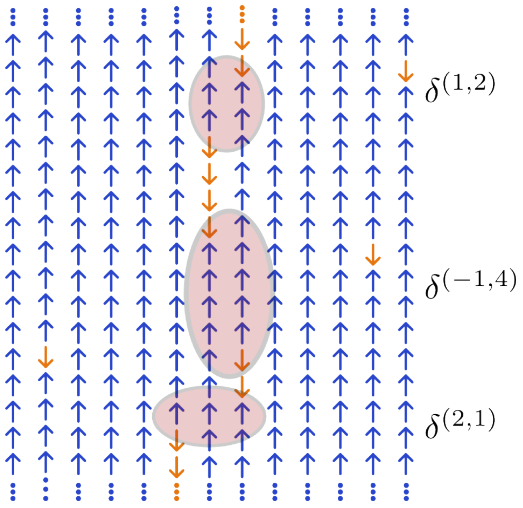

Figure 7.3: **Schematic plot of more complex defects $\delta^{(n,m)}$.** n and m describe the shift of the line in x and y directions, respectively (in units of the lattice constant). Defects with $|n+m| > 1$ are immobile to leading order in $1/\Delta$, as they cannot propagate by a single spin flip. In between the defects the spin-down bound states develop. For example, the $\delta^{(2,1)}$ and the $\delta^{(-1,4)}$ defect are separated by a bound state including two spins. The $\delta^{(-1,4)}$ and the $\delta^{(1,2)}$ defect are separated by a bound state including four spins. Lengthscales are not correctly reproduced in this schematic plot.

We need the momentum distribution $P^{k\bar{k}\to fh}_{k_1,k_2}(q)$ for the creation of a hole with momentum q in a scattering process of a $k+\bar{k}$ pair with momenta k_1 and k_2. This can be calculated along the lines of section 3.2 and reads

$$
\begin{aligned}
&P^{k\bar{k}\to fh}_{k_1,k_2}(q) \\
&= \frac{8J\left|\cos(\frac{k_1+k_2}{2})\sin(\frac{k_1-k_2}{2})\right|\sqrt{J^2-(E_S(k_1,k_2)+2\alpha J\cos(\frac{k_1+k_2}{2})\cos(\frac{k_1+k_2}{2}-q))^2}}{\left|2J\cos(\frac{k_1+k_2}{2})\exp(i\frac{|k_1-k_2|}{2})+\frac{J^2}{2}\Delta_0^{hf}(E_S(k_1,k_2),k_1+k_2)\right|^2} \\
&\Theta\left(J-\left|E_S(k_1,k_2)+2\alpha J\cos(\frac{k_1+k_2}{2})\cos(\frac{k_1+k_2}{2}-q)\right|\right)
\end{aligned}
\tag{7.14}
$$

where $E_S(k_1,k_2) = -J(\cos(k_1)+\cos(k_2))$ is the energy of the incoming $k+\bar{k}$ pair and Θ denotes the Heaviside step function. The total emission probability is $P_{\text{emission}} = \int_{-\pi}^{\pi}\frac{dq}{2\pi}P^{k\bar{k}\to fh}_{k_1,k_2}(q)$. Accordingly, the reflection probability in channel (o1) is $1-P_{\text{emission}}$. The function in Eq. (7.14) depends on three momenta.

During the time evolution more and more spins are emitted from the $1d$ line, which leads to a decrease of the spin-down density in the $1d$ subsystem. In this way defects $\delta^{(n,m)}$ in the line are created. Examples are shown in Fig. 7.3. Here n denotes the shift in $x-$direction and m denotes the shift in $y-$direction, both in units of the lattice spacing. As the defects cannot propagate via a single spin flip they are immobile to leading order in $1/\Delta$

When mobile particles hit these defects new and more complicated defects are created. We have calculated all scattering rates of kinks, antikinks and holes at defects up to $n = 2$ and $m = 10$. In total more than 70 scattering problems have been solved,

all including an emission channel and various reflection and transmission channels. An explicit example is shown below. For large defects $\delta^{(n,m)}$ with $|n| \geq 3$ or $m > 10$ only the reflection and emission channels have been taken into account. Here the transmission probabilities are very small. Fortunately, in all but the kink-antikink scattering at least one immobile particle is involved. Therefore these scatterings can be described by functions of one or two momenta which have been tabulated. The scatterings in the semiclassical simulations have been performed according to this exact two-particle scattering rates.

Finally, we present one example of a more complex scattering event which happens at later times, when larger defects have formed. We have arbitrarily chosen the scattering of a kink at an immobile $\delta^{(1,4)}$ defect. The corresponding outgoing scattering channels are shown in Fig. 7.4. The associated reaction schemes are:

$$k + \delta^{(1,4)} \rightarrow \begin{cases} k + \delta^{(1,4)} & \text{(o1)} \\ f + \delta^{(0,5)} & \text{(o2)} \\ \bar{k} + \delta^{(-1,4)} & \text{(o3)} \\ h + \delta^{(0,3)} & \text{(o4)} \\ \delta^{(-1,4)} + \bar{k} & \text{(o5)} \\ \delta^{(1,4)} + k & \text{(o6)} \\ \delta^{(0,3)} + h & \text{(o7)} \end{cases}$$

(o1) is a simple reflection into the incoming channel. For slow quasiparticles $q \approx 0$ or $q \approx \pm 1$ this is the dominant channel, the probabilities of all other channels vanish as $\sin(k) \sim k$. This leads to very long lifetimes of the slow quasiparticles. However, these are not well described by the semiclassical approach, a they have very long wavelength $\sim 1/k$. (o2) is an emission event. A free spin is emitted and the immobile defect grows by one lattice site. The emission of holes at immobile defects cause an increase of the vertical defect size by two lattices sites (not shown). (o3) describes the transformation of a kink into an antikink. When compared to the incoming channel its propagation shifts the $1d$ line to the right by two lattice sites. In this way defects with large n can be created. In (o4) the kink is transformed into a reflected hole. This decreases the size of the defect by one. (o5)–(o7) are the transmission analogs of (o1), (o3) and (o4). The momentum of the new quasiparticle is fixed by energy conservation. In all but channels (o5) and (o6) the momentum is changed and therefore also the momentum of the defect. However, its kinetic energy is of order $J/\Delta^{a>4}$ and, as

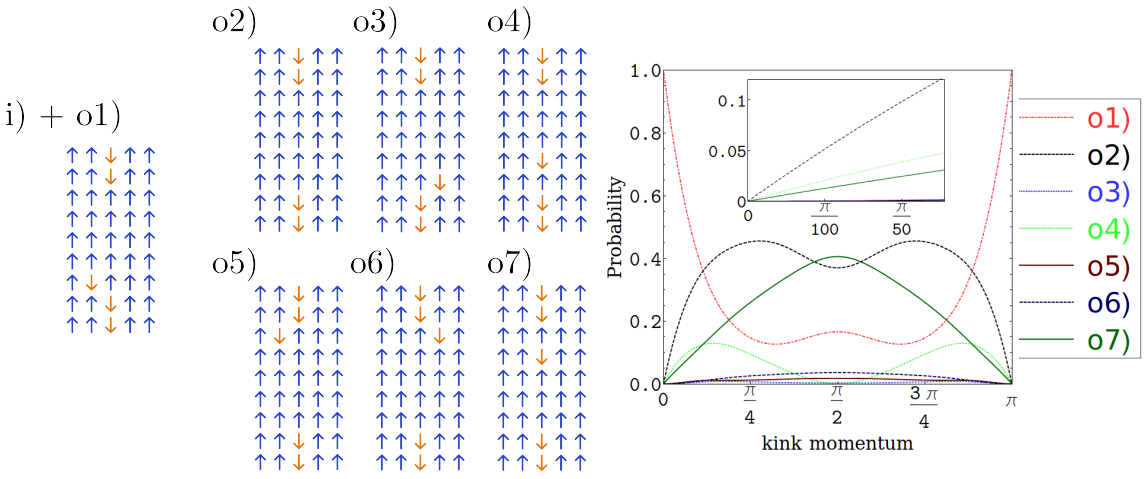

Figure 7.4: **The scattering of a kink at an immobile $\delta^{(1,4)}$ defect.** There are seven outgoing channels (o1)-(o7), depicted in the left panel, including the emission channel (o2). The kink can be reflected on the same (o1) or the other side (o3) of the line. It can be transmitted as a kink on the same (o5) or the other side (o6) of the line. It can also be transformed into a hole either being reflected (o4) or being transmitted (o7). In each channel a different immobile defect remains. The momentum of the mobile particle is not conserved, as the defect can absorb or provide momentum. Only in channels (o5) and (o6) it is conserved due to energy conservation, as the defect cannot absorb energy.
In the right panel the probabilities for the different channels are shown as function of the incoming kink momentum. For small momenta close to 0, and momenta close to π, the reflection probability (o1) approaches 1. As shown in the inset, all other scattering and emission rates vanish linearly with the velocity $\sim \sin(k) \approx k$.

a subleading term, not part of the dynamics. For fast incoming kinks, having a momentum close to $\pm\pi/2$ emission and transmission channels dominate. Fast incoming holes, having a momentum close to $\pm\pi/2$, cannot transform into kinks or antikinks due to energy conservation as $\alpha > 1$ (not shown).

7.3 Time dependent results

The $1d$ semiclassical dynamics can be nicely visualized in worldline pictures. An example is shown in Fig. 7.5. At the initial time, quasiparticle pairs are created according to the quantum mechanical rates, see section 7.1. Kinks and antikinks are shown in green and blue, respectively, and hole wordlines are shown in red. When holes are created, a free spin is emitted as shown by the orange dots. Several scattering events are marked with circled numbers: at ① a reflection of a hole and an antikink takes place. As they have different hopping rates, their dispersions are different, the momenta are changed. ② shows the scattering of two holes: the individual momenta are conserved. Here also an emission event could have taken place, creating a $\delta^{(0,3)}$

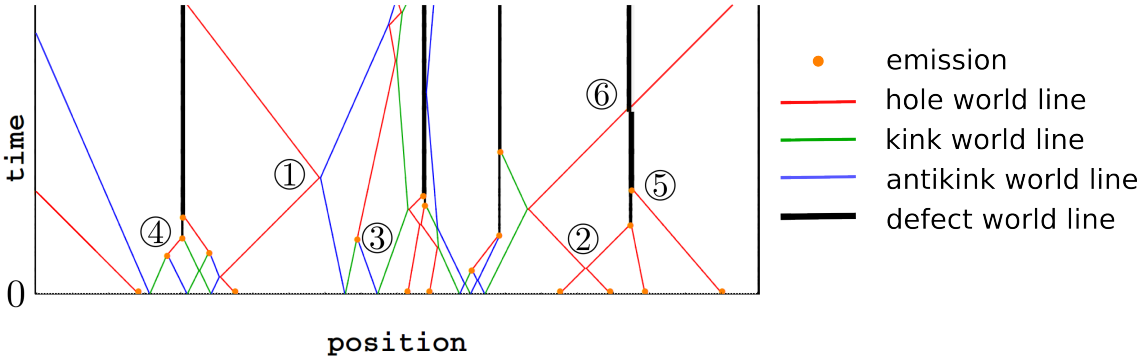

Figure 7.5: **Typical worldline picture describing the semiclassical dynamics.** At $t = 0$ kink-antikink pairs (green and blue worldlines) and holes (red) are created along the $1d$ line. The creation of a hole is accompanied by the emission of a single spin (only shown as an orange dot) in the direction perpendicular to the line, see Fig. 7.2. Subsequent scattering leads to further emission of single spins, see the orange dots. Larger defects form (shown in black), they are immobile to leading order in $1/\Delta$ and have zero velocity. The circled numbers are explained in the main text.

defect, see the other hole-hole scattering nearby. The annihilation of a kink-antikink pair into a hole and an emitted free spin is shown in ③. The momentum of the hole is chosen randomly according to the distribution given above in Eq. (7.14). At ④ a defect (black line) is formed by a hole-kink scattering accompanied by an emission. The defect is immobile, in the approximation considered here, and its wordline is parallel to the time axis. Further emissions increase the size of the defects as shown in ⑤. Here the scattering of a hole into a free spin increases the size of the defect by two lattice sites. The transmission of mobile particles shift the defect as shown in ⑥. Here the transmission of a hole shifts the $\delta^{(0,5)}$ defect by two lattice sites.

As can already be seen from Fig. 7.5 the number of mobile $1d$ quasiparticles drops rapidly during the time evolution. The fraction of remaining quasiparticles as a function of time is shown in Fig. 7.6. The total fraction is shown in black. Due to the high probability for emission of fast particles it drops exponentially at short times $t \lesssim 50\tau_0$. The blue, thinner line shows the fraction of holes. This increases at very short times $t \lesssim 10\tau_0$ due to the annihilation of kink-antikink pairs, see ③ in Fig. 7.5. Both quantities show an algebraic long-time tail for $t \gtrsim 100\tau_0$. The reason here is the small emission rate of slow quasiparticles. In section 7.2 we have seen from an explicit example that the emission probability vanishes linearly for slow quasiparticles with momentum close to 0 or $\pm\pi$. In Fig. 7.7 the time evolution of the quasiparticle momentum distributions are shown. For large times, only momentum states close to 0 or $\pm\pi$ are occupied. For these slow particles, the velocity and the emission probability are both proportional to the momentum q. The occupation of the momentum

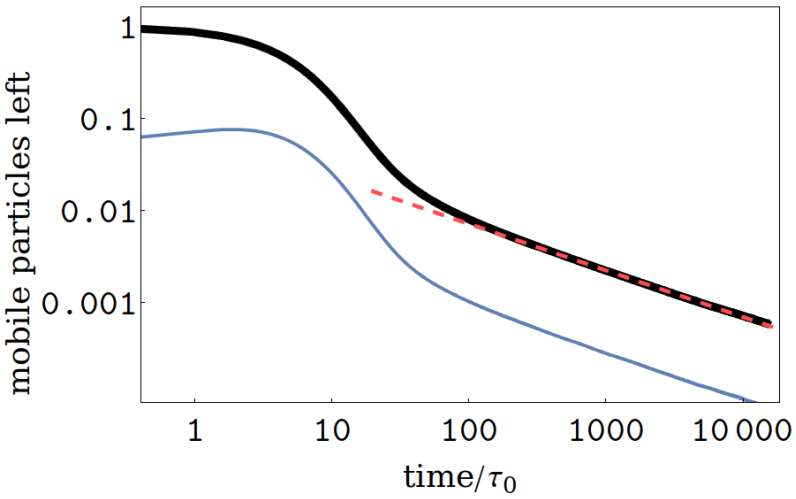

Figure 7.6: **Time evolution of the remaining fraction of mobile particles.** The total quasiparticle fraction is shown by the black line. On short timescales $t/\tau_0 \lesssim 50$ this decays exponentially. For larger times $t/\tau_0 \gtrsim 100$ there is an algebraic long-time tail $\sim (\tau_0/t)^{1/2}$ as shown by the red dashed line. The lower blue thin line shows which fraction of the mobile particles are holes. This increases for short times $t \lesssim 10\,\tau_0$ due to annihilation processes of kink-antikink pairs, see ③ in Fig. 7.5.

modes close to $q = 0$ and $q = \pm\pi$ is thus given by

$$\begin{aligned} & n_q(t+\Delta t) && = n_q(t) - \Delta t|v_q|\; P_{\text{emission}}(q)\; n_q(t) \approx n_q(t) - \Delta t \tilde{J} q^2\; n_q(t) \\ \rightarrow \quad & \tfrac{d}{dt} n_q(t) && = -\tilde{J} q^2\, n_q(t) \\ \rightarrow \quad & n_q(t) && = n_q(0)\, \mathrm{e}^{-\tilde{J} q^2 t} \equiv n_q(0)\, \mathrm{e}^{-t/\tau_{\text{slow}}(q)}. \end{aligned} \tag{7.15}$$

Here $\tilde{J}$ is a constant of order J and we have defined the lifetime as $\tau_{\text{slow}}(q) = 1/(\tilde{J}q^2)$. Then the total number of slow quasiparticle is

$$N_{\text{tot}} \sim \int dq\; \mathrm{e}^{-t/\tau_{\text{slow}}(q)} = \int dq\; \mathrm{e}^{-\tilde{J}q^2 t} \sim \frac{1}{t^{1/2}} \int dq\; \mathrm{e}^{-\tilde{J}q^2} \sim \frac{1}{t^{1/2}}, \tag{7.16}$$

and likewise for momenta close to $\pm\pi$. This leads to a power law decay of total number of quasiparticles.

The initial momentum distribution of kink-antikink pairs and holes is shown by the purple lines in Fig. 7.7. The kinks and antikinks have an approximate $\sin^2$ distribution. However, it is slightly changed when compared to the doublon-distribution calculated in 3.3 due to the presence of the second creation channel. The momentum distribution of the holes is different and flattened at $0, \pm\pi/2, \pm\pi$. The reason is that it is integrated over all possible q_x momenta of the emitted spin. During the time evolution all the weight of the momentum distributions shifts to $q = 0$ and $q = \pm\pi$. When

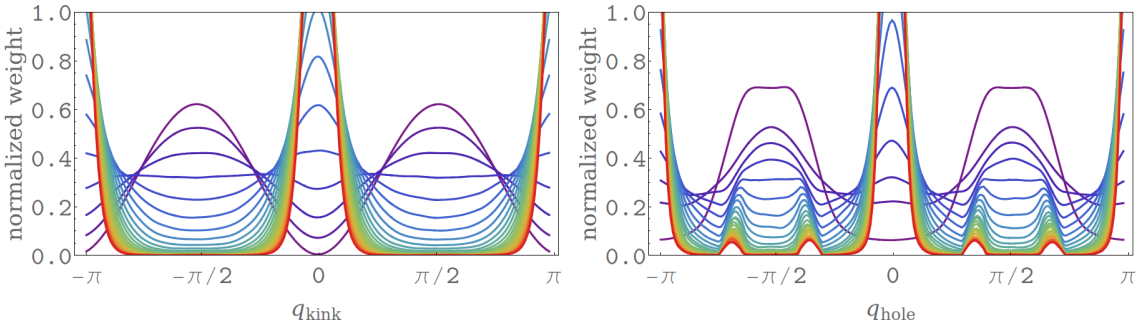

Figure 7.7: **Time evolution of the quasiparticle momentum distributions.** The left panel shows the distribution of kinks and antikinks and the right panel shows the distribution of the holes. The times are from $t = 0\,\tau_0$ (purple lines) to $t \approx 100\,\tau_0$ (red lines). For the kink-antikink pairs the initial distribution is very close to a $\sin^2$ distribution. The hole distribution is different, as the momentum of the emitted spin is integrated out, see Eq. (7.7). For better visibility, each momentum distribution is normalized, $\int n_q dq = 1$. However, one has to keep in mind that the total number of mobile particles drops rapidly as shown in Fig. 7.6. The humps in the hole distribution close to $\pm\pi/2$ are due to the creation of holes by kink-antikink annihilation. Both distributions develop maxima at $k = 0$ and $k = \pm\pi$, corresponding to very slow quasiparticles. These have a high probability of reflection, see Fig. 7.4.

these momenta dominate, also the algebraic tails in the total quasiparticle number become visible. The distributions shown in Fig. 7.7 are all normalized and thus do not reflect the drastic reduction of the particle number. Otherwise, the long-time distributions would be hardly visible: for example at $t = 100\tau_0$ only $\approx 1\,\%$ of the initial quasiparticles are left, see Fig. 7.6. The momentum distribution of the holes develops small humps close to $q = \pm\pi/2$. These arise from the annihilation of kink-antikink which produces holes, see ③ in Fig. 7.5.

Eventually, when all mobile quasiparticles have been emitted from the $1d$ line, the system freezes into a stationary state without any dynamics to leading order in $1/\Delta$. We stopped the simulation when there were ≈ 10 mobile quasiparticles left. These were the slowest of the slowest and they undergo millions of reflections before they are emitted.

7.4 Characterization of the final ensemble

Each final configuration at the end of the simulation is characterized by a collection of bound states and corresponds to a possible outcome of a projective quantum microscope measurement. Here a bound state of size l is defined as a vertical line segment of l down-spins in the ferromagnetic background. Examples are shown in Fig. 7.8.

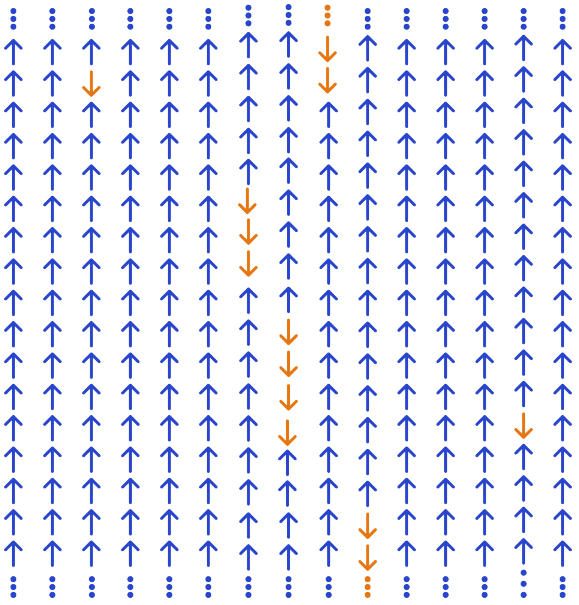

Figure 7.8: **Schematic plot of a possible final configuration.** Two bound states are shown in the center, one with $l = 3$ spins and one containing $l = 4$ spins. They are separated by a $\delta^{(-1,1)}$ defect. The initial spin-line has fragmented into bound states and single emitted spins. While in the simulations the bound states are immobile, they can propagate with a hoping rate $\sim J/\Delta^{(l-1)}$. Furthermore, some bound states can transform into other shapes or even emit further single spins. Lengthscales are not correctly reproduced in this schematic plot.

In the true Ising case $\Delta = \infty$, all bound states are true eigenstates. However, for $\Delta < \infty$, they are dressed by quantum fluctuations. The quantum fluctuations also lead to a propagation of the bound states with a hopping amplitude $\sim J/\Delta^{l-1}$. Therefore their kinetic energy is also of order $\sim J/\Delta^{l-1}$. Furthermore if there are degeneracies in the Ising energy, a bound state can transform into a different shape All theses effects are not covered by the semiclassical approach.

We consider the simplest example, a vertical bound state of two spins. Its Ising energy relative to the ferromagnetic background is $E_B = \Delta J(2+\alpha)$. The state with two single spins has a respective Ising energy of $E_S = \Delta J(1+2\alpha)$. The energy of the bound state is lower by $\Delta E = \Delta\, J\, \alpha$. By means of the methods introduced in section 3.1, we can derive an effective Hamiltonian in the subspace of the bound states. It is easy to see that, to leading order, the effective hopping amplitude in this subspace is given by $J_2 = \frac{(J/2)^2}{-\Delta\,\alpha\,J} = -J/(4\,\Delta\,\alpha)$. The bandwidth of the resulting bound state band is J/Δ. The timescale on which this state propagates is then given by Δ/J. Similarly, one finds that bound states of l spins propagate on a timescale Δ^{l-1}/J.

For larger line segments, and commensurate values of α, resonances with more compact shaped bound states can exist. Also the emission of further spins and bound-states is possible. For example, a line segment with $l = 13$ spins and $\alpha = 2$ can emit by compactification. Its Ising energy is, again relative to the ferromagnetic state, $E_{13} = \Delta J(13+\alpha) = 15\Delta J$. The Ising energy of a single emitted spin is $3\Delta J$. A bound state configuration consisting of a 3×3 spin square with a line of 3 spins attached vertically has 12 down spins and its energy is $12\Delta J$. The Ising energy and the number of spins of this object plus a single spin is exactly the same as for the line segment

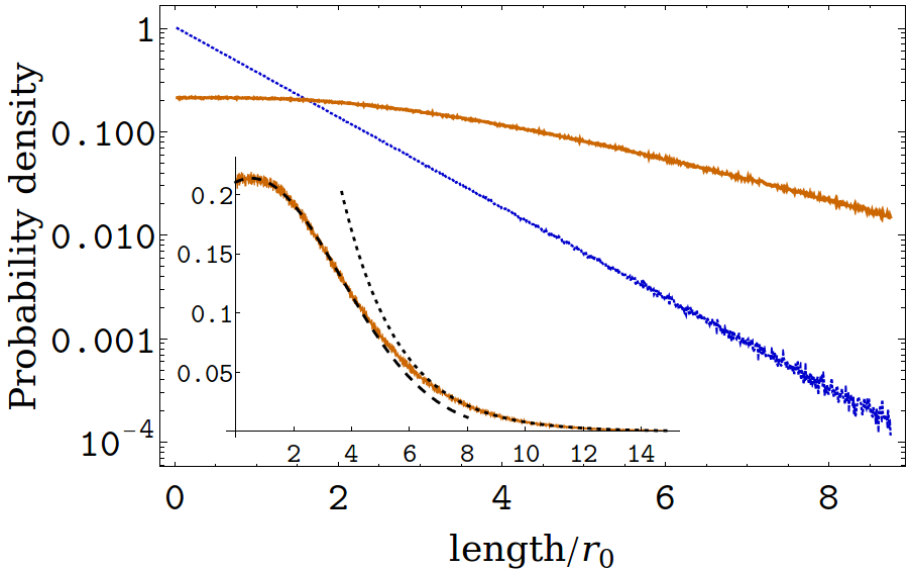

Figure 7.9: **Probability distribution of the bound states.** Shown is the probability to find a line segment of down-spins with the respective length. The dark blue line gives the result directly after the quench. Due to the Poisson statistics of the creation process, it is exponential with decay length $r_0 = 32\Delta^2$. The light orange line shows the results at the end of the simulation, when there are no mobile particles left. The final distribution is exponential only for large ($l \gtrsim 8r_0$) line segments (dotted line in the inset) and decays on the length scale $(1.98 \pm 0.02)r_0$. A broad maximum is located at $(0.51 \pm 0.05)r_0$. Including also the emitted single spins would lead to a huge peak at a length of one lattice site.

with $l = 13$. This means that this is only a quasi-bound state. After long times, it will decay into a bound states with 12 spins. However, to do so a rearrangement of 6 spins is needed and this complex process is highly suppressed on all reasonable timescales. For larger line segments more complex transformations with the emission of more single spins, or smaller bound states, are possible. They all happen on very large timescales, far beyond any experimental timescale.

In Fig. 7.9 we show the initial and the final distributions of the line segment bound states. The length is measured in units of $r_0 = 32\,\Delta^2$. The initial distribution is characterized by an exponential decay, reflecting the Poisson process underlying its creation. The final distribution is flat for $l \lesssim 10\,r_0$ and decays exponentially for $l \geq 10\,r_0$ on a length $(1.98 \pm 0.02)\,r_0$. A maximum is located at $l = (0.51 \pm 0.05)\,r_0$. The expectation value of the distribution is $3.04\,r_0$. These numbers contain information on the possible outcomes of a projective quantum measurement.

At the end of the simulation, also the defects have a characteristic distribution. However, propagation of bound states will further change this distribution. Furthermore, the defects can also propagate along the $1d$ line. $\delta^{(0,3)}$ and $\delta^{(\pm1,2)}$ defects are

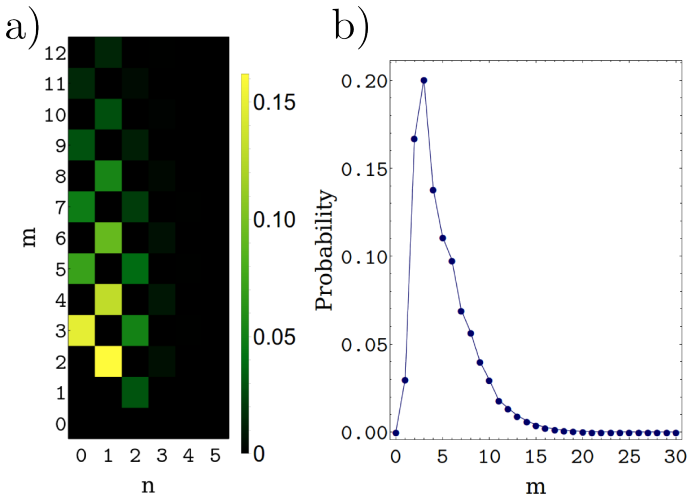

Figure 7.10: **Probability distribution of the immobile defects.** In panel a) we show the distribution $P_{\delta^{(n,m)}}$ of the immobile defects at the end of the simulation, when there are no mobile particles left. The probabilities shown in b) are summed over n. They show a maximum for $m = 3$.

the fastest with hopping rates $\sim J/\Delta^2$. Nevertheless we show the distribution in Fig. 7.10. Due to the possible scatterings only defects $\delta^{(n,m)}$ with $n + m$ odd are produced. Each emission and scattering changes $n + m$ by two. The holes can be denoted by $\delta^{(0,1)}$, while kinks and antikinks correspond to $\delta^{(1,0)}$ and $\delta^{(-1,0)}$, respectively. Therefore the distribution in panel a) shows a checkerboard pattern. When summed over n, the distribution of the bound state distance in y-direction is obtained. It has a maximum at $m = 3$ and an expectation value of $\bar{m} \approx 5$.

All results presented above are valid only in the Ising limit $\Delta \gg 1$. Their validity is restricted to timescales where the bound states are effectively immobile. In addition, $\delta^{(0,3)}$ and $\delta^{(\pm 1,2)}$ propagate with velocities $\sim J/\Delta^2$ and scatter with other defects at times $t \sim \tau_0 \Delta^2 \sim \Delta^4/J$. Furthermore the typical wavelength of the quasiparticles increases with $\sim \sqrt{t}$, as $1/\tau_k \sim k^2$, see Eq. (7.16). It becomes of the order of the mean distance $\rho^{-1} \sim \Delta^2$ when $t \sim \Delta^4/J$. To summarize, the approach is valid on timescales $1/J \ll t \ll \Delta^4/J$.

Although we studied the dynamics in a non-integrable model, the system does not thermalize in the thermodynamic limit. The reason is that the initial state has a finite (in the $x-$direction) region, the $1d$ line, with very high energy density. In the thermal state, the energy has to be distributed homogeneously throughout the whole system. However, it is clear from a light-cone picture, or Lieb-Robinson bounds [63], that there are always regions in space, namely $|x| \gg tJ$, where the energy density cannot have changed yet. In this sense the energy can never be homogeneously distributed and the system can never thermalize. This is different in a finite system where reflections at the boundaries take place. Here we expect that the system thermalizes.

8 Outlook I

A full quantum approach which can describe all regimes of thermalization in non-integrable systems including

(T1) Formation of quasiparticles, if existing

(T2) Prethermalization, if present

(T3) Local equilibration

(T4) Global thermalization

is still lacking. In (T1) one has to identify long-lived excitations which drive the dynamics. In the semiclassical limit considered by us, these were single-particle like excitations, quasiparticles, which were identified by perturbation theory. However if there is no large energy scale which protects single-particle like excitations from decaying, this is different. If a large number of approximately conserved constants of motion exist on short timescales, a prethermalization regime (T2) arises. This can, for example, be realized in a quantum quench setup when the initial state is the groundstate of an integrable model and a small integrability breaking perturbation is turned on [46]. Then scattering is very inefficient and it takes a long time until scattering effects become apparent. If stable quasiparticles exist, and they have a low density, their occupation numbers are conserved for times smaller than the scattering time. This can also lead to a quasi-stationary regime on timescales smaller than the scattering time. Local equilibration (T3) can approximately be described by Boltzmann equations. However we have seen in section 5.3 that, at least in one dimension, correlation effects set in very quickly. Here the Boltzmann equation can not describe the short-time dynamics quantitatively. It can also not capture the physics relevant for global thermalization (T4). Here correlations of conserved quantities are important. This generically leads to hydrodynamic long-time tails.

Numerical methods are constrained by the exponentially large Hilbert space in many-particle systems. Exact diagonalization is restricted to small particle numbers. Direct numerical integration of Kadanoff-Baym equations suffers equally from huge memory consumption and is restricted to small times [183]. Time-dependent density matrix renormalization group methods are not applicable at long times as they suffer from errors due to the Trotter decomposition and runaway times related to the truncation of the Hilbert space [184].

One way to include correlations in the Boltzmann equation is a fluctuating Boltzmann, or Boltzmann-Langevin, equation. Different approaches have been reported

in the literature, see for example [185–190]. Another way might be to include (the relevant) four-point functions (expectation values of four operators) into the theory. Quantum kinetic equations can be obtained by truncation schemes to the BBGKY-hierarchy of correlation functions [191]. This, in principle, also makes it possible to derive equations beyond conventional quantum kinetic (Boltzmann–like) equations. Equivalently, it is possible to use irreducible action methods, see for example [192, 193].

It will be interesting to investigate the effect of the divergent correlation length as seen in sections 4.5 and 6.2 in more detail. Thermalization processes within the KPZ universality class might be a further object of study. Quantum quenches from initial states with long-ranged correlations, provided that the decay is slow enough, are also expected to show a qualitatively different behavior.

The experimental techniques to measure higher-order correlation functions and full quantum distributions will develop further in the future. This can give access to genuine quantum effects, for example the entanglement entropy, which can not be measured by other means. Also here new theoretical methods beyond the semiclassical approach used by us will be needed to describe this measurements theoretically.

PART II

Coulomb disorder in three-dimensional topological insulators

9 Introduction II

The mathematical concept of topology has entered condensed matter physics in the last decade. Topology is the theory of continuous transformations – independent of geometry – and does not need the notion of "distance" and "angle". The prime example is the topological equivalence of a doughnut and a cup, since both have exactly one hole. An apple is different since it has no hole.

The band structure of non-interacting Hamiltonians can be classified using topological concepts. Depending on the dimensionality and the the symmetry class, topological phases can be supported or not [194]. Topological properties of band structures are characterized by discrete topological invariants.

Topological insulators. Many reviews on topological insulators (TIs) are available by now, for example [195, 196]. TIs are characterized by an insulating bulk and conducting surface states which are protected by topology. The topological protection can be removed by symmetry breaking. The topological invariant, an integer in suitable units, can be defined only in insulators. To change it, which is only possible in discrete steps, the band gap has to close. This is the analogue of drilling a hole into an apple to transform it into a doughnut (topologically). If the band structure changes its topology by changing a parameter in the Hamiltonian, the band gap has to close at the transition. If the band structure changes its topology due to a spatial boundary, the band gap has to close at the boundary. This implies the existence of gapless modes at the boundary – *edge states*. The implication "nontrivial bulk band topology" $\Rightarrow$ "gapless edge states" is called *bulk-boundary correspondence*. The inverse is not true.

It became evident that also the *quantum Hall effect* (QHE) can be viewed as a realization of a topological insulator. Shortly after the discovery of the QHE by von Klitzing *et. al.* in 1980 [197], it was realized that the quantization of the Hall conductance can be understood in terms of a topological invariant [198]. This today goes under the name of *TKNN invariant* (named after the authors of [198]: Thouless, Kohmoto, Nightingale and den Nijs) or Chern number (the mathematical concept behind this work). Due to the strong magnetic field in a quantum Hall system, the bands become flat and extensively degenerate and are called *Landau levels*. The topological invariant corresponds to the number of filled Landau levels and can take any integer value. In quantum Hall systems time-reversal symmetry is broken by the magnetic field.

The existence of topological insulators in the presence of time reversal symmetry has been predicted in 2005 by Kane and Mele [199, 200] for two-dimensional systems. Here the topological invariant can take only two values ($\mathbb{Z}_2$-*invariant*). This is known today as the *quantum spin Hall insulator*. The first experimental observation was reported in 2007 by König *et. al.* in HgTe quantum wells [201]. It was demonstrated that the longitudinal conductance is approximately $2e^2/h$ and, in small systems, independent of the system size. This is clear evidence that charge is transported only at the surface and agrees with the theoretical predictions [199, 202].

For three-dimensional topological insulators the first progress from the theory side was made in 2007 by Fu, Kane and Mele [203]. In $3d$ there is no analogue of the quantum Hall effect since here, in the absence of symmetries, only a topologically trivial band structure is supported [194, 204]. But the analogue of the quantum spin Hall insulator (with time reversal symmetry intact) exists, showing also a $\mathbb{Z}_2$-invariant [204]. This is called a *strong topological insulator* (in contrast to a weak topological insulator, which is a layered stack of $2d$ TIs).

The first proposals for the realization of $3d$ topological insulators included the $Bi_{1-x}\,Sb_x$ compounds [205, 206]. In this class of materials the first direct experimental observation (with $x \approx 0.1$) of topological surface states was made [207]. Using angle-resolved photoemission spectroscopy (ARPES), the existence of gapless and linear dispersing surface states was demonstrated. Here it is important to note that there is an odd number of crossings of the Fermi energy: the topological invariant can be calculated as $\nu = \text{number of crossings mod } 2 \in \{0, 1\}$, and $\nu = 0$ means topologically trivial. The authors of [207] also measured the resistivity. They found a value of $\rho(T \to 0) \approx 10^{-4}\,\Omega m$ at low temperatures and a value of $\rho(T \approx 300K) < 10^{-5}\,\Omega m$ at room temperature. Good insulators show resistivities $\rho_{\text{insulator}} > 10^{12}\,\Omega m$, while typical metals have $\rho_{\text{metal}} \approx 10^{-8}\,\Omega m$ (both at room temperature). In this spirit it is not really justified to call the material an insulator. Although the materials show a band gap of order eV the charge transport cannot be explained by the surface states alone.

Doping and compensation. When the $Bi_{1-x}\,Sb_x$ compounds are grown, the Fermi level is in the conduction band as can directly be seen in ARPES measurements [208]. Donors feed the excess electrons into the conduction band. A well-known technique to change the conductivity of semiconductors, having bandgaps of order eV, is doping. Here impurities with suitable chemical properties are introduced in the material on purpose. This has to be done at high temperatures during the growth process, when

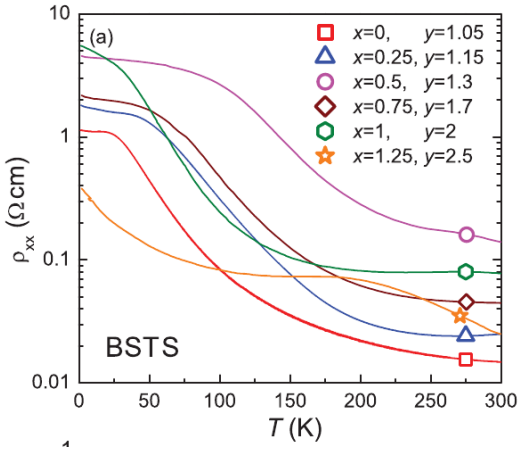

Figure 9.1: (taken from [210]) **The resistivity of different compositions $\mathbf{Bi}_{2-x}\mathbf{Sb}_x\mathbf{Te}_{3-y}\mathbf{Se}_y$.** In the high temperature regime $T \gtrsim 100\,K$ the resistivity shows an activated behavior $\rho_{xx} \sim \exp(E_A/T)$, where E_A denotes the activation energy ($k_B = 1$). At very low temperatures the resistivity saturates – in contrast to real insulators where it diverges. This shows that charge is transported through the sample.

the material crystallizes. Induced acceptors remove the excess electrons from the conduction band, which shifts the band structure relative to the Fermi level. This process is called *compensation* and implies a decreased density of free charge carriers. It was demonstrated that, by partially substituting Sb for Bi in $Bi_2\,Se_3$, the conductivity can be reduced significantly [209]. To further reduce the bulk conductivity Te and Se atoms were added, resulting in the $Bi_{2-x}\,Sb_x\,Te_{3-y}\,Se_y$ compounds (BSTS). Here Te antisite defects and Se vacancies compensate the free charges [210]. A systematic study of the temperature dependence of the BSTS resistivities can be found in [210], see also Fig. 9.1 taken from this publication. The resistivity is increased by a factor $10^2 - 10^3$ compared to the $Bi_{1-x}\,Sb_x$ compounds. The authors of [210] found that the resistivity was sample dependent and varied by a factor of 3 within the same composition.

Charged disorder. Since the dopants are introduced into the material at high temperatures ($T \sim 850$ K, [210]), they are located at random, uncorrelated positions. As the task of the acceptors to remove the excess electrons is fulfilled, as seen by the reduced conductivity, they carry an extra electron and thus are charged. Due to charge neutrality, the same amount of donors has to be positively charged. It is the influence of this randomly distributed localized charges which we will study in the following.

The theory also applies to conventional semiconductors and the topological nature of the materials will be mostly omitted in the theoretical analysis. Only later, we will include the effect of the metallic surface, which provides an additional screening channel. A comprehensive introduction to the theory of compensated semiconductors can be found in the book *Electronic Properties of Doped Semiconductors* by Efros and Shklovskii [211].

Our work. This theoretical work was initiated by an experiment, mainly performed by Nick Borgwardt in the group of Markus Grüninger. In the experiment the optical conductivity of $BiSbTeSe_2$ (BSTS2) was measured. The high-quality sample was fabricated in the group of Yoichi Ando. An unusual increase of the optical weight at low temperatures was found. We will first describe the experimental results and the model we have used.

In the following sections we will present our results. We have used an algorithm invented by Efros and Shklovskii [211] and we have extended this to finite temperatures by a standard Metropolis Monte Carlo method. First, we study the low temperature behavior. The focus will be on emergent lengthscales and the puddle formation. Here the term (electronic) puddles is used for spatially confined regions which have a finite density of electrons or holes. The existence of puddles was predicted in the 1970's by Efros and Shklovskii and others [211]. However, we will find that different lengthscales as suggested by simple scaling arguments govern the puddle formation in the simulated parameter range. Afterwards, the finite temperature results and their connection to the experiment are discussed. It will turn out that the experiment can be consistently explained by the low temperature formation and thermal destruction of puddles. To our knowledge, the experiment demonstrates the first direct observation of the optical response of these bulk puddles. Also their disappearance with increasing temperature has, to our knowledge, not been noticed before neither theoretically nor experimentally. Finally, we will include the effect of the conducting surface. We will only consider the limit of a large density of states on the surface. Here the same lengthscales (parametrically) as in the bulk are found. The experimental results and some of the theoretical results can be found in the publication [P3].

10 The experiment

Although the existence of electron and hole puddles in the bulk of compensated semiconductors has been predicted by Efros and Shklovskii more than 40 years ago [211], direct experimental evidence of this was still lacking until recently. Here we report on the, to our knowledge, first experiment which revealed the optical response of these bulk puddles. Nick Borgwardt Ignacio Vergara and Markus Grüninger performed the optical measurements presented below. Zhiwei Wang, Alexey Taskin, Kouji Segawa and Yoichi Ando grew the used high-quality single crystals and characterized them (actually only a single sample was used). Paul van Loosdrecht, Yoichi Ando and Markus Grüninger designed the experimental study. The experimental techniques will be discussed here only briefly since the focus in this thesis is on the theoretical analysis. For details we refer to the publication [P3]. All figures shown in this section are taken from there.

In graphene the existence of puddles was directly observed in real space by using a single-electron transistor (STE) [212] or scanning tunneling microscopy (STM) measurements [213]. In both experiments highly inhomogeneous carrier densities can be seen. This real space measurements are only possible as graphene is a two-dimensional material. It has turned out that the inclusion of puddles is necessary to understand the transport properties of graphene close to charge neutrality [214–216]. Puddle formation can occur by extrinsic means due to charged impurities in the substrate [214, 215] or intrinsically due to corrugations [217, 218]. In some regards the surface of a $3d$ TI is similar to graphene on a substrate. Puddles on the surface of thin samples ($\sim 10\,nm$) have been shown to influence the transport properties of the surface states [219, 220]. STM measurements on TI surfaces further revealed a highly inhomogeneous local density of states [221]. This is consistent with puddle formation in the bulk since this induces a spatially varying electrostatic potential on the surface. In [221] the correlation length of these energy fluctuations was estimated to $26\,nm$ and their typical size was $20 - 40\,meV$. The authors explained their results with charged bulk dopants but the focus was on the consequences for the surface states. However, surface measurements like STM are not ideally suited to study bulk puddles. In the experiment we will describe now, optical methods were used to directly access the bulk properties.

Optical properties of a solid are equally described by different response functions: optical conductivity $\sigma(\omega) = \sigma_1(\omega) + i\sigma_2(\omega)$, the dielectric function $\varepsilon(\omega) = \varepsilon_1(\omega) + i\varepsilon_2(\omega)$ and the refractive index $\tilde{n}(\omega) = n(\omega) + i\kappa(\omega)$. All three quantities are, in general,

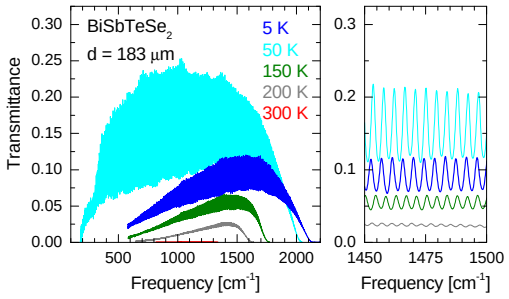

Figure 10.1: **Infrared Transmittance spectra of $BSTS_2$.** The Fabry-Perot interference fringes are caused by multiple reflections at the front and back surface. The interference pattern links refractive index and thickness of the sample. The transmittance is strongly temperature dependent and highest at intermediate temperatures $\sim 50\,K$.

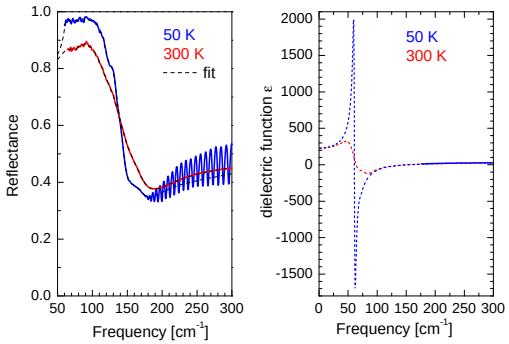

Figure 10.2: **Reflectance and dielectric function at low frequencies.** The dashed lines in the reflectance panel on the left are Drude-Lorentz fits. They do not account for the interference effects. The right panel shows the dielectric function at $50\,K$ and $300\,K$.

complex and carry the same information. They are related via

$$\varepsilon(\omega) = \varepsilon_0 + i\frac{\sigma(\omega)}{\omega}, \quad \tilde{n}(\omega) = \sqrt{\varepsilon(\omega)/\varepsilon_0}. \tag{10.1}$$

n, the real part of the refractive index, gives the renormalization of the speed of light $v = nc$. The imaginary part, κ, describes damping of the light, meaning that energy is absorbed by the solid. Accordingly, the real part of σ is also a measure for the absorption of energy. As solids have huge number of degrees of freedom there are many mechanisms which can absorb energy. In the optical data obtained from experiments, the sum of all optically active resonances is seen. Therefore it can be hard to disentangle the different contributions. To do so, models are needed which then serve as fit functions for the experimental data. The most well-known models are the Drude model, for free charge carriers, and the Lorentz model, for bound charges. Derivations of corresponding expressions for $\sigma(\omega)$ can be found in standard textbooks, see for example [222, 223].

For free charge carriers Drude theory predicts the optical conductivity

$$\sigma_{\text{Drude}}(\omega) = \frac{e^2\, n\, \tau/m^*}{1 + i\omega\tau} = \frac{\sigma_{\text{Drude}}(0)}{1 + i\omega\tau} \rightarrow \sigma_{1,\text{Drude}}(\omega) = \frac{\sigma_{\text{Drude}}(0)}{1 + \omega^2\tau^2} \tag{10.2}$$

where n is the carrier density, e denotes their charge and m^* their effective mass. τ is the scattering time. The scattering time and the carrier density can be temperature

dependent. Integrating the real part of the optical conductivity yields the *optical sum rule*:

$$\int_0^\infty d\omega\, \sigma_{1,\text{Drude}}(\omega) = \frac{\pi e^2}{2} \cdot \overbrace{\frac{N}{m^*}}^{\text{optical weight}} = \underbrace{N\frac{m_e}{m^*}}_{N_{\text{eff}}} \frac{\pi}{2} \frac{e^2}{m_e}. \tag{10.3}$$

This defines the *optical weight* and the effective charge carrier density N_{eff}. We will use both expressions almost synonymously as they are connected by a simple conversion factor, the electron mass m_e.

10.1 Optical properties of solids

Optical properties of a solid, as described above, can be measured by optical spectroscopy. Here monochromatic light field with intensity $\mathtt{I}(\omega)$ is used. When it hits the sample the light can be reflected, with intensity $\mathtt{R}(\omega)$; transmitted, with intensity $\mathtt{T}(\omega)$; absorbed, with intensity $\mathtt{A}(\omega)$; or scattered, with intensity $\mathtt{S}(\omega)$. Energy conservation dictates that $\mathtt{I}(\omega) = \mathtt{R}(\omega) + \mathtt{T}(\omega) + \mathtt{A}(\omega) + \mathtt{S}(\omega)$. The ratios $R(\omega) = \mathtt{R}(\omega)/\mathtt{I}(\omega)$ and $T(\omega) = \mathtt{T}(\omega)/\mathtt{I}(\omega)$ are known as reflectance and transmittance, respectively, and are measurable quantities. If the scattering part is negligible and R and T are measured, the absorption can be determined. From this the response functions can be obtained. In Fig. 10.1 we show experimental results of the transmittance in $BSTS_2$. The most noticeable feature, at first sight, is the strongly oscillating behavior. This is caused by multiple reflections at the front and back surface leading to a pronounced interference pattern. Also note that the transmittance is highest at intermediate temperatures $T \sim 50\,K$ implying that here the absorption is least. In Fig. 10.2 examples for reflectance in the low frequency range measurements are shown. In the right panel we can see that the dielectric constant is very large and that its static value is given by $\varepsilon(\omega \to 0) \approx 200$.

If the sample is thick, or highly absorbing, the transmittance can be effectively zero. Then, only the reflectance can be measured, but one can still obtain the response functions: there is a simple connection between the refractive index and the single-bounce reflectance (no reflections at back surface as ensured by thick sample) at normal incidence (light beam perpendicular to the surface). At an interface between vacuum (with $\tilde{n}_{\text{vac}} = 1$) and a solid with refractive index $\tilde{n}$ it is given by (derivation in appendix A of [224])

$$R(\omega) = \left|\frac{1-\tilde{n}(\omega)}{1+\tilde{n}(\omega)}\right|^2 = \frac{(n(\omega)-1)^2 + \kappa(\omega)^2}{(n(\omega)+1)^2 + \kappa(\omega)^2}. \tag{10.4}$$

Then the response functions can be obtained via a Kramers-Kronig analysis [222, 223]. The real and imaginary part of response functions are connected due to causality. If we apply an electric field $\boldsymbol{E}$ at $t = 0$ the current

$$\boldsymbol{j}(t) = \int_{-\infty}^{\infty} \frac{d\omega}{2\pi} \mathrm{e}^{i\omega t} \sigma(\omega) \boldsymbol{E}(\omega) = \int_{0}^{\infty} dt' \boldsymbol{E}(t') \int_{\infty}^{\infty} \frac{d\omega}{2\pi} \mathrm{e}^{i\omega(t-t')} \sigma(\omega) \tag{10.5}$$

has to be zero for $t < 0$. This implies constraints on $\sigma(\omega)$ – the Kramers-Kronig relations. For a Kramers-Kronig analysis the reflectance has to be known for all frequencies: one has to interpolate the experimental results in the high frequency range. In addition to the reflectance and transmittance measurements at lower frequencies ($\omega < 7500\mathrm{cm}^{-1}$) ellipsometry measurements were performed at higher frequencies ($6500 - 44.000\,\mathrm{cm}^{-1}$). Here and in the following frequencies are given in units of cm^{-1} and the conversion factor to electronvolt is $1\,eV \approx 8065\,\mathrm{cm}^{-1}$. In ellipsometry measurements polarized light is reflected at the sample. Ellipsometry measures the complex ratio of the light amplitude polarized parallel to the plane of incidence and the light amplitude polarized perpendicular to the plane of incidence. With a model analysis the optical response functions can be obtained.

10.2 Experimental results for the optical conductivity

The main quantity which was studied in the experiment is real part of the optical conductivity $\sigma(\omega) = \sigma_1(\omega) + i\sigma_2(\omega)$. In Fig. 10.3 results for σ_1 are shown at different temperatures. The most pronounced feature is the increase of σ_1 by almost two orders of magnitude at frequencies $1000 - 2000\,\mathrm{cm}^{-1}$ depending on the the temperature. This is a manifestation of the bandgap, which is strongly temperature dependent in this class of materials. If the photons have enough energy they can produce particle-hole excitations on a minimal energy cost of the bandgap $\Delta(T)$. At low temperatures $\sim 5\,K$ the sample shows a gap of $\Delta \approx 0.26\,eV$. This is the value we will use later when we compare the theoretical results to the experiment.

Below the gap the main contributions are of electronic and phononic origin. While the phonon and multi-phonon contributions show a narrow peak-like structure, the electronic contributions are expected to be Drude-like, see Eq. (10.2). In the derivation of the Drude formula it is assumed that the charge carriers can move through the whole system. Then the largest response is expected for $\omega \to 0$. Let us consider a different scenario. Suppose we have an insulator with a conducting region which does not extend through the whole sample. In DC transport measurements we will hardly see any response, since the carriers are confined to a finite region and no charge

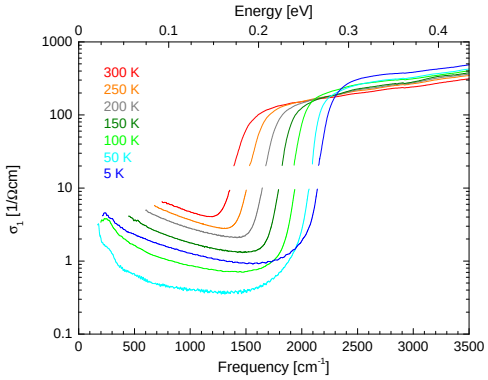

Figure 10.3: **Optical conductivity of BSTS2 on a logarithmic scale.** The drastic increase at $\omega \approx 1500 - 2000\,\mathrm{cm}^{-1}$ is a manifestation of the band gap, which is T dependent here. The lowest response is found at $\sim 50\,K$. At lower T, here only the $5\,K$ curve is shown, the response increases again. We will show later that this can be explained by the thermal destruction of puddles.

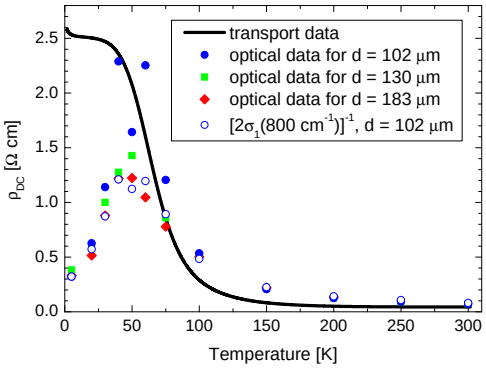

Figure 10.4: **DC resistivity from transport measurements and optical results.** The values from the optical data are interpolated to $\omega \to 0$. While the data at higher temperatures agree within a factor of 2, there is clear discrepancy at $T \lesssim 50\,K$. This is clear hint towards a small cutoff frequency, which is occurs naturally in the presence of puddles as explained in the main text.

can be transported through the sample. However, at higher frequencies the response should be of Drude type since the charges are oscillating in a finite region anyway. Upon lowering the frequency, the oscillation length will increase and at some point there will be a drastic reduction of the response. This is the case when the oscillation length exceeds the (linear) size L of the conducting region. The corresponding energy scale is called the *Thouless energy* ω_c. If the transport within the conducting region is diffusive, with diffusion constant D, the time which is needed to diffusive through is typically $\sim L^2/D$. Hence the maximal frequency at which one can expect a significant contribution is $\omega_c \sim D/L^2$. This scenario is exactly what is expected in the presence of puddles. Thus the experimental hallmark of puddles is a discrepancy in the DC conductivity from transport and optical measurements, given that $\sigma_{\mathrm{optical}}(\omega)$ is known only for $\omega > \omega_c$ and extrapolated to $\omega \to 0$. This is exactly what was found in the experiment. In Fig. 10.4 the DC resistivity is shown together with the optical data. At low temperatures, $T \lesssim 50\,K$, there is an obvious discrepancy. This is a clear signature of spatially confined conducting regions – puddles.

The diffusion constant can be expressed via the mobility μ as $D = \mu T/e$ (***Einstein relation***). μ was extracted from the transport measurements at $300\,K$ to $\mu \sim 62\,cm^2/(Vs)$ which yields $D \approx 2cm^2/s$. We further need the typical size of a pud-

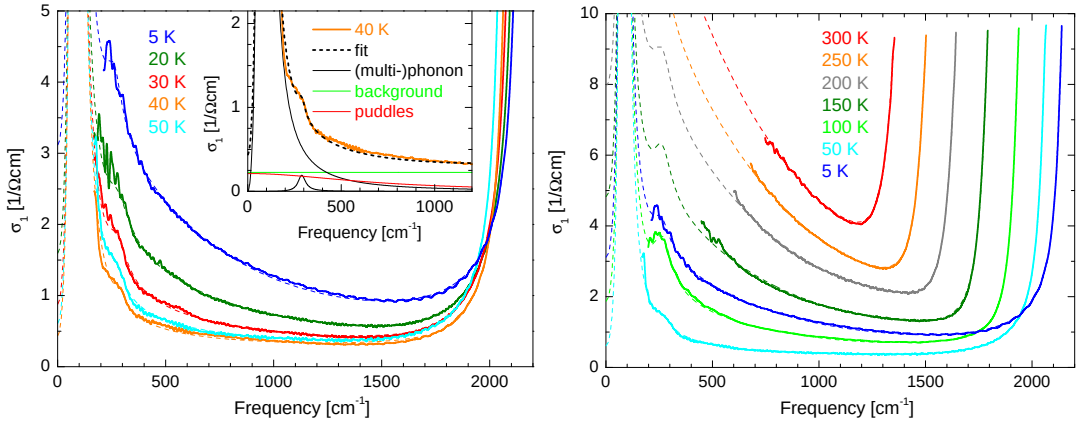

Figure 10.5: **The optical conductivity below the gap.** The left panel shows the results at low temperatures $T \leq 50\,K$. The lowest response is found at $40\,K$, which then gradually increases on lowering the temperature. The inset shows the different contributions for $40\,K$ as fitted by the experimentalists. The right panel shows the data already presented in Fig. 10.3 in more detail.

dle to estimate ω_c. We will see later in sections 12 and 13 that it is difficult to determine the puddles size L_{pudd} precisely. Nevertheless from the parameters given there, and the fact that puddle consists of many dopants separated by a distance $1-10\,nm$, we estimate $L_{\text{pudd}} > 100\,nm$. Then the Thouless energy in the sample is $\omega_c \sim D/L_{\text{pudd}} < 0.1\,\text{cm}^{-1}$, this is far below the smallest frequencies that could be resolved in the experiment, see Fig. 10.3.

In Fig. 10.5 the results for the optical conductivity below the gap are shown. As explained above, this is a sum of different contributions. To isolate the electronic contribution from the rest, a fitting procedure was performed by the experimentalists. In the inset of the left panel in Fig. 10.5 an example is shown. The electronic contribution was fitted with a Drude curve, Eq. (10.2), using the scattering time τ and the effective carrier density N_{eff} as fit parameters. The scattering time was found to be roughly temperature independent in the range $5-300\,K$ with the value $\tau \approx 7\times10^{-15}\,s$. Its inverse, the scattering rate, $1/\tau \approx 1.4\times10^{14}\,s^{-1}$ shows the smallest value observed so far in the BSTS family. Typical values of the scattering rate found before in similar compounds are $1-2$ order of magnitudes smaller [225–232].

10.3 Experimental results for the optical weight

The main result of the experimental study is the temperature dependence of the the optical weight. This is shown in Fig. 10.6 for different sample thicknesses. The striking feature, as could already be anticipated by the data shown in Fig. 10.5, is the

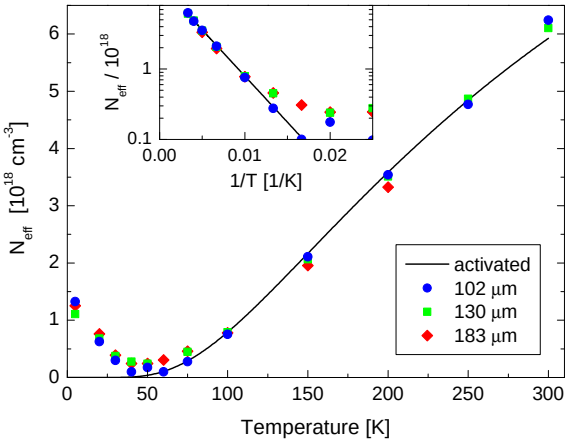

Figure 10.6: **Temperature dependence of N_{eff} for different sample thicknesses.** For temperatures $T \lesssim 50\,K$ the optical weight increases. At $T = 5\,K$, it is larger by a factor ~ 5 when compared to the value at $40\,K$. We attribute this increase to the formation of electron and hole puddles. The mechanism will be explained in details in the next sections. At higher temperatures the experimental results show an activated behavior. This can be seen in the Arrhenius plot ($\log(N_{\text{eff}})$ vs $1/T$) in the inset.

unusual increase at low temperatures $T \lesssim 40\,K$. At $T = 30\,K$ the effective density is $N_{\text{eff}}(30\,K) \approx 2 \times 10^{17}\,\text{cm}^{-3}$ and thus lowered by a factor ~ 5 compared to the value at $5\,K$, where $N_{\text{eff}}(5\,K) \approx 1.2 \times 10^{18}\,\text{cm}^{-3}$. The non-monotonic behavior is in contrast to a simple metal where a saturation occurs at low temperatures and the conductivity is decreased at higher temperatures due to the excitation of phonons. The result is also in contrast to lightly doped semiconductors where the density freezes out at low temperatures. In the experimental results the temperature dependence shows a qualitatively different behavior. The theoretical analysis will reveal that this can be explained by puddle formation at low temperatures $T \lesssim \text{E}_\text{c}$ and their thermal destruction at $T \sim \text{E}_\text{c}$. One important result will be the identification of the energy scale E_c as the typical Coulomb energy between neighboring impurities.

A non-monotonic, but much less pronounced, temperature dependence of N_{eff} has also been found in related materials [225, 231–233]. In these experiments the reduction of N_{eff} at intermediate temperatures was at most by a factor of 2. The authors of [231] speculate about the significance of charge inhomogeneities without giving any theoretical support.

The optical result has to be compared to the transport results in Fig. 10.4. Here the temperature dependence is monotonic. This is clear evidence that the increase of the optical weight at low temperatures has to be attributed to localized charges – puddles. At higher temperatures the optical weight shows an activated behavior $\sim \text{e}^{-E_A/T}$ as can be seen in the Arrhenius plot in the inset. The fitted activation energy is $E_A = 26\,meV$ which is much smaller than the bandgap $\Delta \sim 0.26\,eV = 260\,meV$. A reduced activation energy has also been found in similar systems before, see for example [210]. Skinner *et. al.* suggested the existence of a percolation threshold for hopping conductivity at 0.15Δ [234, 235].

10.4 Contribution of the surface states

What remains to be clarified is the role of the surface states. As we are dealing with a topological insulator, we expect that charge is transported at the surface and that this contributes to σ as measured. To check this the experiment has been performed on three different sample thicknesses – but using the same sample which was cut into thinner pieces. All three results are shown in Fig. 10.6. They agree within the experimental uncertainty. In Fig. 10.7 we show the optical conductivity for all three thicknesses at different temperatures. All results agree within a few percent while the thickness is reduced by almost a factor of 2. If there would be a significant contribution from the surface there would be a much larger influence of the thickness. Although this is intuitively comprehensible, one has to note that the unit of the conductivity depends on the spatial dimension. This is in contrast to the conductance which has (in SI) the unit $1/\Omega$ in all dimensions. But the conductance and its inverse, the resistance, in general dependent on the sample size and therefore are not a useful comparative measure. On the other hand, the conductivity is a material property. For example for a sample of thickness t, if there was no response from the bulk and a $2d$ response of x/Ω, the $3d$ response would be $x/(t\,\Omega) \sim 1/t$.

In principle there are two contributions to the optical conductivity from a Dirac cone on the surface. The first is Drude-like due to a finite density of charge carriers. Let us try to estimate its value. A Dirac cone is characterized by a single parameter: the effective speed of light v_F. For the class of materials at hand it can be deduced from the ARPES measurements in [236]: from Fig. 2 f) in [236] we read off that $E(0.1\text{Å}^{-1}) \approx 0.25\,eV$ and thus $v_F \approx 0.25\,eV/(0.1\text{Å}^{-1}\,\hbar) \sim 4 \times 10^5\,m/s$. The mobility of the surface states was determined in [237] from Hall measurements to $\mu = 1450 cm^2/(Vs)$. Using the Einstein relation for the diffusion constant, $D = \mu T/e$, we find the scatting rate $1/\tau_{\text{surf}} \sim v_F^2/D = ev_F^2/(\mu T) \approx 16 \times 10^{10}(m/s)^2/(1450 cm^2)eV/T \approx \frac{10^{12}}{T[eV]} s^{-1}$. For $T = 50\,K \approx 0.0043\,eV$ this yields $1/\tau_{\text{surf}} \approx 2.3 \times 10^{14} s^{-1}$, very close to the scattering rate found for the bulk. However, for typical surface densities $n_{\text{surf}} \sim 10^{12}\text{cm}^{-2}$ and a thickness of $100\,\mu m$ we find a $3d$ density of $\sim 10^{12}\text{cm}^{-2}/(100\,\mu m) = 10^{14}\text{cm}^{-3}$. This is much too low to have a significant influence since the bulk densities are higher by more than 2 orders of magnitude. There is another contribution to the optical response from the surface due to interband excitations. For the Fermi level very close to the Dirac point this was predicted to be independent of the frequency and of order e^2/h [238, 239]. For a sample thickness of $100\,\mu m$ this would result in a $3d$ conductivity of $\sim 0.004\ (\Omega cm)^{-1}$ again more than two orders of magnitude be-

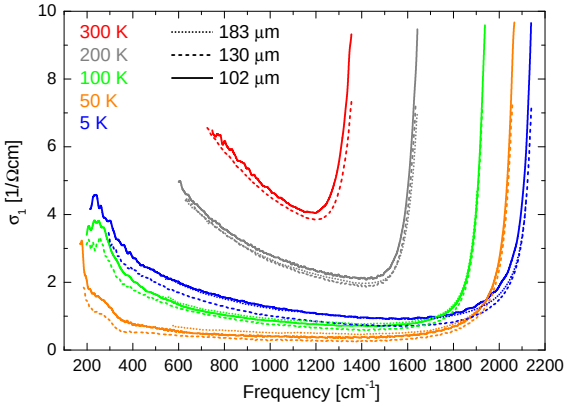

Figure 10.7: **The optical conductivity for different sample thicknesses.** All results agree within a few percent although the thickness was reduced by almost a factor of 2. If the surface states would have a significant influence a more drastic effect would be seen.

low the values observed in the experiment. From this analysis we conclude that the surface states cannot have a significant influence. In [237] a similar system was analyzed and the authors estimated the surface contribution to the total conductance to 6 % for a sample thickness of $\approx 260\,\mu m$.

11 Theoretical description of compensated semiconductors

A characteristic property of a solid state system is how it responds to an applied electric field. This is quantified by the conductivity σ. Often this is even used to divide solids into two classes: insulators and conductors (or metals). Semiconductors are located between the two ends of the spectrum. Typically they show a band gap which is of order of a few eV. An experimental way to change the electronic properties of semiconductors is the artificial insertion of specific impurities, doping.

The first TI-materials were n-doped semiconductors. See, for example, [208] for ARPES measurements on Bi_2 Se_3 and Bi_2 Te_3. In these materials there are free electrons which make it conducting. Thus many bulk properties of those materials, excluding everything related to the topological nature, can be explained by theories designed for semiconductors. To reach a bulk-insulating behavior acceptors are introduced into the material during the growth process [210]. This removes excess electrons from the conduction band. With higher degree of compensation $K = N_A/N_D$, where N_A and N_D are the densities of acceptors and donors respectively, the Fermi level shifts below the conduction band. At perfect compensation, $K = 1$, the Fermi energy is exactly in the middle of the band gap Δ. Here the best insulating behavior is reached. But after the compensation procedure the dopants are charged (actually not all of them as we will see later). It is the effect of these localized charges which we want to investigate in the following. The goal of this section is to motivate the model which is able to describe the experimental results.

11.1 Doped semiconductors

Let us consider a single impurity, say a donor, in a semiconductor with a band gap Δ and dielectric constant ε. We use the effective mass theory by Luttinger and Kohn [211, 240, 241] to estimate the energies of the impurity states. In the simplest case the conduction band has a single minimum at $\boldsymbol{k} = 0$ and can be described by a quadratic dispersion $\mathrm{E}_{\mathrm{band}}(\boldsymbol{k}) = k^2/(2m^*)$ where m^* is the effective mass. This serves as a continuum for the electrons. If we assume that the extent of the electron wavefunction bound to the impurity center is much larger than the lattice constant (to be justified below), we can omit the details of the impurity center and treat it like a positive point charge. In this approximation, the problem is equivalent to that of a Hydrogen atom and can be solved by elementary means. The ionization energy of the impurity is then the modified Rydberg energy which corresponds to the groundstate

energy of the Hydrogen atom:

$$\mathrm{E_{SC}} = \frac{m^* e^4}{2\,(4\pi\varepsilon_0\varepsilon)^2\,\hbar^2} = \frac{m^*}{m_e}\,\frac{1}{\varepsilon^2}\,\mathrm{E_{Ryd}} \approx \frac{m^*}{m_e}\,\frac{1}{\varepsilon^2} 13.6\,eV. \tag{11.1}$$

Accordingly the size of the wavefunction (the extent of the impurity state) is then given by the (modified) Bohr radius

$$a_{\mathrm{SC}} = \frac{4\pi\varepsilon_0\varepsilon\hbar^2}{m^* e^2} = \varepsilon\,\frac{m_e}{m^*}\,a_{\mathrm{B}} \approx \varepsilon\,\frac{m_e}{m^*}\,5.3\times10^{-11}\,m. \tag{11.2}$$

This effective Bohr radius of the impurities we will simply call Bohr radius in the following and it will be denoted by a_{B}. We have seen in Fig. 10.2 that the dielectric constant of the materials under consideration is very large: $\varepsilon(\omega \to 0) \approx 200$. The effective mass is not known precisely but is about $m^* \approx 0.14 - 0.24\,m_e$ in $Bi_2\,Se_3$ [242]. We will use $m^* = 0.2\,m_e$ in the following. Inserting these numbers into Eq. (11.1) and Eq. (11.2) leads to $\mathrm{E_{SC}} \approx 7\times10^{-5}\,eV$ and $a_{\mathrm{SC}} \approx 5\times10^{-8}\,m$. For the material used in the experiment, Bi Sb Te Se_2, the gap is $\Delta \approx 0.26\,eV$ at low temperatures $T \lesssim 50\,K$, see Fig. 10.5. Therefore the binding energy of the impurities is much smaller than the gap: $\mathrm{E_{SC}} \ll \Delta$. This type of impurities, located very close to the band edge, are called *shallow*. Since $\mathrm{E_{SC}} \ll \Delta$ the energy of the shallow impurity states can be approximated by $+\Delta/2$ for the donors and $-\Delta/2$ for the acceptors. Here and in the following the energy is measured with respect to the middle of the band gap. Full compensation then corresponds to $\mu = 0$. Note that the details of the impurity do not matter at all and therefore the result is universal. Furthermore a_{B} is much larger than the lattice constant of the BSTS compounds which is of order $4\,$Å [210].

In a real system there are many impurities and we will denote the total density by $N_{\mathrm{tot}} = N_A + N_D$. Two cases have to be distinguished [211]:
1) lightly doped semiconductors, where the overlap of the impurity states is small ($N_{\mathrm{tot}} a_{\mathrm{B}}^3 \ll 1$) and 2) heavily doped semiconductors, where the overlap of the impurity states is large ($N_{\mathrm{tot}} a_{\mathrm{B}}^3 \gg 1$).
In the experiment the impurity density is not known precisely but there is evidence that it is at least $10^{18}\mathrm{cm}^{-3}$ [210]. Then it is $N_{\mathrm{tot}} a_{\mathrm{B}}^3 > 10^{18}\mathrm{cm}^{-3}\,(5\times10^{-8}\,m)^3 \sim 100 \gg 1$. Hence we are dealing with a heavily doped semiconductor.

In materials where the dielectric constant is smaller (than the very large $\varepsilon \approx 200$) the dopants typically form an *impurity band*. The effective Rydberg energy $13.6\,eV/\varepsilon^2$ is larger and the impurity states do not merge with the conduction or valence band. This type of impurities located "far away" from the band edges are called *deep*. An

impurity band is not a band in the usual sense, in contrast to a regular Bravais lattice the impurity atoms are located at random positions and thus Bloch's theorem is not applicable.

At high compensation, $1 - K = 1 - N_A/N_D \ll 1$, the Fermi level is located close to the middle of the band gap. When the Fermi level shifts below the band edge of the conduction band the charge transport properties change from metallic to activated and the conductivity is $\sigma \sim \mathrm{e}^{-E_A/T}$. Charge carriers have to be thermally activated into the conduction band to contribute to the transport. In heavily doped systems, it was found experimentally that the the activation energy can be significantly lower than the band gap Δ [210]. It was suggested that this is due to the existence of a percolation level for hopping conductivity [234]. Here the charge is not transported by free carriers but rather by hopping of charges on localized orbitals (variable range hopping). This can also change the temperature dependence of the conductivity to $\sigma \sim \mathrm{e}^{-(E_A/T)^x}$ with $x < 1$ [210, 234, 243, 244].

In the following we focus on heavily doped and highly compensated semiconductors as this is the regime of the experiment. We assume that the Bohr radii of acceptors and donors are equal ($= a_\mathrm{B}$). We will denote the density of excess dopants, donors, by N. At $K = 1$ it is $N_A = N_D = N$. We further define the typical interaction energy between neighboring dopants as

$$\mathrm{E_c} = \frac{e^2}{4\pi\varepsilon\varepsilon_0 N^{-1/3}}. \tag{11.3}$$

As aforementioned the dopants are introduced in the material at high temperatures and are located at random positions. When all dopants are charged the electric potential shows large fluctuations [211, 234]. Here the charges are uncorrelated, up to a trivial correlation due to charge neutrality. We will call this the uncorrelated state. In a volume $V \sim R^3$ the typical charge is $Q_R \sim \sqrt{R^3}\, e$. Then the typical potential felt by a charged test particle located in this volume is $\phi_\mathrm{typ}(R) \sim Q_R/R \sim \sqrt{R}$. This means that the potential can increase without bound on larger lengthscales. The potential fluctuations must be suppressed. There are different mechanisms which come to mind.

The first is screening by band states. In the local density approximation the local Fermi level is given by $\mu + e\phi(\boldsymbol{r})$ where $\phi(\boldsymbol{r})$ denotes the electrical potential due to the dopants. This can be locally above the conduction band edge (or below the valence band edge). This leads to regions of finite densities which are able to screen the local fluctuations. As we will show below, in heavily doped semiconductors these densities

are much too low to have a significant influence. Close to the surface there is an additional screening channel from the topological surface states. We will study its influence in section 14.

The next mechanism is screening by excess carriers due to imperfect compensation. The density of the excess electrons is given by $n = N_D - N_A = (1-K)N$. Efros and Shklovskii proposed the following argument [211]. The typical charge density under the conditions described above is $\Delta N(R) \sim e\sqrt{N_{\text{tot}}R^3}/R^3 = e\sqrt{N_{\text{tot}}}/R^{3/2}$ where $N_{\text{tot}} = N_A + N_D = (1+K)N$. This has to be compared to the the density of the excess electrons n. As long as $\Delta N(R) \lesssim n$ the potential fluctuations can be screened by the excess electrons. One can define a length scale r_n by $\Delta N(r_n) \stackrel{!}{=} n$ which gives

$$r_n = N_{\text{tot}}^{1/3}/n^{2/3} = (N_D+N_A)^{1/3}/(N_D-N_A)^{2/3} = \frac{(1+K)^{1/3}}{(1-K)^{2/3}}\, N^{-1/3}. \tag{11.4}$$

This means that potential fluctuations larger than

$$e\phi = N^{-1/3}\sqrt{N_{\text{tot}}r_n}\,\mathrm{E_c} = \frac{(1+K)^{2/3}}{(1-K)^{1/3}}\,\mathrm{E_c} \tag{11.5}$$

can be screened by excess dopants.

But what happens in the limit of full compensation $n \to 0$ (or $K \to 1$)? Here the potential fluctuations can be suppressed by discharging – pairwise neutralization – of dopants. An electron can be transferred from a charged acceptor to a charged donor at an energy cost of the band gap Δ. If the potential fluctuation reaches the energy of the bare impurity states, $\phi = \pm\Delta/(2e)$, at the position of a dopant it can be energetically favorable to discharge (neutralize) this dopant. In regions with very large potential fluctuations this changes the potential landscape in the vicinity significantly. Hence this screening mechanism is a highly non-linear process. This leads to a clustering of neutral dopants and these clusters will be identified with electron and hole puddles.

For $K \to 1$, $\mathrm{E_c}$ is the maximal energy up to which the potential can extend into the bands. If, for example, $e\phi(\boldsymbol{r}) \gg \Delta/2 + \mathrm{E_c}$ the potential fluctuation can be (and will be) suppressed by discharging donors in that region. This is energetically favorable as long as $e\phi \gtrsim \Delta/2 + \mathrm{E_c}$. Upon discharging an additional donor the potential would drop below $\Delta/2$ and the energy gain cannot be larger than Δ anymore. Thus the local Fermi level can be at most $\Delta/2 + \mathrm{E_c}$ and has to be at least $-\Delta/2 - \mathrm{E_c}$.

Let us estimate the corresponding density of band charge carriers for a spherical band with effective mass m^*, say in the conduction band. At very low temperatures

in a volume where the local Fermi level is $\Delta/2 + \mathrm{E_c}$ the electron density is given by

$$n_{\text{band}} \approx 2 \int \frac{d^3\boldsymbol{k}}{(2\pi)^3}\, \Theta\left(\mathrm{E_c} - \frac{\hbar^2 k^2}{2m^*}\right) = \frac{2 * 4\pi}{(2\pi)^3} \int_0^\infty dk\; k^2 \Theta\left(\frac{\sqrt{2m^* \mathrm{E_c}}}{\hbar} - k\right)$$
$$= \frac{1}{3\pi^2} \frac{(2m^* \mathrm{E_c})^{3/2}}{\hbar^3} = \frac{1}{3\pi^2\hbar^3} \left(\frac{2m^* e^2}{4\pi\varepsilon\varepsilon_0}\right)^{3/2} N^{1/2}. \tag{11.6}$$

For the parameters estimated for the experiment ($\varepsilon = 200$, $m^* = 0.2\, m_e$, $N = 10^{18}$ cm^{-3}) we find $n_{\text{band}} \approx 8 \times 10^{15}$ cm^{-3}. For $N = 10^{19}$ cm^{-3} we find $n_{\text{band}} \approx 3 \times 10^{16}$ cm^{-3}. In either case $n_{\text{band}} \ll N_{\text{tot}}$. After this analysis we conclude that charge carriers from the bands cannot play a significant role if $\Delta \gg \mathrm{E_c}$. Using the same parameters as above, and $\Delta = 0.26\, eV$, we find that in the experimental system it is $\Delta/\mathrm{E_c} \sim 75 - 100$. Therefore the bands will not be considered in the analysis presented below which simplifies the model considerably.

11.2 The model

As we have seen above, see Eq. (11.1), the acceptor and donor states have bare energies of approximately $-\Delta/2$ and $+\Delta/2$, respectively. They are immobile and located at random, uncorrelated positions. If they are charged, they interact via long-ranged Coulomb interactions $V(r)$. For convenience we introduce a variable f_i for the i-th dopant at position $\boldsymbol{r}_i$ which distinguishes acceptors ($f_i = -1$) and donors ($f_i = +1$). For a specific realization of the dopant positions (say $\boldsymbol{r}_1, \boldsymbol{r}_2, \dots$), the Hamiltonian reads [234]

$$H = \frac{\Delta}{2} \sum_i f_i n_i + \frac{1}{2} \sum_{i \neq j} V_{ij}\; q_i q_j. \tag{11.7}$$

q_i denotes the charge in units of the elementary charge of the dopant at position $\boldsymbol{r}_i$. It can be either 0 or -1 for acceptors and either 0 or $+1$ for donors. The occupation n_i of the i-th dopant is related to its charge q_i by

$$q_i = \frac{f_i + 1}{2} - n_i. \tag{11.8}$$

To our knowledge the model presented above has been studied for the first time in 2000 by Basylko *et. al.* [245]. It is valid for $\Delta \gg \mathrm{E_c}$ (otherwise one has to include the band states) and $\varepsilon \gg 1$ to ensure that the dopants are shallow. A schematic plot of the model is shown in Fig. 11.1.

The Coulomb interaction V_{ij} between the dopants at $\boldsymbol{r}_i$ and $\boldsymbol{r}_j$ needs some extra attention. If the dopants are far apart, $r_{ij} = |\boldsymbol{r}_i - \boldsymbol{r}_j| \gg N^{-1/3}$, it shows the usual

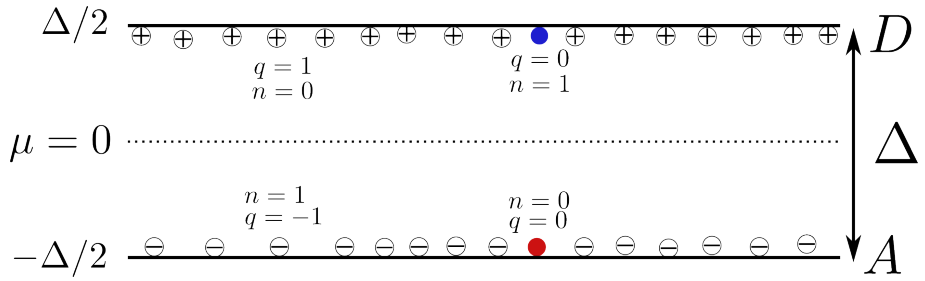

Figure 11.1: **Schematic plot of the model.** For perfect compensation, $K = 1$, the Fermi level μ is located exactly in the middle of the band gap Δ which we choose as our reference energy such that $\mu = 0$. The bare energies of the randomly placed shallow acceptor (A) and donor (D) states are at $-\Delta/2$ and $\Delta/2$, respectively. Each dopant can be either charged or neutral, the charge is indicated by $\pm q$. Occupied acceptors are negatively charged, while empty donors are positively charged. Charged dopants interact via long-ranged Coulomb interactions.

$1/r$ dependence. But if the dopants are close-by, $r_{ij} \lesssim N^{-1/3}$, quantum mechanical effects may play a role. The dopant wavefunction has a finite extent, the effective Bohr radius a_B. We have seen above that this can become quite large, of order $10\,nm$, thereby exceeding $N^{-1/3}$. Skinner *et. al.* [234, 235] suggested to incorporate these quantum effects by a short distance cutoff of the order of the Bohr radius:

$$V_{ij} = \frac{e^2}{4\pi\varepsilon\varepsilon_0\sqrt{|\boldsymbol{r}_i - \boldsymbol{r}_j|^2 + a_\mathrm{B}^2}} \tag{11.9}$$

We will use this approximation in the following to account for the finite extent of the wavefunctions. Furthermore this cutoff removes high energies as the maximal energy of two close-by dopants now is $\sim 1/a_\mathrm{B}$.

For the theoretical analysis it is convenient to rewrite the Hamiltonian, Eq. (11.7), in dimensionless units. To do so we divide Eq. (11.7) by $\mathrm{E_c}$ to obtain

$$\begin{aligned}\frac{H}{\mathrm{E_c}} &= \frac{\Delta}{2\mathrm{E_c}}\sum_i f_i n_i + \frac{1}{2\mathrm{E_c}}\sum_{i\neq j}\frac{e^2}{4\pi\varepsilon\varepsilon_0\sqrt{|\boldsymbol{r}_i - \boldsymbol{r}_j|^2 + a_\mathrm{B}^2}}\,q_i q_j \\ &= \frac{\overline{\Delta}}{2}\sum_i f_i n_i + \frac{1}{2}\sum_{i\neq j}\frac{1}{\sqrt{|\overline{\boldsymbol{r}}_i - \overline{\boldsymbol{r}}_j|^2 + \overline{a_\mathrm{B}}^2}}\,q_i q_j\end{aligned} \tag{11.10}$$

where the quantities with a bar on top are now dimensionless. Energy is measured in units of $\mathrm{E_c}$ and lengths are measured in units of $N^{-1/3}$: $\overline{\Delta} = \Delta/\mathrm{E_c}, \overline{\boldsymbol{r}} = \boldsymbol{r}\,N^{-1/3}, \overline{a_\mathrm{B}} = a_\mathrm{B}\,N^{-1/3}$. In the following we omit the bar, all theoretical results will be presented in dimensionless units. Later we will restore the units for a comparison with the experimental results.

Note that the model is static and does not show any dynamics. In this regard it is similar to a two-species, disordered Ising model with long-ranged interactions. To understand the experimental results in more detail on a microscopic level, one would need a dynamic model which takes into account the response to an applied field and the frequency dependence of the dielectric constant. Nevertheless, the model contains the mechanism which is responsible for the unusual increase of the optical weight at low temperatures as shown in Fig. 10.6.

At zero temperature we are seeking for the groundstate of the model Eq. (11.10). For a simulation with M dopants, there are $\binom{M}{M/2} \sim 2^M/\sqrt{M}$ different configurations. In principle one has to check all these exponentially many possibilities to find the true groundstate. However, there is a trick to find an approximate groundstate – called a *pseudo-groundstate* – in polynomial time invented by Efros and Shklovskii [211, 234]. Let us assume that the system is its lowest energy configuration. We can calculate the energy difference to a state where the occupation of two dopants is swapped. We denote occupations and charges in the groundstate by $\bar{n}$ and $\bar{q}$ respectively. Let us further assume that a dopant at $\boldsymbol{r}_\alpha$ is occupied ($\bar{n}_\alpha = 1$ and $\bar{q}_\alpha = (f_\alpha - 1)/2$) in the groundstate while another dopant at $\boldsymbol{r}_\beta$ is empty ($\bar{n}_\beta = 0$ and $\bar{q}_\beta = (f_\beta + 1)/2$). For two dopants which are both either empty or occupied, the occupation cannot be swapped. The change of the occupation of a single dopant would violate the charge neutrality. A basic excitation is then given by a transition into a state with $n_\alpha = 0$ and $n_\beta = 1$. The corresponding energy difference can be calculated to be

$$
\begin{aligned}
&\Delta E_{(\alpha,\beta)} = E_{\text{exciatation at } (\alpha,\beta)} - E_{\text{groundstate}} \\
&= \frac{\Delta}{2} \sum_{i \neq \alpha,\beta} f_i \bar{n}_i + \frac{\Delta}{2} \left(f_\alpha (1 - \bar{n}_\alpha) + f_\beta (1 - \bar{n}_\beta) \right) + \frac{1}{2} \sum_{i \neq j; i,j \neq \alpha,\beta} V_{ij}\ \bar{q}_i \bar{q}_j + \sum_{i \neq \alpha,\beta} V_{i\alpha}\ \frac{f_\alpha + 1}{2} \bar{q}_i \\
&+ \sum_{i \neq \alpha,\beta} V_{i\beta}\ \frac{f_\beta - 1}{2} \bar{q}_i + V_{\alpha\beta} \left(\frac{f_\alpha + 1}{2} \right) \left(\frac{f_\beta - 1}{2} \right) - \left(\frac{\Delta}{2} \sum_i f_i \bar{n}_i + \frac{1}{2} \sum_{i \neq j} V_{ij}\ \bar{q}_i \bar{q}_j \right) \\
&= \frac{\Delta}{2} \left(f_\beta - f_\alpha \right) + \sum_{i \neq \alpha,\beta} V_{i\alpha}\ \bar{q}_i - \sum_{i \neq \alpha,\beta} V_{i\beta}\ \bar{q}_i + \frac{V_{\alpha\beta}}{2} \left(f_\beta - f_\alpha \right) \\
&= \frac{\Delta}{2} \left(f_\beta - f_\alpha \right) + \sum_{i \neq \alpha} V_{i\alpha}\ \bar{q}_i - \sum_{i \neq \beta} V_{i\beta}\ \bar{q}_i - V_{\alpha\beta} = \frac{\Delta}{2} \left(f_\beta - f_\alpha \right) + \phi_\alpha - \phi_\beta - V_{\alpha\beta}
\end{aligned}
\tag{11.11}
$$

where we have defined the potential at the position $\boldsymbol{r}_j$ as $\phi_j = \sum_{i \neq j} V_{ij}\ q_i$. It is convenient to introduce the single-electron energies as

$$
\epsilon_j = \frac{\Delta}{2} f_j - \phi_j = \frac{\Delta}{2} f_j - \sum_{i \neq j} V_{ij}\ q_i. \tag{11.12}
$$

The meaning of ϵ_j can be understood by realizing that $\epsilon_j = \frac{\delta H(\{n_1,n_2,\dots\})}{\delta n_j}$: it is the energy change due to adding or removing a single particle. At $T = 0$ all states with $\epsilon_j < \mu$ are filled ($n_j = 1$) while all states with $\epsilon_j > \mu$ are empty ($n_j = 0$). Then we know from Eq. (11.11) that in the groundstate the inequality

$$\Delta E_{(\alpha,\beta)} = \epsilon_\beta - \epsilon_\alpha - V_{\alpha\beta} > 0, \text{ for } n_\beta = 0 \text{ and } n_\alpha = 1 \tag{11.13}$$

has to be fulfilled. This is known as the Efros-Shklovskii stability criterion. A pseudo-groundstate is defined by the property that Eq. (11.13) is satisfied for all proper pairs (α, β). But this does not determine the state uniquely. There can be many of these pseudo-groundstates which are very close in energy. In principle the energy can still be lowered by the exchange of two pairs while both intermediate states (reached by only swapping one of the pairs) have a higher energy. This also applies to the exchange of $m > 2$ pairs.

The existence of many almost degenerate minima is the hallmark of a glass [246]. This is why models similar to that presented above are called Coulomb glass or electron glass [247]. The most-studied Coulomb glass model, for example in the book by Efros and Shklovskii [211], is the following lattice model (on a regular lattice):

$$H = \sum_i \Phi_i n_i + \frac{1}{2} \sum_{i \neq j} \frac{n_i \, n_j}{|\boldsymbol{r}_i - \boldsymbol{r}_j|}. \tag{11.14}$$

The disorder is implemented by a random on-site potential Φ_i chosen from a box distribution and $n_i \in \{0, 1\}$ denotes the occupation of lattice site i. This is equivalent to a random-field Ising model with long-ranged, antiferromagnetic interactions. Other related models are the Ising spin glass models where the randomness is implemented by random couplings J_{ij}. For example, the Edwards-Anderson Hamiltonian of an Ising spin glass reads [248]

$$H = -\sum_{\langle i,j \rangle} J_{ij} \, S_i \, S_j \tag{11.15}$$

where $S_i \in \{-1, 1\}$ denotes the spin at lattice site i and $\langle i, j \rangle$ means nearest neighbor interactions only. It is known that finding the groundstate of the Ising spin glass model, Eq. (11.15), is a NP hard problem in $3d$ [249]. It was suggested to be a good candidate for testing quantum annealing [250, 251].

11.3 Numerical implementation

The algorithm to find a pseudo-groundstate works as follows [211, 234, 252]:

(GS1) Randomly choose the positions of the M dopants in a volume $V = L^3$;

(GS2) Choose an initial state which is charge neutral;
Calculate the single-electron energies ϵ_j for all dopants;

(GS3) Randomly choose a pair (α, β) with $n_\beta = 0$ and $n_\alpha = 1$
IF($\Delta E_{(\alpha,\beta)} < 0$)THEN(
Swap occupation to $n_\beta = 1$ and $n_\alpha = 0$;
Update all single-electron energies;)

(GS4) Repeat (GS3) until $\Delta E_{(\alpha,\beta)} > 0$ for all pairs proper (α, β);

(GS5) Calculate the observables of interest;

For $K = 1$ we have always used the state where all acceptors are occupied and all donors are empty as an initial state. For $K < 1$ all MK acceptors and $M(1-K)$ donors (randomly chosen) were initialized with an electron while the remaining MK donors were left empty. The resulting pseudo-groundstate configuration depends on the initial state and on the sequence of exchanged pairs. At the end of the simulation we have checked systematically that $\Delta E_{(\alpha,\beta)} > 0$ is fulfilled for all proper pairs. The average runtime of the algorithm is $\mathcal{O}\left(M^2\right)$:
In (GS1) one has to distribute the M dopants, the runtime is $\sim M$.
In (GS2) all single-electron energies have to be calculated, the runtime is $\sim M^2$.
In (GS3) all single-electron energies have to be changed, the runtime is linear in M.
In (GS4) one has to check the condition Eq. (11.13) for all pairs and the number of pairs is $\sim M^2$. The runtime of (GS5) strongly depends on the observables that are calculated, but for none of those considered this exceeds M^2.
In the worst case a runtime of $\mathcal{O}(M) + \mathcal{O}\left(M^2\right) + \mathcal{O}\left(M \times M^2\right) = \mathcal{O}\left(M^3\right)$ is obtained. But the number of pairs which are exchanged during a single run is rather $\sim M$ and not $\sim M^2$. Then the update step (GS3) has to be executed only $\sim M$ times while in $\sim M^2$ cases no update is needed. Hence the runtime is rather $\mathcal{O}(M)$(from (GS1)) $+\mathcal{O}\left(M^2\right)$(from (GS2)) $+\mathcal{O}\left(M^2\right)$ (from (GS3), no update) $+\mathcal{O}(M \times M)$ (from (GS3) times $\sim M$ updates) $= \mathcal{O}\left(M^2\right)$. The observables in (GS5) depend on the disorder configuration chosen in (GS1). For each observable we have performed a disorder average. Depending on the observable, the disorder average includes $100-1000$ different disorder configurations.

For the finite temperature simulations a standard Metropolis Monte Carlo algorithm was used [253]. The algorithm does not converge to a single state but the configurations fluctuate and the probability to visit a state with energy E is

$\sim \exp(-E/T)$. In this way a canonical ensemble is sampled and thermal expectation values (and fluctuations) of physical observables can be calculated. The implementation works as follows:

(MC1) Randomly choose the potions of the M dopants in a volume $V = L^3$;

(MC2) Choose an initial state which is charge neutral;
Calculate the single-electron energies ϵ_j for all dopants;

(MC3) Randomly choose a pair (α, β) with $n_\beta = 0$ and $n_\alpha = 1$
IF($\Delta E_{(\alpha,\beta)} < 0$) THEN(
Swap occupation to $n_\beta = 1$ and $n_\alpha = 0$;
Update all single-electron energies;)
IF($\Delta E_{(\alpha,\beta)} > 0$) THEN(with a probability $\exp(-\frac{\Delta E_{(\alpha,\beta)}}{T})$:
Swap occupation to $n_\beta = 1$ and $n_\alpha = 0$;
Update all single-electron energies;)

(MC4) Repeat (MC3) until the probability to visit
a state with energy E is $\sim \exp(-E/T)$;

(MC5) Repeat (MC3) as long as you want (say m times);
Calculate the observables of interest when the system has reached a configuration which is uncorrelated to the last configuration at which observables were calculated;

The runtime of steps (MC1) - (MC4) is $\mathcal{O}\left(M^2\right)$ as above with a temperature dependent prefactor. The higher the temperature, the more Monte Carlo steps are accepted. Since observables are calculated m-times during a single Monte Carlo run the algorithm is self-averaging. We have typically used $m = 100$. Then averaging over $10 - 30$ different disorder configurations is sufficient to obtain reasonable results.

To check the accuracy of the pseudo-groundstate algorithm we have used the simulated annealing technique [254]. Here the system is initialized at a high temperature which then is successively reduced to zero. In 15 test runs, with two different annealing schemes each, the largest relative energy difference that we have found was $(E_{\mathrm{PGSalgorithm}} - E_{\mathrm{annealing}})/E_{\mathrm{annealing}} < 10^{-5}$. Depending on the cooling scheme the runtime of the annealing algorithm is much higher. For convenience we will (sometimes) use the term groundstate in the following as a synonym for the pseudo-groundstates.

In the simulations we have used different kind of boundary conditions. Open boundary conditions (OBC) lead to a reduction of the potential fluctuations close to

the surface. To avoid this, one can use periodic boundary conditions (PBC). Here the distance r between two dopants at (x_1, y_1, z_1) and (x_2, y_2, z_2) was calculated as $r^2_{\mathrm{PBC}} = \mathrm{Min}(|x_1 - x_2|, |x_1 - x_2 \pm L/2|)^2$ + $\mathrm{Min}(|y_1 - y_2|, |y_1 - y_2 \pm L/2|)^2$ + $\mathrm{Min}(|z_1 - z_2|, |z_1 - z_2 \pm L/2|)^2$. The simulation volume was chosen as a cube with volume $V = L^3$. In this volume we have used L^3 donor and KL^3 acceptor states, the corresponding dopant number is $(1 + K)\, L^3$. Accordingly, the total density in dimensionless units is $N_{\mathrm{tot}} = 1 + K$. All results presented below are shown for $L \geq 40$ (128.000 dopants). The largest system size that was simulated was $L = 64$ (524.288 dopants).

12 Low temperatures: Puddles and lengthscales

In this section we consider $T = 0$ (pseudo-groundstate) properties of the disordered Coulomb system. The focus will be on emergent lengthscales and on the the mechanisms which lead to puddle formation. In the model introduced in the last section a puddle has a to be identified with a critical accumulation of neutral dopants. We will introduce a measure for that which, however, is not justified by any operational definition. It serves as an auxiliary quantity to estimate the density of charges located in puddles.

12.1 Coulomb gap

A well-known feature of disordered localized charges interacting via long-ranged interactions is the Efros-Shklovskii Coulomb gap [211, 255]. This gap occurs in the groundstate where the single-electron density of states (d. o. s.) vanishes at the Fermi level. The d.o.s. , denoted by $g(\epsilon)$, is the distribution function of the single-particle energies $\epsilon_j = \frac{\Delta}{2} f_j - \phi_j$, its dimension is $1/(\mathsf{ENERGY\ VOLUME})$. The disappearance at the Fermi level is a direct consequence of the groundstate condition, see Eq. (11.13),

$$\epsilon_\beta - \epsilon_\alpha - V_{\alpha\beta} > 0, \text{ for } n_\beta = 0 \text{ and } n_\alpha = 1. \tag{12.1}$$

In the groundstate all states below the Fermi level ($\epsilon < \mu$) are filled with an electron, while all states above the Fermi level ($\epsilon > \mu$) are empty. In the following we present the original argument due to Efros and Shklovskii [255]. Let us assume that the d.o.s. is finite at the Fermi level $g(\mu) = g_0 > 0$ and that the condition in Eq. (12.1) is fulfilled. We consider two states of the same type, both acceptors or both donors, such that $V_{\alpha\beta} > 0$. One of the levels shall have an energy slightly below the Fermi level, while the other shall have an energy slightly above the Fermi level. This results in a small energy difference $\epsilon_\beta - \epsilon_\alpha = \Delta\epsilon$. Via $g_0 = 1/(\Delta\epsilon\, R^3)$ this defines a lengthscale $R = (g_0 \Delta\epsilon)^{-1/3}$. This has to be interpreted as the typical distance between the dopants with energy difference $\Delta\epsilon$. Inserting this into Eq. (12.1) and restoring the prefactors yields $\Delta\epsilon - e^2 (g_0 \Delta\epsilon)^{1/3}/(4\pi\varepsilon\varepsilon_0) > 0$. This inequality is violated for $\Delta\epsilon < e^3 g_0^{1/2}/(4\pi\varepsilon\varepsilon_0)^{3/2}$, in contradiction to the assumption. The conclusion is that the d.o.s. at the Fermi level cannot be finite. The dependence of g on the energy ϵ at small ϵ can be inferred from dimensional considerations: the Coulomb gap is due to the long-ranged Coulomb interaction where $\mathsf{LENGTH} \sim 1/\mathsf{ENERGY}$. Then $g \sim 1/(\mathsf{ENERGY\ LENGTH}^3) \sim \mathsf{ENERGY}^2$. This quadratic behavior $g(\epsilon) \sim \epsilon^2$ for $\epsilon \to 0$

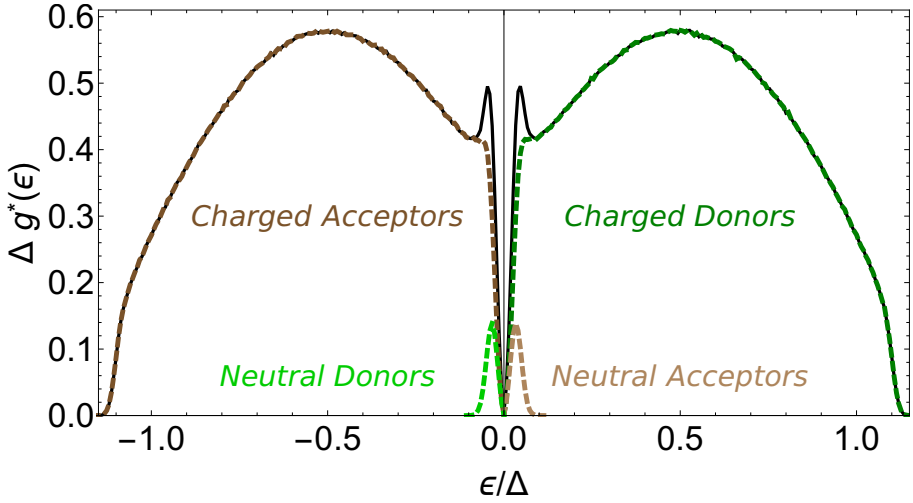

Figure 12.1: **Single-particle density of states in the groundstate.** The single-particle d.o.s. shows a soft gap at the Fermi level $\mu = 0$ the well-known Coulomb gap. States with $\epsilon < 0$ are occupied by an electron while states with $\epsilon > 0$ are empty. In the figure the d.o.s. is split into the four different contributions. The neutral donors form narrow peaks located very close to the Fermi level. The total d.o.s. is given by the black line. Data is shown for $\Delta = 15$, $L = 40$ and $a_{\mathrm{B}} = 1$.

was found in numerical simulations [234, 256, 257] as well as in experiments [258]. In $2d$ the same argument as presented above lead to $g_{2d}(\epsilon) \sim |\epsilon|$ for $\epsilon \to 0$. This has also been observed experimentally [259]. In graphene nanoribbons experimental results also indicate the existence of a Coulomb gap [243, 260].

In Fig. 12.1 we show the dimensionless d.o.s. $g^* = g\,\mathrm{E_c}/N$. One can clearly see the Coulomb gap at $\epsilon = 0$. The d.o.s. is split into the 4 different contributions: occupied donors and acceptors ($\epsilon < 0$) and empty donors and acceptors ($\epsilon > 0$). The density of the states of the neutral dopants shows narrow peaks slightly above (acceptors) or below (donors) the Fermi level which lead to a unique shape of the total density of states. This peaks confining the Coulomb gap have to be identified with the contribution of the neutral dopants. The axes are rescaled in a way that the result is, approximately, independent of Δ. The overlap of the d.o.s. to $\epsilon < -\Delta$ and $\epsilon > \Delta$ has a sharp cutoff at E_c. The results are shown for $\Delta = 15$ which corresponds to $\epsilon/\Delta \approx \pm 1.07$. To achieve such a low noise level as presented in Fig. 12.1 one has to perform a disorder average over more than 300 disorder configurations. For each realization the Fermi level is not exactly located at $\mu = 0$. Thus naive averaging leads to a finite d.o.s. at $\epsilon = 0$. To avoid this issue one can assess the Fermi level of a single realization by the mean of highest occupied and lowest empty single-electron energy $\bar{\mu} = (\epsilon_{\text{max occpd.}} + \epsilon_{\text{min empty}})/2$ [261]. This value is subtracted from each data set and

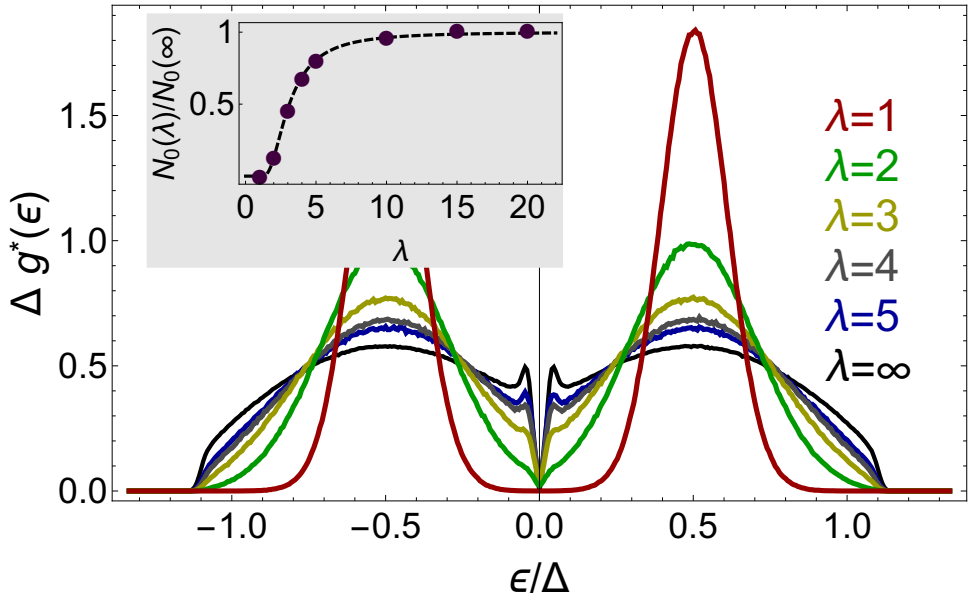

Figure 12.2: **Density of states for externally screened interactions.** The interaction used in the simulations was $V \sim \mathrm{e}^{-r/\lambda}/\sqrt{r^2+a_\mathrm{B}^2}$. The main panel shows that the Coulomb gap is still present for short-ranged interactions $\lambda \gtrsim 2$. The black line ($\lambda = \infty$) is the result for the unscreened interaction as shown in Fig. 12.1. For very small values of $\lambda \sim 1$ the d.o.s. approaches its non-interacting shape and shows a "screening gap". The inset shows the fraction of neutral dopants normalized by the value for $\lambda = \infty$. The dashed line is a guide to the eye. The full width at half maximum is surprisingly small $\lambda_{1/2} \approx 3.1$. All data is for $L = 40$ and $\Delta = 15$.

the d.o.s. vanishes for $\epsilon \to 0$.

To investigate the effect of external screening we have also performed simulations with the interaction

$$V_{\alpha\beta}(\lambda) = \frac{\mathrm{e}^{-|\boldsymbol{r}_\alpha - \boldsymbol{r}_\beta|/\lambda}}{\sqrt{|\boldsymbol{r}_\alpha - \boldsymbol{r}_\beta|^2 + a_\mathrm{B}^2}}. \tag{12.2}$$

Here λ denotes the screening length which is the range of the interaction. In Fig. 12.2 the d.o.s. is shown for different values of λ and $\Delta = 15$. As λ becomes smaller, the d.o.s. has to approach its non-interacting shape, two peaks at $\pm\Delta/2$. However, this happens only at a surprisingly small screening length: for $\lambda = 2$ one can still see a dip in the d.o.s. at $\epsilon \to 0$ and that the Coulomb gap is still existing.

In the inset we show the density of neutral dopants normalized by the value for $\lambda = \infty$ (no external screening). The full width at half maximum is at $\lambda_{1/2} \approx 3.1$ the system size in the simulation was $L = 40$. Within a "screening volume" of size $V_\mathrm{scr} = (\lambda_{1/2})^3$ there are $2 * 3.1^3 \approx 60$ dopants on average. To produce a net charge of at least ± 10 the number of acceptors or donors in V_scr has to be at most 25. The

probability for this to happen is given by $2 \times 2^{-60} \sum_{i=0}^{25} \binom{60}{i} \approx 0.25$. The typical charge in a volume V_{scr} is $\sim \sqrt{60}\, e \approx 7.75\, e$ Hence, it is possible to build up potentials $|\phi| > \Delta/2 = 7.5$ in a screening volume. By contrast, for $\lambda = 1$ there are two dopants on average in a screening volume $\lambda^3 = 1$, and there will (almost) never be a net charge of ± 10. In the simulations for $\lambda = 1$ there was 1 pair of neutral dopants out of 3200000 pairs in total. This estimate was intended to show that the smallness of $\lambda_{1/2}$, albeit surprising, is plausible. The result suggests that the neutralization of dopants is mainly controlled by the local environment. The Coulomb gap survives as long as there are enough dopants in a screening volume, charges that "talk" to each other, to provide potentials of order $\pm\Delta/2$. For short-ranged interactions the Coulomb gap is replaced by a screening gap, as seen for $\lambda = 1$ in Fig. 12.2, and the formation of neutral dopants is totally suppressed. Below we will further investigate the lengthscales which control the puddle formation.

12.2 Correlation functions and lengthscales

A simple scaling argument by Efros, Shklovskii and Skinner [211, 234, 235, 261] suggests that there exists a lengthscale $R_g \sim \Delta^2$ in the correlated groundstate. The short version was already presented in section 11.1. The argument is as follows: in a volume of size $V \sim R^3$ the typical charge in the uncorrelated state is $Q_R \sim \pm e\sqrt{R^3} \sim R^{3/2}$. This implies a typical potential $\phi_R \sim Q_R/R \sim \sqrt{R}$ within that region. The potential is cutoff at $\pm\Delta/2$ and to reach $\phi_R \sim \sqrt{R} \sim \Delta$ a typical distance $R_g \sim \Delta^2$ is needed. Accordingly the charge density in a volume $V = R_g^3$ is $\rho_g \sim Q_V/V \sim \sqrt{R_g^3}/R_g^3 = R_g^{-3/2} \sim 1/\Delta^3$. To summarize, this scaling argument suggests

$$R_g \sim \Delta^2 \text{ and } \rho_g \sim \Delta^{-3}. \tag{12.3}$$

The prefactor can also be calculated from the correlation function of

$$\phi(\boldsymbol{r}_B) - \phi(\boldsymbol{r}_A) = \int_{\gamma_{A\to B}} d\boldsymbol{s} \cdot (\nabla\phi)(\boldsymbol{s}) = \int_{\gamma_{A\to B}} d\boldsymbol{s} \int d^3\boldsymbol{r'}\, \frac{\rho(\boldsymbol{r'})\,(\boldsymbol{r'} - \boldsymbol{s})}{|\boldsymbol{r'} - \boldsymbol{s}|^3} \tag{12.4}$$

to be

$$\langle\, (\phi(\boldsymbol{r}_B) - \phi(\boldsymbol{r}_A))\, (\phi(\boldsymbol{r}_B) - \phi(\boldsymbol{r}_A))\rangle = 8\pi\, |\boldsymbol{r}_B - \boldsymbol{r}_A| = 8\pi R. \tag{12.5}$$

Here and in the following the expectation value $\langle\cdot\rangle$ denotes a disorder average. After disorder averaging all correlation functions only depend on the distance. In the numerical simulations this is also true for PBC while OBC may lead to deviations close to the boundary. Equating Eq. (12.5) with Δ^2 yields, with the dimensions restored,

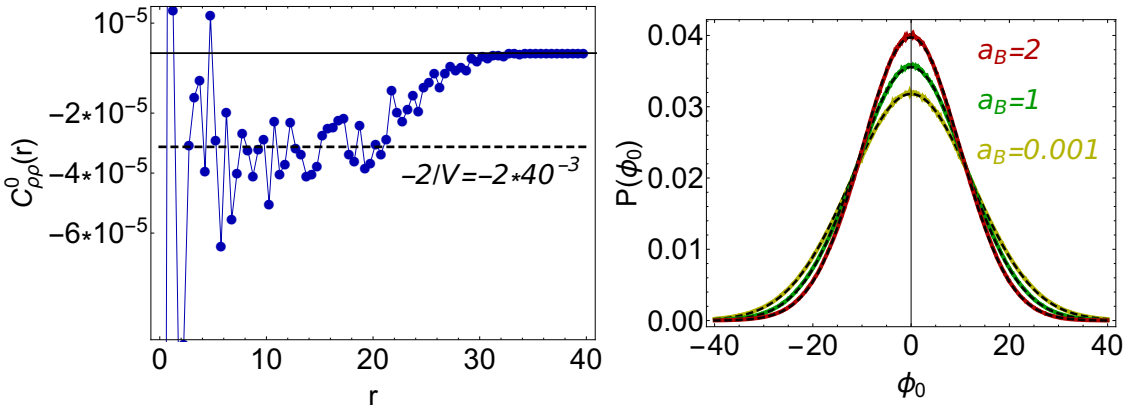

Figure 12.3: **Properties of the uncorrelated state.** The left panel shows the non-local part of the charge-charge correlation function $C^0_{\rho\rho}$, Eq. (12.6), calculated as explained in the main text. We find the expected behavior $C^0_{\rho\rho} = -2/V$. In the simulation we used $L = 40$, then $-2/V = -2/40^3 \approx -3.1 \times 10^{-5}$. The data is averaged over 2000 disorder realizations but the noise level is still quite high. Periodic boundary conditions were used. For $r > L/2 = 20$ the number of charges available decreases (is not $\sim r^2$ anymore) leading to a suppression of $C^0_{\rho\rho}$. In the right panel we show the probability distribution of the potential ϕ_0 in the uncorrelated state for different values of the cutoff a_B. The dashed lines are Gaussian fits to the data. All curves are perfectly Gaussian as expected. The system size was $L = 40$ and the width of the Gaussian is $\sim \sqrt{L}$ as shown in the main text. For $a_B = 0.001$ the fit yields $\sigma = 12.55$ – the value from Eq. (12.8) for spherical symmetry is $\sigma = \sqrt{4.104\, L} = \sqrt{4.104 \times 40} = 12.81$.

$R_g = \frac{N^{-1/3}}{8\pi}\left(\frac{\Delta}{\mathrm{E_c}}\right)^2$. This is exactly the result of Skinner *et. al.* [234, 235]. We will call the scaling behavior $\mathsf{LENGTH} \sim \mathsf{ENERGY}^2$ Gaussian scaling as it arises from uncorrelated charges. To perform the integrals in Eq. (12.5) we have used the charge-charge correlation function of the uncorrelated system. In dimensionless units it is given by

$$\langle \rho_0(\boldsymbol{r})\rho_0(\boldsymbol{r}')\rangle = N_\mathrm{tot}\left(\delta(\boldsymbol{r}-\boldsymbol{r}') - \frac{1}{V}\right) = N_\mathrm{tot}\delta(\boldsymbol{r}-\boldsymbol{r}') + C^0_{\rho\rho}(r). \tag{12.6}$$

The density was $N_\mathrm{tot} = (1+K)$ in the simulations, in this subsection we present only results for perfect compensation, $K = 1$. The second term, $-N_\mathrm{tot}/V$, term ensures charge neutrality:

$$\begin{aligned}&\int d^3\boldsymbol{r} \int d^3\boldsymbol{r}'\ \langle \rho_0(\boldsymbol{r})\rho_0(\boldsymbol{r}')\rangle \\ &= N_\mathrm{tot}\left(\int d^3\boldsymbol{r} - \frac{1}{V}\int d^3\boldsymbol{r} \int d^3\boldsymbol{r}'\right) = N_\mathrm{tot}\left(V - \frac{1}{V}V^2\right) = 0.\end{aligned} \tag{12.7}$$

If there is a charge q at $\boldsymbol{r}$ the rest of the system has charge $-q$ which, after disorder averaging, is homogeneously distributed. In Fig. 12.3 we show the non-local part of $\langle \rho_0(\boldsymbol{r})\rho_0(\boldsymbol{r}')\rangle$. Since we are dealing with a discrete system, there is no unique way to calculate the correlation functions. Here they were obtained as follows: 1) Around each charged dopant we have counted the charge in spherical shells (with thickness $dr = 0.5$) around this dopant. 2) The charges themselves are counted separately which gives the $\delta-$contribution in Eq. (12.6). 3) The result is normalized by the volume such that the δ-peak has weight $N_{\text{tot}} = 2$.

For periodic boundary conditions used here, the number of dopants in each shell grows as $4\pi r^2 dr$ for $r \lesssim L/2$. For $r > L/2$ the number of dopants does not increase as r^2 any more. This leads to a suppression of $C^0_{\rho\rho}(r)$ for $r > L/2$ as seen in the left panel of Fig. 12.3. Although the data is averaged over 2000 disorder realizations, the simulations can be done very quickly as no optimization has to be performed, the noise level is still quite high.

From Eq. (12.6) the (square of the) typical size of the potential can be calculated as

$$\begin{aligned}
\langle \phi_0(\boldsymbol{r})\phi_0(\boldsymbol{r})\rangle = \langle \phi_0(0)\phi_0(0)\rangle &= \int d^3\boldsymbol{r} \int d^3\boldsymbol{r}' \, \frac{\langle \rho_0(\boldsymbol{r})\rho_0(\boldsymbol{r}')\rangle}{r\, r'} \\
&= \int d^3\boldsymbol{s} \int d^3\boldsymbol{R} \, \frac{2\delta(\boldsymbol{s}) - 2/V}{|\boldsymbol{R} + \boldsymbol{s}/2|\, |\boldsymbol{R} - \boldsymbol{s}/2|} \\
&= 2\int d^3\boldsymbol{R} \, \frac{1}{R^2} - \frac{2}{V}\int d^3\boldsymbol{s}\, 4\pi L - \frac{4\pi}{V}\int_0^L ds\, s^3 I(s/L) \\
&= \frac{-4\pi}{V}\int_0^L ds\, s^3 I(s/L) = \frac{-4\pi L^4}{V}\int_0^1 ds\, s^3 I(s) \sim L, \qquad (12.8)
\end{aligned}$$

where L is the linear system size ($V \sim L^3$) and

$$\begin{aligned}
I(x) &= 2\pi\left(\frac{\pi}{4} - 1\right) + \frac{2\pi}{x^2}\left(\text{ArcSin}\left(\frac{4x}{4+x^2}\right) - x\right) - \pi\,\text{ArcTan}\left(\frac{2}{x}\right) \\
&= -2\pi + \frac{\pi}{3}x + \mathcal{O}\left(x^3\right). \qquad (12.9)
\end{aligned}$$

In this calculation we have used spherical symmetry. In general $I(x)$ depends on the boundary conditions and on the geometry of the simulation volume but the leading order in $x = s/L$ has to be a (negative) constant. For spherical symmetry, where $V = 4\pi L^3/3$, we find $\langle \phi_0(\boldsymbol{r})\phi_0(\boldsymbol{r})\rangle = 4.104\, L$. The potential becomes arbitrarily large in a large system and the typical potential is $\phi_{\text{typ}} = \sqrt{\langle \phi_0(0)\phi_0(0)\rangle} \sim \sqrt{L}$. Since the charges are uncorrelated, we expect a Gaussian distribution of the potential. This is shown in the right panel of Fig. 12.3 for $L = 40$ for different values of a_{B}. In the

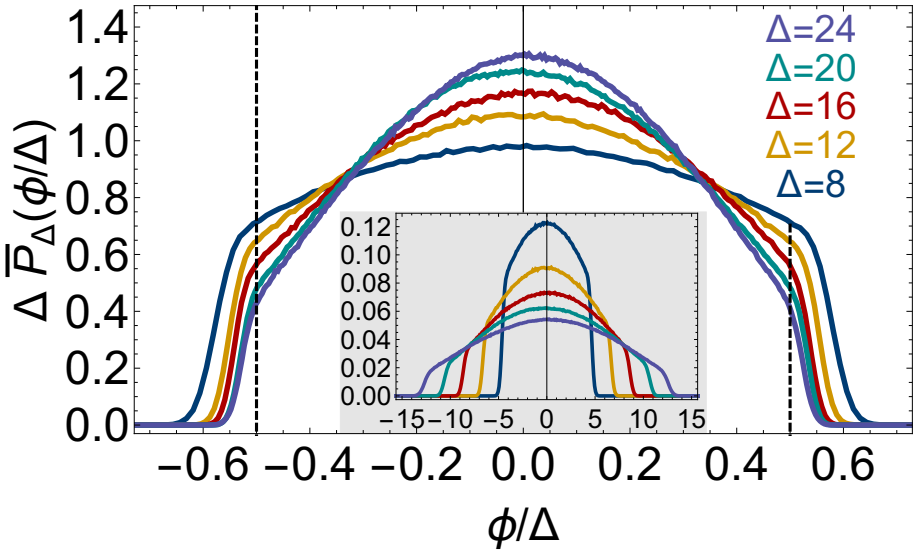

Figure 12.4: **Distribution function of the potential in the groundstate.** The main panel shows the scaled distribution function $\overline{P}_\Delta$ of the potential for $L = 40$ and $\Delta = 8 - 24$. It has a cutoff at $\pm\Delta/2$, as indicated by the dashed lines. Only for $|\phi| > \Delta/2$ neutralization and puddle formation can arise. The inset shows the unscaled data, $P(\phi)$ as a function ϕ.

following scaling analysis we will omit the cutoff $a_{\rm B}$. Later, in section 14 , we will investigate the influence of the the cutoff $a_{\rm B}$ on the lengthscales. In $2d$ a similar calculation as in Eq. (12.8) yields $\langle\phi_0\phi_0\rangle_{2d} \sim \log(L)$ suggesting an exponentially large lengthscale.

The large potential fluctuations $\sim \sqrt{L}$ have to be screened. To investigate this we consider the charge and the potential correlation functions in the groundstate. Since $\phi(\boldsymbol{r}) = \int d^3\boldsymbol{r}' V(|\boldsymbol{r} - \boldsymbol{r}'|)\,\rho(\boldsymbol{r}')$, where V denotes the Coulomb interaction, they contain the same information. In Fig. 12.4 we show the probability distribution of the potential, the inset shows the unscaled data. The weight of the distribution is restricted between $-(\Delta/2+1/a)$ and $(\Delta/2+1/a)$, where $a \approx 1$. The dashed lines indicate the region where $|\phi| > \Delta/2$, it is here that neutralization can arise. The overlap is a measure for the density of neutral dopants. The main panel shows the rescaled $\Delta\overline{P}(\phi/\Delta)$. The height where the different curves cut the dashed lines still depends on Δ. The distributions shown in Fig. 12.4 are not Gaussian anymore and therefore they cannot be fully characterized by their second moment. Nevertheless we anticipate from Fig. 12.4 that $\langle\phi(\boldsymbol{r})\phi(\boldsymbol{r})\rangle \sim \Delta^2$. The distributions have an approximate height of $1/\Delta$ and an approximate width of $\sim \Delta$ which gives $\langle\phi\phi\rangle \sim \Delta^2$ plus subleading corrections. In Fig. 12.5 we show different fits to the numerically calculated $\langle\phi\phi\rangle$

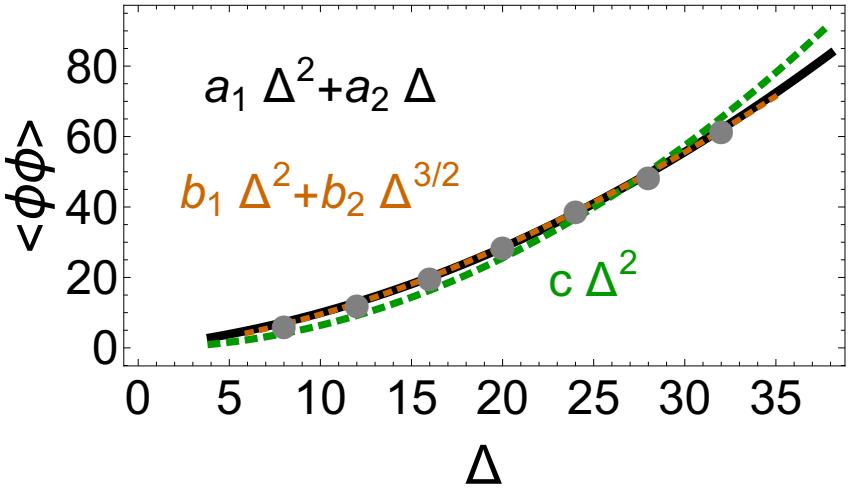

Figure 12.5: **The local potential-potential correlations as a function of Δ.** The leading order term is $\sim \Delta^2$. However, subleading terms are needed to describe the data correctly in the simulated parameter range. The respective fits yield $c = 0.064$, $a_1 = 0.043, a_2 = 0.562$ and $b_1 = 0.016, b_2 = 0.250$.

for different values of Δ. The data cannot be described with a simple $c\,\Delta^2$ fit, see the green dashed line. Subleading terms are needed and we show two different fit functions which match the data.

To investigate this further, we have numerically determined how the probability distribution of the potential is build up in space. To this end we have calculated the potential distributions $P_R(\phi)$ where only charges located within a sphere of radius R contribute. For $R > L$ this is identical to the results shown in Fig. 12.4. We have further calculated the distribution $P_R^{\rm neut}(\phi)$ at the position of the neutral dopants only. For $R > L$ this has to restricted to the region where $|\phi| > \Delta/2$ as necessary for neutralization. In Fig. 12.6 we show numerical results for $L = 50$, $a_{\rm B} = 1$ and $\Delta = 24$. At very small R, $P_R(\phi)$ has only discrete values due to the discreteness of charge. This is shown for the example of $R = 0.25$ in the left panel. Surprisingly, both $P_R(\phi)$ and $P_R^{\rm neut}(\phi)$ reach their final form only when R is of the order of the system size. For intermediate R, P_R is approximately described by a Gaussian distribution, where the width depends on R. An example is shown by the black dashed line. Only when $R \gtrsim 35$ the Gaussian tails of $P_R(\phi)$ vanish leading to a sharp cutoff. Also $P_R^{\rm neut}(\phi)$ reaches its eventual shape, two peaks at $\pm(\Delta/2 + {\rm E_c})$, only for $R \gtrsim 40$. For $5 < R < 30$ $P_R^{\rm neut}$ is almost independent of R showing a well at $\phi = 0$. We have checked that the qualitative behavior is the same in the same in the range $\Delta = 8$ to $\Delta = 32$.

Before we further investigate the correlations of the potential we show some re-

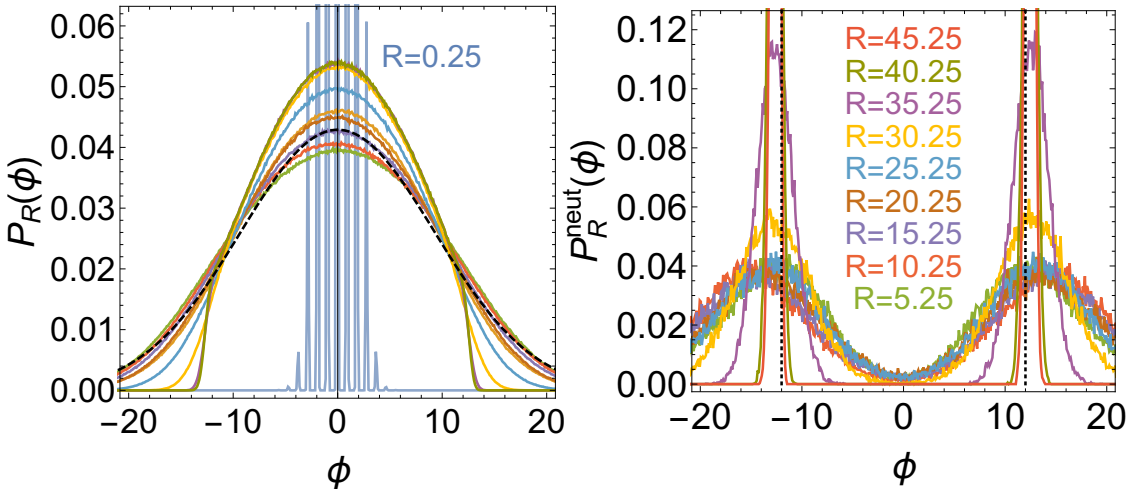

Figure 12.6: **Build up of the potential distributions.** Shown is the data for $L = 50$, $a_B = 1$ and $\Delta = 24$. The potential distribution P_R is calculated using only dopants within a distance R. $P_R^{\text{neut}}(\phi)$ is the distribution at the positions of the neutral dopants. Both, $P_R(\phi)$ and $P_R^{\text{neut}}(\phi)$, develop their final shape only when R is of order of the system size. For very small R the distributions reflect the discreteness of the charge as seen for $R = 0.25$ in the left panel.

sults on the charge correlations. As charges are neutralized in the groundstate the weight of the δ-peak in Eq. (12.6) is reduced. Furthermore also the weight in the non-local part, denoted by $C_{\rho\rho}^{\text{nl}}$, is redistributed. We parametrize

$$\langle \rho(\boldsymbol{r})\rho(\boldsymbol{r}')\rangle = Q_0\delta(\boldsymbol{r}-\boldsymbol{r}') + C_{\rho\rho}^{\text{nl}}(\boldsymbol{r}-\boldsymbol{r}'). \tag{12.10}$$

Thanks to charge neutrality we know that $\int d^3\boldsymbol{r}\, C_{\rho\rho}^{\text{nl}}(\boldsymbol{r}) = -Q_0$. The weight of the δ-peak Q_0 corresponds to $N_{\text{tot}}\,(1-n_0) = 2\,(1-n_0)$ where n_0 is the fraction of neutral dopants. As $n_0 \to 0$ for $\Delta \to \infty$ we expect that it can be described with a scaling ansatz $n_0 \sim \Delta^{-\gamma}$ with $\gamma > 0$. If the charges are screened, the compensation $4\pi \int ds\, s^2\, C_{\rho\rho}^{\text{nl}}(s) = -Q_0$ is realized on a finite lengthscale, the screening length R_s, such that

$$\int_{\boldsymbol{s}<\boldsymbol{R_s}} ds\, W(s)\, C_{\rho\rho}^{\text{nl}}(s) = -Q_0. \tag{12.11}$$

To investigate this we define the screening function

$$S_{\rho\rho}(r) = \int_0^r ds\, W(s)\, C_{\rho\rho}^{\text{nl}}(s). \tag{12.12}$$

The weight function $W(s)$ depends on the geometry and the boundary conditions. For

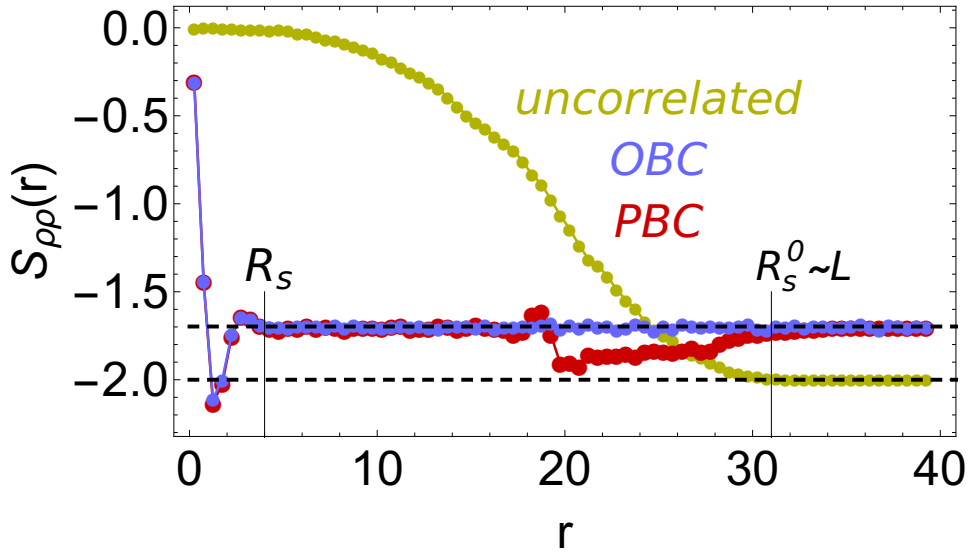

Figure 12.7: **Screening function $S_{\rho\rho}$ for different boundary conditions and in the uncorrelated state.** We have used $\Delta = 0$ here to demonstrate some features of this function. The dashed, black lines indicate the total charge $-Q_0$ that has to be compensated. In the uncorrelated state, when all dopants are charged, the compensation happens only at a length $R_s^0 \sim L$ indicating the absence of screening. In the correlated state the charge compensation happens on a very short lengthscale $R_s \sim 4$ and the charges are screened. A strange effect can be seen for periodic boundary conditions (PBC): while the short distance screening does not depend on the boundary conditions, there are correlations emerging at $r \sim L/2 = 20$.

spherical symmetry is it just $W_{\text{spherical}}(s) = 4\pi s^2$. From the numerical algorithm, as described above, it is clear that we have directly calculated $W(s)\, C^{\text{nl}}_{\rho\rho}(s)$. For small s it is always $W(s) \sim s^2$ independent of the geometry and whether the boundary conditions are open or periodic. Clearly, the screening function fulfills $S_{\rho\rho}(r \to 0) \to 0$ and $S_{\rho\rho}(r \to L) \to -Q_0$.

In Fig. 12.7 we show $S_{\rho\rho}$ for different boundary conditions and in the uncorrelated state. We have chosen $\Delta = 0$ to demonstrate some features of this function. It can be clearly seen that in the uncorrelated state the charge compensation happens on a lengthscale $R_s^0 \sim L$: screening is absent. In the groundstate, however, the compensation happens on a small lengthscale $R_s \sim 4$ and the charges are screened. The weight Q_0 is ≈ 1.7 for $\Delta = 0$, which corresponds to a fraction of neutral dopants $n_0(\Delta = 0) = 1 - Q_0/2 \approx 0.15$. For periodic boundary conditions (PBC) a strange feature emerges at $r \approx L/2 = 20$: there is a finite correlation starting at this length which is absent for open boundary conditions. At $r = L/2$ the weight function for PBC is maximal and the effect may be related to this.

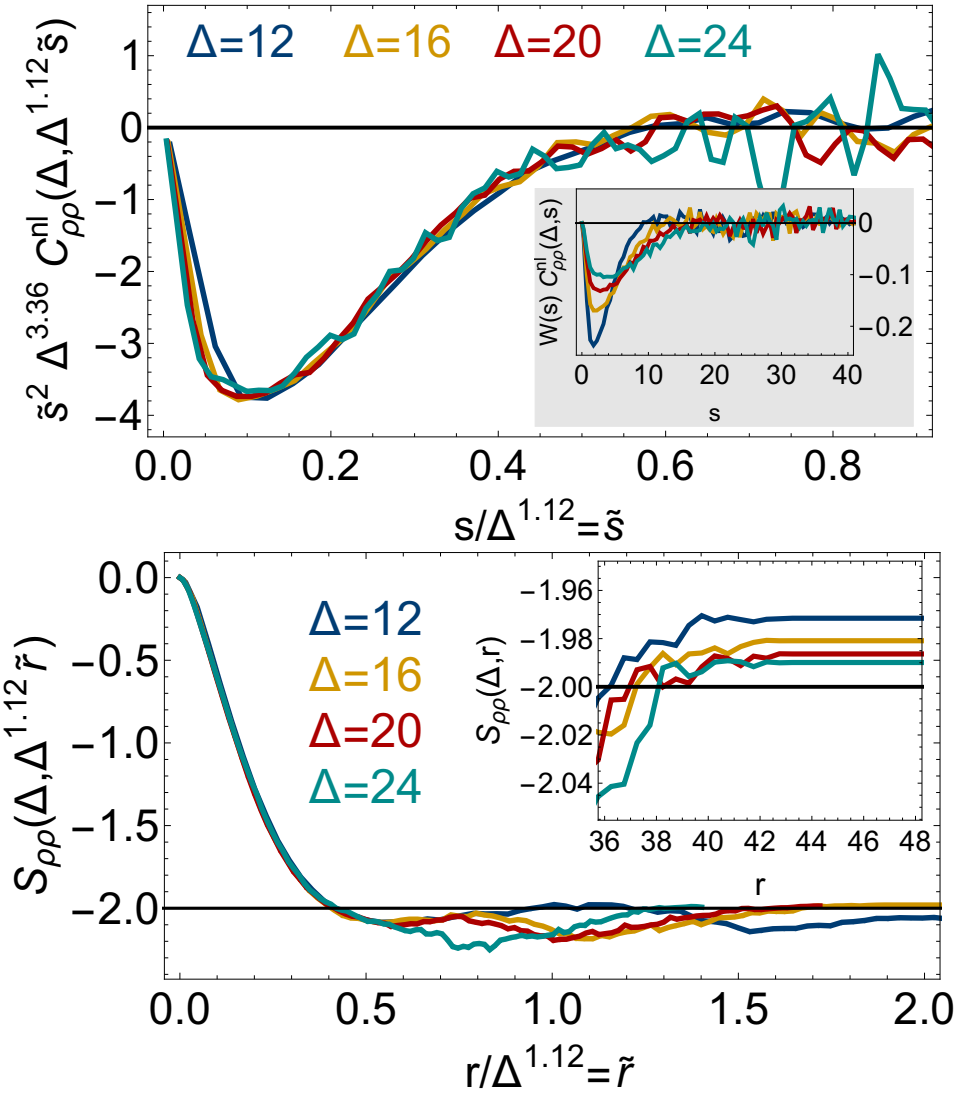

Figure 12.8: **Screening function and the non-local charge-charge correlations.** The upper plot shows the integrand of $S_{\rho\rho}(\Delta,r)=\int_0^r dsW(s)C^{\rm nl}_{\rho\rho}(\Delta,s)$ and the lower plot shows $S_{\rho\rho}(\Delta,r)$. In the main panel of both plots length is scaled by $\Delta^{\alpha=1.12}$. With this value an approximate scaling collapse is obtained for $r,s\lesssim 0.5\Delta^{1.12}$. Scaling with slightly different values in the range $\alpha=1.0-1.2$ also gives reasonable results, see Fig. 12.11 below. This suggests a scaling function $\overline{C^{\rm nl}_{\rho\rho}}(r/\Delta^\alpha)=\Delta^{3\alpha}\,C^{\rm nl}_{\rho\rho}(\Delta,r)$ (since $W(s)ds\sim s^2ds$ at short distances). However, there are deviations for $r,s\gtrsim 0.5\Delta^{1.12}$. The inset in the upper plot shows the unscaled data. The inset of the lower plot shows the charge density $Q_0(\Delta)=2-n_0(\Delta)$ which has to be compensated. Full charge neutrality is reached only at length of the order of the system size ($L=50$ in that plot). Both plots show results for PBC, however, the behavior at large distances differs for different boundary conditions. Parameters used in the plots are $a_{\rm B}=1$ with $L=50$ for $\Delta<20$ and $L=60$ for $\Delta\geq 20$.

In Fig. 12.8 we show $S_{\rho\rho} = \int_0^r ds W(s) C^{\rm nl}_{\rho\rho}(\Delta, s)$ and its integrand for different values of Δ. Within the numerical precision a scaling collapse at short distances can be reached if the length is scaled with $\Delta^{\alpha=1.-1.2}$. We have chosen $\alpha = 1.12$ which shows the best agreement, see Fig. 12.11 below. The plots suggest a scaling function $\overline{C^{\rm nl}_{\rho\rho}}(r/\Delta^\alpha) = \Delta^{3\alpha} C^{\rm nl}_{\rho\rho}(\Delta, r)$. However at larger distances, $r, s \gtrsim 0.5\Delta^\alpha$, deviations are seen. While this is hidden by the noise in the upper plot, it can be clearly seen in $S_{\rho\rho}$. Below we present three different scenarios which might explain this. The negative peak at short distances, $s \lesssim 0.5\Delta^\alpha$, in the upper plot overcompensates the local charge correlations. This can be interpreted as an overscreening where more charge than needed for screening is accumulated. This effect can be seen in the lower plot where $S_{\rho\rho}$ is smaller than the eventual value, and even smaller than -2, for $r \gtrsim 0.4\Delta^\alpha$. The values of $S_{\rho\rho}(\Delta, r \sim L)$ are shown in the inset of the lower plot – total charge neutrality is only reached at $r \sim L = 50$.

As in Eq. (12.8) we can calculate the local correlation function of the potential as

$$\begin{aligned}\langle\phi(\boldsymbol{r})\phi(\boldsymbol{r})\rangle &= \int d^3\boldsymbol{r} \int d^3\boldsymbol{r}' \, \frac{\langle\rho(\boldsymbol{r})\rho(\boldsymbol{r}')\rangle}{r\, r'} = \int d^3\boldsymbol{s} \int d^3\boldsymbol{R} \, \frac{Q_0\delta(\boldsymbol{s}) + C^{\rm nl}_{\rho\rho}(\boldsymbol{s})}{|\boldsymbol{R}+\boldsymbol{s}/2|\,|\boldsymbol{R}-\boldsymbol{s}/2|} \\ &\underset{\text{spherical}}{=} 4\pi L Q_0 + \int d^3\boldsymbol{s}\, s\, C^{\rm nl}_{\rho\rho}(s) \left(I(s/L) + \frac{4\pi L}{s} \right) \\ &= \int ds\; s\, W(s)\, C^{\rm nl}_{\rho\rho}(s)\; I(s/L) \underset{\text{spherical}}{=} 4\pi \int ds\; s^3\, C^{\rm nl}_{\rho\rho}(s)\; I(s/L) \end{aligned} \tag{12.13}$$

where $I(s/L) = -2\pi + \mathcal{O}(s/L)$ was defined in Eq. (12.9). For non-spherical situations a different weight function W has to be used, but it has to be $\sim s^2$ for small s. Also in the evaluation of the $\boldsymbol{R}$ integral spherical symmetry was assumed and $I(s/L)$ might be different for non-spherical situations. If the screening is realized on finite length, $R_s < L$, only the leading order term of I can contribute. Then charge neutrality and the constraint on the potential yield the equations

$$\int ds\, s^2\, C^{\rm nl}_{\rho\rho}(s) \sim -Q_0 = 2(-1 + n_0(\Delta)) \sim \Delta^0 + \mathcal{O}\left(\frac{1}{\Delta^{\gamma>0}}\right) \tag{12.14}$$

$$\int ds\, s^3\, C^{\rm nl}_{\rho\rho}(s) \sim \langle\phi^2\rangle \sim \Delta^2 + \mathcal{O}\left(\Delta^{\delta<2}\right). \tag{12.15}$$

The exponents of the subleading terms γ and δ are not known apriori.

In Fig. 12.9 we show $n_0(\Delta)$. It cannot be described by a simple fit of the form $c\Delta^{-\gamma}$. In the simulated parameter range further terms are needed to fit the data. Three fit functions in the range $\Delta = 16 - 32$ are shown. The gray solid line is a fit $3.73\,\Delta^{-2} - 20.05\,\Delta^{-3}$, the black dashed line is a fit $0.045\,\Delta^{-1} + 1.75\,\Delta^{-2}$ and the red dotted line is a fit $0.51\,\Delta^{-3/2} + 1.69\,\Delta^{-5/2}$. From the fits as shown it is not possible

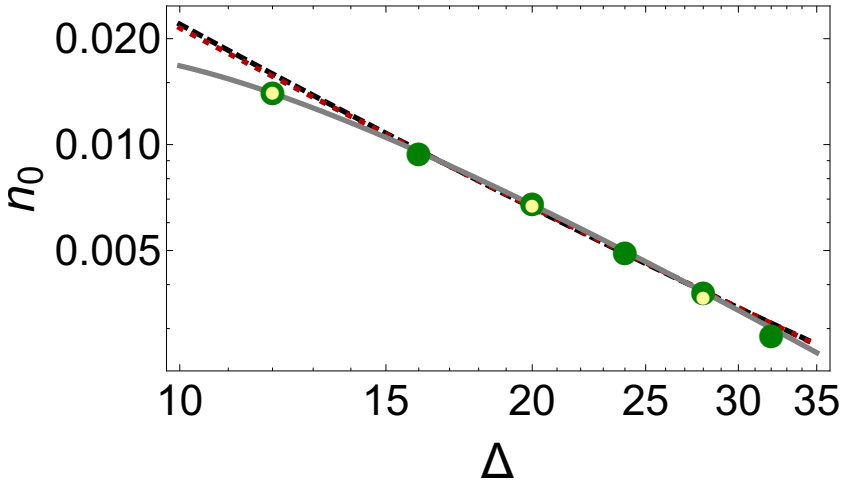

Figure 12.9: **Density of neutral dopants as a function of Δ.** The large green dots are data for $L = 50$ while the smaller light dots are data for $L = 40$. The data cannot be described by a simple fit of the form $a\,\Delta^{-b}$, subleading terms are needed. Three fits with different asymptotic behavior for $\Delta \to \infty$ are shown: the gray solid line is a fit $a_1\,\Delta^{-2} + b_1\,\Delta^{-3}$, the black dashed line is a fit $a_2\,\Delta^{-1} + b_2\,\Delta^{-2}$ and the red dotted line is a fit $a_3\,\Delta^{-3/2} + b_3\,\Delta^{-5/2}$. All fits are in the range $\Delta = 16 - 32$.

to decide on the asymptotic behavior. The last point at $\Delta = 32$ might suffer slightly from finite size effects. The lighter smaller dots are results for $L = 40$.

We can also express the energy of the system in terms of $C^{\rm nl}_{\rho\rho}$: the Coulomb interaction energy $H_{\rm C}$ is

$$\begin{aligned}\langle H_{\rm C}\rangle &= \frac{1}{2}\sum_{i\neq j}\frac{\langle q_i q_j\rangle}{|\boldsymbol{r}_i - \boldsymbol{r}_j|} \to \frac{1}{2}\int d^3\boldsymbol{r}\int d^3\boldsymbol{r}'\,\frac{C^{\rm nl}_{\rho\rho}(|\boldsymbol{r}-\boldsymbol{r}'|)}{|\boldsymbol{r}-\boldsymbol{r}'|}\\ &= \frac{1}{2}\int d^3\boldsymbol{R}\int d^3\boldsymbol{s}\,\frac{C^{\rm nl}_{\rho\rho}(s)}{s} = 2\pi\,V\int ds\,s\,C^{\rm nl}_{\rho\rho}(s). \qquad (12.16)\end{aligned}$$

The local part of the charge-charge correlations does not contribute due to the $i \neq j$ constraint on the sum and would give a contribution $\sim V\log(L)$ in the continuum limit. The neutralization energy, $H_{\rm n} = V\,\Delta\,n_0$, can be calculated from Eq. (12.14) as

$$\langle H_{\rm n}\rangle = V\,\Delta\,n_0 = V\,\Delta(1 - Q_0/2) = V\,\Delta + 2\pi\,V\,\Delta\int ds\,s^2\,C^{\rm nl}_{\rho\rho}(s) \sim V\,\Delta^{1-\gamma}. \qquad (12.17)$$

In the uncorrelated state, where $C^{\rm nl}_{\rho\rho}(s) = -2/V$ and $n_0 = 0$, it is

$$\frac{\langle H_0\rangle_{\rm uc}}{V} = \Delta + 2\pi\,\Delta\int_0^L ds\,s^2\left(\frac{-2}{V}\right) = \Delta - \frac{4\pi\,\Delta}{3V}L^3 = 0 \quad \left(V = \frac{4\pi}{3}L^3\right), \qquad (12.18)$$

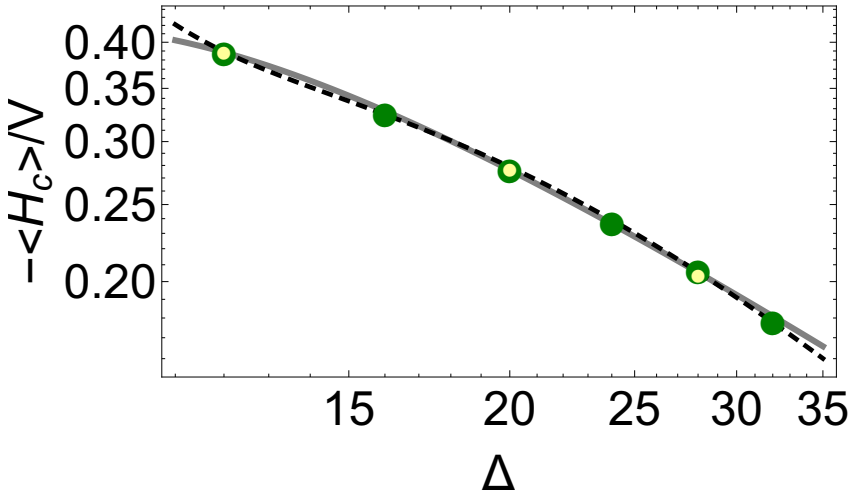

Figure 12.10: **Coulomb energy density as a function of Δ.** Shown are the negative values in a log-log plot. The large green dots are data for $L = 50$ while the smaller light dots are data for $L = 40$. The data cannot be described by a simple fit of the form $a\,\Delta^{-b}$. Two fits including subleading terms are shown. The solid gray line is a fit $a_1\,\Delta^{-1}+b_1\,\Delta^{-3/2}+c_1\,\Delta^{-2}$ while the dashed black line is a fit $a_1\,\Delta^{-2}+b_1\,\Delta^{-5/2}+c_1\,\Delta^{-3}$. Both fits can describe the data and it is not possible to decide on the asymptotic behavior for $\Delta \to \infty$.

$$\frac{\langle H_{\rm C}\rangle_{\rm uc}}{V} = 2\pi \int_0^L ds\, s \left(\frac{-2}{V}\right) = -2\pi \frac{L^2}{V} = \mathcal{O}\left(L^{-1}\right). \tag{12.19}$$

The total energy density can be written as

$$\frac{\langle H\rangle}{V} = \frac{\langle H_{\rm n} + H_{\rm C}\rangle}{V} = \Delta + 2\pi \int ds\, s\, C^{\rm nl}_{\rho\rho}(\Delta, s)\,(1 + s\,\Delta)\,. \tag{12.20}$$

In Fig. 12.10 we show $-\frac{\langle H_{\rm C}\rangle}{V}$ as a function of Δ. No fit of the form $a\,\Delta^{-b}$ can describe the data. The best fits were obtained including two subleading corrections. Two examples are shown in Fig. 12.10. The solid gray line is a fit $4.08\,\Delta^{-1} + 21.71\,\Delta^{-3/2} - 68.26\,\Delta^{-2}$, and the dashed black line is a fit $678.5\,\Delta^{-2} - 3839.2\,\Delta^{-5/2} + 5820.3\,\Delta^{-3}$. Both fits match the data equally well in the range $\Delta = 12 - 32$.

To summarize, we have found a set of equations for disordered $3d$ Coulomb systems which relate the energy density, the charge density and the local potential correlation function. For systems with spherical symmetry they read:

$$\frac{\langle H_{\rm C}\rangle}{V} = 2\pi \int ds\, s^1\, C^{\rm nl}_{\rho\rho}(\Delta, s), \tag{12.21}$$

$$\frac{\langle H_{\rm n}\rangle}{V} = 2\pi\,\Delta \int ds\, s^2\, C^{\rm nl}_{\rho\rho}(s) + \Delta, \tag{12.22}$$

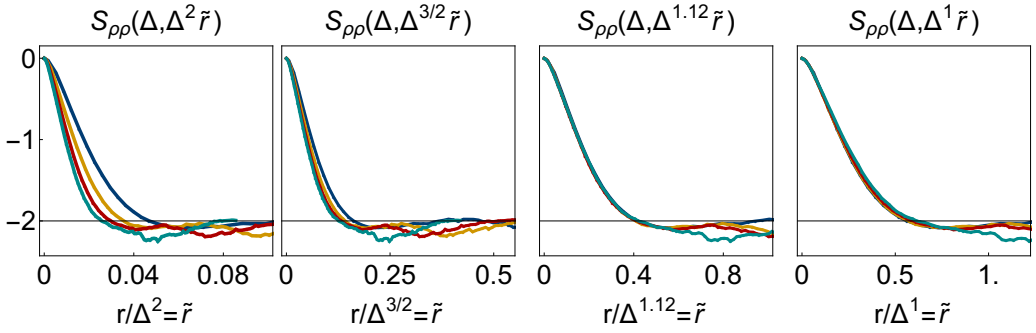

Figure 12.11: **Different scalings of $S_{\rho\rho}$.** The data is the same as used in Fig. 12.8. This motivates our choice $\alpha_{\text{num}} = 1.12$. A scaling with Δ^2 can be clearly excluded in the simulated parameter range.

$$\frac{\langle Q \rangle}{V} = -4\pi \int ds\, s^2\, C^{\text{nl}}_{\rho\rho}(\Delta, s), \tag{12.23}$$

$$\langle \phi\, \phi \rangle = -8\pi^2 \int ds\, s^3\, C^{\text{nl}}_{\rho\rho}(\Delta, s) + \mathcal{O}\left(L^{-1}\right). \tag{12.24}$$

Let us first consider by means of scaling what happens if we assume that there is a single lengthscale. Then $C^{\text{nl}}_{\rho\rho}(\Delta, s)$ has a scaling form $C^{\text{nl}}_{\rho\rho}(\Delta, s) = \Delta^{-\beta}\, \overline{C^{\text{nl}}_{\rho\rho}}(s/\Delta^{\alpha})$, where the scaling function $\overline{C^{\text{nl}}_{\rho\rho}}$ does not depend on Δ. We then find from the leading order in Eqns. (12.23) and (12.24), and Eqns. (12.14) and (12.15),

$$\Delta^0 \sim \int ds\, s^2\, C^{\text{nl}}_{\rho\rho}(\Delta, s) = \int ds\, s^2\, \Delta^{-\beta}\, \overline{C^{\text{nl}}_{\rho\rho}}(s/\Delta^{\alpha}) = \Delta^{-\beta+3\alpha} \int ds\, s^2\, \overline{C^{\text{nl}}_{\rho\rho}}(s) \tag{12.25}$$

$$\Delta^2 \sim \int ds\, s^3\, C^{\text{nl}}_{\rho\rho}(\Delta, s) = \int ds\, s^3\, \Delta^{-\beta}\, \overline{C^{\text{nl}}_{\rho\rho}}(s/\Delta^{\alpha}) = \Delta^{-\beta+4\alpha} \int ds\, s^3\, \overline{C^{\text{nl}}_{\rho\rho}}(s). \tag{12.26}$$

This implies $-\beta + 3\alpha = 0$ and $-\beta + 4\alpha = 2$ and therefore $\alpha = 2$ and $\beta = 6$. There is a length $R_s \sim \Delta^2$ and a typical charge density $\sim 1/\Delta^3$. This is a refined version of the argument due to Skinner and Shklovskii presented above in Eq. (12.3). However, this is not consistent with our numerical results. They suggest that there is a lengthscale $\sim \Delta^{\alpha_{\text{num}}}$ with α_{num} in the range $1.0 - 1.2$. Here and in the following the subscript "num" indicates the values estimated from the numerical results. Later, in section 14, we will see more evidence for a lengthscale $\sim \Delta^{\alpha \approx 1}$ also for larger values of Δ up to ~ 40. In Fig. 12.11 we show 4 different scalings of the screening function $S_{\rho\rho}$. A scaling $\sim \Delta^2$ can be clearly excluded in the simulated parameter range. The plot motivates our choice $\alpha = 1.12$ as used in Fig. 12.8. Below we present 3 scenarios which are, more or less, consistent with the numerical results. All of them have influence in the experimental relevant regime $\Delta \gtrsim 20$ [234].

Scenario I. We cannot fully exclude that we have not yet reached the scaling regime with the simulated parameter range. This would mean that eventually, for very large Δ, there is a lengthscale $R_s \sim \Delta^2$ and a typical charge density $\sim 1/\Delta^3$. The scaling function would fulfill $C_{\rho\rho}^{\rm nl}{}^{(I)}(\Delta, s) = \Delta^{-6}\, \overline{C_{\rho\rho}^{\rm nl}}^{(I)}(s/\Delta^2)$ and the Coulomb energy density would be $\sim -1/\Delta^2$.

In Fig. 12.12 the width of the potential distribution $P_R(\phi)$, see Fig. 12.6, is shown. $\langle\phi\phi\rangle_R$ is calculated by taking into account only charges within a sphere of radius R. On a short lengthscale $\sim 0.5\Delta$ a large potential builds up which exceeds the eventual value at $R \to L$. In the left panel it is seen that the potential reaches its final value only when $R \sim L$. The large values of $\langle\phi\phi\rangle_{R\sim\Delta}$ make it possible that the potential changes by Δ on a lengthscale $\sim \Delta$. The maximum $\langle\phi\phi\rangle_{\rm max}$ is well described by a fit function $f_{\rm max}(\Delta) \approx 1.04\,\Delta^{1.39}$ (not shown). In Fig. 12.5 two fit functions for the asymptotic value $\langle\phi\phi\rangle_L \equiv \langle\phi\phi\rangle$ were shown: $f_1(\Delta) = 0.043\,\Delta^2 + 0.562\,\Delta$ and $f_2(\Delta) = 0.016\,\Delta^2 + 0.562\,\Delta^{3/2}$. If we interpolate these fits to larger of Δ we find that $f_{\rm max}(\Delta) = f_1(\Delta)$ at $\Delta_1 \approx 160$ and $f_{\rm max}(\Delta) = f_2(\Delta)$ at $\Delta_2 \approx 325$. It might be that such large values of Δ are needed for the eventual crossover when $\langle\phi\phi\rangle$ exceeds $\langle\phi\phi\rangle_{R\sim\Delta}$. These values are far beyond any values that can be numerically simulated with present day computers. They are also larger than the typical values in the highly compensated topological insulators.

Scenario II. Let us consider the situation when the result depends system size L. We make the ansatz

$$C_{\rho\rho}^{\rm nl}{}^{(II)}(\Delta, s) = \Delta^{-\beta_1}\, \overline{C_{\rho\rho}^{\rm nl}}^{(IIa)}(s/\Delta^{\alpha_1}) + \Delta^{\beta_2} L^{-\xi}\, \overline{C_{\rho\rho}^{\rm nl}}^{(IIb)}(s/L), \tag{12.27}$$

where the numerical results suggest that $\alpha_1 = \alpha_{\rm num} = 1.1 \pm 0.1$ and $\beta_1 = 3\alpha_{\rm num} = \beta_{\rm num} = 3.3 \pm 0.3$, see Fig. 12.8. This gives the leading order term in Eq. (12.25) and a subleading term $\sim \Delta^{\alpha_{\rm num}}$ in Eq. (12.26). The corresponding Coulomb energy gain is $\sim \Delta^{-\alpha_{\rm num}}$. From Eqns. (12.14) and (12.15) we find

$$\Delta^0 + c_1\, \frac{1}{\Delta^{\gamma>0}} \sim \int ds\, s^2\, C_{\rho\rho}^{\rm nl}(s) \qquad \sim \Delta^0 + c_3\, \Delta^{\beta_2} L^{3-\xi} \tag{12.28}$$

$$\Delta^2 + c_2\, \Delta^{\delta<2} \sim \int ds\, s^3\, C_{\rho\rho}^{\rm nl}(s) I(s/L) \sim \Delta^1 + c_4\, \Delta^{\beta_2} L^{4-\xi}. \tag{12.29}$$

If $\beta_2 = 2$ and $\xi = 4$ we find that $\langle \phi\, \phi\rangle \sim \Delta^2\, L^0$. The contribution to the charge density and energy density are $\frac{\langle Q\rangle}{V} \sim \Delta^2 L^{-1}$ and $\frac{\langle H_{\rm C}\rangle}{V} \sim \Delta^2 L^{-2}$, respectively. This is consistent with the result shown in Fig. 12.12 where a clear system size dependence

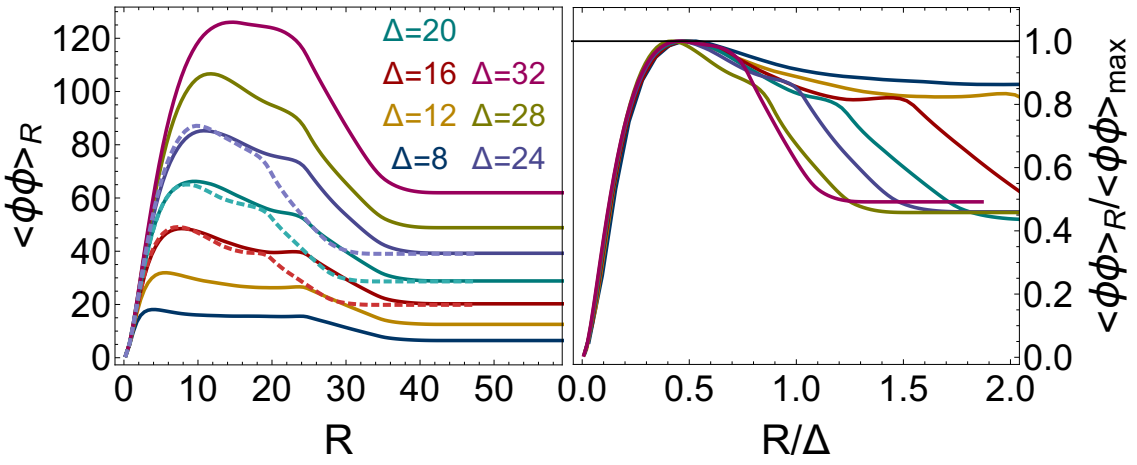

Figure 12.12: **The width of the potential distributions $P_R(\phi)$.** It was calculated as the second moment of the distributions $P_R(\phi)$ shown Fig. 12.6. In the left panel the solid lines are results for $L = 50$ while the dashed lines are results for $L = 40$. The asymptotic values at $R \sim L$ coincide suggesting the absence of finite size effects. Also the behavior at short distances $R \lesssim 20$ is approximately independent of L. In the right panel the data are divided by their maximum value. When R is scaled by $\Delta^{\alpha \approx 1}$ the short distance behavior, $R \lesssim 0.5\,\Delta$, is independent of Δ.

can be seen in the left panel. While the short distance and the asymptotic behavior are not much influenced by the system size, there is an intermediate regime where L matters. This scenario implies the absence of screening: full charge neutrality is reached only on lengthscales of the order of the system size.

Scenario III. Let us consider the scaling behavior when there are two lengthscales. We make the ansatz

$$C_{\rho\rho}^{\mathrm{nl}\,(III)}(\Delta, s) = \Delta^{-\beta_1}\, \overline{C_{\rho\rho}^{\mathrm{nl}}}^{(IIIa)}(s/\Delta^{\alpha_1}) + \Delta^{-\beta_2}\, \overline{C_{\rho\rho}^{\mathrm{nl}}}^{(IIIb)}(s/\Delta^{\alpha_2}), \tag{12.30}$$

where we again choose $\alpha_1 = \alpha_{\mathrm{num}}$ and $\beta_1 = \beta_{\mathrm{num}}$ according to the numerical results. If we include the subleading terms in Eqns. (12.14) and (12.15) we find

$$\Delta^0 + c_1\, \frac{1}{\Delta^{\gamma>0}} \sim \int ds\, s^2\, C_{\rho\rho}^{\mathrm{nl}}(s) \sim \Delta^0 + c_3\, \Delta^{-\beta_2+3\alpha_2} \tag{12.31}$$

$$\Delta^2 + c_2\, \Delta^{\delta<2} \sim \int ds\, s^3\, C_{\rho\rho}^{\mathrm{nl}}(s) \sim c_4\, \Delta^{-\beta_2+4\alpha_2} + \Delta^{\alpha_{\mathrm{num}}}. \tag{12.32}$$

From the second contribution, $\overline{C_{\rho\rho}^{\mathrm{nl}}}^{(2)}$, we then get the relations $-\gamma = -\beta_2 + 3\alpha_2$ and $2 = -\beta_2 + 4\alpha_2$. This are two equations for three unknown variables and we would need

an additional equation to solve this. We can deduce that $\gamma = \alpha_2 - 2 > 0$ and therefore $\alpha_2 > 2$. From the numerical results, we can also see that $\gamma \geq 1$, see Fig. 12.9. This leads to $\alpha_2 \geq 3$ and $\beta_2 \geq 10$. This scenario implies that the lengthscale dependence as seen in Figs. 12.8 and 12.12 is a finite size effect where the $\Delta^{\alpha \geq 3}$ scale is squeezed by the system size. This further includes an overscreening on a scale $\sim \Delta^{1.1 \pm 0.1}$ while full charge neutrality, screening, is only realized on a length $\sim \Delta^{\alpha_2 \geq 3}$.

The pseudo-groundstate algorithm is tailored to minimize the total energy. This is the sum of the neutralization energy Δn_0 and the Coulomb energy and we expect a competition of this two terms. Neutralization of a pair at an energy cost of Δ can arise as long as the Coulomb energy gained by this is $> \Delta$. The total energy is given as, see Eq. (12.20),

$$\begin{aligned} \langle H_\mathrm{n} + H_\mathrm{C} \rangle &= V \left(\Delta/2 + \pi\, \Delta \int ds\, s^2\, C^{\mathrm{nl}}_{\rho\rho}(\Delta, s) + 2\pi \int ds\, s\, C^{\mathrm{nl}}_{\rho\rho}(\Delta, s) \right) \\ &= V \left(\Delta/2 + 2\pi \int ds\, s\, C^{\mathrm{nl}}_{\rho\rho}(\Delta, s) \left(1 + s\, \frac{\Delta}{2} \right) \right). \end{aligned} \tag{12.33}$$

In all scenarios the constant term $V\Delta/2$ is canceled by the contribution leading to $\langle Q \rangle / V \sim \Delta^0$. In scenario I there is no subleading term to $\langle H_\mathrm{n} \rangle$ and in scenario II it is $\sim \Delta^2 L^{-1} \to 0$.

In the following we make the additional assumption that both energy contributions scale in the same way for large Δ: $\langle H_\mathrm{n} \rangle \sim \langle H_\mathrm{C} \rangle \sim \Delta^{-\nu}$. While plausible, this is not justified apriori. In scenario III the leading order in $\langle H_\mathrm{C} \rangle$ is $\sim \Delta^{-\alpha_\mathrm{num}}$. To obtain the same scaling for the neutralization energy we need $\alpha_2 = 3 + \alpha_\mathrm{num} = 4.1 \pm 0.1$ and $\beta_2 = 10 + 4\alpha_\mathrm{num} = 14.4 \pm 0.4$. This implies $\gamma = 1 + \alpha_\mathrm{num} = 2.1 \pm 0.1$ and $n_0 \sim \Delta^{-1-\alpha_\mathrm{num}}$. This is consistent with the numerically found n_0, see Fig. 12.9. The total energy gain is $\sim \Delta^{-\alpha_\mathrm{num}}$. From I in Eq. (12.13) we expect corrections of order Δ^4/L which is of course by no means small for the parameters used here. It is not possible to numerically check the scaling $C^{\mathrm{nl}\,(IIIb)}_{\rho\rho}(\Delta, s) = \Delta^{-(10+4\alpha_\mathrm{num})}\, \overline{C^{\mathrm{nl}}_{\rho\rho}}^{(IIIb)}(s/\Delta^{3+\alpha_\mathrm{num}})$.

One can also include a further term in scenario I which accounts for the neutral dopants. The typical charge density accumulated in a screened volume $V_S \sim (\Delta^2)^3$ is $\sim V_S^{-3/2} \sim \Delta^{-3}$. To ensure charge neutrality in V_S the density of neutral dopants has to be $n_0 \sim \Delta^{-3}$. If we change the scaling function to

$$C^{\mathrm{nl}\,(I)}_{\rho\rho}(\Delta, s) = (\Delta^{-6} - a_{(I)} \Delta^{-9})\, \overline{C^{\mathrm{nl}}_{\rho\rho}}^{(I)}(s/\Delta^2), \tag{12.34}$$

the new term gives a subleading contribution to the total charge, which is then $Q_0^{(I)} =$

$N_{\mathrm{tot}}(1 - a_{(I)}\Delta^{-3})$. It also accounts for a neutralization energy $\sim 1/\Delta^2$ in agreement with the Coulomb energy. However, the total energy gain is only $\sim 1/\Delta^2$ and thus smaller by a factor of $\Delta^{2-\alpha_{\mathrm{num}}\approx 0.9}$ when compared to scenarios II and III.

Based on the numerical results presented in this section, it is not possible to rule out one of the scenarios. Larger values of Δ are needed to see the eventual scaling behavior. However, for larger values of Δ, larger systems sizes are needed to avoid finite size effects, and these can not be simulated with reasonable computational effort. For analytical insights, a tailored disorder renormalization group or replica method is probably needed.

12.3 Puddles

In the modeling, an electronic puddle corresponds to a spatial accumulation of neutral dopants. Electron puddles are formed by neutral donors, while hole puddles are formed by neutral acceptors. Neutral dopants, and therefore puddles, can emerge only in regions where the potential exceeds half of the band gap. Only then the interaction energy gained by discharging a pair of dopants can be larger than the band gap Δ. In Fig. 12.13 we show a typical $1d$-cut of the potential. The local energies $\phi(\boldsymbol{r}) \pm \Delta/2$ of acceptors (lower solid line) and donors (upper solid line) can exceed the Fermi level μ. Here electron and hole puddles can form as indicated by the colored regions in the figure. A typical $3d$ configuration is shown in Fig. 12.14. Neutral acceptors and donors are colored differently. One can see that neutral dopants of equal type tend to form clusters, which have to be identified with the puddles.

Since the effective Bohr radius of a neutral dopant is very large, see section 11, the wave functions of electrons or holes of close-by neutral dopants overlap. Furthermore the potential fluctuations within a puddle are small $\sim \mathrm{E_c}$, see Fig. 12.13. Charges in

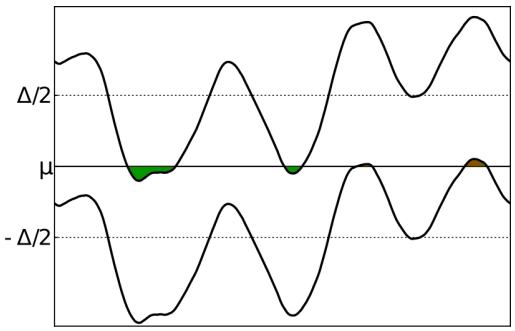

Figure 12.13: **Typical potential fluctuations in the groundstate.** Shown is the energy diagram (energy vs. space). The dashed lines indicate the upper and lower band edges. The solid lines show the potential fluctuations $\phi(\boldsymbol{r}) \pm \Delta/2$ as seen by acceptors (lower line) and donors (upper line). When this crosses the Fermi level μ puddle formation arises. Electron puddles formed by neutral donors are shown in green, while hole puddles formed by neutral acceptors are shown in brown. The fluctuations of the potential do not exceed the Fermi level by more than E_c. The data is obtained from a simulation where $\Delta = 5$.

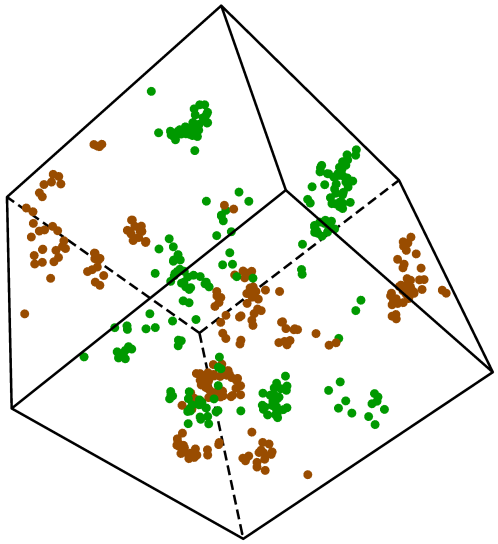

Figure 12.14: **Real space picture of puddles.** Neutral donors are shown in green, while neutral acceptors are shown in brown. One can clearly see the clustering of neutral dopants of the same kind. These clusters are the electronic puddles, which form locally conducting regions in space. The data is obtained from a simulation where $\Delta = 10$.

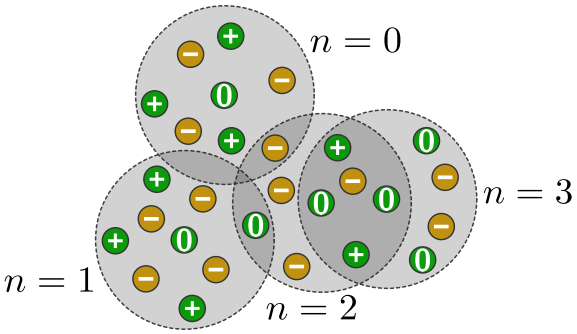

Figure 12.15: **Schematic plot of puddle identification.** To estimate the puddle density we consider an imaginary sphere of radius $r = 1.42\,N^{-1/3}$ (explained in the main text) around each neutral dopant. The fraction of spheres with n additional neutral dopants of the same type is denoted by $p_0(n)$. We define the puddle density as $p_p = \sum_{n\geq 4} p_0(n)$. This $2d$ plot does not reflect any properties of the $3d$ system.

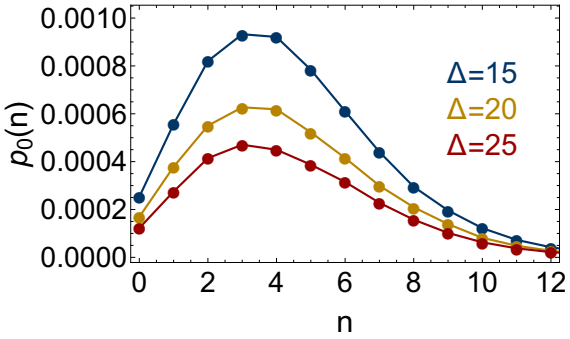

Figure 12.16: **The fraction of neutral dopants with n neutral neighbors.** The quantity $p_0(n)$ is explained in the caption of Fig. 12.15. In the groundstate, neutral dopants show a tendency to form clusters as seen by the maximum at $n = 3 - 4$.

such regions are mobile and can contribute to the optical weight. However, there has to be some critical accumulation which cannot be deduced from the static model. A theory taking into account the response to the applied field and the frequency dependence of the dielectric constant would be needed.

The problem is to find an appropriate measure for the density of charge carriers located within the puddles. A neutral dopant contributing to a puddle shall have neutral dopants of the same type in its vicinity. Therefore, to decide whether a neutral dopant belongs to a puddle or not, we count the number of neutral dopants of the same type within a sphere of radius $r_0 = 1.42N^{-1/3}$. This, somewhat arbitrary, choice is made such that on average there are 12 dopants of the same type within the sphere. This corresponds to the number of nearest neighbors in a close-packing of spheres. In the following when we use the term "y has x neighbors" we always refer to the imaginary sphere with radius $1.42N^{-1/3}$ as explained above. In Fig. 12.15 we show a schematic $2d$ plot of an electron puddle. The color indicates the type of the dopant, green corresponds to acceptors, while donors are colored brown. The symbol on each dopant indicates its charge. Around each neutral dopant we draw a sphere and count the number of neutral donors n within the sphere, examples with $n = 0, 1, 2, 3$ are shown. Note that this $2d$ plot does not reflect any properties of the $3d$ system and is shown only for illustration purposes.

As an observable we calculate the fraction of neutral dopants with n neutral

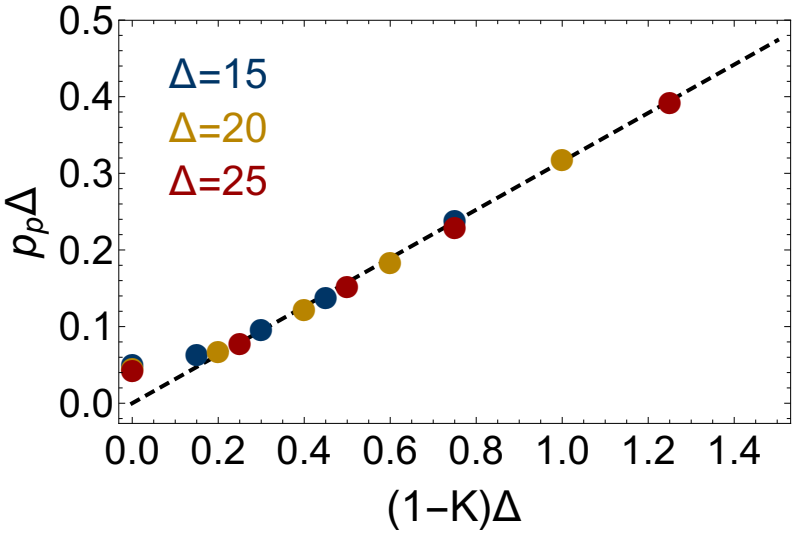

Figure 12.17: **Puddle density at lower compensation.** For $(1-K)\Delta \gtrsim 0.3$ the puddle density does not depend Δ anymore but is fully controlled by the excess dopants. The black dashed line is a fit $p_p = 0.316(1-K)$.

neighbors, denoted by $p_0(n)$. We then, again somewhat arbitrarily, define that a neutral dopant belongs to a puddle if it has at least 4 neutral neighbors. We have checked that the results do not depend qualitatively on this choice. A similar criterion to identify clusters in disordered systems was used in [262]. We define the fraction of dopants located within a puddle as

$$p_p = \sum_{n\geq 4} p_0(n). \tag{12.35}$$

Then the density of dopants located in puddles, we will call this the puddle density, is $(N_A + N_D)p_p$. This is, of course, unrelated to any operational definition of puddles. A proper definition would be to identify a puddle by its contribution to the optical weight.

In Fig. 12.16 we show the distribution of $p_0(n)$ in the groundstate for perfect compensation, $K = 1$, and $\Delta = 15, 20, 25$. One can clearly see the tendency to form clusters: isolated neutral dopants are rare and the curves show a maximum at $n = 3-4$.

Up to now we have discussed only the case of perfect compensation $N_A = N_D$. For imperfect compensation, $K = N_A/N_D < 1$, puddles will be dominantly formed by donors leading to $n-$doped regions. The excess density of neutral donors is $(1-K)N_D$. When this becomes larger than the puddle density at perfect compensation, we expect that the puddles are mainly formed by the excess donors. This is shown in Fig. 12.17.

For $(1-K)\Delta \gtrsim 0.3$ the puddle density is independent of Δ. A fit, shown by the black dashed line, yields $p_p \approx 0.32(1-K)$.

This is not in agreement with the arguments given in section 11.1, see in particular the discussion related to Eq. (11.5). Following Efros and Shklovskii [211], it was stated that potential fluctuations larger than $\frac{(1+K)^{2/3}}{(1-K)^{1/3}}\,\mathrm{E_c}$ can be screened by excess dopants. This implies a crossover as a function of $\Delta^3 \frac{1-K}{(1+K)^2} \overset{K\to 1}{\sim} \Delta^3(1-K)$. This can be clearly excluded in the parameter regime shown in Fig. 12.17. The discrepancy is a manifestation of the different lengthscales as discussed above.

13 Puddle destruction at finite temperatures

In this section we will study the finite temperature dependence of the disordered Coulomb system by a Monte Carlo algorithm as introduced in section 11. Finite temperature Monte Carlo simulations have been performed for disordered Coulomb systems before [247, 256, 257, 263–265]. The model simulated in these references is the Coulomb glass model as introduced in Eq. (11.14). This model also shows a Coulomb gap at $T = 0$, and the focus in the references given above is on the finite temperature behavior of the Coulomb gap or on the possible existence of a glass transition. The Coulomb glass model was claimed to have a glass transition at finite temperatures within mean-field theory [266–268], but this was not confirmed numerically in $3d$ [256, 257].

However, we have not found any finite T simulations for the model of shallow impurities, Eq. (11.10), in the literature. In our analysis the focus is on the temperature behavior of the puddles. In section 12 we have seen that electronic puddles, accumulations of neutral dopants, form at low temperatures. We will show in the following that the puddles disappear on a temperature scale given by the Coulomb interaction of neighboring dopants E_c. At higher temperatures the puddles reappear in a thermally activated manner. This mechanism can explain the experiment presented in section 10 qualitatively.

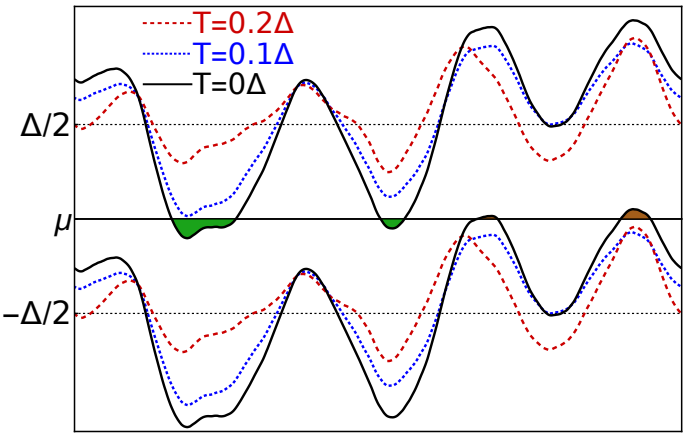

Figure 13.1: **Typical spatial potential fluctuations at finite temperatures.** Compared to the $T = 0$ case, the black line, the potential fluctuations are reduced at finite temperatures. This implies that the potential is screened by thermal fluctuations. The potential does not exceed the band edges at $\pm\Delta/2$ any more. The data is obtained from a simulation where $\Delta = 5$.

13.1 Thermal screening

The main effect of finite temperatures can be already be anticipated from Fig. 13.1: the fluctuations of the potential are reduced with increasing temperature. This can be seen in more detail in Fig. 13.2. In the left panel we show the d.o.s. at finite

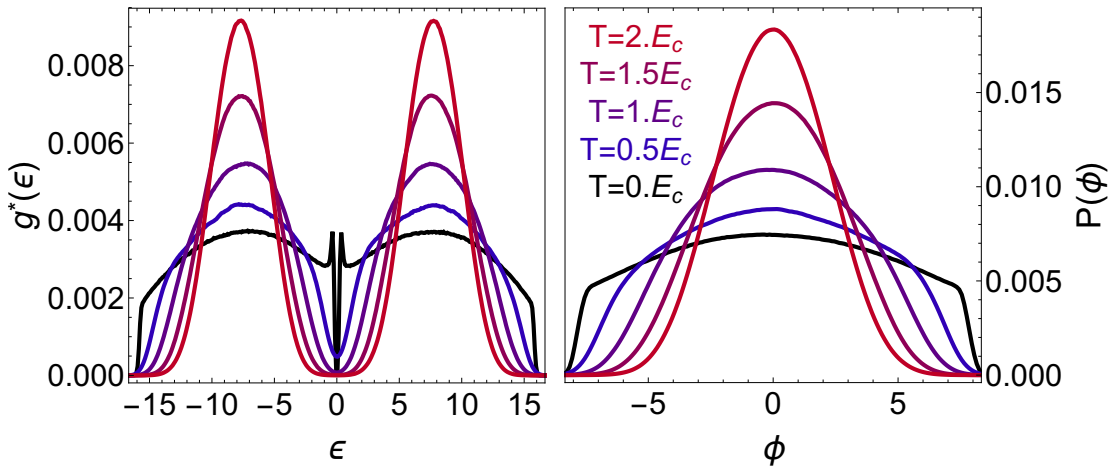

Figure 13.2: **Single-particle density of states and potential distribution at finite temperatures.** The left panel shows the d. o. s. which shows a Coulomb gap at $T = 0$. At intermediate $T \sim \mathrm{E_c}/2$ the Coulomb gap vanishes and there is a finite d.o.s. at $\epsilon = 0$. With increasing T, a thermal gap builds up. The right panel shows that the potential fluctuations are suppressed at finite temperatures. With increasing temperature the width of the potential distribution is reduced approaching its non-interacting shape. Parameters used in this plot are $\Delta = 15$, $a_\mathrm{B} = 2$, $L = 40$ ($T > 0$) and $L = 50$ ($T = 0$).

temperatures. It shows a Coulomb gap in the groundstate, see section 12.1. At temperatures $T \leq \mathrm{E_c}$ the Coulomb gap vanishes and there is a finite d.o.s. at $\epsilon = 0$. At higher temperatures the gap at reappears but it is of different origin. With increasing temperature the d.o.s. approaches its non-interacting shape: two peaks at $\pm\Delta/2$ reflecting the bare dopant energies. One can notice a similarity to the results for an externally screened interaction, see section 12.1. Therefore we call this effect *thermal screening*. It is also seen in the distribution of the potential as shown in the right panel of Fig. 13.2. With increasing temperature the potential fluctuations, the width of the distribution, are reduced. This implies an enhanced screening.

The thermal screening can also be seen in the simulations of the Coulomb glass model. Here the non-interacting d.o.s. is just a flat distribution reflecting that the random on-site energies are chosen from a box distribution. In [264], for example, the d.o.s. at finite T was studied. In Fig. 1 b) there it can be clearly seen that the it approaches a box shape with increasing temperature. In [257] it was found that the d.o.s. $g(\epsilon \to 0, T) \sim T^2$, in agreement with simple scaling arguments since $g(\epsilon \to 0, T = 0) \sim \epsilon^2$. We have not checked this. In [268] it was pointed out that simple Thomas-Fermi theory predicts a screening length $r_s \sim g(\mu, T)^{-1/2} \sim 1/T$. To our

knowledge this has also not been checked numerically.

13.2 Numerical results

We now want to study the effect of the thermal screening on the puddle formation. In Fig. 13.3 we show the density of neutral dopants n_0 as a function of the temperature for $K = 1$ and $K = 0.95$. One can see that it increases with increasing temperature. At low temperatures n_0 saturates at a finite value, see section 12. For $K = 0.95$ this value is independent of Δ. This monotonic temperature behavior can not explain the experimental observations. This is another justification for our assumption that isolated neutral dopants do not contribute to the optical weight in the frequency range studied in the experiment. Therefore we analyze the puddle density.

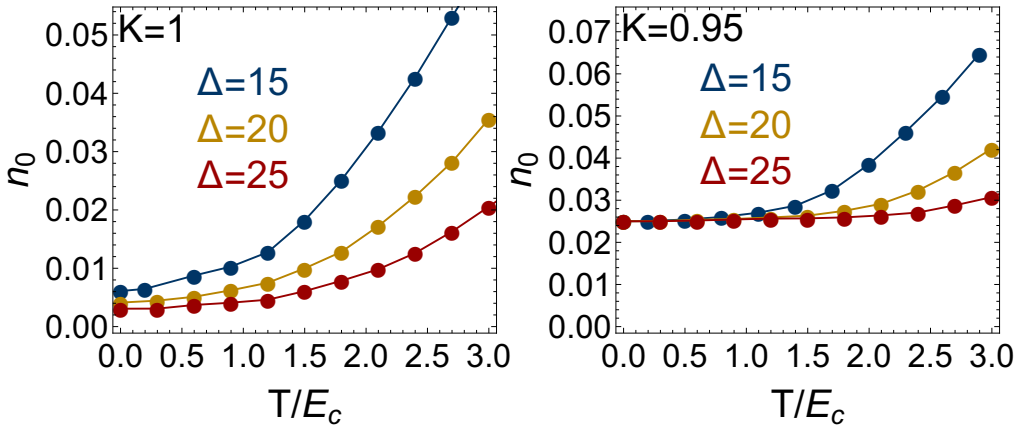

Figure 13.3: **Density of neutral dopants at finite temperatures.** It increases with increasing temperature and can not explain the non-monotonic behavior found in the experiment. For $K = 0.95$ the low temperature density is independent of the temperature. At higher temperatures an activated behavior is seen.

p_p, as introduced in Eq. (12.35), is very sensitive on the choice of the short distance cutoff a_B. In Fig. 13.4 results for $a_B = 0.5, 1, 2$ are shown. For $a_B = 2$, p_p shows a very pronounced minimum and the puddle density is highly suppressed on a temperature scale $T \sim E_c$. For $a_B = 1$ there is still a minimum, albeit much less pronounced. For $a_B = 0.5$ there is almost no reduction of p_p at temperatures $T \sim E_c$. In the following we present only results for $a_B = 2$.

In Fig. 13.5 we show the distribution of neutral dopants $p_0(n)$ at different temperatures and $\Delta = 15$. n_0 is obtained as $p_p = \sum_{n=0}^{\infty} p_0(n)$. The main effect we are interested in is the reduction of the neutral dopants located in puddles $p_p = \sum_{n\geq 4} p_0(n)$. In

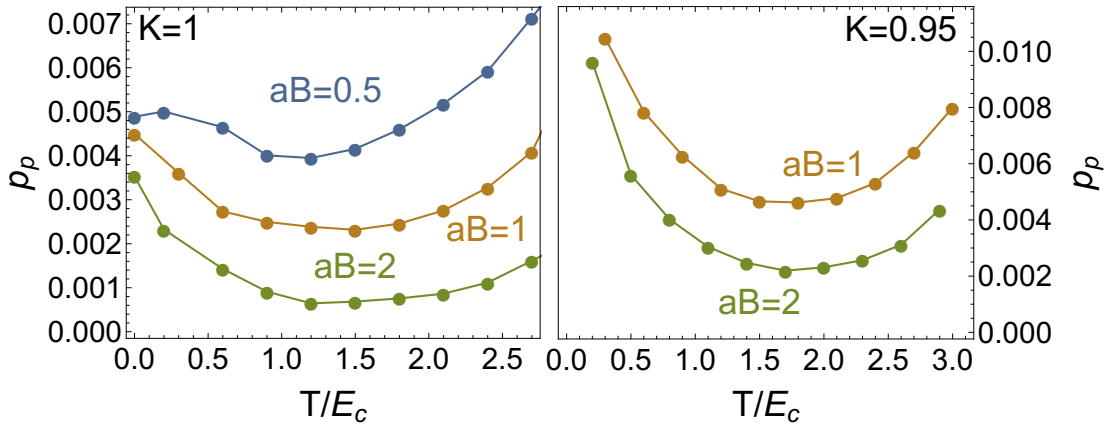

Figure 13.4: **Cutoff dependence of p_p.** This quantity, as defined in section 12.3, is very sensitive on the choice of the short distance cutoff $a_{\rm B}$. Results are shown for $\Delta = 15$ and $L = 40$. In the following only results for $a_{\rm B} = 2$ are presented where a drastic reduction of p_p arises on a temperature scale $T \sim {\rm E_c}$.

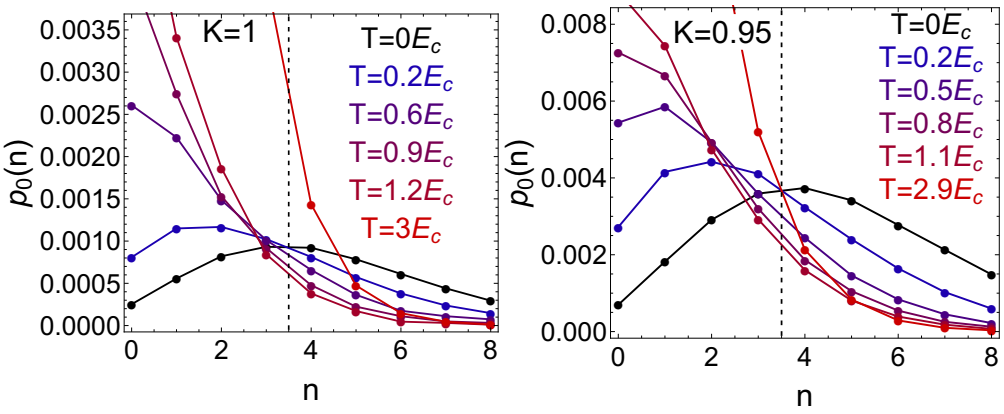

Figure 13.5: **Distribution of neutral dopants at finite temperatures.** Results are shown for $\Delta = 15$ with $K = 1$ (left panel) and $K = 0.95$ (right panel). The density of neutral dopants with a small number of neutral neighbors increases with temperature. By contrast, the density of neutral dopants with many neutral neighbors decreases for temperatures $T \lesssim {\rm E_c}$. At higher temperatures it increases again due to thermal activation.

the groundstate, $p_0(n)$ shows a maximum at $n = 3-4$ indicating the correlation origin of the puddles. At finite temperatures the total number of neutral dopants increases, see Fig. 13.3, but p_p decreases: most of the thermally activated neutral dopants are isolated or only have a very small number of neutral nearest neighbors. Within the puddles thermal fluctuations recharge neutral dopants which leads to a significant reduction of neutral dopants with more than 3 neutral neighbors. As can be seen in the left panel of Fig. 13.5, at $K = 1$ the occupation at $n = 3$ is almost independent

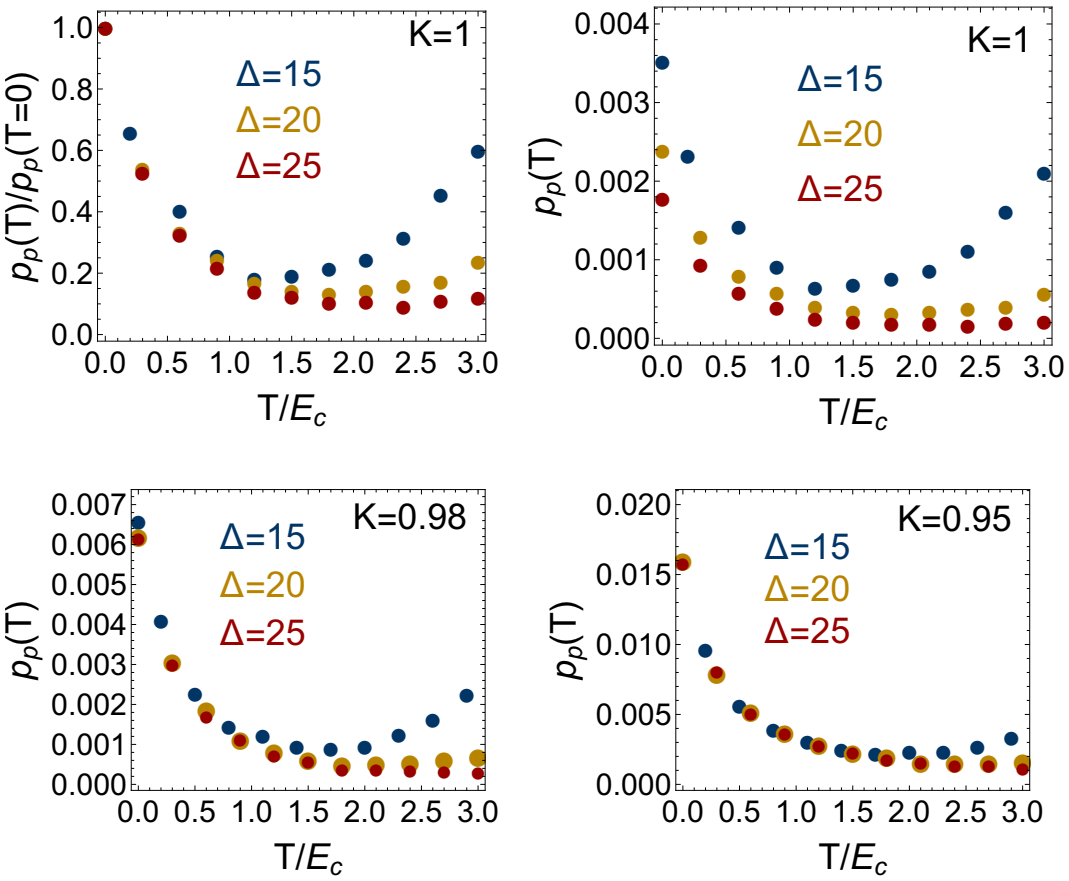

Figure 13.6: **Puddle density at finite temperatures.** At low temperatures p_p decreases on a scale $T \sim \mathrm{E_c}$ independent of the band gap Δ. At higher temperatures puddles are thermally activated, the activation energy depends on Δ and K. For $K = 1$ two plots are shown. In the left panel the data are normalized by the $T = 0$ value. Then the puddle destruction is almost independent of Δ. The $T = 0$ value of p_p does not show scaling behavior in the simulated parameter range.

of the temperature. This is compatible with our definition of puddles with $n_{\mathrm{min}} = 4$: thermal fluctuations outside the puddles increases the number of neutral dopants, while thermal fluctuations within the puddles reduce the number of neutral dopants.

In Fig. 13.6 we show the puddle density for different values of Δ and K. For all simulated parameters, p_p decreases on a temperature scale $T \sim \mathrm{E_c}$. For larger T thermal activation reincreases p_p. While the decrease at low T is independent of Δ, the activation energy depends on Δ. For $K = 0.98$ and $K = 0.95$ the results at low temperatures are completely independent of Δ. The values are proportional to the excess density and approximately given by $0.32\, N(1 - K)$, see Fig. 12.17. For $K = 0.98$ this gives 0.0064 and for $K = 0.95$ this gives 0.016 in agreement with Fig. 13.6. This shows

that the puddles are almost exclusively formed by the donors. This can be directly seen by plotting the contributions to p_p from acceptors and donors independently (not shown).

13.3 Comparison to the experiment

As shown in section 10, the main result of the experimental study was the temperature dependence of the optical weight or, equivalently, the effective carrier density $N_{\text{eff}} = N_{\text{exp}}\, m_e/m^*$. Qualitatively we can explain the minimum in the experiment, see Fig. 10.6, by thermal screening effects as explained above. The density drops at a typical temperature scale $\sim \mathrm{E_c} = \frac{e^2 N^{1/3}}{4\pi\varepsilon\varepsilon_0}$ independent of Δ, the increase is of an activated origin and therefore does depend on Δ. The dopant density N is not precisely known for the sample used in the experiment. It was estimated to $N \approx 10^{19} - 10^{20}\,\mathrm{cm}^{-3}$ by the experimentalists. Inserting this, and $\varepsilon = 200$, we find

$$\mathrm{E_c^{exp}} = \frac{e^2 (10^{19} \ldots 10^{20})^{1/3}}{4\pi \times 200 \varepsilon_0\, cm} \approx 20 \ldots 40 K. \tag{13.1}$$

This is in good agreement with the temperature scale for the minimum found in the experiment, see Fig. 10.6, which was seen at $30 - 40\,K$.

For the dimensionless gap, $\Delta/\mathrm{E_c}$, we then find $0.26\,eV/(30 \ldots 40K) \approx 75 - 150$. To estimate the density of charge carriers located in puddles, $N_{\text{pudd}} = N_{\text{eff}}\; m^*/m_e$, we need the effective mass. In [242] it was measured to $m^* = 0.14 - 0.24\, m_e$ in $Bi_2\,Se_3$ depending on the orientation. As in section 11, we will use $m^* = 0.2\, m_e$. This yields $N_{\text{exp}} \approx 0.2 N_{\text{eff}} \approx 2 \times 10^{17}\,\mathrm{cm}^{-3}$ at low temperatures. This leads to a puddle density of $N_{\text{pudd}}/N_{\text{exp}} = 0.002 - 0.005$ at $5K$. As seen in Fig. 13.6 the value for $T \to 0$ is expected to be a bit larger. Hence, the experimental system was probably in the excess dominated regime, see Fig. 12.17, where the $K = 1$ behavior is not that important. Estimating the experimental K_{exp} via $p_p \approx 0.316(1-K)$ as found in section 12.3, we find $K_{\text{exp}} = 0.97 - 0.99$ for $N = (4 - 10) \times 10^{19}\,\mathrm{cm}^{-3}$. Here we have assumed that the $T = 0$ value is 1.5 times the value at $T = 5\,K$, which is approximately fulfilled for all values of K. In Fig. 13.7 we compare the experimental results to simulations with $\Delta = 25$ and $K = 0.98$. In this regime the results for $T \lesssim \mathrm{E_c}$ are independent of Δ, see Fig. 13.6. The experimental data are scaled to the dimensionless units as used in the simulation. We have assumed $\varepsilon = 200$ and $m^* = 0.2\, m_e$ to calculate $\mathrm{E_c}$ and $N_{\text{exp}} = N_{\text{eff}}\, m^*/m_e$. Results for different values of N are shown. We can see that the results for $N \approx 7 \times 10^{19}\,\mathrm{cm}^{-3}$ give the best agreement.

However, in Fig. 13.4 we have shown that our definition of p_p is very sensitive

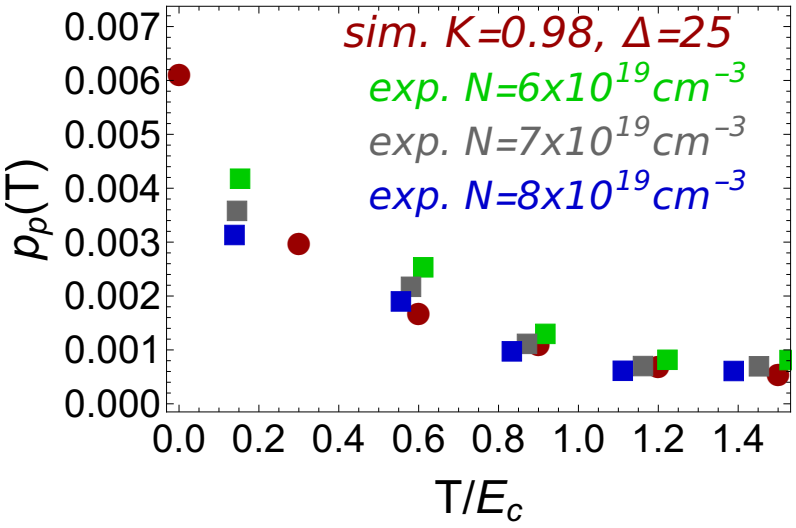

Figure 13.7: **The experimental data in the dimensionless units used in the simulations.** To convert the data we have used $\varepsilon = 200$, $m^* = 0.2\,m_e$ and different values of N as shown. K is estimated in the main text to $0.97 - 0.99$, here we compare the data with the theoretical results for $K = 0.98$.

to the choice of a_{B}. Furthermore, it was defined in a somewhat arbitrary manner unrelated to any operational definition. Nevertheless, the characteristic energy scale of the decrease in the density connects the experimental results with the simulations. It is independent of the choice of a_{B}, see Fig. 13.4. By using the experimentally unknown N and K as fit parameters, one can also reach a quantitative agreement. The parameters obtained in this way ($N_{\mathrm{exp}} \approx 7 \times 10^{19}\,\mathrm{cm}^{-3}$ and $K_{\mathrm{exp}} \approx 0.98$) are reasonable and well within the realistic experimental range.

14 Including the surface states

In the previous sections we have omitted the main feature which make the materials under study interesting: the fact that they are topological insulators (TIs). In section 10 we have shown that the influence of the surface states was negligible in the experiment. Therefore we have not included them in the theoretical analysis. But close to the surface, or for thin samples, the surface states and the charges in the bulk influence each other. In this section we want to investigate how this effect arises and we want to quantify what "close to the surface" or "thin samples" mean. The surface states contribute an additional screening channel and we want to investigate how far the effect reaches into the bulk. To study the influence of the surface in detail, we have to review some basic properties of $2d$ Dirac systems and screening theory.

14.1 Dirac systems

Since the surface states form a Dirac cone on the surface their electronic properties are similar to that of graphene [269, 270]. While graphene has four Dirac cones in the first Brillouin zone, the surface of a TI shows an odd number of Dirac cones. We will consider static properties of a single Dirac cone only.

A $2d$ Dirac system is characterized by two bands with a linear dispersion $E_\pm(\boldsymbol{q}) = \pm\hbar v_F q$. The density of electrons ($\mu > 0$) or holes ($\mu < 0$) for a single Dirac cone at $T = 0$ is given by (n_F is the Fermi function)

$$n_{e/h} = \int \frac{d^2\boldsymbol{q}}{(2\pi)^2}\, n_F(E(q)) = \frac{1}{8\pi}\left(\frac{\mu}{\hbar v_F}\right)^2. \tag{14.1}$$

Note that the spin degree of freedom, while present in graphene, is absent on the surface of topological insulators due to spin-momentum locking.

The interaction strength on the surface is characterized by the effective fine structure constant

$$\alpha = \frac{e^2}{4\pi\varepsilon_{\mathrm{s}}\hbar v_F} \text{ where } \varepsilon_{\mathrm{s}} = \frac{\varepsilon(z<0)+\varepsilon(z>0)}{2} = \frac{\varepsilon_{\mathrm{out}}+\varepsilon_{\mathrm{TI}}}{2}. \tag{14.2}$$

Here we have assumed that the TI surface is located at $z = 0$. The TI, with dielectric constant $\varepsilon_{\mathrm{TI}}$, is located at $z > 0$ and at $z < 0$ we have a different material, possibly vacuum, with a different dielectric constant $\varepsilon_{\mathrm{out}}$. We will use this convention throughout the rest of this section. If we insert realistic values, $v_F = c/1500$ (from [221], c

denotes the speed of light) and $\varepsilon_{\mathrm{TI}} = 200\,\varepsilon_0$, we find

$$\alpha = (2\varepsilon_0/\epsilon)\,(c/v_F)\,\alpha_{\mathrm{QED}} \approx 15\alpha_{\mathrm{QED}} \approx 0.11 \tag{14.3}$$

Evaluation of the bubble diagram yields the static polarization function

$$\Pi^R(\omega \to 0, q, \mu = 0, T = 0) = \frac{1}{2\pi}\,\frac{q}{\hbar v_F} \tag{14.4}$$

$$\Pi^R(\omega \to 0, q, \mu \gg T) = \frac{1}{2\pi}\,\frac{|\mu|}{(\hbar v_F)^2}. \tag{14.5}$$

The Fourier transformation of the Coulomb interaction $V(\boldsymbol{r}) = e^2/(4\pi\varepsilon\varepsilon_0 r)$ in two dimensions gives $U(\boldsymbol{q}) = e^2/(2\varepsilon_{\mathrm{s}} q)$. In random phase approximation (RPA) the effective interaction is given by

$$U_{\mathrm{RPA}}(\boldsymbol{q}, \omega \to 0) = \frac{1}{U^{-1}(\boldsymbol{q}) + \Pi^R(\boldsymbol{q}, \omega \to 0)}, \tag{14.6}$$

$$U_{\mathrm{RPA}}(\boldsymbol{q}, \omega \to 0, \mu \gg T) = \frac{e^2}{4\pi\varepsilon_{\mathrm{s}}(q + q_{\mathrm{s}})}, \tag{14.7}$$

where $q_{\mathrm{s}} = \alpha|\mu|/(\hbar v_F)$. For $\mu \neq 0$ the interaction is screened on a length $r_s = q_{\mathrm{s}}^{-1}$. In intrinsic graphene, where the Fermi level is exactly at the Dirac cone ($\mu = 0$), it is found that $\Pi(\boldsymbol{q}, \omega \to 0) \sim q$, see Eq. (14.4), and screening is a non-linear effect.

14.2 Screening theory

In the following we want to study the screening of the bulk potential by the Dirac cone on the surface. We denote the $2d$ coordinates on the surface ($z = 0$) by $\boldsymbol{x}$ and the corresponding wavevectors by $\boldsymbol{q}$. The $3d$ coordinates are denoted by $\boldsymbol{r}$. The distance of a point from the surface is denoted by d: we will use $\boldsymbol{r} = (\boldsymbol{x}, d)$ or $\boldsymbol{r} = (\boldsymbol{y}, d)$. The total potential on surface will be denoted by $\phi_{\mathrm{s}}(\boldsymbol{x})$ and is given by the external potential ϕ_{ext} plus the induced potential ϕ_{ind} as

$$\phi_{\mathrm{s}}(\boldsymbol{x}) = \phi_{\mathrm{ext}}(\boldsymbol{x}) + \phi_{\mathrm{ind}}(\boldsymbol{x}) = \phi_{\mathrm{ext}}(\boldsymbol{x}) + \int d^2\boldsymbol{x}'\,\frac{\rho_{\mathrm{ind}}(\boldsymbol{x}')}{4\pi\varepsilon_{\mathrm{s}}|\boldsymbol{x} - \boldsymbol{x}'|}. \tag{14.8}$$

Here ρ_{ind} is the induced surface charge density. The external potential is due to the randomly distributed acceptors and donors in the bulk. For charges q_j located at $\boldsymbol{r}_j = (\boldsymbol{y}_j, d_j)^T$ ($d_j > 0$) the bulk potential in a homogenous background (no space

dependence of the dielectric constant) is

$$\phi_{\text{ext}}^{\text{bulk}}(\boldsymbol{r}) = \sum_j \frac{q_j}{4\pi\varepsilon_{\text{TI}}} \frac{1}{|\boldsymbol{r} - \boldsymbol{r}_j|}. \tag{14.9}$$

To obtain the external potential $\phi_{\text{ext}}(\boldsymbol{q})$ on the surface, we first have to include the jump of the dielectric constant. The potential in the bulk ($z > 0$) in the presence of a dielectric boundary at $z = 0$ is given by [271]

$$\phi_{\text{ext}}^{\text{bulk}}(\boldsymbol{r}) = \sum_j \frac{q_j}{4\pi\varepsilon_{\text{TI}}} \left(\frac{1}{|\boldsymbol{r} - \boldsymbol{r}_j|} + \frac{\varepsilon_{\text{TI}} - \varepsilon_{\text{out}}}{\varepsilon_{\text{TI}} + \varepsilon_{\text{out}}} \frac{1}{|\boldsymbol{r} - \tilde{\boldsymbol{r}}_j|} \right) \tag{14.10}$$

where $\tilde{\boldsymbol{r}}_j = (\boldsymbol{y}_j, -d_j)^T$ is the mirror point of $\boldsymbol{r}_j$ outside the TI. If $\varepsilon_{\text{out}} \gg \varepsilon_{\text{TI}}$ the second contribution are just the mirror charges and the potential for $z < 0$ is zero. This would be the case if a very good conductor is placed at $z < 0$ and leads to the classical method of image charges [271]. However, in the experiments we have $\varepsilon_{\text{out}} \approx \varepsilon_0 \ll \varepsilon_{\text{TI}} \approx 200\,\varepsilon_0$. On the surface $z = 0$ we find

$$\begin{aligned} \phi_{\text{ext}}(\boldsymbol{x}) &= \sum_j \frac{Q_j}{4\pi\varepsilon_{\text{TI}}} \left(\frac{1}{\sqrt{|\boldsymbol{x} - \boldsymbol{y}_j|^2 + d_j^2}} + \frac{\varepsilon_{\text{TI}} - \varepsilon_{\text{out}}}{\varepsilon_{\text{TI}} + \varepsilon_{\text{out}}} \frac{1}{\sqrt{|\boldsymbol{x} - \boldsymbol{y}_j|^2 + d_j^2}} \right) \\ &= \sum_j \frac{Q_j}{4\pi\varepsilon_{\text{s}}} \frac{1}{\sqrt{|\boldsymbol{x} - \boldsymbol{y}_j|^2 + d_j^2}}. \end{aligned} \tag{14.11}$$

The bulk dielectric constant ε_{TI} is replaced by the mean of the bulk and the outer dielectric constant $\varepsilon_{\text{s}} = (\varepsilon_{\text{TI}} + \varepsilon_{\text{out}})/2$. We perform a partial Fourier transformation in the $2d$ coordinates and obtain

$$\phi_{\text{ext}}(\boldsymbol{q}) = \sum_j \int d^2\boldsymbol{x}\, \frac{\mathrm{e}^{i\boldsymbol{x}\boldsymbol{q}} q_j}{4\pi\varepsilon_{\text{s}} \sqrt{|\boldsymbol{x} - \boldsymbol{y}_j|^2 + d_j^2}} = \sum_j \mathrm{e}^{i\boldsymbol{y}_j\boldsymbol{q}}\, \frac{q_j\, \mathrm{e}^{-qd_j}}{2\varepsilon_{\text{s}} q} \tag{14.12}$$

where $\boldsymbol{q}$ is the $2d$ wavevector parallel to the surface. To linear order the induced charge density is given by [272]

$$\rho_{\text{ind}}(\boldsymbol{x}') = \int d^2\boldsymbol{x}''\, \chi(\boldsymbol{x}', \boldsymbol{x}'') \phi_{\text{s}}(\boldsymbol{x}'') \overset{\text{if } \chi(\boldsymbol{x}', \boldsymbol{x}'') = \chi(\boldsymbol{x}' - \boldsymbol{x}'')}{\longrightarrow} \rho_{\text{ind}}(\boldsymbol{q}) = \chi(\boldsymbol{q}) \phi_{\text{s}}(\boldsymbol{q}) \tag{14.13}$$

where we have defined the polarizability $\chi(\omega, \boldsymbol{q}) = -e^2 \Pi(\omega, \boldsymbol{q})$. To arrive at this result we consider the density in Thomas-Fermi approximation [261]

$$\rho_{\text{ind}}(\boldsymbol{x}) = -e(n[\phi_{\text{s}}(\boldsymbol{x})] - n_0), \tag{14.14}$$

where n_0 is the density (of electrons or holes) in the homogenous system without the external potential and $n[\phi_{\rm s}(\boldsymbol{x})]$ is the density with a induced surface potential $\phi_{\rm s}$. The homogenous density was given in Eq. (14.1) as $n_{e/h} = \frac{\mu^2}{4\pi(\hbar v_F)^2}$. Within the local density approximation it is $\mu[\phi_{\rm s}(\boldsymbol{x})] \to \mu(\boldsymbol{x}) = \mu + e\phi_{\rm s}(\boldsymbol{x})$. In this approximation the induced charge density is given by (assuming $\mu \geq 0$ for the moment, the case $\mu < 0$ is analog)

$$\rho_{\rm ind}(\boldsymbol{x}) = \frac{-e}{4\pi(\hbar v_F)^2}\left((\mu + e\phi_{\rm s}(\boldsymbol{x}))^2 - \mu^2\right) = \frac{-e^2}{4\pi(\hbar v_F)^2}\left(2\mu + e\,\phi_{\rm s}(\boldsymbol{x})\right)\,\phi_{\rm s}(\boldsymbol{x}). \tag{14.15}$$

Inserting this in Eq. (14.8) yields a non-linear equation for the surface potential $\phi_{\rm s}$:

$$\phi_{\rm s}(\boldsymbol{x}) = \phi_{\rm ext}(\boldsymbol{x}) - \alpha \int d^2\boldsymbol{x}'\, \frac{|2\mu + e\,\phi_{\rm s}(\boldsymbol{x}')|\;\phi_{\rm s}(\boldsymbol{x}')}{4\pi\,\hbar v_F\,|\boldsymbol{x} - \boldsymbol{x}'|}, \tag{14.16}$$

For $\mu \to 0$ a non-linear equation is obtained:

$$\phi_{\rm s}(\boldsymbol{x}) = \phi_{\rm ext}(\boldsymbol{x}) - \frac{e\alpha}{4\pi\hbar v_F}\int d^2\boldsymbol{x}'\, \frac{\phi_{\rm s}(\boldsymbol{x}')|\phi_{\rm s}(\boldsymbol{x}')|}{|\boldsymbol{x} - \boldsymbol{x}'|}. \tag{14.17}$$

When α is small, which is the case for the typical TIs under study (where $\alpha \sim 0.1$, see Eq. (14.3)), this can be solved iteratively. Inserting the external potential, Eq. (14.11), gives the result as a power series in α. To order α^2 one obtains a two-body interaction, higher powers of α lead to interactions involving more than two charges (3-body for α^4 etc.).

In the following we will consider the linear case only. From Eq. (14.16) we see that this is justified when the chemical potential is much larger than the typical potential fluctuations ($|\mu| \gg |e\phi_{\rm typ}|$). Then the linear formula Eq. (14.13) is obtained and it is $\rho_{\rm ind} \sim \phi_{\rm s}$. In this case we obtain from Eq. (14.8)

$$\phi_{\rm s}(\boldsymbol{x}) = \;\phi_{\rm ext}(\boldsymbol{x}) + \int d^2\boldsymbol{x}' \int d^2\boldsymbol{x}''\, \frac{\chi(\boldsymbol{x}', \boldsymbol{x}'')\,\phi_{\rm s}(\boldsymbol{x}'')}{4\pi\varepsilon_{\rm s}|\boldsymbol{x} - \boldsymbol{x}'|}, \tag{14.18}$$

and Fourier transformation yields

$$\begin{aligned}\phi_{\rm s}(\boldsymbol{q}) =& \phi_{\rm ext}(\boldsymbol{q}) + \frac{\chi(\boldsymbol{q})}{2\varepsilon_{\rm s} q}\,\phi_{\rm s}(\boldsymbol{q}) \\ \Rightarrow \phi_{\rm s}(\boldsymbol{q}) =& \frac{q}{q - \chi(\boldsymbol{q})/(2\varepsilon_{\rm s})}\,\phi_{\rm ext}(\boldsymbol{q}) = \frac{q}{q + \frac{e^2}{2\varepsilon_{\rm s}}\Pi(\omega = 0, \boldsymbol{q})}\,\phi_{\rm ext}(\boldsymbol{q}).\end{aligned} \tag{14.19}$$

In the limit $|\mu| \gg T$ we then find

$$\phi_{\rm s}(\boldsymbol{q}) = \frac{q}{q + q_{\rm s}}\phi_{\rm ext}(\boldsymbol{q}) \tag{14.20}$$

where $q_\mathrm{s} = \alpha|\mu|/\hbar v_F$ is the inverse screening length, see Eq. (14.7). The corresponding induced charge density on the surface is

$$\rho_\mathrm{ind}(\boldsymbol{q}) = \frac{-2\varepsilon_\mathrm{s} q_\mathrm{s} q}{q+q_\mathrm{s}} \sum_j \mathrm{e}^{i\boldsymbol{y}_j\boldsymbol{q}} \frac{q_j\,\mathrm{e}^{-qd_j}}{2\varepsilon_\mathrm{s} q} = \frac{q_\mathrm{s}}{q+q_\mathrm{s}} \sum_j (-q_j)\,\mathrm{e}^{-qd_j}\,\mathrm{e}^{i\boldsymbol{y}_j\boldsymbol{q}}. \tag{14.21}$$

Fourier transformation yields

$$\rho_\mathrm{ind}(\boldsymbol{x}) = \frac{q_\mathrm{s}}{2\pi} \sum_j (-q_j) \int_0^\infty dq\, \frac{q\,\mathrm{e}^{-d_j q}}{q+q_\mathrm{s}}\, J_0(q|\boldsymbol{x}-\boldsymbol{y}_j|), \tag{14.22}$$

where J_0 is zero-order Bessel function of the first kind. Accordingly the potential, which is induced in the bulk by the surface charge, is

$$\begin{aligned}
\phi_\mathrm{ind}^\mathrm{bulk}(\boldsymbol{r}=(\boldsymbol{x},z)) &= \int d^2\boldsymbol{x'}\, \frac{\rho_\mathrm{ind}(\boldsymbol{x'})}{4\pi\varepsilon_\mathrm{s}|\boldsymbol{r}-\boldsymbol{x'}|} \\
&= \frac{1}{4\pi\varepsilon_\mathrm{s}} \sum_j (-q_j) \int dq\, \frac{q_\mathrm{s}}{q+q_\mathrm{s}}\, \mathrm{e}^{-q(z+d_j)} J_0(q|\boldsymbol{x}-\boldsymbol{y}_j|) && (14.23) \\
&= \frac{q_\mathrm{s}}{4\pi\varepsilon_\mathrm{s}} \sum_j (-q_j) \int dq\, \frac{1}{q+1}\, \mathrm{e}^{-q(q_\mathrm{s}z+q_\mathrm{s}d_j)} J_0(qq_\mathrm{s}|\boldsymbol{x}-\boldsymbol{y}_j|), && (14.24)
\end{aligned}$$

where we have rescaled $q \to qq_\mathrm{s}$ in the last line. We now consider the strong screening limit of Eq. (14.23). When $q_\mathrm{s} d_j \gg 1$ for all j, or $zq_\mathrm{s} \gg 1$, one can approximate $\frac{1}{q+1} \to 1$. Since the minimal d_j is of order $N^{-1/3}$ the first case corresponds to $q_\mathrm{s} N^{-1/3} \gg 1$. For $N = 10^{19}\,\mathrm{cm}^{-3}$ and $\alpha \approx 0.11$, as above, we obtain $q_\mathrm{s} N^{-1/3} \approx 3.86 \times |\mu|/eV$. Thus the TIs investigated in the experiments are probably not in this regime. Nevertheless, its interesting and instructive to investigate the effect. In this strong screening limit we find for the induced bulk potential

$$\begin{aligned}
\phi_\mathrm{ind}^\mathrm{bulk}(\boldsymbol{r}) &\underset{q_\mathrm{s}N^{-1/3}\to\infty}{\longrightarrow} \frac{1}{4\pi\varepsilon_\mathrm{s}} \sum_j (-q_j) \int dq\, \mathrm{e}^{-q(z+d_j)} J_0(q|\boldsymbol{x}-\boldsymbol{y}_j|) \\
&= \frac{1}{4\pi\varepsilon_\mathrm{s}} \sum_j \frac{-q_j}{\sqrt{|\boldsymbol{x}-\boldsymbol{y}_j| + (z+d_j)^2}} = \frac{1}{4\pi\varepsilon_\mathrm{s}} \sum_j \frac{(-q_j)}{|\boldsymbol{r}-\tilde{\boldsymbol{r}}_j|}. && (14.25)
\end{aligned}$$

The total potential in the bulk is then given as the sum of the external potential, the potential due to the jump in the dielectric constant and the potential of the induced surface charges:

$$\phi(\boldsymbol{r}; z>0) = \sum_j \frac{q_j}{4\pi} \left(\frac{1}{\varepsilon_\mathrm{TI}|\boldsymbol{r}-\boldsymbol{r}_j|} + \frac{\varepsilon_\mathrm{TI}-\varepsilon_\mathrm{out}}{\varepsilon_\mathrm{TI}+\varepsilon_\mathrm{out}} \frac{1}{\varepsilon_\mathrm{TI}|\boldsymbol{r}-\tilde{\boldsymbol{r}}_j|} - \frac{1}{\varepsilon_\mathrm{s}|\boldsymbol{r}-\tilde{\boldsymbol{r}}_j|} \right)$$

$$= \sum_j \frac{q_j}{4\pi\varepsilon_{\text{TI}}} \left(\frac{1}{|\boldsymbol{r} - \boldsymbol{r}_j|} - \frac{1}{|\boldsymbol{r} - \tilde{\boldsymbol{r}}_j|} \right). \tag{14.26}$$

The dielectric constant of the outer region, ε_{out}, drops out and the result corresponds to that obtained from the method of image charges. We will call this the mirror-charge limit. For completeness, we also give the potential on the other side of the boundary, outside the TI,

$$\phi(\boldsymbol{r}; z < 0) = \sum_j \frac{q_j}{4\pi\varepsilon_{\text{eff}}} \frac{1}{|\boldsymbol{r} - \boldsymbol{r}_j|}, \tag{14.27}$$

with an effective dielectric constant $\varepsilon_{\text{eff}} = \varepsilon_{\text{out}} \frac{\varepsilon_{\text{out}} + \varepsilon_{\text{TI}}}{\varepsilon_{\text{out}} - \varepsilon_{\text{TI}}}$. If $\varepsilon_{\text{out}} \neq \varepsilon_{\text{TI}}$, this is in contrast to the usual result where the mirror charges are due to a bulk conductor. Here the potential on the other side of the boundary is zero.

In the strong screening limit the induced surface charge density, Eq. (14.22), simplifies to

$$\begin{aligned} \rho_{\text{ind}}(\boldsymbol{x}) &= \frac{q_{\text{s}}}{2\pi} \sum_j (-q_j) \int_0^\infty dq \, \frac{q \, \mathrm{e}^{-d_j q}}{q + q_{\text{s}}} \, J_0(q|\boldsymbol{x} - \boldsymbol{y}_j|) \\ &= \frac{1}{2\pi} \sum_j (-q_j) \int_0^\infty dq \, q \, \mathrm{e}^{-d_j q} \, J_0(q|\boldsymbol{x} - \boldsymbol{y}_j|) \\ &= \frac{1}{2\pi} \sum_j (-q_j) \frac{d_j}{\left(d_j^2 + |\boldsymbol{x} - \boldsymbol{y}_j|^2 \right)^{3/2}}. \end{aligned} \tag{14.27}$$

Its Fourier transform reads

$$\rho_{\text{ind}}(\boldsymbol{q}) = \int d^2\boldsymbol{x} \, \mathrm{e}^{i\boldsymbol{q}\boldsymbol{x}} \rho_{\text{ind}}(\boldsymbol{x}) = \sum_j (-q_j) \mathrm{e}^{-d_j q} \, \mathrm{e}^{i\boldsymbol{q}\boldsymbol{y}_j}. \tag{14.28}$$

The total charge induced on the surface by a single charge Q at a distance d_0 is then given by the $\boldsymbol{q} = \boldsymbol{0}$ component of a single charge in Eq. (14.28), or explicitly from Eq. (14.27)

$$\int d^2\boldsymbol{x} \left(\frac{-Q}{2\pi} \right) \frac{d_0}{\left(d_0^2 + |\boldsymbol{x} - \boldsymbol{y}_0|^2 \right)^{3/2}} = -Q \int_0^\infty dx \frac{d_0 x}{\left(d_0^2 + x^2 \right)^{3/2}} = -Q. \tag{14.29}$$

The induced surface charge exactly compensates the charge Q, which leads to a dipole field at distances much larger than d_0.

14.3 Numerical implementation

To implement the result obtained above into the algorithm we have to consider the additional contributions to the energy. As in section 11 we will use dimensionless units in the following. Energies are measured in units of $\mathrm{E_c} = e^2 N^{1/3}/(4\pi\varepsilon_{\mathrm{TI}})$, lengths are measured in units of $N^{-1/3}$ and charges are measured in units of the elementary charge e. In principle, there are three new contributions to the energy when we include the surface states: the kinetic energy of the surface states, surface–surface interaction energy and surface-bulk interaction energy.

1) In the homogenous system the kinetic energy density (for $\mu \gg T$) is given by

$$e_{\mathrm{kin}} = \int \frac{d^2\boldsymbol{q}}{(2\pi)^2}\, E_{\pm}(\boldsymbol{q}) n_F(\boldsymbol{q}) = \frac{|\mu|^3}{4\pi(\hbar v_F)^2},$$

and, for a system with volume $V = L^3$, the total kinetic energy is $L^2 e_{\mathrm{kin}}$. The bulk energies scale as L^3 and therefore we can neglect the kinetic energy of the surface states at this point.

2) With $U_{2d}(q) = \frac{1}{2\varepsilon_{\mathrm{s}} q}$, the $2d$ Fourier transform of $U(x) = \frac{1}{4\pi\varepsilon_{\mathrm{s}} x}$ and Eq. (14.28), the surface-surface interaction energy is obtained to be

$$\begin{aligned} H_{\mathrm{s-s}} &= \frac{1}{2}\int d^2\boldsymbol{x} \int d^2\boldsymbol{x}'\, \rho_{\mathrm{ind}}(\boldsymbol{x})\, \rho_{\mathrm{ind}}(\boldsymbol{x}') U\left(\boldsymbol{x}-\boldsymbol{x}'\right) \\ &= \frac{1}{2}\int \frac{d^2\boldsymbol{q}}{(2\pi)^2}\, \rho_{\mathrm{ind}}(\boldsymbol{q})\, \rho_{\mathrm{ind}}(-\boldsymbol{q})\, U(\boldsymbol{q}) \\ &= \frac{1}{8\pi\varepsilon_{\mathrm{s}}} \sum_{j,m} q_m q_j \int dq \mathrm{e}^{-(d_j+d_m)q} J_0\left(|\boldsymbol{y}_j - \boldsymbol{y}_m| q\right) \\ &= \frac{1}{2}\sum_{j,m} \frac{q_m q_j}{4\pi\varepsilon_{\mathrm{s}}} \frac{1}{\sqrt{(d_j+d_m)^2 + |\boldsymbol{y}_j - \boldsymbol{y}_m|^2}} \end{aligned} \tag{14.30}$$

3) The surface-bulk interaction energy can be calculated from Eq. (14.26) as

$$\begin{aligned} H_{\mathrm{s-b}} &= \frac{1}{2}\sum_m q_m \phi_{\mathrm{ind}}^{\mathrm{bulk}}(\boldsymbol{r}_m) = -\frac{1}{2}\sum_{j,m} \frac{q_j q_m}{|\boldsymbol{r}_m - \tilde{\boldsymbol{r}}_j|} \\ &= -\frac{1}{2}\sum_{m\neq j} \frac{q_j q_m}{|\boldsymbol{r}_m - \tilde{\boldsymbol{r}}_j|} - \sum_m \frac{q_m^2}{2d_m}. \end{aligned} \tag{14.31}$$

The full dimensionless Hamiltonian including the surface-bulk interaction reads:

$$H = \sum_m \left(f_m n_m \frac{\Delta}{2} - \frac{q_m^2}{2d_m} \right)$$

$$+\frac{1}{2}\sum_{m\neq j} q_m q_j \left(\frac{1}{\sqrt{|\boldsymbol{r}_m-\boldsymbol{r}_j|^2+a_B^2}}-\frac{1}{\sqrt{|\boldsymbol{r}_m-\tilde{\boldsymbol{r}}_j|^2+a_{\mathrm{B}}^2}}\right)$$
$$=\sum_m \left(f_m n_m \frac{\Delta}{2}-\frac{q_m^2}{2d_m}\right)+\frac{1}{2}\sum_{m\neq j} q_m q_j V_{mj}^{\mathrm{eff}}. \tag{14.32}$$

Here we have restored the short distance cutoff and we have defined an effective interaction V^{eff}. The self interaction term $-q^2/(2d)$ describes the effect that a single charge q interacts with its mirror charge $-q$ at a distance $2d$ via the induced surface charge. A calculation analogously to that presented in Eq. (11.11) shows that we can use the same algorithm as before when the single-particle energies are changed to

$$\epsilon_m = \left(\frac{\Delta}{2}+\frac{1}{2d_m}\right) f_m - \sum_{j\neq m} q_j\, V_{jm}^{\mathrm{eff}}. \tag{14.33}$$

14.4 Numerical results

Some of the results presented below were obtained in collaboration with Qingyufei Terenz Feng during his research internship, and can also be found in his report [273]. To investigate the boundary effects on the bulk properties we have to find an appropriate observable. We have chosen the density of neutral dopants as a function of the distance from the surface $n_0(d)$. Deep in the bulk, this is constant after disorder averaging. In Fig. 14.1 we show $n_0(d)$ for different boundary conditions with $\Delta = 12$ and $a_{\mathrm{B}} = 1$. For the mirror-charge boundary conditions, we see that there are no neutral dopants close to the surface since the potential approaches zero there. For open boundary conditions (OBC), the formation of neutral dopants is also suppressed close to the surface. This is plausible since charges are located only at one side and it is harder to build up large potentials. For a dielectric jump on the surface from the vacuum value $\varepsilon_{\mathrm{out}} = \varepsilon_{\mathrm{vac}} = \varepsilon_0$ to $\varepsilon_{\mathrm{TI}} = 200\,\varepsilon_0$ in the bulk, there are more neutral dopants close to the surface. This is a direct consequence of Eq. (14.10) which was used for the effective interaction in this simulation. For $\varepsilon_{\mathrm{TI}} \gg \varepsilon_{\mathrm{out}}$ the potential is increased by almost a factor of 2 close to the surface.

From Fig. 14.1 we can see that there is a lengthscale associated with the boundary: at a distance $d \approx 4$, $n_0(d)$ reaches its bulk value independent of the boundary conditions. As a measure for the penetration depth of the surface effects we define l_{surf} as the distance from the surface where $n_0(d)$ reaches half of its bulk value. This is the full width at half maximum (FWHM). In Fig. 14.1 this is approximately given by $l_{\mathrm{surf}} \approx 2$ as indicated by the dashed line. We have seen in section 12 that neutral

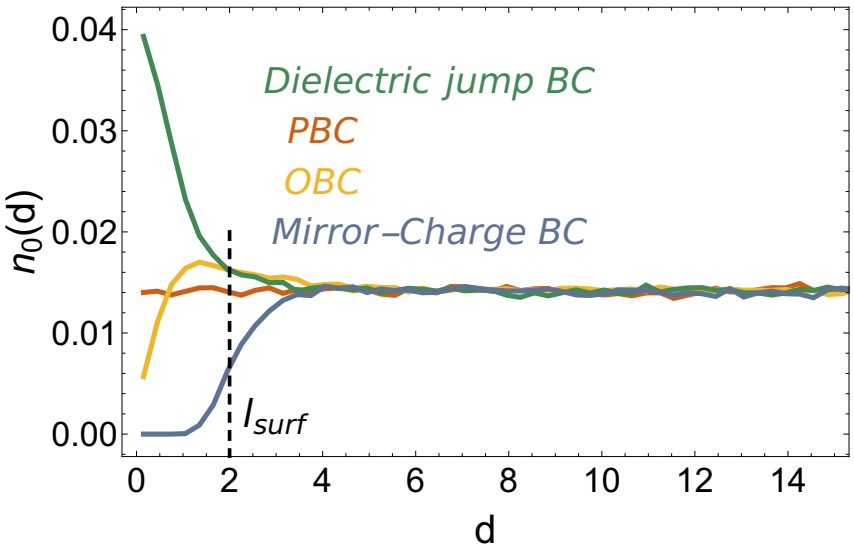

Figure 14.1: **The density of neutral dopants for different boundary conditions.** Boundary conditions parallel to the surface are periodic. For periodic boundary conditions (PBC) there is no effect. For open boundary conditions (OBC) the density very close to the surface is approximately one half of the bulk value. For a jump in the dielectric constant from $\varepsilon_{\text{out}} = 1$ to $\varepsilon_{\text{TI}} = 200$ the density is enhanced. For the mirror-charge boundary conditions, where the potential is zero at $d = 0$, there are no neutral dopants for $d \lesssim 1$. For $d \gtrsim 4$ all curves reach the same bulk value independent of the boundary conditions. The dashed line indicates the full width at half maximum for the mirror-charge boundary conditions denoted by l_{surf}. Parameters used in this plot are $\Delta = 12$, $L = 40$ and $a_{\text{B}} = 1$.

dopants are necessarily located in regions where the potential is $|\phi| > \Delta/2$. In the mirror-charge limit the potential on the surface is zero. Therefore the penetration depth l_{surf}, as defined above, can be interpreted as the typical lengthscale on which the potential changes from zero to $\pm\Delta/2$.

Let us consider first what happens in the uncorrelated system where all dopants are charged. Here the charge-charge correlations are given by

$$\langle \rho_{\text{MC}}(x,y,z)\rho_{\text{MC}}(z',y',z')\rangle = \delta(x-x')\delta(y-y')\left(\delta(z-z') - \delta(z+z')\right) - 1/V. \quad (14.34)$$

Here and in the following the subscript MC indicates the mirror-charge boundary conditions. The normalization is chosen such that the TI-volume ($z > 0$) is still charge neutral:

$$\int_V d^3\boldsymbol{r} \int_V d^3\boldsymbol{r}' \langle \rho_{\text{MC}}(x,y,z)\rho_{\text{MC}}(z',y',z')\rangle = 0 \quad (14.35)$$

We are interested in the typical potential $\phi^{\text{typ}}_{\text{MC}}(d) = \sqrt{\langle \phi_{\text{MC}}(0,0,d)\phi_{\text{MC}}(0,0,d)\rangle}$ at a

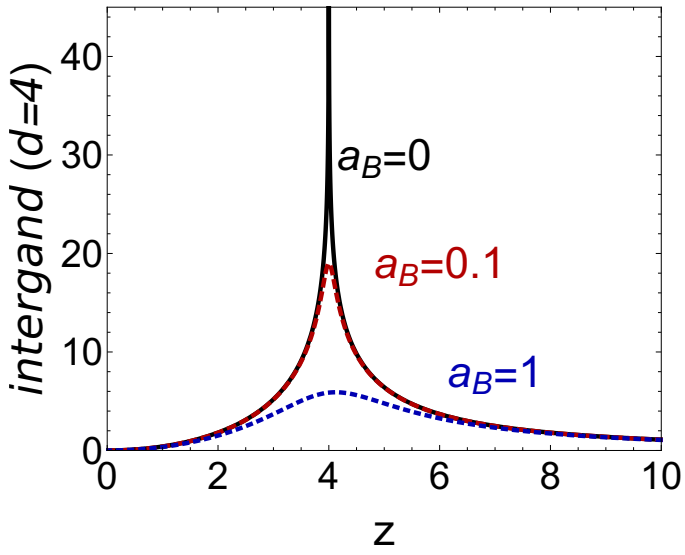

Figure 14.2: **The integrand of Eq. (14.36) for $d = 4$ and different values of $a_{\rm B}$.** The plot shows the average contributions to a typical fluctuation at $d = 4$. For $a_{\rm B} = 0$ it diverges at $z = d$ but the peak has zero weight. For $a_{\rm B} > 0$ contributions from the interval $z \in [d - a_{\rm B}, d + a_{\rm B}]$ are suppressed. For $z \gg d + a_{\rm B}$ all curves decay as $\frac{2\pi d^2}{z^2}$.

distance d away from the surface. For simplicity we assume $x = y = 0$. Then it is

$$
\begin{aligned}
&\langle \phi_{\rm MC}(0,0,d)\phi_{\rm MC}(0,0,d)\rangle \\
&= \int d^3\boldsymbol{r} \int d^3\boldsymbol{r}' \frac{\langle \rho_{\rm MC}(\boldsymbol{r})\rho_{\rm MC}(\boldsymbol{r}')\rangle}{\sqrt{x^2+y^2+(z-d)^2+a_B^2}\sqrt{x'^2+y'^2+(z'-d)^2+a_B^2}} \\
&= 2\pi \int_0^\infty dr \int_{-\infty}^\infty dz \left(\frac{r}{r^2+(z-d)^2+a_B^2} - \frac{r}{\sqrt{r^2+(z-d)^2+a_B^2}\sqrt{r^2+(z+d)^2+a_B^2}} \right) \\
&= \pi \int_0^\infty dz\, {\rm Log} \left(\frac{\left({\rm a_B^2} + {\rm d^2} + {\rm z^2} + \sqrt{({\rm a_B^2}+{\rm d^2})^2 + 2({\rm a_B^2}-{\rm d^2}){\rm z^2} + {\rm z^4}} \right)^2}{4({\rm a_B^2}+({\rm z}-{\rm d})^2)({\rm a_B^2}+({\rm z}+{\rm d})^2)} \right) .
\end{aligned}
\tag{14.36}
$$

The integrand is shown in Fig. 14.2. It shows the average contributions to a typical potential fluctuation at d. For $a_{\rm B} = 0$, there is a logarithmic divergence at $z = d$. However, this divergence has zero weight, meaning that it does not contribute to the integral. If we integrate the peak from $d - \epsilon$ to $d + \epsilon$, we obtain $4\pi\epsilon \ln(d/\epsilon)$ which vanishes for $\epsilon \to 0$. For $a_{\rm B} > 0$, the peak is truncated at $d \pm a_{\rm B}$. Therefore we conclude that the corrections for finite $a_{\rm B} \ll d$ are $\sim -a_{\rm B} \ln(d/a_{\rm B})$, and thus can not be obtained by a finite perturbation series at $a_{\rm B} = 0$. For $a_B = 0$ the integral Eq. (14.36) can be solved exactly and we obtain

$$
\langle \phi_{\rm MC}(0,0,d)\phi_{\rm MC}(0,0,d)\rangle = 4\pi d. \tag{14.37}
$$

Since the charge distribution is uncorrelated we expect that the probability distribution of the potential at a distance d away from the surface, denoted by $P_d(\phi)$, is

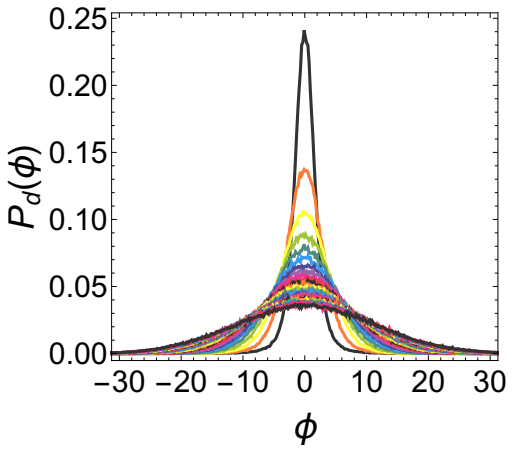

Figure 14.3: **Probability distribution of the uncorrelated potential ϕ at a different distances d.** Shown are distances $d = 0.25, 0.5, \ldots, 8$. All curves have a Gaussian shape, and the width increases with the distance from the surface d. Data from simulation with $L = 50$.

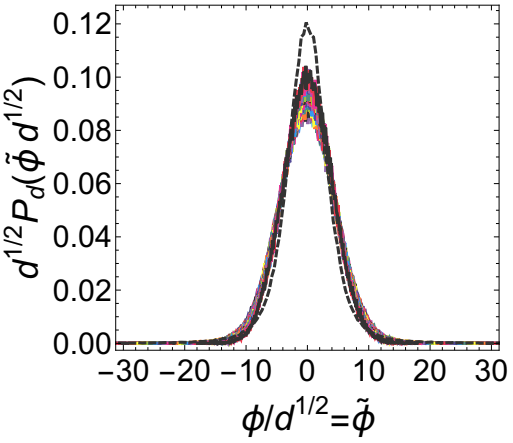

Figure 14.4: **Same data as shown in Fig. 14.3 scaled with $\sqrt{d}$.** The black line is a Gaussian with width $\sigma = 4.4$. From Eq. (14.36) we expect $\sigma = \sqrt{4\pi} \approx 3.54$. The discrepancy is due to periodic boundary conditions in x and y direction and geometrical effects. For $d = 0.25$ (black, dashed line) the scaling behavior is not yet reached.

Gaussian. According to Eq. (14.37) we expect a width $\sigma = \sqrt{4\pi d}$ such that $P_d(\phi) = 1/\sqrt{2\pi(4\pi d)}\exp\left(-\phi^2/(2\times 4\pi d)\right)$. In Figs. 14.3 and 14.4 we show this probability distribution for distances $d = 0.25, 0.5, \ldots, 8$ and $a_{\mathrm{B}} = 0.001$. In Fig. 14.4 we have scaled the data as $\sqrt{d}P_d(\tilde{\phi}\sqrt{d})$ which then, indeed, are independent of d for $d \gtrsim 0.5$. The black line is a Gaussian fit with width $\sigma = 4.4$. We attribute the discrepancy to the value obtained above, $\sigma = \sqrt{4\pi} \approx 3.54$, to the different boundary conditions and to a different geometry of the simulation volume compared to the spherical symmetry used in the derivation of Eq. (14.36). The scaling $\phi^{\mathrm{typ}}_{\mathrm{MC}}(d) \sim \sqrt{d}$, and the fact the potential fluctuations are suppressed for $|\phi| \gtrsim \Delta/2$, suggest that $l_{\mathrm{surf}}(\Delta) \sim \Delta^2$. This argument is in total analogy to the argument for the bulk lengthscale $R_g \sim \Delta^2$ presented by Skinner *et. al.* [234, 235], see section 12 for the details. However we will show below that this scaling LENGTH $\sim$ ENERGY^2, while present in the uncorrelated system, is not present in the correlated groundstate (in the simulated parameter range).

In the limit $d \ll a_B$ we obtain from Eq. (14.36)

$$\langle \phi_{\mathrm{MC}}(0,0,d)\phi_{\mathrm{MC}}(0,0,d)\rangle \overset{d\ll a_{\mathrm{B}}}{\longrightarrow} \pi \int_0^\infty dz \frac{2d^2\pi z^2}{(a_B^2+z^2)^2} = \frac{\pi^2 d^2}{2a_B}. \tag{14.38}$$

This would lead to a scaling LENGTH $\sim$ ENERGY and suggests, following the same

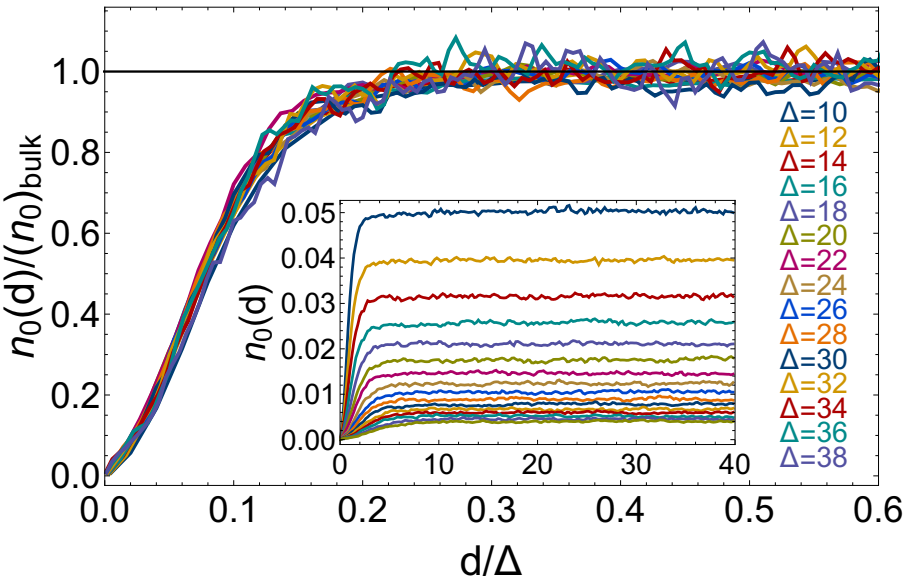

Figure 14.5: **The density of neutral dopants $n_0(d)$ at a distance d from the surface.** Data from simulations with $L = 50$ and $a_\mathrm{B} = 0.001$. The scaling in the inset shows that the bulk value is reached at $d \sim 0.3\,\Delta$.

reasoning as above, $l_\mathrm{surf}(\Delta) \sim \Delta$. We have first chosen the very small $a_B = 0.001$ for the following analysis to ensure that we are not in this limit. We have also checked the Gaussian scaling for larger values of a_B (not shown). The scaling behavior is still fulfilled but starts only at larger values of d.

In Fig. 14.5 we show the density of neutral dopants $n_0(d)$ as a function of the distance d from the surface for $\Delta = 10 - 38$. With increasing Δ the bulk value $(n_0)_\mathrm{bulk}$ decreases and the penetration depth l_surf increases. In the inset the unscaled data is shown. To study the penetration length the y-axis is normalized by the bulk value. We can see that scaling of the distance d by $\Delta^{\alpha \approx 1}$ results in an approximate scaling collapse of the data. Fig. 14.6 shows the numerically calculated full width at half maximum. To obtain the fit, we first have calculated the bulk value by averaging over the region where $n_0(d)$ has saturated. Then we have used an interpolating function n_0^int to numerically solve $n_0^\mathrm{int}(d_{FWHM}) = 1/2(n_0)_\mathrm{bulk}$ for d_{FWHM}. The result for the fit function slightly depends on the Δ values that are fitted. A fit of the form $l_\mathrm{surf}(\Delta) = c\,\Delta^\alpha$ yields

$$l_\mathrm{surf}(\Delta, a_\mathrm{B} \to 0) = c\,\Delta^\alpha, \text{ with } c = 0.65 - 0.77 \text{ and } \alpha = 0.99 - 1.04. \tag{14.39}$$

We have plotted $l_\mathrm{surf} = 0.07\,\Delta^{1.02}$ in Fig. 14.6, which matches the numerical data for $\Delta = 14$ to $\Delta = 36$. The exponent is in analogy to the scaling found in the bulk, see

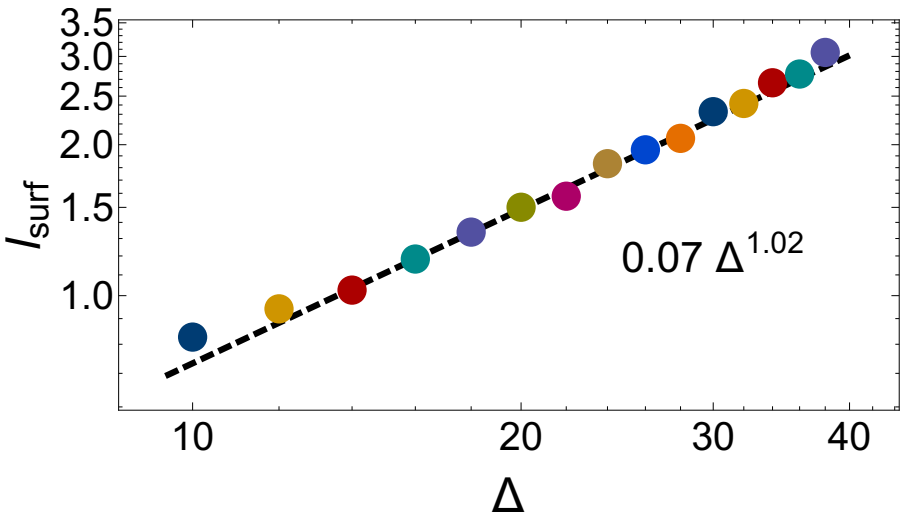

Figure 14.6: **Full width at half maximum as a measure for the penetration depth.** The result is obtained from the data shown in Fig. 14.5 as explained in the main text. The data are well described by a fit $\sim \Delta^{\alpha \approx 1}$, in agreement with length-scales found in the bulk.

section 12.2. Note that the parameters, $L = 50$ and $a_B = 0.001$, are the same as used in Fig. 14.4 where we can clearly observe the LENGTH $\sim$ ENERGY^2 scaling.

To exclude any finite-size or cutoff effects we have also performed simulations with $L = 60$ (432000 dopants) and $a_B = 0.01$. The results are shown in Figs. 14.7 and 14.8, respectively. In both cases the results agree within the size of the noise of the bulk values with the simulations for $L = 50$ and $a_B = 0.001$. From Fig. 14.8 we can also see that we are not in the regime of Eq. (14.38), which also predicts a scaling LENGTH $\sim$ ENERGY, since then the prefactor would depend on a_B. Therefore we have to conclude that the Gaussian scaling LENGTH $\sim$ ENERGY^2 is not present in the groundstate for the simulated parameter range.

Now, that we have excluded possible issues we consider the case $a_B \sim 1$. In Fig. 14.9, $n_0(d)$ is shown for different values of a_B and $\Delta = 12$. The data for $a_B \approx 0$ are the same as shown as above ($a_B = 0.001$). The formation of neutral dopants is totally suppressed up to $d \approx a_B$. For $d \lesssim a_B$ all charges are screened by their mirror charges and no large potential can build up. In the inset of Fig. 14.1 it can be seen that also the bulk value $(n_0)_{\text{bulk}}$ depends on a_B. The maximal potential provided by a single dopant is $\sim 1/a_B$. When a_B is small the number of dopants needed to create a potential of order $\pm\Delta/2$ is smaller. Therefore the number of neutral dopants is larger for smaller values of a_B. For the results shown above, where $a_B = 0.001$, a single dopant can neutralize another dopant if they are accidentally located very close to each other

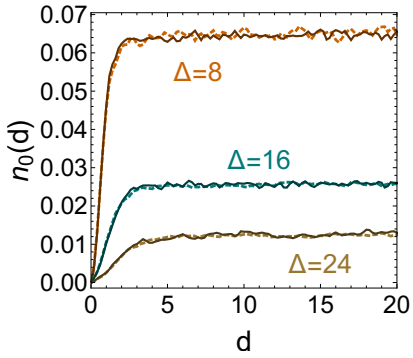

Figure 14.7: **Absence of finite size effects.** The dashed lines are the same data as shown in Fig. 14.5 with $L = 50$. The solid lines are data for $L = 60$. There are no finite size effects visible in the data.

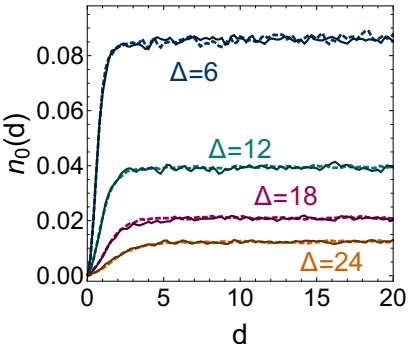

Figure 14.8: **Absence of cutoff effects.** The dashed lines are the same data as shown in Fig. 14.5, with $a_\mathrm{B} = 0.001$. The solid lines are data for $a_\mathrm{B} = 0.01$. For these values of a_B, the result does not depend on a_B.

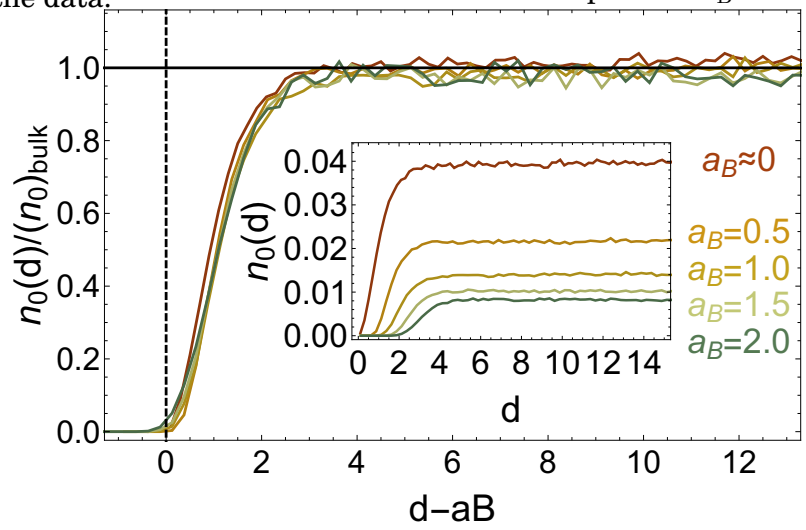

Figure 14.9: **Cutoff dependence of $n_0(d)$.** The inset shows the unscaled data. Neutralization starts only for $d \gtrsim a_\mathrm{B}$ and the bulk value depends on a_B. If d is shifted by a_B and n_0 is normalized by its bulk value all the data collapse onto a single curve as shown in the main panel. This implies that the full width at half maximum is shifted by $\sim a_\mathrm{B}$. Data is shown for $\Delta = 12$ and $L = 50$.

within a distance $r \lesssim 1/\Delta$. For larger values of a_B this effect vanishes. Nevertheless, the bulk values for $a_\mathrm{B} = 1$ are larger by almost a factor of 2 compared to $a_\mathrm{B} = 2$, as can be seen in the inset of Fig. 14.9. When d is shifted by a_B and the data are scaled with the bulk values, the full width at half maximum, approximately, is the same for all curves (when measured from 0). This is shown in the main panel of Fig. 14.9. The effect of a_B on the penetration depth is that it is increased by $\approx a_\mathrm{B}$. Therefore we expect that for $a_\mathrm{B} \sim 1$ the scaling behavior as shown above for $a_\mathrm{B} = 0.001$ is still valid

when d is shifted by $\approx a_{\mathrm{B}}$.

In Fig. 14.10 we present results for $a_{\mathrm{B}} = 1$ and $\Delta = 10 - 26$. The unscaled data is shown in the inset of the upper plot. Neutralization only starts at $d \gtrsim a_{\mathrm{B}} = 1$. When d is shifted by $\approx a_{\mathrm{B}} = 1$ we again find an approximate scaling collapse when the x-axis is scaled by $\Delta^{\alpha \approx 1}$. This is shown in the main panel of Fig. 14.10, where n_0 is normalized by its bulk value. The shift is a subleading effect for $\Delta \to \infty$ but for the values of Δ shown in Fig. 14.10 the scaling behavior can be improved significantly. The penetration depth is as small as $2 - 4$ and a shift by 1 influences the scaling behavior. We have determined the full width at half maximum as explained above to obtain numerical value for the scaling exponent α. The results depend on the shift. For a shift of $a_{\mathrm{B}} = 1$ the fits yield, depending on the fit interval, $l_{\mathrm{surf}}(\Delta) - a_{\mathrm{B}} \approx 0.066 - 0.074\,\Delta^{1.09-1.14}$. The prefactor is the same as found above for $a_{\mathrm{B}} = 0.001$, see Eq. (14.39). But the exponent $\alpha \approx 1.1$ is slightly larger than 1. When d is shifted by $0.8 a_{\mathrm{B}} = 0.8$ we obtain $l_{\mathrm{surf}}(\Delta) - 0.8 a_{\mathrm{B}} \approx 0.106 - 0.118\,\Delta^{0.98-1.01}$. Here we reproduce the exponent $\alpha \approx 1$ as in Fig. 14.6 but the prefactor is slightly larger. The fits are shown in the lower panel of Fig. 14.10. Both describe the data equally well. To obtain certainty, one would have to perform simulations for larger values of Δ where the subleading shift effect vanishes.

From the analysis we conclude that the penetration depth of the surface effects is $l_{\mathrm{surf}}(\Delta) \sim \Delta^{\alpha}$, where α is around 1.05 but definitely not 2 in the simulated parameter range. Therefore we estimate that

$$l_{\mathrm{surf}}(\Delta, a_{\mathrm{B}}) \approx b\, a_{\mathrm{B}} + c\, \Delta^{\alpha}, \text{ where}$$
$$b \approx (0.9 \pm 0.1),\ c \approx (0.085 \pm 0.035), \text{ and } \alpha \approx (1.06 \pm 0.07). \qquad (14.40)$$

Unfortunately, it was not possible to determine the FWHM in a reasonable way for single runs since the noise level is too high. From this it would be possible to obtain the values and the error bars of the the numbers b, c and α in Eq. (14.40) on a statistical basis.

To get a feeling for the numbers we insert the material parameters from the experiment. For $\Delta = 100$, $N = 10^{19}\,\mathrm{cm}^{-3}$ and $a_{\mathrm{B}} = N^{-1/3} = 4.6\,\mathrm{nm}$ we find $l_{\mathrm{surf}} \approx (12 \pm 4)\, N^{-1/3} \sim 37 - 74\,\mathrm{nm}$. For $N = 10^{18}\,\mathrm{cm}^{-3}$ we find $l_{\mathrm{surf}} \sim 80 - 160\,\mathrm{nm}$. This means that for samples with a thickness $\sim \mu m$ we expect that puddle formation arises. When the Fermi level is close to the Dirac point, and the linear screening theory breaks down, we expect the effects to be even smaller, see Eq. (14.16), thanks to the smallness of the effective fine structure constant.

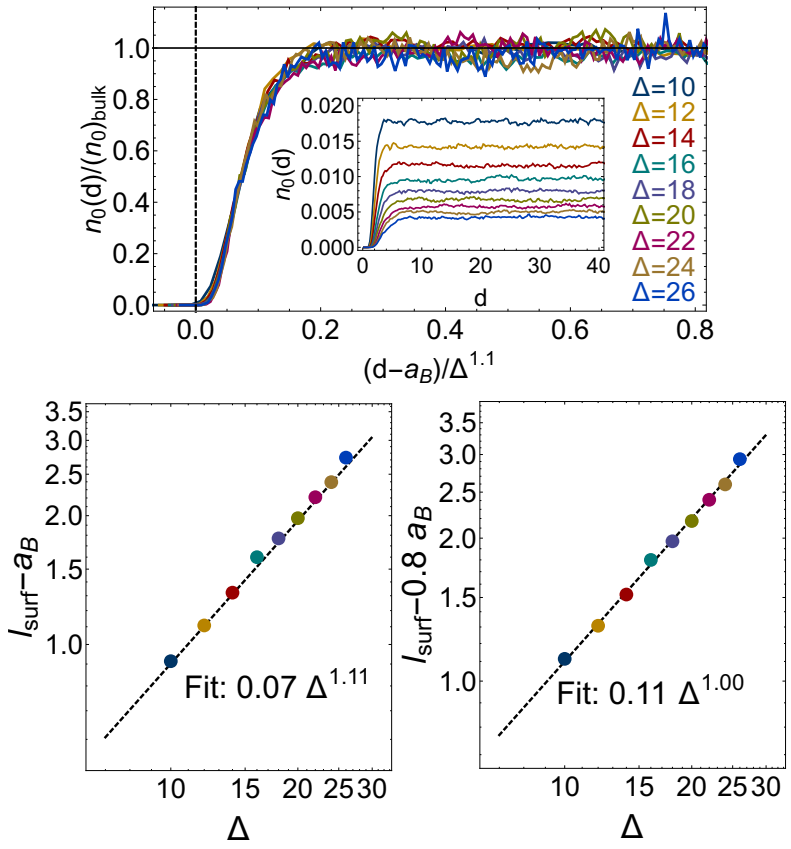

Figure 14.10: **Scaling of the surface penetration depth l_{surf} for $a_{\mathrm{B}} = 1$.** The upper plot shows the density of neutral dopants as a function of the distance d from the surface. The result in Fig. 14.9 suggests a shift of l_{surf} by $a_{\mathrm{B}} = 1$. The lower panel shows two different fits to the full width at half maximum. Both describe the data in the full range $\Delta = 10 - 26$.

We are aware of one other study that investigated the surface screening in $3d$ disordered TIs by Skinner and Shklovskii [261] (reviewed in [235]). Here also non-linear effects were studied. The authors assumed that all donors and acceptors in the bulk are ionized. Motivated by the the STM experiment [221] the size of the fluctuations of the surface-potential was calculated self-consistently by solving the non-linear Eq. (14.16) numerically.

14.5 Connection to the bulk lengthscales

The results above indicate that there is a lengthscale $\sim \Delta^{\alpha \approx 1.05}$ related to the mirror-charge boundary conditions. The length obtained by counting the number of neutral dopants at a distance d away from the surface. Neutralization implies that the potential is $|\phi| > \Delta/2$. On the surface the potential is zero and the lengthscale can be interpreted as the typical length on which the potential changes from zero to $\pm\Delta/2$.

We can define a related quantity in the bulk. With regard to the position of a neutral dopant neutralization of a dopant of the other type requires a change of the potential by Δ. Therefore, we define $n_{AD(DA)}(d)$ as the density of neutral acceptors (donors) at a distance d from a neutral donor (acceptor). The corresponding length-

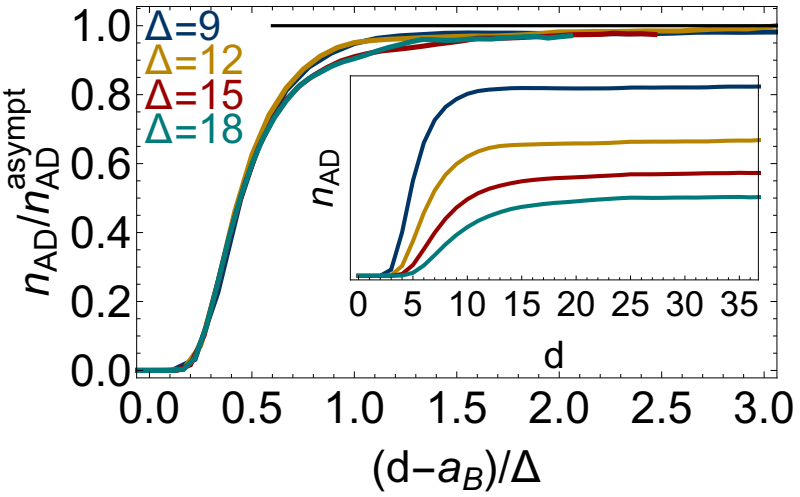

Figure 14.11: **Scaling of the bulk density $n_{AD}(d)$.** The quantity $n_{AD} = n_{DA}$ is explained in the main text and related to $n_0(d)$ studied above. The value of n_{AD} is normalized by the asymptotic value at large distances $d \to L$. If a_B is subtracted from d then the data collapse onto a single curve for $d \lesssim a_\mathrm{B} + 0.6\,\Delta$ when scaled with Δ.

scale is the typical length on which the potential changes from $\Delta/2$ to $-\Delta/2$ ($-\Delta/2$ to $\Delta/2$). For $K = 1$, the only value of K considered here, it is $n_{AD} = n_{DA}$. In Fig. 14.11 we show numerical results for $a_\mathrm{B} = 1$, $L = 50$ and different values of Δ. A scaling collapse at small distances $d - a_\mathrm{B} \lesssim 0.6\,\Delta$ can be obtained by plotting n_{AD} as a function of $(d - a_\mathrm{B})\Delta^{-1}$. The shift by a_B improves the scaling behavior but it is not as important as for $n_0(d)$ close to the surface. The inset shows the unscaled data. At large d n_{AD} is constant. The data in the main panel are normalized by this asymptotic value n_{AD}^{asympt}. The plot suggest that the potential changes from $\pm\Delta/2$ to $\mp\Delta/2$ on a typical length $\sim \Delta^{\alpha\approx 1}$. This is in agreement with the results found in section 12.2.

15 Outlook II

In graphene, electronic puddles are well established and important to understand almost all transport experiments close to charge neutrality. Further experiments are needed to clarify the role of the puddles in topological insulators, also in view of possible future applications of the BSTS and related materials. For topological insulator surfaces which are not highly doped, there will be a complex interplay between surface states and the bulk charges. Non-linear effects are important and may lead to different behavior. In graphene, disorder restricts the possibility to reach ultralow densities of charge carriers. Furthermore, the influence of the magnetic field on the puddle formation has to be investigated. First interesting experimental results have been obtained [274].

The numerical results show that some aspects of the theory of compensated semiconductors may have to be revised. However, the existence of a parametrically different lengthscale needs to be settled. We have not found any numerical evidence for a lengthscale $\sim \Delta^2$ in the simulated parameter regime up to $\Delta \sim 40$. This has influence in the experimentally relevant regime. To get further analytic insight, a tailored disorder renormalization group or replica method is probably needed. The results further show that the puddle formation and the density of states depend sensitively on the temperature. This may be important to understand the transport behavior in the bulk and on the surface. It is worthwhile to further investigate the thermal screening effect and the lengthscales related to this.

Teilpublikationen

[P1] J. Lux, J. Müller, A. Mitra, and A. Rosch, *Hydrodynamic long-time tails after a quantum quench*, Phys. Rev. A **89**, 053608 (2014).

[P2] J. Lux and A. Rosch, *Quench dynamics and statistics of measurements for a line of quantum spins in two dimensions*, Phys. Rev. A **91**, 023617 (2015).

[P3] N. Borgwardt, J. Lux, I. Vergara, Zhiwei Wang, A. A. Taskin, Kouji Segawa, P. H. M. van Loosdrecht, Yoichi Ando, A. Rosch, M. Grüninger, *Revealing puddles of electrons and holes in compensated topological insulators*, ArXiv e-prints 1508.03212 (2015).

References

[1] J. Rammer and H. Smith, *Quantum field-theoretical methods in transport theory of metals*, Rev. Mod. Phys. **58**, 323–359 (1986).

[2] A. Kamenev, *Field Theory of Non-Equilibrium Systems* (Cambridge University Press, Cambridge, UK, 2011).

[3] L. M. Sieberer, M. Buchhold, and S. Diehl, *Keldysh Field Theory for Driven Open Quantum Systems*, ArXiv e-prints 1512.00637 (2015).

[4] H. Aoki, *et al.*, *Nonequilibrium dynamical mean-field theory and its applications*, Rev. Mod. Phys. **86**, 779–837 (2014).

[5] A. J. Daley, C. Kollath, U. Schollwöck, and G. Vidal, *Time-dependent density-matrix renormalization-group using adaptive effective Hilbert spaces*, Journal of Statistical Mechanics: Theory and Experiment **2004**, P04005 (2004).

[6] H. Bethe, *Zur Theorie der Metalle*, Zeitschrift für Physik **71**, 205–226.

[7] M. Karbach and G. Müller, *Introduction to the Bethe ansatz I*, Computers in Physics **11**, 36–43 (1997).

[8] M. Karbach, K. Hu, and G. Müller, *Introduction to the Bethe ansatz II*, Computers in Physics **12**, 565–573 (1998).

[9] M. T. Batchelor, *The Bethe ansatz after 75 years*, Physics Today **60**, 36 (2007).

[10] S. Sachdev, *Quantum Phase Transitions*, 2nd edition (Cambridge University Press, Cambridge, UK, 2011).

[11] S.-i. Tomonaga, *Remarks on Bloch's Method of Sound Waves applied to Many-Fermion Problems*, **5**, 544–569 (1950).

[12] A. Faribault, P. Calabrese, and J.-S. Caux, *Bethe ansatz approach to quench dynamics in the Richardson model*, Journal of Mathematical Physics **50**, 095212 (2009).

[13] P. Calabrese, F. H. L. Essler, and M. Fagotti, *Quantum Quench in the Transverse-Field Ising Chain*, Phys. Rev. Lett. **106**, 227203 (2011).

[14] P. Calabrese, F. H. L. Essler, and M. Fagotti, *Quantum quench in the transverse field Ising chain: I. Time evolution of order parameter correlators*, Journal of Statistical Mechanics: Theory and Experiment **2012**, P07016 (2012).

[15] P. Calabrese, F. H. L. Essler, and M. Fagotti, *Quantum quenches in the transverse field Ising chain: II. Stationary state properties*, Journal of Statistical Mechanics: Theory and Experiment **2012**, P07022 (2012).

[16] J.-S. Caux and F. H. L. Essler, *Time Evolution of Local Observables After Quenching to an Integrable Model*, Phys. Rev. Lett. **110**, 257203 (2013).

[17] D. Iyer, H. Guan, and N. Andrei, *Exact formalism for the quench dynamics of integrable models*, Phys. Rev. A **87**, 053628 (2013).

[18] B. Wouters, *et al.*, *Quenching the Anisotropic Heisenberg Chain: Exact Solution and Generalized Gibbs Ensemble Predictions*, Phys. Rev. Lett. **113**, 117202 (2014).

[19] W. Liu and N. Andrei, *Quench Dynamics of the Anisotropic Heisenberg Model*, Phys. Rev. Lett. **112**, 257204 (2014).

[20] R. Orbach, *Linear Antiferromagnetic Chain with Anisotropic Coupling*, Phys. Rev. **112**, 309–316 (1958).

[21] E. H. Lieb and F. Y. Wu, *Absence of Mott Transition in an Exact Solution of the Short-Range, One-Band Model in One Dimension*, Phys. Rev. Lett. **20**, 1445–1448 (1968).

[22] B. S. Shastry, *Exact Integrability of the One-Dimensional Hubbard Model*, Phys. Rev. Lett. **56**, 2453–2455 (1986).

[23] J. M. Luttinger, *An Exactly Soluble Model of a Many-Fermion System*, Journal of Mathematical Physics **4**, 1154–1162 (1963).

[24] N. Andrei, *Diagonalization of the Kondo Hamiltonian*, Phys. Rev. Lett. **45**, 379–382 (1980).

[25] E. H. Lieb and W. Liniger, *Exact Analysis of an Interacting Bose Gas. I. The General Solution and the Ground State*, Phys. Rev. **130**, 1605–1616 (1963).

[26] E. H. Lieb, *Exact Analysis of an Interacting Bose Gas. II. The Excitation Spectrum*, Phys. Rev. **130**, 1616–1624 (1963).

[27] M. Rigol, V. Dunjko, V. Yurovsky, and M. Olshanii, *Relaxation in a Completely Integrable Many-Body Quantum System: An Ab Initio Study of the Dynamics of the Highly Excited States of 1D Lattice Hard-Core Bosons*, Phys. Rev. Lett. **98**, 050405 (2007).

[28] J.-S. Caux and R. M. Konik, *Constructing the Generalized Gibbs Ensemble after a Quantum Quench*, Phys. Rev. Lett. **109**, 175301 (2012).

[29] E. Ilievski, M. Medenjak, and T. Prosen, *Quasilocal Conserved Operators in the Isotropic Heisenberg Spin-*$1/2$ *Chain*, Phys. Rev. Lett. **115**, 120601 (2015).

[30] H. Ishii, *et al.*, *Direct observation of Tomonaga-Luttinger-liquid state in carbon nanotubes at low temperatures*, Nature **426**, 540–544 (2003).

[31] T. Kinoshita, T. Wenger, and D. Weiss, *A quantum Newton's cradle*, Nature **440**, 900–903 (2006).

[32] M. Gring, *et al.*, *Relaxation and Prethermalization in an Isolated Quantum System*, Science **337**, 1318–1322 (2012).

[33] T. Langen, *et al.*, *Local emergence of thermal correlations in an isolated quantum many-body system*, Nature Physics **9**, 640–643 (2013).

[34] R. Geiger, T. Langen, I. E. Mazets, and J. Schmiedmayer, *Local relaxation and light-cone-like propagation of correlations in a trapped one-dimensional Bose gas*, New Journal of Physics **16**, 053034 (2014).

[35] T. Langen, *et al.*, *Experimental observation of a generalized Gibbs ensemble*, Science **348**, 207–211 (2015).

[36] M. Mehta, *Random Matrices* (Elsevier/Academic Press, Amsterdam, NL, 2004).

[37] D. Poilblanc, *et al.*, *Poisson vs. GOE Statistics in Integrable and Non-Integrable Quantum Hamiltonians*, EPL (Europhysics Letters) **22**, 537 (1993).

[38] P. Bocchieri and A. Loinger, *Quantum Recurrence Theorem*, Phys. Rev. **107**, 337–338 (1957).

[39] J. H. Eberly, N. B. Narozhny, and J. J. Sanchez-Mondragon, *Periodic Spontaneous Collapse and Revival in a Simple Quantum Model*, Phys. Rev. Lett. **44**, 1323–1326 (1980).

[40] W. Thirring, *Lehrbuch der Mathematischen Physik - 4. Quantenmechanik großer Systeme* (Springer, Wien, New York, 1980).

[41] M. Greiner, O. Mandel, T. Hansch, and I. Bloch, *Collapse and revival of the matter wave field of a Bose-Einstein condensate*, Nature **419**, 51–54 (2002).

[42] M. Köhl, *et al.*, *Fermionic Atoms in a Three Dimensional Optical Lattice: Observing Fermi Surfaces, Dynamics, and Interactions*, Phys. Rev. Lett. **94**, 080403 (2005).

[43] I. Bloch, *Ultracold atoms in optical lattices*, Nature Physics **1**, 23–30 (2005).

[44] I. Bloch, J. Dalibard, and W. Zwerger, *Many-body physics with ultracold gases*, Rev. Mod. Phys. **80**, 885–964 (2008).

[45] J. Berges, S. Borsányi, and C. Wetterich, *Prethermalization*, Phys. Rev. Lett. **93**, 142002 (2004).

[46] M. Kollar, F. A. Wolf, and M. Eckstein, *Generalized Gibbs ensemble prediction of prethermalization plateaus and their relation to nonthermal steady states in integrable systems*, Phys. Rev. B **84**, 054304 (2011).

[47] N. Nessi, A. Iucci, and M. A. Cazalilla, *Quantum Quench and Prethermalization Dynamics in a Two-Dimensional Fermi Gas with Long-Range Interactions*, Phys. Rev. Lett. **113**, 210402 (2014).

[48] M. Marcuzzi, J. Marino, A. Gambassi, and A. Silva, *Prethermalization in a Nonintegrable Quantum Spin Chain after a Quench*, Phys. Rev. Lett. **111**, 197203 (2013).

[49] D. A. Smith, *et al.*, *Prethermalization revealed by the relaxation dynamics of full distribution functions*, New Journal of Physics **15**, 075011 (2013).

[50] P. W. Anderson, *More Is Different*, Science **177**, 393–396 (1972).

[51] H. Poincaré, *Sur le problème des trois corps et les équations de la dynamique*, Acta mathematica **13**, 1–270 (1890).

[52] H. D. Zeh, *The Physical Basis of The Direction of Time*, 4th edition (Springer, 2001).

[53] J. Eisert, M. Cramer, and M. B. Plenio, *Colloquium : Area laws for the entanglement entropy*, Rev. Mod. Phys. **82**, 277–306 (2010).

[54] D. Basko, I. Aleiner, and B. Altshuler, *Metal-insulator transition in a weakly interacting many-electron system with localized single-particle states*, Ann. Phys. **321**, 1126–1205 (2006).

[55] R. Nandkishore and D. Huse, *Many-Body Localization and Thermalization in Quantum Statistical Mechanics*, Ann. Rev. of Cond. Mat. Phys. **6**, 15–38 (2015).

[56] P. W. Anderson, *Absence of Diffusion in Certain Random Lattices*, Phys. Rev. **109**, 1492–1505 (1958).

[57] A. Lagendijk, B. van Tiggelen, and D. Wiersma, *Fifty years of Anderson localization*, Physics Today **62**, 24–29 (2009).

[58] M. Schreiber, *et al.*, *Observation of many-body localization of interacting fermions in a quasirandom optical lattice*, Science **349**, 842–845 (2015).

[59] P. Bordia, *et al.*, *Coupling Identical 1D Many-Body Localized Systems*, ArXiv e-prints 1509.00478 (2015).

[60] J. M. Deutsch, *Quantum statistical mechanics in a closed system*, Phys. Rev. A **43**, 2046–2049 (1991).

[61] M. Srednicki, *Chaos and quantum thermalization*, Phys. Rev. E **50**, 888–901 (1994).

[62] M. Rigol, V. Dunjko, and M. Olshanii, *Thermalization and its mechanism for generic isolated quantum systems*, Nature **452**, 854–858 (2008).

[63] E. H. Lieb and D. W. Robinson, *The finite group velocity of quantum spin systems*, Communications in Mathematical Physics **28**, 251–257 (1972).

[64] H. J. Metcalf and P. van der Straten, *Laser Cooling and Trapping* (Springer, New York, 1999).

[65] R. Grimm, M. Weidemüller, and Y. B. Ovchinnikov, *Optical Dipole Traps for Neutral Atoms*, volume 42 of *Advances In Atomic, Molecular, and Optical Physics*, pp. 95–170 (Academic Press, 2000).

[66] A. Lamacraft, *Cold Atoms for Condensed Matter Theorists* (Lecture Notes, Oxford, 2006).

[67] I. Bloch, J. Dalibard, and S. Nascimbène, *Quantum simulations with ultracold qunatum gases*, Nature Physics **8**, 267–276 (2012).

[68] D. M. Weld, *et al.*, *Spin Gradient Thermometry for Ultracold Atoms in Optical Lattices*, Phys. Rev. Lett. **103**, 245301 (2009).

[69] A. Omran, *et al.*, *Microscopic Observation of Pauli Blocking in Degenerate Fermionic Lattice Gases*, Phys. Rev. Lett. **115**, 263001 (2015).

[70] A. Aspect, *et al.*, *Laser Cooling below the One-Photon Recoil Energy by Velocity-Selective Coherent Population Trapping*, Phys. Rev. Lett. **61**, 826–829 (1988).

[71] W. D. Phillips, *Nobel Lecture: Laser cooling and trapping of neutral atoms*, Rev. Mod. Phys. **70**, 721–741 (1998).

[72] T. Takekoshi, B. M. Patterson, and R. J. Knize, *Observation of Optically Trapped Cold Cesium Molecules*, Phys. Rev. Lett. **81**, 5105–5108 (1998).

[73] J. F. Barry, *et al.*, *Magneto-optical trapping of a diatomic molecule*, Nature **512**, 286–289 (2014).

[74] D. E. Pritchard, *Cooling Neutral Atoms in a Magnetic Trap for Precision Spectroscopy*, Phys. Rev. Lett. **51**, 1336–1339 (1983).

[75] J. Fortágh and C. Zimmermann, *Magnetic microtraps for ultracold atoms*, Rev. Mod. Phys. **79**, 235–289 (2007).

[76] D. Leibfried, R. Blatt, C. Monroe, and D. Wineland, *Quantum dynamics of single trapped ions*, Rev. Mod. Phys. **75**, 281–324 (2003).

[77] L.-M. Duan and C. Monroe, *Colloquium : Quantum networks with trapped ions*, Rev. Mod. Phys. **82**, 1209–1224 (2010).

[78] M. Greiner, *et al.*, *Quantum phase transition from a superfluid to a Mott insulator in a gas of ultracold atoms*, Nature **415**, 39–44 (2002).

[79] B. Capogrosso-Sansone, N. V. Prokof'ev, and B. V. Svistunov, *Phase diagram and thermodynamics of the three-dimensional Bose-Hubbard model*, Phys. Rev. B **75**, 134302 (2007).

[80] T. Bourdel, *et al.*, *Experimental Study of the BEC-BCS Crossover Region in Lithium 6*, Phys. Rev. Lett. **93**, 050401 (2004).

[81] S. Giorgini, L. P. Pitaevskii, and S. Stringari, *Theory of ultracold atomic Fermi gases*, Rev. Mod. Phys. **80**, 1215–1274 (2008).

[82] K. M. O'Hara, *et al.*, *Observation of a Strongly Interacting Degenerate Fermi Gas of Atoms*, Science (2002).

[83] T.-L. Ho, *Universal Thermodynamics of Degenerate Quantum Gases in the Unitarity Limit*, Phys. Rev. Lett. **92**, 090402 (2004).

[84] J. M. Sage, S. Sainis, T. Bergeman, and D. DeMille, *Optical Production of Ultracold Polar Molecules*, Phys. Rev. Lett. **94**, 203001 (2005).

[85] K.-K. Ni, *et al.*, *A High Phase-Space-Density Gas of Polar Molecules*, Science **322**, 231–235 (2008).

[86] A. Chotia, *et al.*, *Long-Lived Dipolar Molecules and Feshbach Molecules in a 3D Optical Lattice*, Phys. Rev. Lett. **108**, 080405 (2012).

[87] A. Micheli, G. K. Brennen, and P. Zoller, *A toolbox for lattice-spin models with polar molecules*, Nature Physics **2**, 341–347 (2006).

[88] J. F. Sherson, *et al.*, *Single-atom-resolved fluorescence imaging of an atomic Mott insulator*, Nature **467**, 68–72 (2010).

[89] T. Fujisawa, T. Hayashi, R. Tomita, and Y. Hirayama, *Bidirectional Counting of Single Electrons*, Science **312**, 1634–1636 (2006).

[90] S. Gustavsson, *et al.*, *Counting Statistics of Single Electron Transport in a Quantum Dot*, Phys. Rev. Lett. **96**, 076605 (2006).

[91] L. Fricke, *et al.*, *Counting Statistics for Electron Capture in a Dynamic Quantum Dot*, Phys. Rev. Lett. **110**, 126803 (2013).

[92] W. S. Bakr, *et al.*, *A Quantum Gas Microscope for detecting single atoms in a Hubbard regime optical lattice*, Nature **462**, 74–77 (2009).

[93] E. Haller, *et al.*, *Single-atom imaging of fermions in a quantum-gas microscope*, Nature Physics **11**, 738–742 (2015).

[94] L. W. Cheuk, *et al.*, *Quantum-Gas Microscope for Fermionic Atoms*, Phys. Rev. Lett. **114**, 193001 (2015).

[95] M. F. Parsons, *et al.*, *Site-Resolved Imaging of Fermionic* ^{6}Li *in an Optical Lattice*, Phys. Rev. Lett. **114**, 213002 (2015).

[96] W. S. Bakr, *et al.*, *Probing the Superfluid to Mott Insulator Transition at the Single-Atom Level*, Science **329**, 547–550 (2010).

[97] M. Endres, *et al.*, *Observation of Correlated Particle-Hole Pairs and String Order in Low-Dimensional Mott Insulators*, Science **334**, 200–203 (2011).

[98] R. Islam, *et al.*, *Measuring entanglement entropy in a quantum many-body system*, Nature **528**, 77–83 (2015).

[99] N. Malossi, *et al.*, *Full Counting Statistics and Phase Diagram of a Dissipative Rydberg Gas*, Phys. Rev. Lett. **113**, 023006 (2014).

[100] T. Schweigler, *et al.*, *On solving the quantum many-body problem*, ArXiv e-prints 1505.03126 (2015).

[101] K. Sakmann and M. Kasevich, *Single-shot simulations of dynamic quantum many-body systems*, Nature Physics (2016).

[102] T. Fukuhara, *et al.*, *Quantum dynamics of a mobile spin impurity*, Nature Physics **9**, 235–241 (2013).

[103] Cheneau Marc, *et al.*, *Light-cone-like spreading of correlations in a quantum many-body system*, Nature **481**, 484–487 (2012).

[104] S. Trotzky, *et al.*, *Probing the relaxation towards equilibrium in an isolated strongly correlated one-dimensional Bose gas*, Nature physics **8**, 325 – 330 (2012).

[105] T. Fukuhara, *et al.*, *Microscopic observation of magnon bound states and their dynamics*, Nature (2013).

[106] S. Hild, *et al.*, *Far-from-Equilibrium Spin Transport in Heisenberg Quantum Magnets*, Phys. Rev. Lett. **113**, 147205 (2014).

[107] P. M. Preiss, *et al.*, *Strongly correlated quantum walks in optical lattices*, Science **347**, 1229–1233 (2015).

[108] C. Weitenberg, *et al.*, *Single-spin addressing in an atomic Mott insulator*, Nature **471**, 319–324 (2011).

[109] A. B. Kuklov and B. V. Svistunov, *Counterflow Superfluidity of Two-Species Ultracold Atoms in a Commensurate Optical Lattice*, Phys. Rev. Lett. **90**, 100401 (2003).

[110] L.-M. Duan, E. Demler, and M. D. Lukin, *Controlling Spin Exchange Interactions of Ultracold Atoms in Optical Lattices*, Phys. Rev. Lett. **91**, 090402 (2003).

[111] J. R. Schrieffer and P. A. Wolff, *Relation between the Anderson and Kondo Hamiltonians*, Phys. Rev. **149**, 491–492 (1966).

[112] C. L. Cleveland and R. Medina A., *Obtaining a Heisenberg Hamiltonian from the Hubbard model*, American Journal of Physics **44**, 44–46 (1976).

[113] C. Dasgupta and S.-k. Ma, *Low-temperature properties of the random Heisenberg antiferromagnetic chain*, Phys. Rev. B **22**, 1305–1319 (1980).

[114] M. Moeckel and S. Kehrein, *Interaction Quench in the Hubbard Model*, Phys. Rev. Lett. **100**, 175702 (2008).

[115] P. Barmettler, D. Poletti, M. Cheneau, and C. Kollath, *Propagation front of correlations in an interacting Bose gas*, Phys. Rev. A **85**, 053625 (2012).

[116] P. Calabrese and J. Cardy, *Evolution of entanglement entropy in one-dimensional systems*, Journal of Statistical Mechanics: Theory and Experiment **2005**, P04010 (2005).

[117] P. Calabrese and J. Cardy, *Quantum quenches in extended systems*, Journal of Statistical Mechanics: Theory and Experiment **2007**, P06008 (2007).

[118] S. Sachdev and K. Damle, *Low temperature spin diffusion in the one-dimensional quantum $O(3)$ nonlinear σ model*, Phys. Rev. Lett. **78**, 943–946 (1997).

[119] S. Sachdev and A. P. Young, *Low Temperature Relaxational Dynamics of the Ising Chain in a Transverse Field*, Phys. Rev. Lett. **78**, 2220–2223 (1997).

[120] H. Rieger and F. Iglói, *Semiclassical theory for quantum quenches in finite transverse Ising chains*, Phys. Rev. B **84**, 165117 (2011).

[121] P. Grassberger, W. Nadler, and L. Yang, *Heat Conduction and Entropy Production in a One-Dimensional Hard-Particle Gas*, Phys. Rev. Lett. **89**, 180601 (2002).

[122] P. Cipriani, S. Denisov, and A. Politi, *From Anomalous Energy Diffusion to Levy Walks and Heat Conductivity in One-Dimensional Systems*, Phys. Rev. Lett. **94**, 244301 (2005).

[123] L. Delfini, *et al.*, *Energy diffusion in hard-point systems*, The European Physical Journal Special Topics **146**, 21–35 (2007).

[124] L. Onsager, *Reciprocal Relations in Irreversible Processes. I.*, Phys. Rev. **37**, 405–426 (1931).

[125] L. Onsager, *Reciprocal Relations in Irreversible Processes. II.*, Phys. Rev. **38**, 2265–2279 (1931).

[126] R. Kubo, M. Yokota, and S. Nakajima, *Statistical-Mechanical Theory of Irreversible Processes. II. Response to Thermal Disturbance*, Journal of the Physical Society of Japan **12**, 1203–1211 (1957).

[127] R. Kubo, *Statistical-Mechanical Theory of Irreversible Processes. I. General Theory and Simple Applications to Magnetic and Conduction Problems*, Journal of the Physical Society of Japan **12**, 570–586 (1957).

[128] R. Kubo, *The fluctuation-dissipation theorem*, Reports on Progress in Physics **29**, 255 (1966).

[129] L. D. Landau and E. M. Lifshitz, *Fluid Mechanics*, volume 6 of *Course of Theoretical Physics*, 2nd edition (Pergamon Press, Oxford, UK, 1987).

[130] D. Vollhardt and P. Wölfle, *Anderson Localization in* ≤ 2 *Dimensions: A Self-Consistent Diagrammatic Theory*, Phys. Rev. Lett. **45**, 842–846 (1980).

[131] P. C. Hohenberg and B. I. Halperin, *Theory of dynamic critical phenomena*, Rev. Mod. Phys. **49**, 435–479 (1977).

[132] D. Forster, *Hydrodynamic fluctuations, broken symmetry, and correlation functions* (W. A. Benjamin, Inc. Reading Massachusetts, 1975).

[133] G. E. Uhlenbeck and L. S. Ornstein, *On the Theory of the Brownian Motion*, Phys. Rev. **36**, 823–841 (1930).

[134] A. Einstein, *Über die von der molekularkinetischen Theorie der Wärme geforderte Bewegung von in ruhenden Flüssigkeiten suspendierten Teilchen*, Annalen der Physik **322**, 549–560 (1905).

[135] M. H. Ernst, E. H. Hauge, and J. M. J. Leeuwen, *Asymptotic time behavior of correlation functions. III. Local equilibrium and mode-coupling theory*, Journal of Statistical Physics **15**, 23–58 (1976).

[136] R. Zwanzig, *Memory Effects in Irreversible Thermodynamics*, Phys. Rev. **124**, 983–992 (1961).

[137] H. Mori, *Transport, Collective Motion, and Brownian Motion*, Progress of Theoretical Physics **33**, 423–455 (1965).

[138] A. Fick, *Ueber Diffusion*, Annalen der Physik **170**, 59–86 (1855).

[139] D. Chandler and I. Oppenheim, *Fluctuation Theory and Critical Phenomena*, The Journal of Chem. Phys. **49**, 2121–2127 (1968).

[140] A. Altland and B. Simons, *Condensed matter field theory*, 2nd edition (Cambridge Univ. Press, Cambridge, 2010).

[141] H. van Beijeren, R. Kutner, and H. Spohn, *Excess Noise for Driven Diffusive Systems*, Phys. Rev. Lett. **54**, 2026–2029 (1985).

[142] H. van Beijeren, *Exact Results for Anomalous Transport in One-Dimensional Hamiltonian Systems*, Phys. Rev. Lett. **108**, 180601 (2012).

[143] H. Spohn, *Nonlinear Fluctuating Hydrodynamics for Anharmonic Chains*, Journal of Statistical Physics **154**, 1191–1227 (2014).

[144] C. B. Mendl and H. Spohn, *Equilibrium time-correlation functions for one-dimensional hard-point systems*, Phys. Rev. E **90**, 012147 (2014).

[145] S. G. Das, *et al.*, *Numerical test of hydrodynamic fluctuation theory in the Fermi-Pasta-Ulam chain*, Phys. Rev. E **90**, 012124 (2014).

[146] C. B. Mendl and H. Spohn, *Current fluctuations for anharmonic chains in thermal equilibrium*, Journal of Statistical Mechanics: Theory and Experiment **2015**, P03007 (2015).

[147] Y. Li, *et al.*, *1D momentum-conserving systems: the conundrum of anomalous versus normal heat transport*, New Journal of Physics **17**, 043064 (2015).

[148] M. Kardar, G. Parisi, and Y.-C. Zhang, *Dynamic Scaling of Growing Interfaces*, Phys. Rev. Lett. **56**, 889–892 (1986).

[149] M. Prähofer and H. Spohn, *Exact Scaling Functions for One-Dimensional Stationary KPZ Growth*, Journal of Statistical Physics **115**, 255–279 (2004).

[150] B. J. Alder and T. E. Wainwright, *Velocity Autocorrelations for Hard Spheres*, Phys. Rev. Lett. **18**, 988–990 (1967).

[151] B. J. Alder and T. E. Wainwright, *Decay of the Velocity Autocorrelation Function*, Phys. Rev. A **1**, 18–21 (1970).

[152] T. E. Wainwright, B. J. Alder, and D. M. Gass, *Decay of Time Correlations in Two Dimensions*, Phys. Rev. A **4**, 233–237 (1971).

[153] Y. Pomeau and P. Resibois, *Time dependent correlation functions and mode-mode coupling theories*, Physics Reports **19**, 63 – 139 (1975).

[154] J. R. Dorfman, T. R. Kirkpatrick, and J. V. Sengers, *Generic Long-Range Correlations in Molecular Fluids*, Annual Review of Physical Chemistry **45**, 213–239 (1994).

[155] T. R. Kirkpatrick and J. R. Dorfman, *Nonequilibrium is different*, Phys. Rev. E **92**, 022109 (2015).

[156] J. R. Dorfman, T. R. Kirkpatrick, and J. V. Sengers, *Why Non-equilibrium is Different*, ArXiv e-prints 1512.02679 (2015).

[157] M. H. Ernst, E. H. Hauge, and J. M. J. van Leeuwen, *Asymptotic Time Behavior of Correlation Functions*, Phys. Rev. Lett. **25**, 1254–1256 (1970).

[158] J. R. Dorfman and E. G. D. Cohen, *Velocity Correlation Functions in Two and Three Dimensions*, Phys. Rev. Lett. **25**, 1257–1260 (1970).

[159] J. R. Dorfman and E. G. D. Cohen, *Velocity-Correlation Functions in Two and Three Dimensions: Low Density*, Phys. Rev. A **6**, 776–790 (1972).

[160] M. H. Ernst, E. H. Hauge, and J. M. J. Leeuwen, *Asymptotic time behavior of correlation functions. II. Kinetic and potential terms*, Journal of Statistical Physics **15**, 7–22 (1976).

[161] T. R. Kirkpatrick, E. G. D. Cohen, and J. R. Dorfman, *Fluctuations in a nonequilibrium steady state: Basic equations*, Phys. Rev. A **26**, 950–971 (1982).

[162] T. R. Kirkpatrick, E. G. D. Cohen, and J. R. Dorfman, *Light scattering by a fluid in a nonequilibrium steady state. II. Large gradients*, Phys. Rev. A **26**, 995–1014 (1982).

[163] D. Belitz, T. R. Kirkpatrick, and T. Vojta, *How generic scale invariance influences quantum and classical phase transitions*, Rev. Mod. Phys. **77**, 579–632 (2005).

[164] P. Kovtun and L. G. Yaffe, *Hydrodynamic fluctuations, long-time tails, and supersymmetry*, Phys. Rev. D **68**, 025007 (2003).

[165] S. Caron-Huot and O. Saremi, *Hydrodynamic long-time tails from Anti de Sitter space*, Journal of High Energy Physics **2010**, 1–31 (2010).

[166] K. Kawasaki and I. Oppenheim, *Logarithmic Term in the Density Expansion of Transport Coefficients*, Phys. Rev. **139**, A1763–A1768 (1965).

[167] J. Dorfman and E. Cohen, *On the density expansion of the pair distribution function for a dense gas not in equilibrium*, Physics Letters **16**, 124 – 125 (1965).

[168] Y. Pomeau, *Transport Theory for a Two-Dimensional Dense Gas*, Phys. Rev. A **3**, 1174–1194 (1971).

[169] S. Lepri, R. Livi, and A. Politi, *Thermal conduction in classical low-dimensional lattices*, Physics Reports **377**, 1 – 80 (2003).

[170] H. B. Callen, *The Application of Onsager's Reciprocal Relations to Thermoelectric, Thermomagnetic, and Galvanomagnetic Effects*, Phys. Rev. **73**, 1349–1358 (1948).

[171] N. Strohmaier, *et al.*, *Observation of Elastic Doublon Decay in the Fermi-Hubbard Model*, Phys. Rev. Lett. **104**, 080401 (2010).

[172] J. P. Ronzheimer, *et al.*, *Expansion Dynamics of Interacting Bosons in Homogeneous Lattices in One and Two Dimensions*, Phys. Rev. Lett. **110**, 205301 (2013).

[173] M. Eckstein, M. Kollar, and P. Werner, *Thermalization after an Interaction Quench in the Hubbard Model*, Phys. Rev. Lett. **103**, 056403 (2009).

[174] S. Sorg, L. Vidmar, L. Pollet, and F. Heidrich-Meisner, *Relaxation and thermalization in the one-dimensional Bose-Hubbard model: A case study for the interaction quantum quench from the atomic limit*, Phys. Rev. A **90**, 033606 (2014).

[175] M. Pinkwart, *Thermalization and Integrability in the one-dimensional Bose-Hubbard Model* (Bachelor thesis, Universität zu Köln, 2014).

[176] M. Garst and A. Rosch, *Transport in a classical model of a one-dimensional Mott insulator: Influence of conservation laws*, EPL (Europhysics Letters) **55**, 66 (2001).

[177] B. Bauer, *et al.*, *The ALPS project release 2.0: open source software for strongly correlated systems*, Journal of Statistical Mechanics: Theory and Experiment **2011**, P05001 (2011).

[178] Jordens Robert, *et al.*, *A Mott insulator of fermionic atoms in an optical lattice*, Nature **455**, 204–207 (2008), 10.1038/nature07244.

[179] H. Kim and D. A. Huse, *Ballistic Spreading of Entanglement in a Diffusive Nonintegrable System*, Phys. Rev. Lett. **111**, 127205 (2013).

[180] F. Lange, *Equilibrierung und Hydrodynamik in offenen Systemen* (Bachelor thesis, Universität zu Köln, 2014).

[181] V. Born, M.and Fock, *Beweis des Adiabatensatzes*, Zeitschrift für Physik **51**, 165–180 (1928).

[182] L.-M. Duan, E. Demler, and M. D. Lukin, *Controlling Spin Exchange Interactions of Ultracold Atoms in Optical Lattices*, Phys. Rev. Lett. **91**, 090402 (2003).

[183] M. Bonitz, *private communication* (Bad Honnef, 2015).

[184] D. Gobert, C. Kollath, U. Schollwöck, and G. Schütz, *Real-time dynamics in spin-$\frac{1}{2}$ chains with adaptive time-dependent density matrix renormalization group*, Phys. Rev. E **71**, 036102 (2005).

[185] M. Bixon and R. Zwanzig, *Boltzmann-Langevin Equation and Hydrodynamic Fluctuations*, Phys. Rev. **187**, 267–272 (1969).

[186] J. Randrup and B. Remaud, *Fluctuations in one-body dynamics*, Nuclear Physics A **514**, 339–366 (1990).

[187] P. G. Reinhard, E. Suraud, and S. Ayik, *The Boltzmann-Langevin Equation Derived from the Real-Time Path Formalism*, Ann. Phys. (N.Y.) **213** (1992).

[188] S. Ayik, *Long-range correlations in Boltzmann-Langevin model*, Zeitschrift für Physik A Hadrons and Nuclei **350**, 45–49 (1994).

[189] E. Calzetta and B. L. Hu, *Stochastic dynamics of correlations in quantum field theory: From the Schwinger-Dyson to Boltzmann-Langevin equation*, Phys. Rev. D **61**, 025012 (1999).

[190] E. Calzetta, *Fourth-order full quantum correlations from a Langevin–Schwinger–Dyson equation*, Journal of Physics A: Mathematical and Theoretical **42**, 265401 (2009).

[191] M. Bonitz, *Quantum Kinetic Equations*, 1st edition (B. G. Teubner, Leipzig, 1998).

[192] J. Berges, *n-particle irreducible effective action techniques for gauge theories*, Phys. Rev. D **70**, 105010 (2004).

[193] M. Kronenwett and T. Gasenzer, *Far-from-equilibrium dynamics of an ultracold Fermi gas*, Applied Physics B **102**, 469–488 (2011).

[194] A. Altland and M. R. Zirnbauer, *Nonstandard symmetry classes in mesoscopic normal-superconducting hybrid structures*, Phys. Rev. B **55**, 1142–1161 (1997).

[195] M. Z. Hasan and C. L. Kane, *Colloquium : Topological insulators*, Rev. Mod. Phys. **82**, 3045–3067 (2010).

[196] X.-L. Qi and S.-C. Zhang, *Topological insulators and superconductors*, Rev. Mod. Phys. **83**, 1057–1110 (2011).

[197] K. v. Klitzing, G. Dorda, and M. Pepper, *New Method for High-Accuracy Determination of the Fine-Structure Constant Based on Quantized Hall Resistance*, Phys. Rev. Lett. **45**, 494–497 (1980).

[198] D. J. Thouless, M. Kohmoto, M. P. Nightingale, and M. den Nijs, *Quantized Hall Conductance in a Two-Dimensional Periodic Potential*, Phys. Rev. Lett. **49**, 405–408 (1982).

[199] C. L. Kane and E. J. Mele, *Quantum Spin Hall Effect in Graphene*, Phys. Rev. Lett. **95**, 226801 (2005).

[200] C. L. Kane and E. J. Mele, *Z_2 Topological Order and the Quantum Spin Hall Effect*, Phys. Rev. Lett. **95**, 146802 (2005).

[201] M. König, *et al.*, *Quantum Spin Hall Insulator State in HgTe Quantum Wells*, Science **318**, 766–770 (2007).

[202] B. A. Bernevig, T. L. Hughes, and S.-C. Zhang, *Quantum Spin Hall Effect and Topological Phase Transition in HgTe Quantum Wells*, Science **314**, 1757–1761 (2006).

[203] L. Fu, C. L. Kane, and E. J. Mele, *Topological Insulators in Three Dimensions*, Phys. Rev. Lett. **98**, 106803 (2007).

[204] A. P. Schnyder, S. Ryu, A. Furusaki, and A. W. W. Ludwig, *Classification of topological insulators and superconductors in three spatial dimensions*, Phys. Rev. B **78**, 195125 (2008).

[205] L. Fu and C. L. Kane, *Topological insulators with inversion symmetry*, Phys. Rev. B **76**, 045302 (2007).

[206] S. Murakami, *Phase transition between the quantum spin Hall and insulator phases in 3D: emergence of a topological gapless phase*, New Journal of Physics **9**, 356 (2007).

[207] Hsieh D., *et al.*, *A topological Dirac insulator in a quantum spin Hall phase*, Nature **452**, 970–974 (2008).

[208] B. Zhou, *et al.*, *Controlling the carriers of topological insulators by bulk and surface doping*, Semiconductor Science and Technology **27**, 124002 (2012).

[209] Analytis James G., *et al.*, *Two-dimensional surface state in the quantum limit of a topological insulator*, Nat Phys **6**, 960–64 (2010), 10.1038/nphys1861.

[210] Z. Ren, *et al.*, *Optimizing $Bi_{2-x}Sb_xTe_{3-y}Se_y$ solid solutions to approach the intrinsic topological insulator regime*, Phys. Rev. B **84**, 165311 (2011).

[211] A. L. Efros and B. I. Shklovskii, *Electronic Properties of Doped Semiconductors* (Springer Berlin Heidelberg, 1984).

[212] J. Martin, *et al.*, *Observation of electron-hole puddles in graphene using a scanning single-electron transistor*, Nature Physics **4**, 144–148 (2008).

[213] Zhang Yuanbo, *et al.*, *Origin of spatial charge inhomogeneity in graphene*, Nature Physics **5**, 722–726 (2009).

[214] S. Adam, E. H. Hwang, V. M. Galitski, and S. Das Sarma, *A self-consistent theory for graphene transport*, Proceedings of the National Academy of Sciences **104**, 18392–18397 (2007).

[215] E. H. Hwang, S. Adam, and S. D. Sarma, *Carrier Transport in Two-Dimensional Graphene Layers*, Phys. Rev. Lett. **98**, 186806 (2007).

[216] R. V. Gorbachev, *et al.*, *Strong Coulomb drag and broken symmetry in double-layer graphene*, Nature Physics **8**, 896–901 (2012).

[217] V. Geringer, *et al.*, *Intrinsic and extrinsic corrugation of monolayer graphene deposited on* SiO_2, Phys. Rev. Lett. **102**, 076102 (2009).

[218] M. Gibertini, *et al.*, *Electron-hole puddles in the absence of charged impurities*, Phys. Rev. B **85**, 201405 (2012).

[219] Kim Dohun, *et al.*, *Surface conduction of topological Dirac electrons in bulk insulating Bi2Se3*, Nat Phys **8**, 459–463 (2012), 10.1038/nphys2286.

[220] D. Kim, *et al.*, *Ambipolar Surface State Thermoelectric Power of Topological Insulator Bi2Se3*, Nano Letters **14**, 1701–1706 (2014).

[221] H. Beidenkopf, *et al.*, *Spatial fluctuations of helical Dirac fermions on the surface of topological insulators*, Nature Physics **7**, 939–943 (2011).

[222] L. D. Landau and E. M. Lifshitz, *Fluid Mechanics*, volume 8 of *Course of Theoretical Physics*, 2nd edition (Pergamon Press, Oxford, UK, 1963).

[223] F. Wooten, *Optical Properties of Solids*, 1st edition (Academic Press, Inc., London, UK, 1972).

[224] M. Fox, *Optical Properties of Solids*, 1st edition (Oxford University Press, Oxford, UK, 2002).

[225] G. A. Thomas, *et al.*, *Large electronic-density increase on cooling a layered metal: Doped* $\mathrm{Bi_2Te_3}$, Phys. Rev. B **46**, 1553–1556 (1992).

[226] A. D. LaForge, *et al.*, *Optical characterization of Bi_2Se_3 in a magnetic field: Infrared evidence for magnetoelectric coupling in a topological insulator material*, Phys. Rev. B **81**, 125120 (2010).

[227] A. Segura, *et al.*, *Trapping of three-dimensional electrons and transition to two-dimensional transport in the three-dimensional topological insulator Bi_2Se_3 under high pressure*, Phys. Rev. B **85**, 195139 (2012).

[228] P. Di Pietro, *et al.*, *Optical conductivity of bismuth-based topological insulators*, Phys. Rev. B **86**, 045439 (2012).

[229] A. Akrap, *et al.*, *Optical properties of Bi_2Te_2Se at ambient and high pressures*, Phys. Rev. B **86**, 235207 (2012).

[230] K. W. Post, *et al.*, *Thickness-dependent bulk electronic properties in Bi_2Se_3 thin films revealed by infrared spectroscopy*, Phys. Rev. B **88**, 075121 (2013).

[231] S. V. Dordevic, *et al.*, *Signatures of charge inhomogeneities in the infrared spectra of topological insulators Bi_2Se_3, Bi_2Te_3 and Sb_2Te_3*, Journal of Physics: Condensed Matter **25**, 075501 (2013).

[232] Y. Aleshchenko, *et al.*, *Infrared spectroscopy of Bi_2Te_2Se*, JETP Letters **99**, 187–190 (2014).

[233] B. C. Chapler, *et al.*, *Infrared electrodynamics and ferromagnetism in the topological semiconductors* $\mathrm{Bi_2Te_3}$ *and Mn-doped* $\mathrm{Bi_2Te_3}$, Phys. Rev. B **89**, 235308 (2014).

[234] B. Skinner, T. Chen, and B. I. Shklovskii, *Why Is the Bulk Resistivity of Topological Insulators So Small?*, Phys. Rev. Lett. **109**, 176801 (2012).

[235] B. Skinner, T. Chen, and B. Shklovskii, *Effects of bulk charged impurities on the bulk and surface transport in three-dimensional topological insulators*, Journal of Experimental and Theoretical Physics **117**, 579–592 (2013).

[236] T. Arakane, *et al.*, *Tunable Dirac cone in the topological insulator* $Bi_{2-x}Sb_xTe_{3-y}Se_y$, Nature Comm. **3**, 636 (2012).

[237] Z. Ren, *et al.*, *Large bulk resistivity and surface quantum oscillations in the topological insulator* Bi_2Te_2Se, Phys. Rev. B **82**, 241306 (2010).

[238] Z. Li and J. P. Carbotte, *Hexagonal warping on optical conductivity of surface states in topological insulator* Bi_2Te_3, Phys. Rev. B **87**, 155416 (2013).

[239] D. Schmeltzer and K. Ziegler, *Optical conductivity for the surface of a Topological Insulator*, ArXiv e-prints:1302.4145 (2013).

[240] J. M. Luttinger and W. Kohn, *Motion of Electrons and Holes in Perturbed Periodic Fields*, Phys. Rev. **97**, 869–883 (1955).

[241] F. Bassani, G. Iadonisi, and B. Preziosi, *Electronic impurity levels in semiconductors*, Reports on Progress in Physics **37**, 1099 (1974).

[242] K. Eto, *et al.*, *Angular-dependent oscillations of the magnetoresistance in* Bi_2Se_3 *due to the three-dimensional bulk Fermi surface*, Phys. Rev. B **81**, 195309 (2010).

[243] M. Y. Han, J. C. Brant, and P. Kim, *Electron Transport in Disordered Graphene Nanoribbons*, Phys. Rev. Lett. **104**, 056801 (2010).

[244] T. Chen and B. I. Shklovskii, *Anomalously small resistivity and thermopower of strongly compensated semiconductors and topological insulators*, Phys. Rev. B **87**, 165119 (2013).

[245] S. A. Basylko, *et al.*, *Coulomb gap in a model with finite charge-transfer energy*, Phys. Rev. B **63**, 024201 (2000).

[246] L. Berthier and G. Biroli, *Theoretical perspective on the glass transition and amorphous materials*, Rev. Mod. Phys. **83**, 587–645 (2011).

[247] J. H. Davies, P. A. Lee, and T. M. Rice, *Electron Glass*, Phys. Rev. Lett. **49**, 758–761 (1982).

[248] S. F. Edwards and P. W. Anderson, *Theory of spin glasses*, Journal of Physics F: Metal Physics **5**, 965 (1975).

[249] F. Brahona, *On the computional complexity of Ising spin glass models*, J. Phys. A: Math. Gen. **15**, 3241–3253 (1982).

[250] T. Kadowaki and H. Nishimori, *Quantum annealing in the transverse Ising model*, Phys. Rev. E **58**, 5355–5363 (1998).

[251] G. E. Santoro, R. Martoňák, E. Tosatti, and R. Car, *Theory of Quantum Annealing of an Ising Spin Glass*, Science **295**, 2427–2430 (2002).

[252] S. D. Baranovskii, A. L. Efros, B. L. Gelmont, and B. I. Shklovskii, *Coulomb gap in disordered systems: computer simulation*, Journal of Physics C: Solid State Physics **12**, 1023 (1979).

[253] N. Metropolis, *et al.*, *Equation of State Calculations by Fast Computing Machines*, The Journal of Chemical Physics **21**, 1087–1092 (1953).

[254] S. Kirkpatrick, C. D. Gelatt, and M. P. Vecchi, *Optimization by Simulated Annealing*, Science **220**, 671–680 (1983).

[255] A. Efros and B. Shklovskii, *Coulomb gap and low temperature conductivity of disordered systems*, Journal of Physics C: Solid State Physics **8**, L49 (1975).

[256] B. Surer, *et al.*, *Density of States and Critical Behavior of the Coulomb Glass*, Phys. Rev. Lett. **102**, 067205 (2009).

[257] M. Goethe and M. Palassini, *Phase Diagram, Correlation Gap, and Critical Properties of the Coulomb Glass*, Phys. Rev. Lett. **103**, 045702 (2009).

[258] J. G. Massey and M. Lee, *Direct Observation of the Coulomb Correlation Gap in a Nonmetallic Semiconductor, Si: B*, Phys. Rev. Lett. **75**, 4266–4269 (1995).

[259] V. Y. Butko, J. F. DiTusa, and P. W. Adams, *Coulomb Gap: How a Metal Film Becomes an Insulator*, Phys. Rev. Lett. **84**, 1543–1546 (2000).

[260] C. Stampfer, *et al.*, *Energy Gaps in Etched Graphene Nanoribbons*, Phys. Rev. Lett. **102**, 056403 (2009).

[261] B. Skinner and B. I. Shklovskii, *Theory of the random potential and conductivity at the surface of a topological insulator*, Phys. Rev. B **87**, 075454 (2013).

[262] E. Allahyarov E., K. Sandomirski, S.U. Egelhaaf, and H. Lowen, *Crystallization seeds favour crystallization only during initial growth*, Nature Communications **6** (2015).

[263] A. Möbius, M. Richter, and B. Drittler, *Coulomb gap in two- and three-dimensional systems: Simulation results for large samples*, Phys. Rev. B **45**, 11568–11579 (1992).

[264] M. Sarvestani, M. Schreiber, and T. Vojta, *Coulomb gap at finite temperatures*, Phys. Rev. B **52**, R3820–R3823 (1995).

[265] M. H. Overlin, L. A. Wong, and C. C. Yu, *Effect of increasing disorder on the critical behavior of a Coulomb system*, Phys. Rev. B **70**, 214203 (2004).

[266] M. Müller and L. B. Ioffe, *Glass Transition and the Coulomb Gap in Electron Glasses*, Phys. Rev. Lett. **93**, 256403 (2004).

[267] S. Pankov and V. Dobrosavljević, *Nonlinear Screening Theory of the Coulomb Glass*, Phys. Rev. Lett. **94**, 046402 (2005).

[268] M. Müller and S. Pankov, *Mean-field theory for the three-dimensional Coulomb glass*, Phys. Rev. B **75**, 144201 (2007).

[269] A. H. Castro Neto, *et al.*, *The electronic properties of graphene*, Rev. Mod. Phys. **81**, 109–162 (2009).

[270] S. Das Sarma, S. Adam, E. H. Hwang, and E. Rossi, *Electronic transport in two-dimensional graphene*, Rev. Mod. Phys. **83**, 407–470 (2011).

[271] J. D. Jackson, *Classical Electrodynamics*, 3rd edition (John Wiley & Sons, Inc., New Jersey, USA, 1991).

[272] L. H. Ho, A. P. Micolich, A. R. Hamilton, and O. P. Sushkov, *Ground-plane screening of Coulomb interactions in two-dimensional systems: How effectively can one two-dimensional system screen interactions in another*, Phys. Rev. B **80**, 155412 (2009).

[273] Q. T. Feng, *Numerical Research on the Potential Screening of Topological Insulators* (Research Internship, Universität zu Köln, 2015).

[274] O. Breunig, *private communication* (Cologne, 2016).